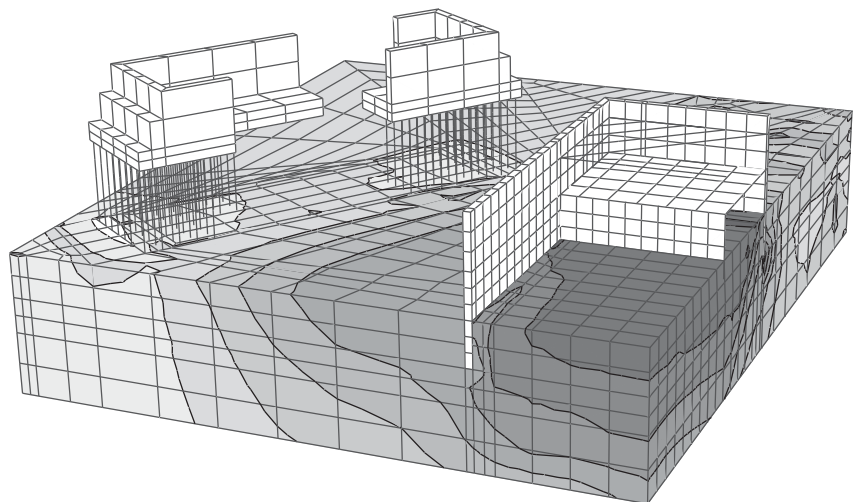


Universität Stuttgart

Small-Strain Stiffness of Soils and its Numerical Consequences

Thomas Benz



2007 - Mitteilung 55_{.PDFV2}
des Instituts für Geotechnik
Herausgeber P. A. Vermeer



Small-Strain Stiffness of Soils and its Numerical Consequences

Von der Fakultät für Bau- und Umweltingenieurwissenschaften
der Universität Stuttgart
zur Erlangung der Würde eines Doktors der Ingenieurwissenschaften (Dr.-Ing.)
genehmigte Abhandlung,

vorgelegt von
THOMAS BENZ
aus Tübingen

Hauptberichter: Prof. Dr.-Ing. Pieter A. Vermeer
Mitberichter: Prof. Guy T. Houlsby, MA DSc FREng FICE
Prof. Dr.-Ing. habil. Christian Mieke

Tag der mündlichen Prüfung: 20. September 2006

Institut für Geotechnik der Universität Stuttgart

2007

Mitteilung 55
des Instituts für Geotechnik
Universität Stuttgart, Germany, 2007

Editor:

Prof. Dr.-Ing. P. A. Vermeer

©Thomas Benz
Institut für Geotechnik
Universität Stuttgart
Pfaffenwaldring 35
70569 Stuttgart

All rights reserved. No part of this publication may be reproduced, stored in a retrieval system, or transmitted, in any form or by any means, electronic, mechanical, photocopying, recording, scanning or otherwise, without the permission in writing of the author.

Keywords: Small-strain stiffness, constitutive soil models

Printed by e.kurz + co, Stuttgart, Germany, 2007

ISBN 978-3-921837-55-9
(D93 - Dissertation, Universität Stuttgart)

Preface

In the seventies when I began to do research it was realised that soil behaviour was highly non-linear, but at that time we still underestimated the extent of it. At that time I should have had the book by Tsytoich (1973)¹, who taught soil mechanics at the Moscow Civil Engineering Institute. In 1976 this book was translated into English and I read it some ten years later. In this book Professor Tsytoich introduces a structural soil strength for stress increments as induced by external loads. Up to its structural strength soil behaves extremely stiff as there is no rearrangement of particles. Once stress increments exceed this threshold value, soils show the nowadays well-known stress-dependent stiffness, as for instance expressed by hyperbolic and/or exponential rules.

In practical analysis of foundation settlements the high initial small-strain stiffness has always been taken into account by the introduction of a so-called limit depth; below this depths strains were simply assumed to be negligibly small. Tsytoich does not use the name "limit depth", but calls it depth of the active compression zone. In finite element calculations I always accounted for this limit depth by using relatively shallow meshes. From a mathematical point of view the subsoil should obviously be modelled by infinite boundaries, but because of the small-strain stiffness only relatively shallow finite layer had to be discretised. On using the new constitutive model by Dr. Thomas Benz this dilemma on the depth of finite element meshes is non-existent. Boundaries can now be chosen so far away that they do not influence the computed stress distribution and the constitutive model ensures that the deep part of the mesh behaves virtually incompressible. The new HS-Small model is obviously not only relevant for the analysis of foundations, but also for the analysis of settlements due to tunnelling or deep excavations, as shown in this dissertation study.

The focus of this study is on the small-strain stiffness of non-cemented soils, but the model may also be applied to somewhat bonded soils. In recent years the behaviour of sensitive and/or structured clays has got much attention from researches and it would seem that their findings can also be modelled by the new HS-small model. In order to do so one may have to choose relatively large values for the strain range parameter $\gamma_{0.7}$, as used in the HS-Small model.

This thesis on a new computational model for the behaviour of soils at small strains is a scholarly piece of work, covering a very wide scope of material. The new model is developed, and calibrated, and in my opinion extremely useful for engineering problems. I am also indebted to the Federal Waterways Engineering and Research Institute in Karlsruhe who have sponsored this study. Within this institute Dr. Radu Schwab has advised Thomas Benz and it has been a real pleasure for me to work with them.

Pieter A. Vermeer
Stuttgart, March 2007

¹ N. Tsytoich. *Soil Mechanics*. Mir Publishers, Moscow, 1976. (translation from the 1973 Russian edition)

Acknowledgments

This Dissertation would not have been completed without the support and the patience of Professor Pieter Vermeer and Radu Schwab. I thank Pieter for giving me the opportunity to join his research team and for his extensive help. Likewise, I thank Radu for the unlimited help, advice and support he provided at the Federal Waterways Engineering and Research Institute (BAW). This Dissertation emanated from a research project that was initiated and funded by the BAW.

I thank all colleagues at the BAW in Karlsruhe and at the Institute of Geotechnical Engineering in Stuttgart for their friendly help and for the pleasant years. In particular, I am grateful to the following persons (in random order) for the exchange of thoughts, critical reviews, beta testing, proof reading, etc: Markus Herten, Marcin Cudny, Markus Wehnert, Sven Möller, Ayman Abed, Martino Leoni, Heiko Neher, Josef Hintner, Annette Lächler, Andrej Mey, Regina Kauther, Oliver Stelzer, Bernd Zweschper, Florian Scharinger, Professor Helmut Schweiger, Professor Dimitrios Kolymbas, Professor Christian Miehe, Professor Guy Houlsby and Gráinne McCloskey. Further, I thank Paul Bonnier from Plaxis B.V. for his valuable assistance with the numerical implementation.

I am very grateful to my family, in particular to my parents and to Marlis. Thanks to their support and love I was able to actually write this Dissertation.

Thomas Benz
Stuttgart, March 2007

Contents

1	Introduction	1
2	Terminology and definitions	5
3	Experimental evidence for small-strain stiffness	9
3.1	Small-strain stiffness measurements	10
3.1.1	Laboratory tests	12
3.1.1.1	Local measurements	12
3.1.1.2	Bender elements	12
3.1.1.3	Resonant column and torsional shear	13
3.1.2	In-situ tests	14
3.1.2.1	Cross hole seismic	14
3.1.2.2	Down hole seismics	15
3.1.2.3	Suspension logging	15
3.1.2.4	Seismic cone and seismic flat dilatometer	15
3.1.2.5	Spectral Analysis of Surface Waves (SASW)	15
3.2	Parameters that affect small-strain stiffness	16
3.2.1	The influence of shear strains and volumetric strain	16
3.2.2	The influence of confining stress	19
3.2.3	The influence of void ratio	21
3.2.4	The influence of soil plasticity	23
3.2.5	The influence of the overconsolidation ratio (OCR)	23
3.2.6	The influence of diagenesis	24
3.2.7	The influence of loading history	25
3.2.8	The influence of strain rate and inertia effects	28
3.2.9	Other factors that influence small-strain stiffness	30
3.3	Correlations for small-strain stiffness	31
3.3.1	Correlations between G_0 and e , p' and OCR	31
3.3.2	Correlations between G_0 and CPT, SPT and c_u	34
3.3.2.1	Cone penetration (CPT) and standard penetration (SPT)	34
3.3.2.2	Estimating G_0 from conventional tests - Chart by Alpan	35
3.3.3	Correlations for the stiffness modulus reduction curve	35
3.3.4	Summary	38

4	Small-strain stiffness at the soil particle level	39
4.1	Soil fabric and soil structure	39
4.2	Micromechanical considerations	41
4.2.1	The influence of strain amplitude	42
4.2.2	The influence of confining stress and void ratio	44
4.2.3	The influence of cementation	46
4.2.4	Summary	47
5	Existing small-strain stiffness constitutive models	49
5.1	A brief history of small strain modeling	49
5.2	The Simpson Brick model	50
5.3	Models known from soil dynamics	51
5.4	The Jardine model	53
5.5	Multi (or Infinite) surface models	55
5.6	Intergranular Strain for the Hypoplastic model	56
5.7	A critical review of small-strain stiffness models regarding their use in routine design	58
6	The Small-Strain Overlay model	59
6.1	Model formulation	59
6.1.1	Material history and history mapping	59
6.1.2	From strain history to stiffness	62
6.1.3	Initial loading and reloading	63
6.1.4	Effects of mean stress, void ratio, and OCR	65
6.2	A first model validation in element tests	66
6.2.1	Triaxial tests	66
6.2.2	Biaxial test	66
6.2.3	Strain response envelopes	69
6.2.4	Cyclic mobility	72
6.3	Thermodynamic considerations	72
7	HS-Small, a small-strain extension of the Hardening Soil model	75
7.1	Constitutive relations for infinitesimal plasticity	75
7.2	The Hardening Soil model	77
7.3	The HS-Small model	82
7.3.1	Small-Strain formulation	83
7.3.2	Mobilized dilatancy	85
7.3.3	Yield surface and plastic potential - HS-Small(MN) only	86
7.3.4	Generalized model formulation - HS-Small(MN) only	91
7.4	Local integration of the constitutive equations	94
7.4.1	Return mapping onto the yield surface	97
7.4.2	The closest point projection algorithm	98
7.4.3	The consistent algorithmic tangent stiffness tensor	100
7.4.4	Corner and apex problems	102

8	Validation and verification of the HS-Small model	105
8.1	Element tests	105
8.2	Boundary value problems	115
8.2.1	Tunnels	118
8.2.1.1	Steinhaldenfeld NATM tunnel	118
8.2.1.2	Heinenoord Tunnel	120
8.2.2	Excavations	121
8.2.2.1	Excavation in Berlin sand	123
8.2.2.2	Excavation in Ruple clay (Offenbach)	126
8.2.3	Spread Foundations	130
8.2.3.1	Texas A&M University spread footing on sand	130
8.2.4	Initialization of the HS-Small model	134
8.2.5	Capabilities and limitations of the HS-Small model	136
9	3D case study Sulfeld Lock	139
10	Conclusions	147
	Bibliography	150
A	Small-Strain Overly Fortran Code	167
B	Return mapping in Fortran code	173
C	Two surface return strategy	177
D	Material data	179

Abstract

This thesis is concerned with the stiffness of soils at small strains and constitutive models that can be applied to simulate this. The strain range in which soils can be considered truly elastic, i.e. where they recover from applied straining almost completely, is very small. With increasing strain amplitude, soil stiffness decays non-linearly: Plotting soil stiffness against $\log(\text{strain})$ yields characteristic S-shaped stiffness reduction curves. At the minimum strain which can be reliably measured in classical laboratory tests, i.e. tri-axial tests and oedometer tests without special instrumentation, soil stiffness is often less than half its initial value. If this non-linear variation of soil stiffness at small strains is considered in the analysis of soil-structure interaction, analysis results improve considerably: The width and shape of settlement troughs are more accurately modeled, excavation heave is reduced to a more realistic value, etc. The importance of small-strain stiffness in engineering practice is therefore well recognized. As the few existing small-strain stiffness models are either research orientated, and/or applicable to specific loading paths only, the objective of this thesis is to develop a small-strain stiffness model for the engineering community.

The newly developed Small-Strain Overlay model is based on the Hardin-Drnevich model [52]. Similar to the Hardin-Drnevich model, the Small-Strain Overlay model has two input parameters. Both input parameters have a clear physical meaning. For strains below the limit of classical laboratory testing, the Small-Strain Overlay model calculates the actual strain dependent stiffness. This stiffness can subsequently be deployed in many existing elastoplastic constitutive models. One of them is the well known Hardening Soil (HS) model as implemented in the finite element code PLAXIS V8 [21]. In this thesis, the Small-Strain Overlay model is combined with the HS model. The resulting *HS-Small* model is additionally enhanced by a Matsuoka-Nakai failure criterion. The HS-Small model is validated in element tests and various 2D and 3D boundary value problems. In the validation sequence, all effects that are commonly attributed to small-strain stiffness in soil-structure interaction can be recognized.

Although the thesis' main concern is with the development of a small-strain stiffness model, it also provides much information and data that may be helpful in using it. This information and data comprise an introduction to available small-strain stiffness testing methods, many empirical small-strain stiffness correlations and sample model applications.

After a short introduction to the topic in Chapter 1 and clarification of important terminology in Chapter 2, the thesis is organized thematically in three parts:

- **Tests and correlations - Chapter 3** Firstly, small-strain stiffness is discussed from an experimental point of view. The most important small-strain stiffness testing methods are introduced. Different parameters that affect small-strain stiffness are identified. The influence of the most significant of these parameters, regarding small-strain stiffness, is quantified in a collection of empirical correlations. In the absence of experimental data, these correlations may prove very helpful in using the new model.
- **Model building and formulation - Chapter 4 to 7** Secondly, the new Small-Strain Overlay model and its combination with the HS model is formulated. This main part of the thesis also contains a critical review of existing small-strain models. Important numerical aspects, for example the local integration of the incrementally formulated HS-Small equations, are presented at the end of the model building and formulation section.
- **Code verification and model validation - Chapter 8 to 9** Finally, the HS-Small model is validated in element tests, several 2D boundary value problems, and a state-of-the-art 3D boundary value problem. Initialization of the HS-Small model and a new possibility for verifying the proper extent of boundary conditions are discussed within the validation section as well.

Results from the study presented in this thesis are concluded in Chapter 10.

Zusammenfassung

Die vorliegende Arbeit beschäftigt sich mit der Steifigkeit von Geomaterialien unter kleinen Dehnungen und deren Beschreibung in Stoffmodellen. Der Dehnungsbereich, in dem Geomaterialien als elastisch angesehen werden können - in dem sich also nach einer Entlastung der ursprüngliche Dehnungszustand nahezu wieder einstellt - ist sehr klein. Außerhalb dieses sehr kleinen Bereiches zeigen Versuche eine nicht lineare Steifigkeitsabnahme mit zunehmender Dehnung. Aufgetragen über den Logarithmus der aufgebrauchten Dehnung, ergibt sich für die Abnahmefunktion der Steifigkeit eine charakteristische S-förmige Kurve. Bereits bei der kleinsten Dehnung, die noch zuverlässig in klassischen Laborversuchen (d.h. Dreiaxiale Versuche und Oedometer Versuche ohne spezielle Instrumentierung) gemessen werden kann, hat sich die Steifigkeit, bezogen auf ihren Ausgangswert, oftmals schon um mehr als die Hälfte reduziert. Bei Berücksichtigung dieses nicht-linearen Verhaltens in Boden-Bauwerk Interaktionsproblemen erhöht sich die Genauigkeit von berechneten Setzungen und Verschiebungen erheblich: Die laterale Ausdehnung und Form von Setzungsmulden wird erheblich besser abgebildet, Hebungen in Baugrubensohlen realistischer berechnet, etc. Die Bedeutung von nicht-linearem Bodenverhalten bei kleinen Dehnungen wird daher auch in der praktischen geotechnischen Entwurfs- und Bemessungsarbeit allgemein als hoch eingeschätzt. Da die wenigen bisher verfügbaren Stoffmodelle zur Abbildung dieses Verhaltens, aber hauptsächlich forschungsorientiert, oder nur für vorgegebene Belastungsarten anwendbar sind, wird in der vorliegenden Arbeit ein neues, praxisorientiertes Modell entwickelt.

Das neu entwickelte Small-Strain Overlay Model basiert auf einem hyperbolischen Ansatz nach Hardin und Drnevich [52]. In Analogie zu diesem hat das neu entwickelte Modell lediglich zwei Eingabeparameter. Beiden Parametern ist eine klare physikalische Bedeutung zugeordnet. Für Dehnungen unterhalb der Genauigkeitsgrenze von klassischen Laborversuchen ermittelt das Small-Strain Overlay Modell eine dehnungsabhängige, isotrope Steifigkeit, die dann als quasi-elastische Steifigkeit in einem beliebigen elastoplastischen Stoffmodell weiter verwendet werden kann. Ein solches elastoplastisches Modell ist z.B. das Hardening Soil Modell, welches in das FE Programm PLAXIS V8 [21] implementiert ist. Mit diesem wird das Small-Strain Overlay Modell in der vorliegenden Arbeit kombiniert. Die als *HS-Small* Modell bezeichnete Kombination wird zusätzlich durch ein optionales Matsuoka-Nakai Versagenskriterium erweitert. Das HS-Small Modell wird in einer Reihe von Element-Tests und einer Vielzahl von 2D und 3D Randwertproblemen validiert. In den Randwertproblemen können im Vergleich mit dem HS Modell, all die Phänomene beobachtet werden, die in der Regel der nicht-linearen Abnahme der Steifigkeit unter kleinen Dehnungen zugeschrieben werden.

Obwohl das primäre Ziel der vorliegenden Arbeit die Entwicklung eines Stoffmodells ist, enthält diese auch zahlreiche Informationen und Daten, die sich bei der Nutzung des neuen Modells als hilfreich herausstellen können. Diese Informationen und Daten bestehen unter anderem aus einer Übersicht über vorhandene Testverfahren zur Ermittlung der Bodensteifigkeit unter kleinen Dehnungen und einer Sammlung empirischer Korrelationen.

Nach einer kurzen Einführung in das Thema in Kapitel 1 und einiger Begriffsklärungen in Kapitel 2, untergliedert sich die Arbeit in drei thematische Teile:

- **Versuche und Korrelationen - Kapitel 3**

Zunächst wird die Bodensteifigkeit unter kleinen Dehnungen unter einem experimentellen Gesichtspunkt betrachtet. Zum einen werden die wichtigsten Versuche zu deren Bestimmung vorgestellt, zum anderen wird der Einfluss verschiedener Faktoren, wie z.B. bodenmechanische Parameter und Belastungsgeschichte, auf die Versuchsergebnisse untersucht. Diese Untersuchung mündet in einer Sammlung empirischer Korrelationen, welche insbesondere dann hilfreich sind, wenn das Small-Strain Overlay Modell (oder des HS-Small Modell) angewendet werden soll und keine Versuchsdaten vorliegen.

- **Modellbildung und Formulierung - Kapitel 4 bis 7**

Im zweiten und umfangreichsten Teil dieser Arbeit wird das Small-Strain Overlay Model und das HS-Small Model entwickelt. Neben den konstituierenden Gleichungen umfasst dieser Teil auch einen kritischen Überblick über bereits vorhandene Stoffgesetze, die Steifigkeit von Böden unter kleinen Dehnungen prinzipiell beschreiben können. Numerische Aspekte, wie z.B. die Integration der inkrementell formulierten konstitutiven Gleichungen werden am Ende des zweiten Teils der Arbeit behandelt.

- **Kontrolle der Implementierung und Modell Validierung - Kapitel 8 bis 9**

Letztlich wird das HS-Small Modell in einer Reihe von Elementversuchen sowie einiger 2D Randwertprobleme und eines umfangreichen 3D Randwertproblems überprüft und validiert. An Hand der Randwertprobleme wird des Weiteren die Möglichkeiten der Modellinitialisierung diskutiert sowie eine Bewertungsmethode für die Randabstände von Berechnungsausschnitten vorgeschlagen.

Die Schlußfolgerungen aus der vorliegenden Arbeit sind in Kapitel 10 zusammengefaßt.

Chapter 1

Introduction

“One of the major problems in ground engineering in the 1970s and earlier was the apparent difference between the stiffness of soils measured in laboratory tests and those back-calculated from observations of ground movements (e.g. Cole & Burland [29], St John [84], Wroth [195], Burland [23]). These differences have now largely been reconciled through the understanding of the principal features of soil stiffness and, in particular, the very important influence of non-linearity. This is one of the major achievements of geotechnical engineering research over the past 30 years.” (Atkinson [7])

In particular the non-linear influence of strain on soil stiffness has been extensively investigated over the past decades. The maximum strain at which soils exhibit almost fully recoverable behavior is found to be very small. The very small-strain stiffness associated with this strain range, i.e. shear strains $\gamma_s \leq 1 \times 10^{-6}$, is believed to be a fundamental property of all types of geotechnical materials including clays, silts, sands, gravels, and rocks (Tatsuoka et al., 2001) under static and dynamic loading (Burland [24]) and for drained and undrained loading conditions (Lo Presti et al. [140]). With increasing strain, soil stiffness decays non-linearly. On a logarithmic scale, stiffness reduction curves exhibit a characteristic S-shape, see Figure 1.1.

The smallest shear strain that can be reliably measured in conventional soil testing, e.g. triaxial or oedometer tests without special instrumentation, is $\gamma_s \approx 1 \times 10^{-3}$. By definition Atkinson [7] terms strains smaller than the limit of classical laboratory testing ($\gamma_s < 1 \times 10^{-3}$), small strains. Strains, $\gamma_s > 1 \times 10^{-3}$ are termed large or larger strains. The limit of classical laboratory testing coincides at the same time with characteristic shear strains that can be measured near geotechnical structures (Figure 1.1). However, the soil stiffness that should be used in the analysis of geotechnical structures is not the one that relates to these final strains. Instead, very small-strain soil stiffness and its non-linear dependency on strain amplitude should be properly taken into account in all analysis that strive for reliable predictions of displacements. The Rankine lectures by Simpson [168] and Atkinson [7], or the Bjerrum Memorial lecture by Burland [24] are just a few occasions where this has been highlighted. As yet, small-strain stiffness has not been widely implemented in engineering practice. Considering numerical analysis, this may be due to a lack of capable, yet user-friendly constitutive models. The main objective of this thesis is to provide such a capable and sufficiently simple small-strain stiffness model for engineering practice.

The user-friendliness of a constitutive model largely depends on the input parameters. They should be limited in their number, easy to understand in their physical meaning, and easy to quantify based on test data or experience. The level of sophistication

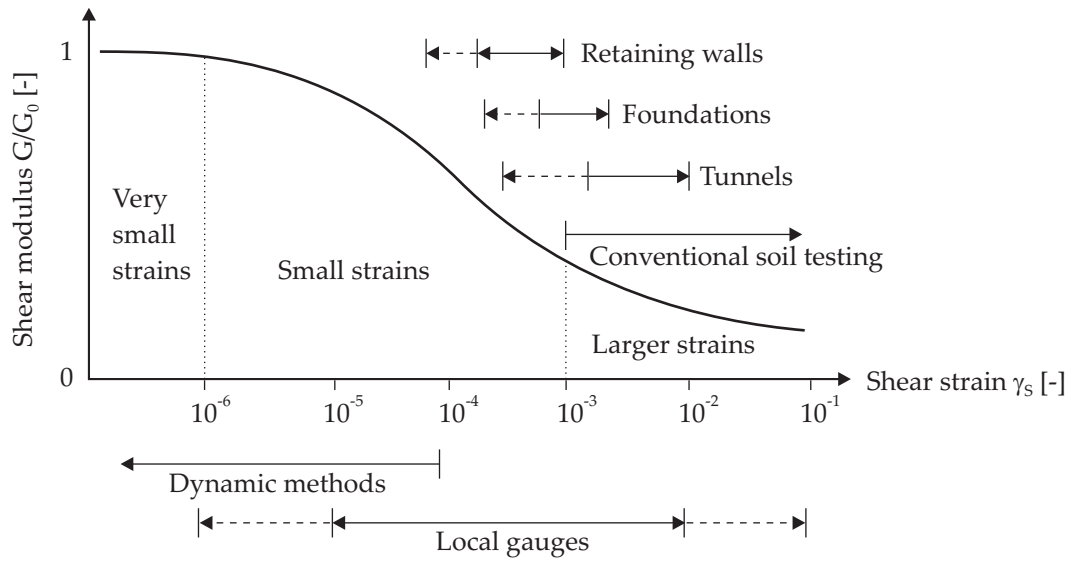


Figure 1.1: Characteristic stiffness-strain behavior of soil with typical strain ranges for laboratory tests and structures (after Atkinson & Sallfors [9] and Mair [109])

of a model is tied to the extent to which it is able to reproduce the experimentally observed functional relationships. The premise of fulfilling the objective defined above is therefore a thorough description of experimental observations. It is only through this that the model's parameters and mechanisms can be decided upon, or in the words of Ernst Mach: "The description of functional relationships is an explanation in itself". The methodology applied in this thesis is mostly inductive reasoning. Figure 1.2 explains the terminology used to describe the different stages within the model building and validation process. The model is formulated incrementally. Therefore the code verification and model validation are regarded as separate processes.

Although the main objective of this thesis is the development of a simple and capable small-strain stiffness constitutive model, it also acts as a compilation of information and data that might be helpful in using it. This information and data comprise empirical correlations that can be useful in quantifying small-strain stiffness, an introduction to available testing methods and sample applications in 2- and 3-dimensional finite element analysis.

The outline of this thesis is as follows:

- Chapter 2 introduces some definitions and conventions used throughout the thesis.
- Chapter 3 concentrates on the experimental aspects and the quantitative description of small-strain stiffness. After introducing the experimental concepts of laboratory and in-situ testing, the influence of various parameters on small-strain stiffness is studied. Readily available test data and correlations from literature are presented at the end of this chapter.

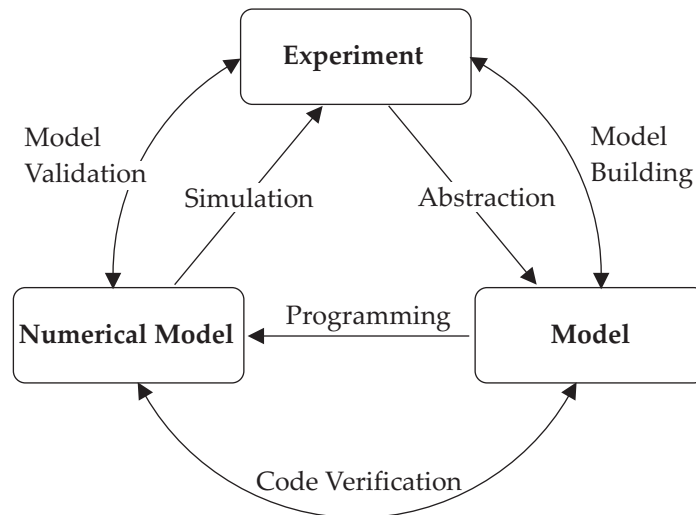


Figure 1.2: Terminology used in the model building and validation process.

- Chapter 4 looks at the small-strain stiffness phenomena at a micromechanical level. This deductive part of the thesis is mainly aimed at providing a more fundamental explanation of some observations made in Chapter 3.
- Chapter 5 summarizes the best known existing small-strain stiffness models. These range from simple 1D models in stress or strain space to complex formulations, for example the Intergranular Strain [129] concept. All models are briefly appraised regarding their value in practical applications.
- Chapter 6 introduces a new small-strain stiffness model, the Small-Strain Overlay model. The Small-Strain Overlay model is a straight-forward model that is largely based on the well known Hardin-Drnevich relation [52], which is introduced in Chapter 5. Its dependency on the material's strain history, however, is formulated in multi-axial strain space. A first model validation is undertaken in a number of element tests on sandy soils and clays.
- In Chapter 7 the Small-Strain Overlay model is combined with an existing elastoplastic model. The elastoplastic model chosen for this purpose is the Hardening Soil (HS) model as implemented in the finite element code PLAXIS V8. The resulting *HS-Small* model is further enhanced with the Matsuoka-Nakai [114] failure criterion and a modified flow rule. A possible implicit integration algorithm for the new model is presented at the end of the chapter where other numerical issues are briefly discussed as well.
- Chapter 8 covers the verification process of the HS-Small model. This includes the evaluation of numerous element tests and boundary value problems from the following problem categories: deep excavations, tunnels, and foundations. In analyzing the boundary value problems, the impact of the HS-Small model on the

different problem categories is quantified. More general issues, as for example possible initialization procedures for the HS-Small model, are discussed at the end of this chapter.

- Chapter 9 contains a case study of the large navigable lock, Sülfeld. The lock Sülfeld is currently being reconstructed right next to the high-speed railway link between Hannover and Berlin. A state of the art 3D finite element analysis of the deep excavation is conducted in order to predict the construction activity's influence on the railway tracks. It is shown how the HS-Small model could significantly enhance the reliability of this analysis.
- Finally, Chapter 10 presents the main conclusions of this study.

Chapter 2

Terminology and definitions

This thesis is mainly concerned with pre-failure deformation characteristics of soils. Continuum mechanics is generally employed as the analysis tool. In soil mechanics however, there is not a clear consensus in how to define some stress and strain properties in this framework (e.g. sign convention). This chapter briefly introduces the stress and strain definitions, notations, and invariants used in the following chapters.

- **Tensor notation** Tensorial quantities are generally expressed in indicial notation. The order of a tensor is indicated by the number of unrepeated (free) subscripts. Whenever a subscript appears exactly twice in a product, that subscript will take on the values 1, 2, 3 successively, and the resulting terms are summed (Einstein's summation convention). The Kronecker delta δ_{ij} takes the value 1 or 0 if $i = j$ or $i \neq j$ respectively. In the rare occasions where indicial notation is not used in this thesis, first-order tensors (vectors) are denoted by lowercase Latin or Greek bold letters, second-order tensors are denoted by uppercase Latin or Greek bold letters, and fourth-order tensors are denoted by Calligraphic letters.
- **Stress and strain** Infinitesimal deformation theory is applied. Cauchy stress is related to linearized infinitesimal strain. Eigenvalues of stress and strain tensors (principal stresses and strains) are denoted by one subscript only, e.g. σ_i and ε_i with $i = 1, 2, 3$. Without loss of generality, let

$$\sigma_1 \geq \sigma_2 \geq \sigma_3. \quad (2.1)$$

The Roscoe stress invariants p (mean stress) and q (deviatoric stress), are defined as:

$$p = \frac{\sigma_{ii}}{3} \quad \text{and} \quad q = \sqrt{\frac{3}{2}(\sigma_{ij} - \frac{1}{3}\delta_{ij}\sigma_{kk})(\sigma_{ij} - \frac{1}{3}\delta_{ij}\sigma_{kk})}, \quad (2.2)$$

In triaxial compression with $\sigma_1 \geq \sigma_2 = \sigma_3$, the Roscoe invariants simplify to

$$p = \frac{1}{3}(\sigma_{\text{axial}} + 2\sigma_{\text{lateral}}) \quad (2.3)$$

$$q = (\sigma_{\text{axial}} - \sigma_{\text{lateral}}). \quad (2.4)$$

In analogy to the stress invariants, volumetric strain ε_v and shear strain γ_s are defined as:

$$\varepsilon_v = \varepsilon_{ii} \quad \text{and} \quad \gamma_s = \sqrt{\frac{3}{2}(\varepsilon_{ij} - \frac{1}{3}\delta_{ij}\varepsilon_{kk})(\varepsilon_{ij} - \frac{1}{3}\delta_{ij}\varepsilon_{kk})}, \quad (2.5)$$

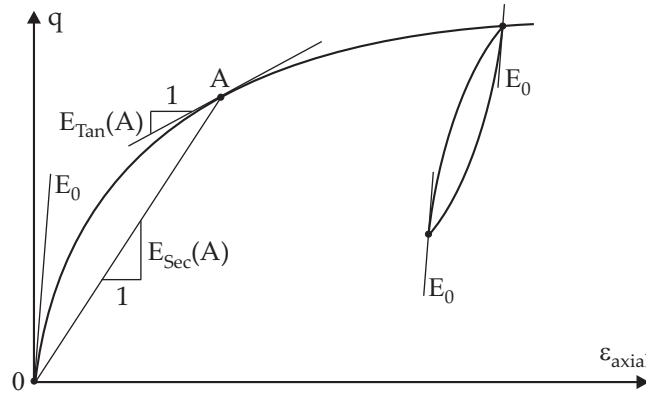


Figure 2.1: Definition of secant and tangent moduli in triaxial stress-strain space.

which simplify to

$$\varepsilon_v = \varepsilon_{axial} + 2\varepsilon_{lateral} \quad (2.6)$$

$$\gamma_s = (\varepsilon_{axial} - \varepsilon_{lateral}), \quad (2.7)$$

in triaxial compression. Shear strain relates to the deviatoric strain invariant ε_q as follows:

$$\gamma_s = \frac{3}{2}\varepsilon_q = \frac{3}{2}\sqrt{\frac{2}{3}(\varepsilon_{ij} - \frac{1}{3}\delta_{ij}\varepsilon_{kk})(\varepsilon_{ij} - \frac{1}{3}\delta_{ij}\varepsilon_{kk})}. \quad (2.8)$$

Other invariants of the stress tensor are later introduced in Chapter 7, where they are deployed to describe yield criteria.

- **Sign convention** The sign convention of soil mechanics is used: Compressive stress and strain is taken as positive. Tensile stress and strain is taken as negative.
- **Total and effective quantities** Effective stress is generally denoted by a prime, e.g. p' . An exception to this rule is made in Chapter 7 where effective stresses are considered exclusively. Friction angle and cohesion are always taken to be effective values without any special indication by a prime.
- **Tangent and secant moduli** Tangent stiffness is used in numerical calculations. Secant stiffness is generally used to describe experimental results. Figure 2.1 depicts the definition and difference of tangent and secant stiffness moduli.
- **Very small, small, and larger strains** Very small strains are defined as strains at which a soil exhibits almost fully recoverable, or almost elastic behavior. Considering that there can be no *true* elasticity in soils, the very small strain range is difficult to quantify. For the purpose of this thesis, the transition between very small strains and small strains is assumed in the range $1 \times 10^{-6} \leq \gamma_s \leq 1 \times 10^{-5}$. The borderline between small strains and larger strains is commonly drawn at the limit of classical

laboratory testing, which is according to Atkinson [7] $\gamma_s \approx 1 \times 10^{-3}$ (see Figure 1.1). In this thesis however, the limit of classical laboratory testing is taken as the shear strain where the stiffness modulus reduction curve equals the unloading-reloading stiffness observed in classical laboratory testing.

- **Small-strain stiffness** Small-strain stiffness is the stiffness of soils at small shear strains. The maximum soil stiffness found in stiffness reduction curves is in this thesis referred to as initial, or maximum soil stiffness. Initial shear and Young's moduli are denoted as G_0 and E_0 respectively. Often, initial soil stiffness is also called very small-strain stiffness, as it is commonly associated to the very-small-strain range as defined above. In this thesis, small-strain stiffness is always discussed along with the respective stiffness reduction curve in the range of very small and small strains. The term *small-strain stiffness model* consequently refers in this thesis to a constitutive soil model that is applicable to very small and small strains; *Small-strain stiffness measurements* include stiffness measurements at very small and small strains; etc.

Chapter 3

Experimental evidence for small-strain stiffness

From dynamic response analysis, it has been found that "most soils have curvilinear stress-strain relationships as shown in Figure 3.1. The shear modulus is usually expressed as the secant modulus determined by the extreme points on the hysteresis loop while the damping factor is proportional to the area inside the hysteresis loop. It is readily apparent, that each of this properties will depend on the magnitude of the strain for which the hysteresis loop is determined and thus, both shear moduli and damping factors must be determined as functions of the induced strain in a soil specimen or soil deposit." (Seed & Idriss [162])

In soil dynamics, small-strain stiffness has been a well known phenomena for a long time. The above conclusions by Seed & Idriss for example were drawn more than 35 years ago. In static analysis however, the findings from soil dynamics have long been disregarded, or even considered not to be applicable. Seemingly differences between static and dynamic soil stiffness have been attributed to the nature of loading (e.g. inertia forces and strain rate effects) rather than to the magnitude of applied strain, which is generally small in dynamic conditions (earthquakes excluded).

Nowadays, it is commonly accepted that inertia forces and strain rate have little influ-

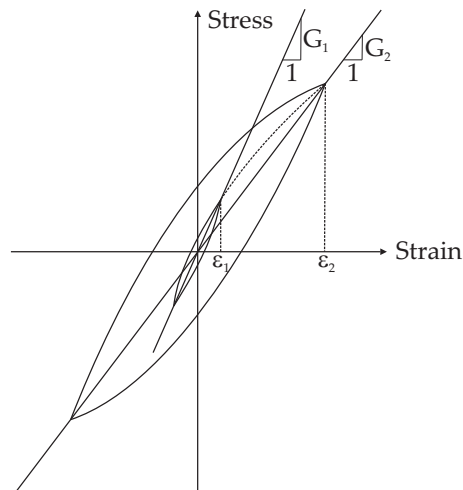


Figure 3.1: Stress-strain hysteresis loops presented by Seed & Idriss [162]. The secant shear modulus of a closed stress-strain loop decays monotonically with its strain amplitude: $G_2 < G_1$ for $\varepsilon_2 > \varepsilon_1$.

ence on small-strain stiffness. Experimental evidence for the influence of strain rate, but also other parameters that more significantly affect small-strain stiffness is presented in this chapter. This chapter is exclusively dedicated to the experimental aspects of small-strain stiffness. It provides a brief summary of laboratory and in-situ small-strain stiffness testing methods and a discussion of quantitative experimental findings.

3.1 Small-strain stiffness measurements

Small-strain soil stiffness can be measured in laboratory and/or field tests. Applicable laboratory tests are triaxial tests with local strain measurements (e.g. Jardine et al. [80]); bender elements (e.g. Shirley & Hampton [165], Dyvik & Madshus [37], Brignoli et al. [20]); resonant column (e.g. Hardin & Drnevich [53]); and torsional shear tests. Resonant column and torsional shear devices are both available for hollow cylindrical samples, as well (Broms & Casbarian [22]). Field or in-situ tests for indirect identification of very small-strain stiffness generally rely on geophysical principles: cross hole seismic (Stokoe & Woods [175]), down hole seismic (e.g. Woods [194]), suspension logging (e.g. Nigbor & Imai, [130]), seismic cone (e.g. Robertson et al. [150]), seismic flat dilatometer (e.g. Hepton [56]), and spectral analysis of surface waves (e.g. Stokoe et al. [174]) are most commonly used.

Surface based seismic reflection and refraction methods are nowadays less often used to acquire very small-strain stiffness data. The impedance contrasts in shallow soil layers are often not pronounced enough to allow these methods to compete with the aforementioned in-situ tests in terms of data resolution and reliability. From a historical perspective however, these were the first geophysical methods, which Engineers and Geologists used for subsurface characterization, from the beginning of the 20th century. Though it was not until the 1960s and 1970s, that geophysics also became popular in geotechnical engineering. Back then, borehole seismic techniques were first employed for site characterization. The next major development of seismic techniques for use in geotechnical engineering occurred in 1984 when the seismic cone penetration test was presented. The latest development is the spectral analysis of surface waves, which took off at the end of the 1990s.

Some of the laboratory tests and all of the in-situ tests mentioned above are indirect tests. In contrast to direct tests, indirect tests measure other quantities than those desired and relate them through mathematical relationships. Seismic techniques, as indirect testing methods for very small-strain stiffness, yield wave propagation velocity profiles. Assuming linear elastic material behavior, elastic stiffness relates to wave propagation velocity as follows:

$$v_p = \sqrt{\frac{\lambda + 2G}{\rho}} \quad \text{and} \quad (3.1)$$

$$v_s = \sqrt{\frac{G}{\rho}} \quad (3.2)$$

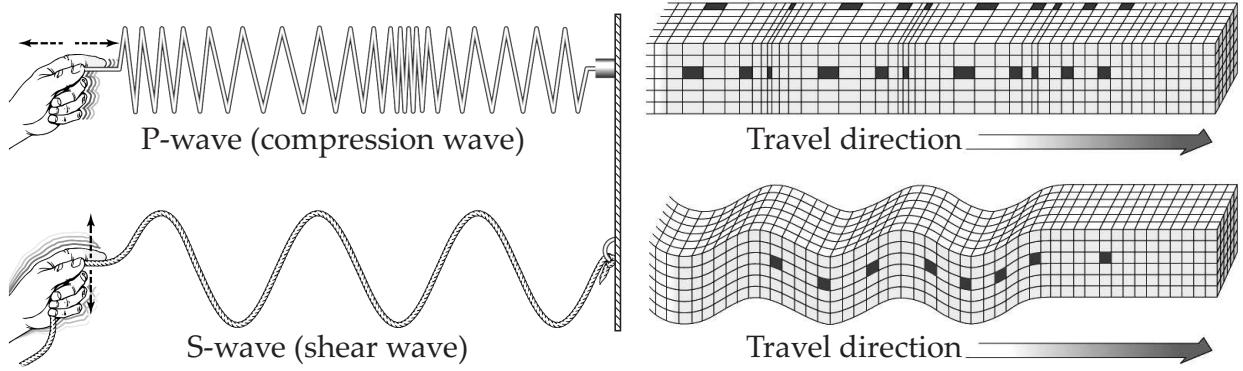


Figure 3.2: P-wave (top) and S-wave (bottom) particle motion: The particle motion in P-waves is longitudinal whereas it is transverse in S-waves. The particle motion vector in the plane perpendicular to the direction of propagation, is referred to as polarization (only S-waves).

where v_p is the propagation velocity of pressure, or primary (P-) waves, v_s is the propagation velocity of shear or secondary (S-) waves, and λ , and G are Lamé's constants (G is also termed the shear modulus). The expression of Lamé's constants as a function of Young's modulus and Poisson's ratio is generally more convenient for engineers:

$$G = \frac{E}{2(1 + \nu)} \quad (3.3)$$

$$\lambda = \frac{\nu E}{(1 + \nu)(1 - 2\nu)}. \quad (3.4)$$

Figure 3.2 illustrates the particle motion in P- and S-waves.

Seismic techniques are said to belong to the class of dynamic tests because they operate at higher frequencies than static, or quasi-static tests as for example triaxial tests with local strain gauges. In static and quasi-static tests, effects that are due to inertia forces are considered negligible. It is common practice to distinguish between quasi-static and dynamic tests based on the frequency of loading. The AK 1.4 of the German Geotechnical Association (DGGT) for example, suggests to consider loading frequencies below 10 Hz as quasi-static [156]. Unfortunately, this definition is useless in monotonic loading situations, e.g. impact situations. In repeated loading its shortcoming is that it does not consider load amplitudes. Assuming a harmonic excitation of the form $a = a_{max} \sin \omega t$, where a_{max} is the amplitude of displacement, stress gradients due to inertia effects are proportional to $a_{max} \omega^2$. Only when these stress gradients are small compared to the overall stress level divided by some characteristic length, one can assume quasi-static loading. Stress gradients can in this way serve as an indicator for quasi-static or dynamic loading in tests with no load reversals (monotonic tests) and tests with at least one load reversal (cyclic tests). From this, it is clear that generally but by no means necessarily, dynamic tests are at the same time cyclic tests.

What follows in the remaining part of this section, is a more detailed discussion of the

laboratory and in-situ tests mentioned above, excluding surface based seismic refraction and reflection. The latter is covered in more detailed in Forel et al. [42], but will not be repeated here due to its limited applicability to geotechnical engineering.

3.1.1 Laboratory tests

3.1.1.1 Local measurements

Conventionally, axial strain in triaxial testing is calculated from the relative movement between the apparatus' top cap and its fixed base pedestal. Besides possible small compliances of the apparatus' loading system, sample bedding is a major problem in deriving reliable small-strain stiffness data from such tests: The sample bedding at the beginning of the test is neither perfect, nor guarantees uniform straining.

Imperfections in sample bedding are generally due to the sample preparation process. It is very likely that the sample does not have perfectly parallel and smooth ends, so that the top cap may not have full contact instantaneously. In this case there is a rapid deformation at the beginning of the test until the cap is bedded properly. At this point, however, the small-strain range may already have been exceeded. On top of that, the restraints in the bedding planes cause the sample to strain non-uniformly over its height. Therefore, most conventional triaxial tests tend to give apparent soil stiffnesses much lower than those inferred from dynamic testing with small displacement amplitudes (Jardine et al. [80]). One solution is to equip the test specimen with local strain transducers.

Local strain transducers are not sensitive to compliances of the testing equipment (other than the transducer itself) and imperfect sample bedding. They cannot completely eliminate the effects of bedding restraints though. An appropriate ratio of sample height to diameter is therefore still recommended. The weight of the instrumentation is to be compensated by an adequate suspension. For very small-strain stiffness measurements, transducer resolution should be $\varepsilon \leq 5 \times 10^{-5}$. Transducers that can achieve this high resolution and which can at the same time be integrated in triaxial cells are e.g. Linear Variable Differential Transformers (LVDT), Digital Displacement Transducers, Hall Effect Transducers, etc.

3.1.1.2 Bender elements

Carrying out small-strain stiffness measurements with local strain transducers on a regular basis is expensive. Local measurements are therefore generally confined to research projects. The measurement of wave velocities in triaxial samples is less costly. Low voltage piezo-ceramic transducers named "bender elements" have been commonly used for this purpose since their introduction at the end of the 1970s (Shirley & Hampton [165]). Bender elements can both transmit and receive signals, and thus can readily measure wave velocities in a sample when supplied on both sides of it. The element itself is a thin piezo-ceramic plate that makes contact to the sample (Figure 3.3). Bender elements can be clamped to samples for measuring horizontal traveltimes, as well.

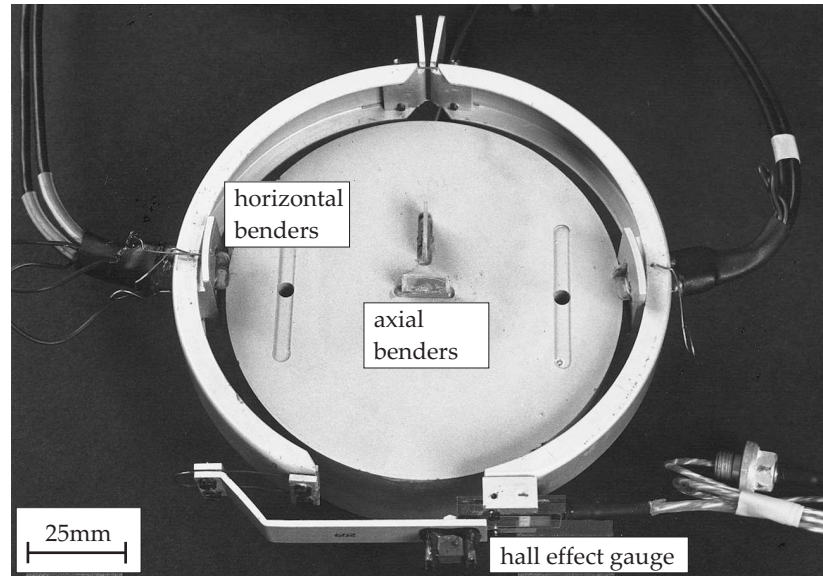


Figure 3.3: Bender elements mounted in a top plate and to a radial belt. Photograph by Pennington et al. [136]

Originally, bender elements could transmit and receive S-waves only. Providing a sample's density ρ is known, the knowledge of shear wave velocity is sufficient to calculate its shear modulus G_0 from Equation 3.2. Unfortunately, S-waves are slower than P-waves ($v_s \approx \frac{1}{2}v_p$) so that they always have noisy first arrivals (in this context, reflected P-waves and surface waves are considered noise). Less valuable is the isolated knowledge of P-wave velocity as this is governed by both elastic constants. Ideal is the knowledge of both, S and P wave velocities, which can be simultaneously measured using newly developed bender-extender elements (Lings & Greening [104]).

Compared to local strain transducers, the obvious disadvantage of bender, and bender-extender elements is their restriction to the very small-strain range, e.g. $\gamma_s < 1 \times 10^{-6}$. The geophysical nature of the indirect bender element stiffness measurements can sometimes be troublesome too: Due to the low signal to noise ratio, the time at which the first wave arrives is usually subject to interpretation. Sample preparation on the other hand is simple. Commercially offered bender element mounts for top cap and base pedestal along with user-friendly software promote bender elements as a feasible option for routine lab testing. Figure 3.3 shows the integration of bender elements into a top cap and into a radial belt.

3.1.1.3 Resonant column and torsional shear

Resonant column and torsional shear devices can load soil samples not only triaxially but also torsionally. The basic difference between resonant column and torsional shear testing is the frequency and amplitude of loading.

Torsional shear tests are static, or quasi-static cyclic tests where an axially confined

cylindrical sample is sheared through rotating one of the apparatus' end plates. The basic advantage of torsional shear testing over triaxial testing is that the bedding has a minimum effect on the test result. Resonant column tests are cyclic tests, in which an axially confined cylindrical soil specimen is set in a fundamental mode of vibration by means of torsional or longitudinal excitation of one of its ends. Once the fundamental mode of resonance frequency is established, the measured resonant frequency can be related to the column's stiffness using a theoretical elastic solution, which provides satisfactory results in the very small-strain range.

Nowadays, resonant column testing and torsional shear testing can usually be accomplished within a single device. Various dynamic boundary conditions introduced in different test devices have only negligible effects on test results ([87]). A further refinement of resonant column and torsional shear tests is the hollow cylinder apparatus. Obeying the same principles, the hollow cylinder apparatus allows for pressurizing an additional inner cell in the now tubular or hollow sample. Torsional shear stress acting on the sample is now well defined. Additionally, an independent inner cell pressure allows rotation of the major principal stress axis, at any angle from the horizontal to the vertical. Unfortunately, all of these tests, resonant column, torsional shear, and hollow cylinder are expensive and are therefore rarely used in routine design.

3.1.2 In-situ tests

3.1.2.1 Cross hole seismic

Cross hole seismic surveys require a minimum of two vertically drilled boreholes. In one of the boreholes an energy source is lowered to the target soil layer's depth. In the neighboring borehole(s), at least one receiver is placed at the same depth. From the source signal's first arrival at the receiver station(s), it is possible to calculate horizontal wave propagation velocities. When readings are taken at different source and receiver depths, classical cross hole seismic tests can provide propagation velocities for all, ideally horizontal, soil layers. From these velocities, maximum soil stiffness is calculated in the same way as in the bender element test, but often without knowing the soil's exact density.

Nowadays, cross hole tomography usually replaces conventional cross hole seismic tests. Cross hole tomography uses a string of receivers instead of just one receiver, so that multiple ray paths can be recorded for a single source signal. The additional information recorded can then, through tomographic techniques, be inverted to velocity and stiffness profiles with improved spatial resolution.

Cross hole surveying is probably the most reliable in-situ small-strain stiffness testing method, but also the most expensive one: Shear wave borehole sources generate too little energy to obtain economical borehole spacings. On top of that, the distances between the boreholes must be known exactly, which typically demands inclinometer readings in each borehole.

3.1.2.2 Down hole seismics

Down hole seismic surveys require the drilling of only one borehole, in which a string of receivers is placed. The energy source, generally a hammer blow against a steel plank, is now located at the surface. Compared to cross hole seismic, the troublesome borehole source and the costs of multiple boreholes are eliminated. The main drawback of down hole seismic tests are the almost vertical and very lengthy raypaths of sometimes additionally refracted waves. Down hole surveys can thus be considered an integral measurement over different soil layers. However, having receiver recordings from different depths, the initial stiffness of different soil layers can be back-calculated.

3.1.2.3 Suspension logging

Similar to down hole seismic surveys, suspension logging provides velocity data from a single borehole. In suspension logging, source and receivers are placed in the same borehole where they are separated by a few meters drilling suspension only. Unlike in all other seismic techniques reviewed so far, the focus in suspension logging is not on wave propagation velocity of direct waves, but rather on the propagation velocities of waves that travel along the borehole's walls. Suspension logging can generate an approximate very small-strain stiffness profile of the borehole's vicinity.

3.1.2.4 Seismic cone and seismic flat dilatometer

The commercially available seismic cone and seismic flat dilatometer are hybrid tests that combine down hole seismic surveying with penetration, and dilatometer testing respectively. Instead of placing seismic receivers in a predrilled hole, they are now pushed in. The energy source is located at the surface like in conventional down hole surveys. Standard- or cone penetration, pressuremeter, and flat dilatometer testing devices without integrated seismic receivers cannot deliver very small-strain soil stiffness directly. Still, they can provide some less reliable small-strain information by means of integral deformation measurements or empirical relationships.

3.1.2.5 Spectral Analysis of Surface Waves (SASW)

Spectral Analysis of Surface Waves (SASW) is a non-intrusive geophysical technique for evaluating subsurface shear wave velocity profiles. Using this technique, source and receivers are both located at the surface. Instead of analyzing traveltimes of P- and S-body waves as in most other seismic techniques, SASW uses the dispersive character of Rayleigh surface waves. Long wavelength, low frequency Rayleigh waves penetrate the subsurface deeper than high frequency Rayleigh waves. Since the propagation velocity of waves increases with increasing confining pressure and hence depth, longer wavelength (low frequency) waves travel faster than shorter wavelength (high frequency) waves. The ease and speed of SASW measurements in the field combined with automated data processing and inversion techniques probably makes SASW the most efficient in-situ small-strain stiffness exploration technique.

3.2 Parameters that affect small-strain stiffness

Based on a literature review, the influence of various parameters on small-strain stiffness is identified and quantified here. In order to ease the quantitative description of small-strain stiffness, and in particular its decay, the following notation is introduced:

- G_0 and E_0 denote the maximum small-strain shear modulus and Young's modulus respectively.
- $\gamma_{0.7}$ denotes the shear strain, at which the shear modulus G is decayed to 70 percent of its initial value G_0 .

The tuples $(G_0, 0)$ and $(G_{0.7}, \gamma_{0.7})$ mark two points of the small-strain stiffness degradation curve. The entire degradation curve can be reasonably well extrapolated from these two points, for example by using the Hardin-Drnevich [52] relationship, which is introduced later in this chapter. In soil dynamics, the decay of small-strain stiffness with applied strain is usually quantified as damping. Damping is a measure for energy dissipation in closed load cycles. With the Hardin-Drnevich model, the shear strain $\gamma_{0.7}$ can be related to damping: The larger the value of $\gamma_{0.7}$, the less the damping. The specific threshold value of 70 percent is chosen here following a recommendation of Santos & Correia [155] which is introduced later in this chapter, as well.

Strain amplitude, void ratio, confining stress, and the amount of in-situ interparticle bonding turn out to be the most important parameters that affect the stiffness of soils at small strains. This result was basically published by Seed & Idris [162] as early as 1970, particle bonding excluded. Their results are illustrated in Figure 3.4. A complete list of parameters that will be discussed in the following section is given in Table 3.1, which is mainly based on the works by Hardin & Drnevich [53]. In Table 3.1, the original classification of parameter importance by Hardin & Drnevich was updated wherever more recent research results suggested it.

3.2.1 The influence of shear strains and volumetric strain

Soils conserve their initial stiffness G_0 only at very small strains. With increasing strain, soil stiffness decreases. Soils instantaneously recover their initial stiffness upon load reversals. Therefore, the accumulated strain since the last load reversal is the main variable in small-strain stiffness modulus reduction. With the help of scalar valued strain invariants, the accumulated strain since the last load reversal is usually expressed as strain amplitude. In primary or virgin loading, strain amplitude refers to the reference configuration at the onset of loading.

In literature, small-strain stiffness data is almost exclusively treated as a function of deviatoric strain amplitudes, e.g. shear strain γ_s . Although small-strain stiffness has first been recognized and analyzed in soil dynamics, the background of this is not only historical. In deviatoric loading, damping in the small strain range is less during unloading-reloading than in primary loading, but still of the same magnitude (see Masing's rule later in this chapter). In isotropic loading, damping in small strain unloading-reloading

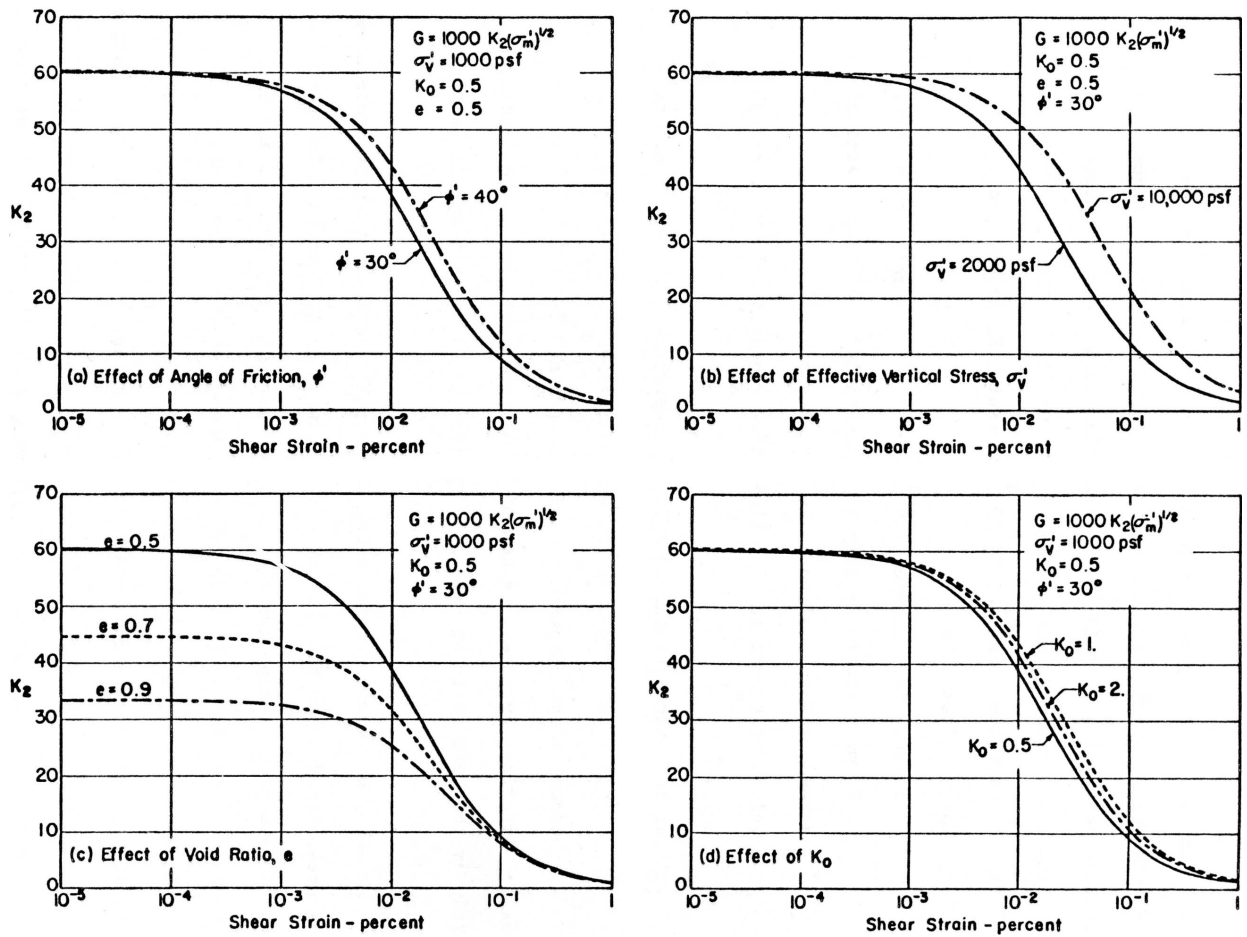


Figure 3.4: Small-strain stiffness decay as a function of (a) effective friction angle ϕ' , (b) vertical effective stress σ'_v , (c) void ratio e , and (d) K_0 [162].

Table 3.1: Parameters affecting the stiffness of soils at small-strains (modified after Hardin & Drnevich [53]).

Parameter	Importance to ^a			
	G_0		$\gamma_{0.7}$	
	Clean sands	Cohesive soils	Clean sands	Cohesive soils
Strain amplitude	V	V	V	V
Confining stress	V	V	V	V
Void ratio	V	V	R*	V
Plasticity index (PI)*	-	V	-	V
Overconsolidation ratio	R	L	R	L
Diagenesis*	V*	V*	R*	R*
Strain history*	R	R	V	V
Strain rate	R	R	R	R*
Effective material strength	L	L	L	L
Grain Characteristics (size,shape,gradation)	L*	L*	R	R
Degree of saturation	R	V	L	L*
Dilatancy	R	R	R	R

^a V means Very Important, L means Less Important, and R means Relatively Unimportant

* Modified from the original table presented in Hardin & Drnevich[53]

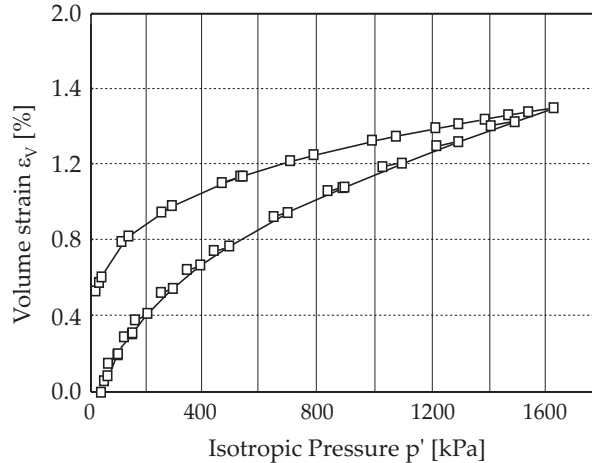


Figure 3.5: Isotropic compression test interrupted by small-strain cycles (after Lade & Abelev [98]).

is much less than in primary loading: Figure 3.5 shows a recent test result by Lade & Abelev [98]. In their test, Lade & Abelev compared the stiffness in isotropic loading and unloading to that obtained when interrupting the continuous loading process by small load cycles. In primary loading, soil stiffness within the load cycles is found to be higher than the soil stiffness in continuous loading. Load cycling during unloading on the other hand did not show any significant stiffness increase. This is also in agreement with the findings of Zdravkovic & Jardine [202]: "The secant and tangent bulk moduli curves developed during swelling fall relatively gently with strain, remaining far above the tangent compression value".

The remaining part of this chapter is hence focused on the reduction of soil stiffness with shear strain. The terms strain and shear strain are sometimes used as synonyms. Small-strain stiffness in volumetric loading is again discussed in the next chapter.

3.2.2 The influence of confining stress

Similar to the well known Ohde [131] or Janbu [77] type power laws for larger strains (see Chapter 7), Hardin & Richard [54] proposed the following relationship between the initial modulus G_0 and the effective confining stress p' :

$$G_0 \propto (p')^m, \quad (3.5)$$

which has not yet been superseded. Hardin & Richard themselves used the power law exponent $m = 0.5$ for both, cohesive and non-cohesive soils. Today, their exponent is widely confirmed for non-cohesive soils: All recent correlations use exponents in the range of $0.40 \leq m \leq 0.55$. For cohesive soils, the exponent $m = 0.5$ is controversial. Many researchers confirmed it, others found exponents as high as $m = 1.0$.

At this point, it has to be considered that confining stress influences the degradation of small-strain stiffness as well: Damping decreases with increasing confining stress.

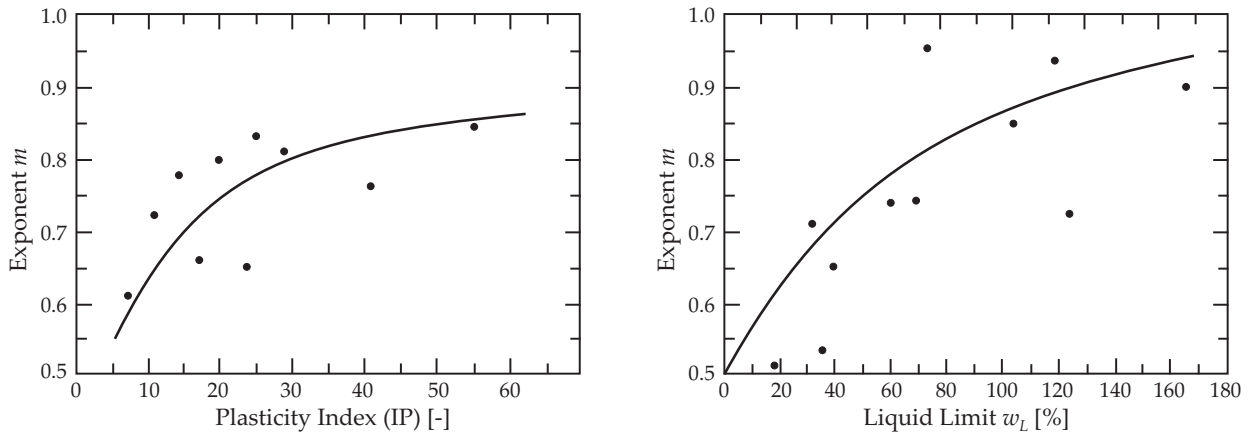


Figure 3.6: The power law exponent m as a function of plasticity index (PI) and liquid limit w_L (after Viggiani & Atkinson [187], and Hicher [57]).

Correlating secant stiffnesses at greater strain amplitudes ($\gamma_s > 1 \times 10^{-6}$) yields therefore higher m values than strictly using low strain Bender element measurements (e.g. $\gamma_s < 1 \times 10^{-6}$). Additionally, it has to be taken into account that Hardin & Richard, like many others, use a void ratio term in their relationship (see Equation 3.8), which also relates to confining stress. Considering that non-cohesive soils are typically less compressible than cohesive soils, the scatter in the exponent m for cohesive soils can readily be explained. Without taking into account void ratio in their relationship, Viggiani & Atkinson [187] compiled the exponents m for different clays at very small strains as a function of plasticity index; Hicher [57] compiled them as a function of Liquid Limit. Both charts are shown in Figure 3.6. Small-strain stiffness data for a Kaolin clay with PI 20 and LL 43 acquired by Rammah et al. [146] even correlated well, with $m = 1.0$. This suggests that whenever void ratio is assumed constant in the corresponding relationship, the small-strain power law exponents m are equal (sands) or only a little less (clays) than the exponents generally obtained in large strain oedometer and triaxial tests, e.g. $m = 0.5$ for sands and $m = 0.7 \dots 1.0$ for clays.

Normalized modulus reduction curves, as for example the ones shown in Figure 3.8, indicate that the threshold shear strain $\gamma_{0.7}$ is also mean stress dependent. Only a few relationships between confining stress and reduction of small-strain stiffness are proposed in literature though. That by Ishibashi & Zhang [70] varies the exponent m in Equation 3.5 non-linearly with strain, as proposed earlier by Iwasaki et al. [76], [75]. A general recommendation for practical application can hardly be given though from their analysis. Darendeli & Stokoe [30] developed normalized modulus reduction curves from an extensive study on over 100 undisturbed specimens from depths of 3 to 263 m. From their data, the threshold shear strain $\gamma_{0.7}$ correlates very well to confining pressure p' where:

$$\gamma_{0.7} = (\gamma_{0.7})_{ref} \left(\frac{p'}{p_{ref}} \right)^{\hat{m}}, \quad (3.6)$$

and $p_{ref} = 100$ kPa is a reference pressure, $(\gamma_{0.7})_{ref}$ is the threshold shear strain at

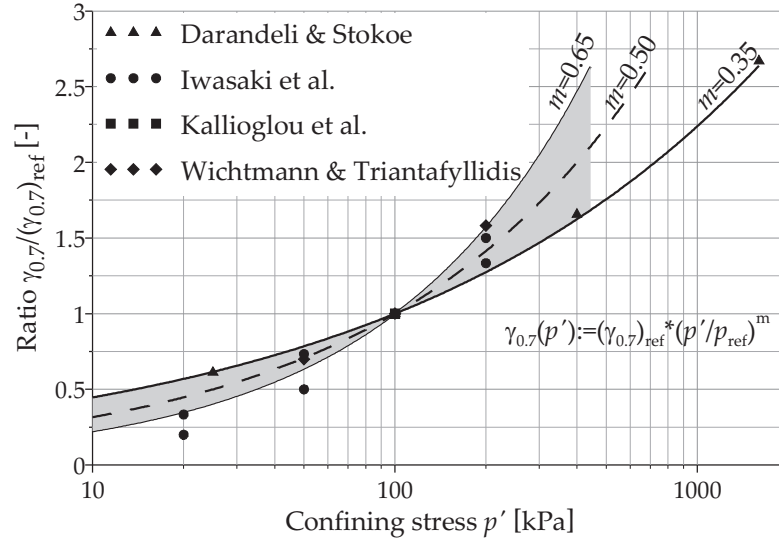


Figure 3.7: Correlation between confining stress p' and shear strain $\gamma_{0.7}$.

$p' = p_{ref}$, and $\hat{m} = 0.35$. In Figure 3.7, the result from Darandeli & Stokoe is presented together with other test data on non-plastic soils, i.e. data by Iwasaki et al. [76] that was later used by Ishibashi & Zhang [70] for their correlation. From this representation it can be concluded that a) the power law works reasonably well also for the threshold shear strain and b) the power law exponent for non-plastic soils under moderate confining pressures is typically $0.35 < \hat{m} < 0.65$. According to Stokoe et al. [89], Equation 3.6 can be used in combination with $\hat{m} = 0.35$ in plastic soils, as well. Other test data does not always support this statement. Biarez & Hicher [16], for example, find the threshold shear strain $\gamma_{0.7}$ of Kaolinite ($PI = 30$) largely unaffected by confining stresses in the range of $p' = 100 \dots 300$ kPa.

3.2.3 The influence of void ratio

The most frequently applied relationship between void ratio and initial soil stiffness dates back to Hardin & Richart [54], as well. Based on their measurements of wave propagation velocities in Ottawa sand, they proposed a linear dependency between propagation velocity v , and void ratio e of the form:

$$v = a(b - e)p'^{\frac{n}{2}}. \quad (3.7)$$

From this linear dependency, Hardin & Richart derived their well known formula for void ratio dependency of G_0 to:

$$G_0 \propto \frac{(2.17 - e)^2}{1 + e} \quad \text{and} \quad (3.8)$$

$$G_0 \propto \frac{(2.97 - e)^2}{1 + e} \quad (3.9)$$

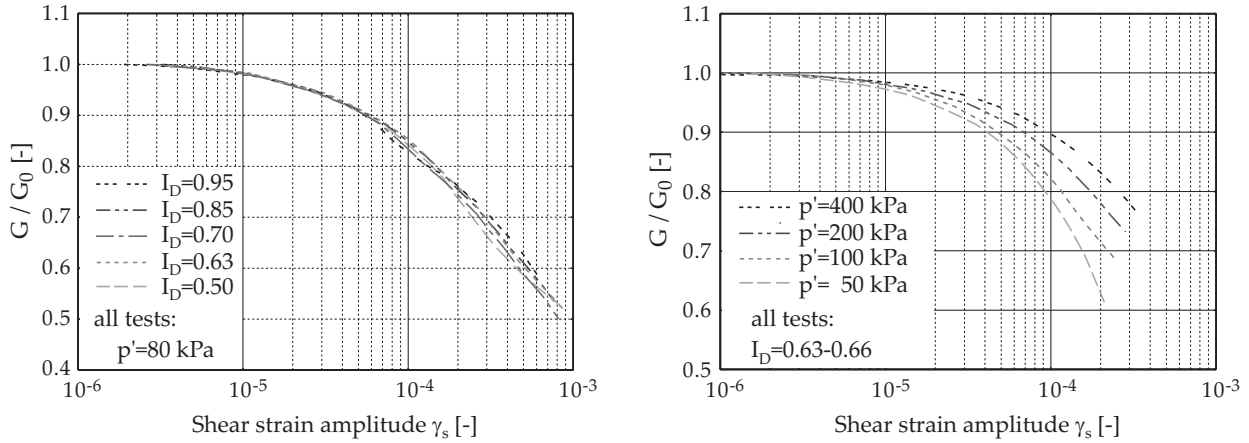


Figure 3.8: Influence of void ratio e (left) and confining stress p' (right) on the decay of small-strain stiffness (after Wichtmann & Triantafyllidis [193]). The influence of void ratio is expressed by the density index $I_D = \frac{e - e_{min}}{e_{max} - e_{min}}$.

for round-grained sands ($e < 0.80$), and angular-grained sands ($e > 0.60$) respectively. Hardin & Black [50], [51] later indicated that Equation 3.9 also correlates reasonably well for clays with low surface activity. For clays with higher surface activity, the basic structure of relationship 3.9 is often maintained, only the coefficient 2.97 is replaced by a somewhat increased one (see Table 3.3).

Other relationships between void ratio and initial stiffness found in literature are typically of the form:

$$G_0 \propto e^{-x} \quad (3.10)$$

where the exponent x is quantified for instance as:

- $x = 0.8$ (for sand - Fioravante [40])
- $x = 1.0$ (for sand and clay - Biarez & Hicher [16])
- $x = 1.3$ (for cemented sands, fine-grained soils - Lo Presti [141])
- $1.1 \leq x \leq 1.5$ (for various clays - Lo Presti & Jamiolkowski [139]).

The influence of void ratio on the threshold shear strain $\gamma_{0.7}$ is apparently very limited in non-cohesive soils. This can be observed for example in normalizing the results of Figure 3.4.c or in the more recent results presented by Wichtmann & Triantafyllidis [193] (Figure 3.8). Damping in cohesive soils on the other hand is linked to void ratio. In cohesive soils, void ratio also correlates to plasticity index (PI), as higher plasticity is generally a prerequisite for a more open soil structure and thus a higher void ratio. Yet, void ratio is also related to the confining stress and overconsolidation ratio. Therefore, the influence of void ratio on the threshold shear strain $\gamma_{0.7}$ is not discussed in this section. Instead the effects of PI, OCR, and p' on $\gamma_{0.7}$ are discussed in the following sections.

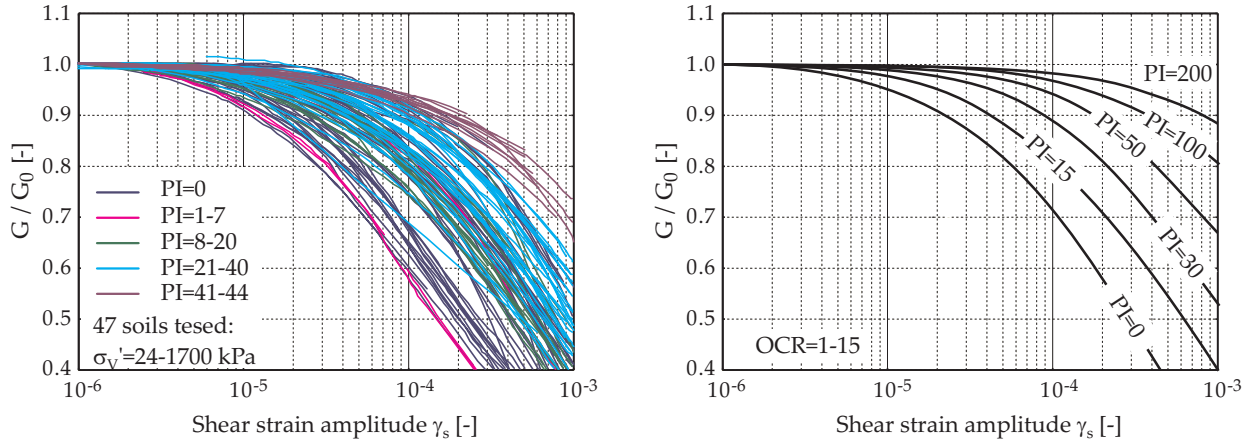


Figure 3.9: Influence of plasticity index (PI) on stiffness reduction: Left database for soils with different PI; Right: PI-chart by Vucetic & Dobry (after Hsu & Vucetic [64], and Vucetic & Dobry [188] respectively).

3.2.4 The influence of soil plasticity

In relating small-strain stiffness reduction curves to the plasticity index (PI or I_p), Vucetic & Dobry [188] proposed the modulus reduction chart (PI-chart) shown in Figure 3.9. These well known curves have been compiled from the results of 16 different publications of 12 or more research groups. The original data showed considerable scatter so the PI-chart should be used with care, especially for $PI \geq 30$. For lower plasticity clays, the PI-chart is in reasonable agreement with many recently published test results. The threshold shear strain $\gamma_{0.7}$ at $p' = 100$ kPa of clean sands for example, is tested in the limits $8 \times 10^{-5} \leq \gamma_{0.7} \leq 2 \times 10^{-4}$, where the chart by Vucetic & Dobry suggests $\gamma_{0.7} \approx 1 \times 10^{-4}$.

Stokoe et al. [89] also agree reasonably well with the PI-chart by Vucetic & Dobry up to $PI = 15$. Subsequently, they suggest lower threshold shear strains. Generally, Stokoe et al. propose a linear increase of $\gamma_{0.7}$ from $\gamma_{0.7} \approx 1 \times 10^{-4}$ for $PI = 0$ up to $\gamma_{0.7} \approx 6 \times 10^{-4}$ for $PI = 100$.

3.2.5 The influence of the overconsolidation ratio (OCR)

In cohesive soils G_0 increases with OCR. The amount of increase depends upon the soil's plasticity. Hardin & Black [49] proposed an empirical relationship of the form:

$$G_0 \propto \text{OCR}^k \quad (3.11)$$

where they define OCR as the ratio of maximum past vertical effective stress to the current vertical effective stress ($\text{OCR} = \frac{\sigma'_{v,OC}}{\sigma'_v}$), and k is a parameter that is varying between 0 for sands and 0.5 for high plasticity clays. Atkinson & Little [8] came up with a different relationship for tests on undisturbed London Clay:

$$G_0 \propto m \log R_0, \quad (3.12)$$

where R_0 is defined as the ratio of maximum past effective mean stress to the current effective mean stress ($R_0 = \frac{p'_{OC}}{p'}$). Houlsby & Wroth [63] then combined the power law proposed by Hardin & Black [49] with the overconsolidation ratio R_0 to give:

$$G_0 \propto R_0^k. \quad (3.13)$$

Again the empirical parameter k increases with clay plasticity. For clays with $10 < PI < 40$, Atkinson & Viggiani found $0.20 < k < 0.25$. For practical applications this seems a relatively small variation, such that it is sometimes proposed to neglect the effect of OCR on G_0 completely, e.g. in Lo Presti & Jamiolkowski [139]. However, overconsolidation cannot be neglected in the inherent and stress-induced anisotropy of small-strain stiffness, which is discussed later in Section 3.2.7.

In non-plastic soils, overconsolidation has only a small effect on the normalized modulus reduction curve. In plastic soils, overconsolidation markedly increases the threshold shear strain $\gamma_{0.7}$. The increase of $\gamma_{0.7}$ with overconsolidation OCR can after Stokoe et al. [89] be approximated as:

$$\gamma_{0.7} = (\gamma_{0.7})_{ref} + 5 \times 10^{-6} PI(OCR)^{0.3}, \quad (3.14)$$

where $(\gamma_{0.7})_{ref}$ is here a reference threshold shear strain for a non-overconsolidated, non-plastic soil, e.g. $(\gamma_{0.7})_{PI=0,OCR=1} \approx 1e-4$. For overconsolidated soils, the findings by Stokoe et al. [89] and Vucetic & Dobry [188] are thus also in better agreement for soils with higher plasticity (Note that the PI-chart by Vucetic & Dobry is independent of overconsolidation).

3.2.6 The influence of diagenesis

Diagenesis refers to postdepositional processes, involving seawater, meteoric water, or subsurface brines, that alter sediments or sedimentary rocks up to the point of metamorphism, and include burial, compaction, dissolution, and precipitation, (Morse and Mackenzie [124]). Diagenetic processes alter the stiffness of soils with time: Generally, any process that alters the existing interparticle structure within a soil will also alter its stiffness. Diagenetic processes that have a considerable effect are cementation and aging, which in the classical sources (Lambe & Whitman [182], Mitchell [120], Terzaghi et al. [179]) are defined as a change in various mechanical properties resulting from secondary compression under a constant external load. Although traditionally linked to clays (e.g. Bjerrum [17]), aging is also known to occur in sands, sandstones, and clayey sands (e.g. Mesri et al. [117], Schmertmann [159]). Cementation, which is not necessarily linked to secondary compression, is particularly important to the stiffness of sandy soils. Fernandez & Santamarina [39] for example, found that "small-strain stiffness of sands can increase by an order of magnitude or more due to cementation".

The time-dependent increase of G_0 due to aging in clays may be linked to engineering properties, e.g. the secondary consolidation coefficient C_α with empirical expressions of the type proposed by Anderson & Stokoe [4]

$$\frac{G_0(t)}{G_0(t_p)} = \left[1 + N_{G,1} \log \frac{t}{t_p} \right] \quad (3.15)$$

or the one proposed in Shibuya et al. [164]

$$\frac{G_0(t)}{G_0(t_p)} = \left[\frac{t}{t_p} \right]^{N_{G,2}} \quad (3.16)$$

where t_p is the time required to reach the end of primary consolidation, t is any time ($t > t_p$), $G_0(t_p)$ is the maximum stiffness at time t_p , and $N_{G,x}$ is an empirical material factor. Lo Presti et al. [140] proposed the following relationship:

$$N_{G,1} = C_\alpha^{0.5}, \quad (3.17)$$

which was confirmed by additional test results of Lohani et al. [107].

Diagenetic effects of a soil can be readily lost upon changing its state of stress. Disturbed soil samples may therefore show considerably different small-strain behavior than undisturbed samples. Toki et al. [180] prepared a database from case studies in Japan (Figure 3.10) that show a clear correlation between sampling method and the reliability of very small-strain stiffness laboratory measurements. Employing in-situ freezing methods yields the best agreement between in-situ $G_{0,Field}$ and laboratory $G_{0,Lab}$ determined stiffness values. Thin wall sampling also gives reliable laboratory results, except for sands, which are densified during sampling. More commonly used sampling methods for sands and soft rocks, however, often disturb the samples so much that the laboratory determined $G_{0,Lab}$ is as low as $0.25G_{0,Field}$. Results from the ROSRINE (Resolution Of Site Response Issues from the Northridge Earthquake) study, which is an on-going study set up after the 1994 Northridge earthquake, show similar reduction factors. Here, a general trend is depicted between the ratio $\frac{G_{0,Lab}}{G_{0,Field}}$ and the in-situ shear wave velocity (Figure 3.10).

3.2.7 The influence of loading history

Masing [111] described the **hysteresis** in stress-strain behavior in the form of the following two rules:

- The shear modulus in unloading is equal to the initial tangent modulus for the initial loading curve.
- The shape of the unloading and reloading curves is equal to the initial loading curve, except that its scale is enlarged by a factor of two.

Although Masing's original work was concerned with the value of the proportional limit of brass under cyclic loading, his rules appear to describe the actual behavior of soil under cyclic loading reasonably well. In irregular cyclic loading however, the above rules have to be extended. A detailed discussion of possible extensions is for example given in Pyke [143], which is also summarized in Section 6.1.3 of this thesis.

In terms of the above introduced threshold shear strain $\gamma_{0.7}$, Masing's second rule is fulfilled by writing:

$$(\gamma_{0.7})_{\text{initial loading}} = \frac{1}{2}(\gamma_{0.7})_{\text{reloading}} \quad (3.18)$$

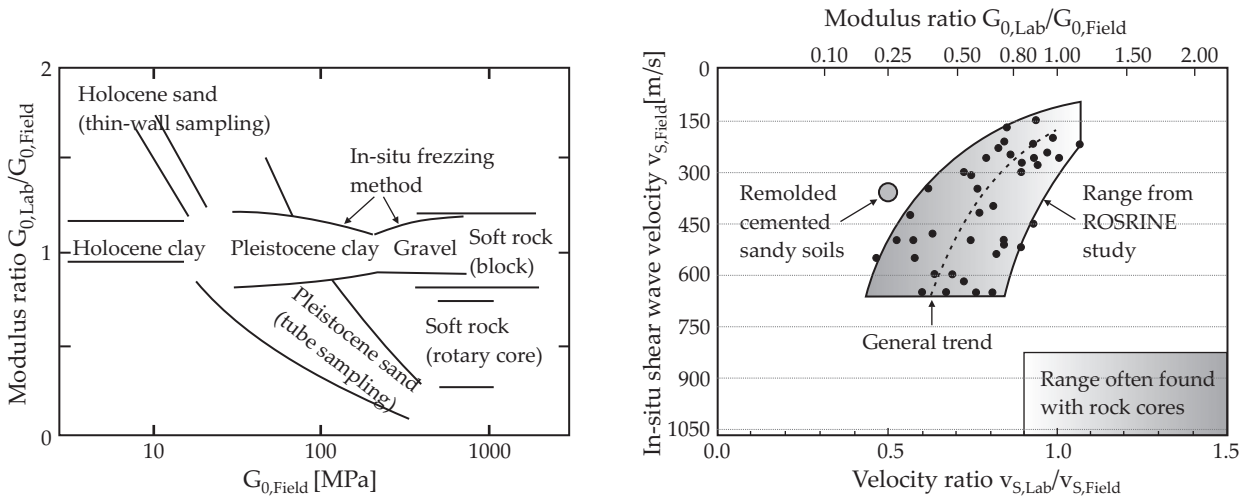


Figure 3.10: Differences in the ratio of laboratory-to-field stiffness. Left: Data from Japanese case studies (after Toki et al. [180]). Right: Results from the US American ROSRINE study (after Stokoe & Santamarina [173]).

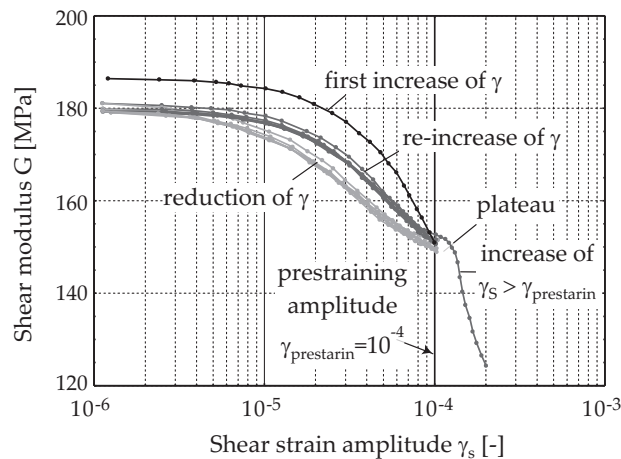


Figure 3.11: Influence of cyclic prestraining on small-strain stiffness (after Wichtmann & Triantafyllidis [193]).

Although experimental data often confirms Masing's rules, the threshold shear strain $\gamma_{0.7}$ in unloading-reloading increases not always to the extent described by Masing. An example presented in Wichtmann & Triantafyllidis [193] is shown in Figure 3.11. Here, a sample was cyclic loaded to investigate the effects of cyclic prestraining. In this particular example, the modulus G_0 slightly decayed in cyclic loading. In other samples, which are not shown here, it also slightly increased so that no correlation between the number of applied prestraining cycles and G_0 is found. Part one of Masing's rule on the other hand is confirmed. Normalizing all load cycles for their individual maximum also confirms the second part.

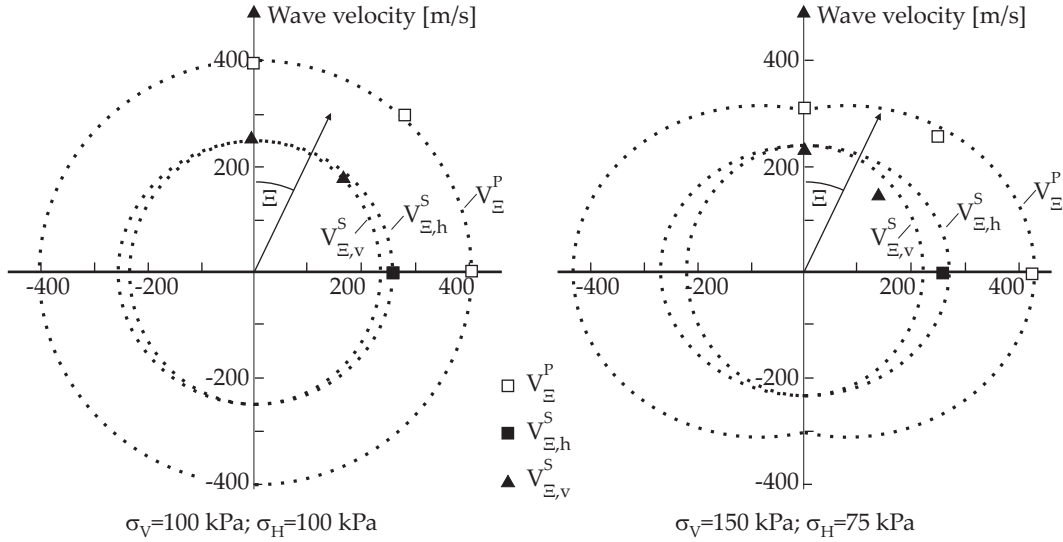


Figure 3.12: Polar plot of wave speeds as a function of their inclination ($\Xi = 0$:= vertically travelling waves, $\Xi = 90^\circ$:= horizontally travelling waves). Isotropic loading yields almost isotropic wave speeds (left); axial unloading to a stress ratio of 2 decreases axial stiffness (right). Dotted lines give the results from a cross anisotropic model after Bellotti et al. [14].

A second, and probably as important an effect of loading history is the formation of stress or strain **induced anisotropy**. This has been examined i.a. by Hoque & Tatsuoka [61], Bellotti et al. [14], and Yu & Richart [200]. In summary these studies conclude that principal stress ratios ($\frac{\sigma'_1}{\sigma'_3} > 1$) increase the maximum small-strain stiffness in the direction of the highest principal stress (σ'_1). The stiffness in the direction of the minor principal stress (σ'_3) is almost unaffected up to stress ratios of ($\frac{\sigma'_1}{\sigma'_3} = 3$). For higher stress ratios, stiffness decreases in the minor principal stress direction. Figure 3.12 illustrates these findings by a comparison of wave speeds at different stress ratios. The stress ratio in normally consolidated soils is $K_0 = 0.5$. When back-calculated from cross hole measurements, the vertical stiffness of normally consolidated soils can thus be underestimated up to 30%.

Even though Figure 3.12 indicates near isotropic stiffness in isotropic loading conditions, the issue of **inherent anisotropy** cannot be neglected in many soils, either. Inherent anisotropy is attributed to the genesis of soils, for example depositional processes, as well as to their diagenesis (see Section 3.2.6). Often, the stiffness in the horizontal (bedding) plane appears to be 20 – 30% higher than the one in the vertical plane (Bellotti et al. [14], Chaudhary et al. [28]). In a way, isotropic stiffness might therefore be a reasonable assumption for practical applications, considering that inherent anisotropy compensates somewhat for stress induced anisotropy in normally consolidated soils.

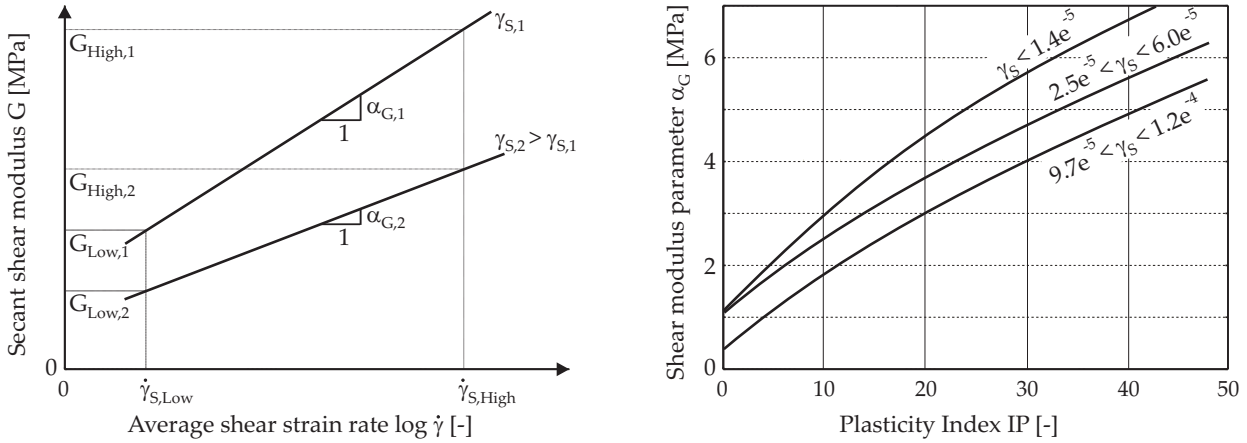


Figure 3.13: The strain-rate shear modulus parameter and its dependence on strain amplitude, and plasticity Index (PI). After Vucetic et al. [190].

3.2.8 The influence of strain rate and inertia effects

Systematic experimental investigations revealed that in many soils the small-strain modulus G_0 increases with the rate of loading (e.g. Whitman [192], Matesic & Vucetic [112], and Vucetic & Tabata [189]). This so called strain rate effect can be attributed to viscosity and thus to soil plasticity as there is virtually no such strain rate effect in sands. The strain rate effect in cohesive soils increases with plasticity index. As a measure for the increase, Yong & Japp [198] define the stress or strain rate shear modulus parameter to:

$$\alpha_G = \frac{(\Delta G_S)}{\Delta \log \dot{\gamma}}. \quad (3.19)$$

In this way, the strain rate shear modulus parameter α_G defines the slope of the stress versus strain rate line in a semi-logarithmic format. In plotting the parameter α_G versus strain rate and amplitude (Figure 3.13), the following correlation becomes clear: The strain rate effect increases with strain rate and soil plasticity, but decreases with shear strain amplitude. Vucetic et al. [190] first quantified the strain rate effect as a function of plasticity index (PI) and liquid limit w_L but with significant uncertainties.

From Figure 3.13 and 3.14 it can be concluded that small-strain stiffness is only a little biased by common straining rates. This is in agreement with findings from dynamic tests, where inertia effects have to be considered on top of strain rate effects. Stokoe et al. [172] conclude from a recent study that "for excitation frequencies changing from 1 to about 100 Hz, G_0 increases by about 5% to 30%, with the effect generally increasing with increasing PI". Many other researchers found similar trends. Georgiannou et al. [44], for example, report a 10% increase of G_0 in different clays and marl due to dynamic loading. In sands, only a very small or no increase is found (Hicher [57]). The Japanese working hypothesis that soil parameters for earthquake analysis can be derived from static tests is therefore validated from a practical point of view.

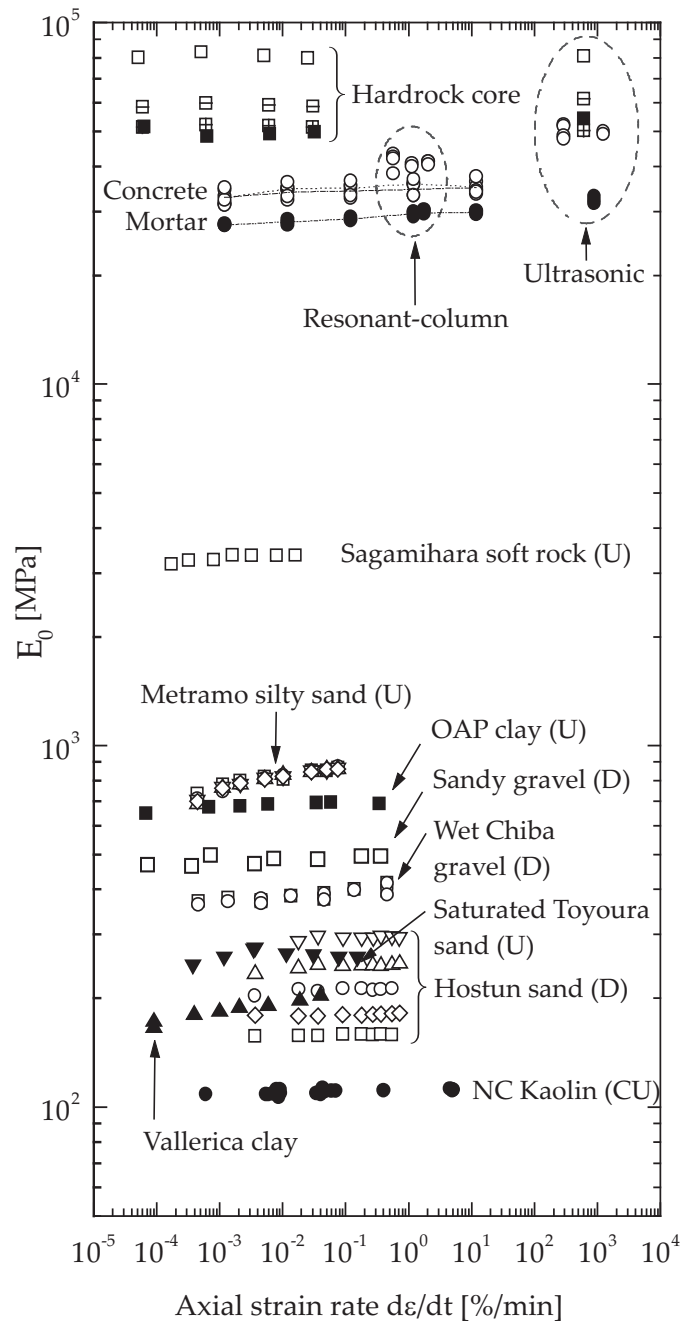


Figure 3.14: Strain rate effect on the Young's modulus E_0 after Tatsuoka [177].

3.2.9 Other factors that influence small-strain stiffness

Small-strain stiffness is only slightly influenced by the effective angle of friction for granular soils. An example is given in Figure 3.4, where the threshold shear strain $\gamma_{0.7}$ is somewhat higher in the sample with a higher angle of friction. As the effective angle of friction can be related to the density index, this observation is in good agreement to the one discussed in Section 3.2.3. Grain shape, also has little effect on the small-strain stiffness. Dilatancy is not activated in the range of small strains at all.

Mean grain diameter and grain size distribution, on the other hand, are reported to influence small-strain stiffness of poorly graded soils considerably. Iwasaki & Tatsuoka [74] found the shear modulus, G_0 , to be approximately 10 – 25% reduced in well graded sands compared to poorly graded sands. The addition of 2% – 5% fines then showed another decrease in G_0 of about 20%. Fine contents is also important for the effect of saturation on small-strain stiffness.

In fully saturated samples, pore water has an indirect impact on small-strain stiffness: Dry and saturated clean sands show exactly the same G_0 modulus, at equal effective confining pressures. Therefore pore water can be ruled out as a parameter that affects the shear modulus G_0 of clean sands, except for its influence on mean effective stress. The water contents in clay play a major role, if it is close to the liquid limit. Then, the shear modulus G_0 decays to a minimum threshold value, which can be related to the undrained shear strength c_u by:

$$G_0 = I_R c_u \quad (3.20)$$

Anderson & Woods [5] determined the dimensionless soil parameter I_R for many clays within the band $300 < I_R < 1800$. Considering that the undrained shear strength of most clays decays to $c_u \approx 1.7$ kPa when they approach the liquid limit [199], their shear modulus can be as low as 500 kPa. Such low shear moduli at the liquid limit have, for example, been verified by Holzlöhner [59].

In partially saturated samples, capillary effects have to be considered in the presence of fines (Stokoe & Santamarina [173]). Capillary forces at interparticle contacts increase the shear modulus G_0 with decreasing level of saturation and decreasing grain diameter of fines. With decreasing saturation, fine clay particles increasingly migrate to interparticle contacts of sand and silt grains. There, they form clay buttresses and bridges that increase small-strain stiffness (see also Section 3.2.6).

When discussing the effect of saturation, it should be finally noted that for temperatures below 0°C, the role of pore water is obviously different. In saturated clays, for example, a 3000% to 5000% increase of G_0 is to be expected for a temperature decrease from 20°C to –10°C.

3.3 Correlations for small-strain stiffness

3.3.1 Correlations between G_0 and e , p' and OCR

Tables 3.2 to 3.4 provide a number of very small-strain stiffness correlations on the basis of the modified Hardin & Black [49] equation:

$$G_0 = A f(e) \text{OCR}^k \left(\frac{p'}{p_{ref}} \right)^m, \quad (3.21)$$

where G_0 is the maximum small-strain shear modulus in MPa, p' is the mean effective stress in kPa, $p_{ref} = 100$ kPa is a reference pressure equal to the atmospheric pressure, OCR is the overconsolidation ratio, and A , $f(e)$, k , m are the correlated functions and parameters given in Tables 3.2 to 3.4. The type of OCR used in a specific relationship is denoted by the subscript of k : $()_1$ indicates the use of vertical stress based OCR values, $()_2$ indicates the use of mean pressure based OCR values (see Section 3.2.5). The symbols e_{min} and e_{max} stand for minimum and maximum void ratio respectively. D_{50} is the mean grain diameter and U_C is the uniformity coefficient.

None of the relationships given in Tables 3.2 to 3.4 addresses explicitly the second independent elastic constant: It is a common simplification to assume Poisson's ratio a constant in the small-strain range, although it increases slightly with applied strain. At least in granular materials, Poisson's ratio is found to be almost independent of the mean effective stress and is only slightly influenced by void ratio. Poisson's ratio instead appears to depend on grain-size distribution, e.g. Biarez & Hicher found $\nu = 0.18$ for poorly graded sand and $\nu = 0.23$ for well-graded sand. As a general guideline, it can be assumed that $0.10 \leq \nu \leq 0.30$ for the small-strain range. Finally it should be acknowledged that the use of a pressure dependent shear modulus as introduced in Equation 3.21 together with a constant void ratio can violate thermodynamical principles.

The tables are sorted for the grain size D_{50} , or PI instead of for author or reference. Ranges in the parameters A , and m refer to the extreme limits due to inherent anisotropy, if anisotropic measurements are available. All relationships given in Tables 3.2 to 3.4 are illustrated in Figure 3.15 for the respective range of void ratios.

As a rule of thumb, either the simple relationship by Biarez & Hicher [16]

$$E_0[\text{MPa}] = \frac{140}{e} \sqrt{\frac{p'}{p_{ref}}} \quad (3.22)$$

or the relationship by Hardin & Black [51]

$$G_0[\text{MPa}] = 33 \frac{(2.97 - e)^2}{1 + e} \sqrt{\frac{p'}{p_{ref}}} \quad (3.23)$$

can be used to estimate E_0 and G_0 in various soils. Here again, e is void ratio, p' is the mean effective stress in kPa, and $p_{ref} = 100$ kPa is the reference pressure equal to the atmospheric pressure. The relationship by Biarez & Hicher was proposed for all soils with $w_l < 50\%$, the one by Hardin & Black was derived for undisturbed clayey soils and crushed sands.

Table 3.2: Relations for the shear modulus G_0 of CLEAN SANDS and GRAVELS.

Soil tested	D_{50} [mm]	U_C [-]	A [-]	$f(e)$ [-]	k [-]	m [-]	Ref.
Kenya carbonate sand	0.13	1.86	101-129	$e^{-0.8}$	0	0.45-0.52	[40]
Toyoura sand (subangular)	0.16	1.46	71-87	$\frac{(2.17-e)^2}{1+e}$	0	0.41-0.51	[61]
Toyoura sand (subangular)	0.19	1.56	84-104	$\frac{(2.17-e)^2}{1+e}$	0	0.50-0.57	[28]
Silica sand (subangular)	0.20	1.10	80	$\frac{(2.17-e)^2}{1+e}$	0	0.50	[88]
Silica sand (subangular)	0.20	1.70	62	$\frac{(2.17-e)^2}{1+e}$	0	0.50	[88]
Silica sand (subangular)	0.20	1.10	62	$\frac{(2.17-e)^2}{1+e}$	0	0.50	[88]
Toyoura sand (subangular)	0.22	1.35	72	$e^{-1.3}$	0	0.45	[141]
H.River sand (subangular)	0.27	1.67	72-81	$\frac{(2.17-e)^2}{1+e}$	0	0.50-0.52	[96]
Glass ballotini (spheres)	0.27	1.28	64-69	$\frac{(2.17-e)^2}{1+e}$	0	0.55-0.56	[96]
Hostun sand (angular)	0.31	1.94	80	$\frac{(2.17-e)^2}{1+e}$	0	0.47	[60]
Silica sand (angular)	0.32	2.80	48	$\frac{(2.17-e)^2}{1+e}$	0	0.50	[88]
Ticino sand (subangular)	0.50	1.33	61-64	$\frac{(2.17-e)^2}{1+e}$	0	0.44-0.53	[61]
Ticino sand (subangular)	0.54	1.50	71	$\frac{(2.27-e)^2}{1+e}$	0	0.43	[141]
Silica sand	0.55	1.80	275	$\frac{(1.46-e)^2}{1+e}$	0	0.42	[193]
Ticino sand (subangular)	0.55	1.66	79-90	$e^{-0.8}$	0	0.43-0.48	[40]
SLB sand (subround)	0.62	1.11	82-130	$\frac{(2.17-e)^2}{1+e}$	0	0.44-0.53	[61]
Ottawa sand No. 20-30	0.72	1.20	69	$\frac{(2.17-e)^2}{1+e}$	0	0.50	[54]
Quiou carbonate sand	0.75	4.40	71	$e^{-1.3}$	0	0.62	[141]
Decomposed granite	1.30	≈ 75	45	1	0	0.88	[86]
Hime gravel (subround)	1.73	1.33	53-94	$\frac{(2.17-e)^2}{1+e}$	0	0.45-0.51	[61]
Chiba gravel	7.90	≈ 10	76	$\frac{(2.17-e)^2}{1+e}$	0	0.50	[122]

Table 3.3: Relations for the shear modulus G_0 of CLAYS.

Soil tested	PI [%]	A [-]	$f(e)$ [-]	k [-]	m [-]	Ref.
Avezzano clay (Holocene-Pleistocene)	10-30	74	$e^{-1.27}$	NA	0.46	[139]
Garigliano clay (Holocene)	10-40	44	$e^{-1.11}$	NA	0.58	[139]
Montaldo di Castro clay (Pleistocene)	15-34	50	$e^{-1.33}$	NA	0.40	[139]
Speswhite caolin clay (recon.)	24	40	1	0.20 ₂	0.65	[187]
Recon. Vallericca clay (Pleistocene)	27	44	1	...	0.85	[147]
Kaolin clay	35	45	$\frac{(2.97-e)^2}{1+e}$	NA	0.50	[110]
Pisa clay (Pleistocene)	23-46	50	$e^{-1.43}$	NA	0.44	[139]
London clay (reconstituted)	41	13	1	0.25 ₂	0.76	[187]
Panigaglia clay (Holocene)	44	52	$e^{-1.30}$	NA	0.50	[139]
Fucino clay (Holocene-Pleistocene)	45-75	64	$e^{-1.52}$	NA	0.40	[139]
Bentonite	60	4.5	$\frac{(4.40-e)^2}{1+e}$	NA	0.50	[110]

Table 3.4: Proposed relationships for the shear modulus G_0 of entire soil groups.

Soil tested	e_{min} [-]	e_{max} [-]	A [-]	$f(e)$ [-]	m [-]	Ref.
Clean sands with $C_u < 1.8$	0.5	1.1	57	$\frac{(2.17-e)^2}{1+e}$	0.40	[74] ¹
All soils with $w_l < 50\%^*$	0.4	1.8	59	$\frac{1}{e}$	0.50	[16] ²
Undisturbed clayey soils & crushed sand	0.6	1.5	33	$\frac{(2.97-e)^2}{1+e}$	0.50	[51] ³
Undisturbed cohesive soils	0.6	1.5	16	$\frac{(2.97-e)^2}{1+e}$	0.50	[90] ⁴
Loess	1.4	4.0	1.4	$\frac{(7.32-e)^2}{1+e}$	0.60	[92] ⁵

¹ Iwasaki & Tatsuoka² Biarez & Hicher (assumes $\nu = 0.2$)³ Hardin & Black⁴ Kim et al.⁵ Kokusho et al.

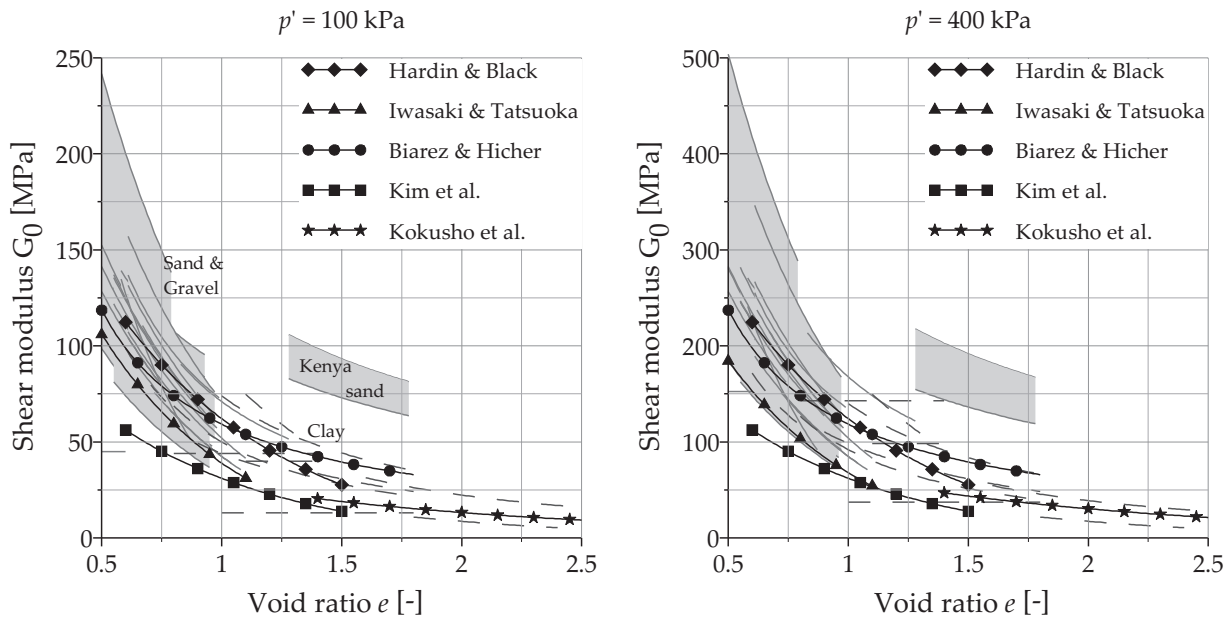


Figure 3.15: Shear modulus G_0 versus void ratio e , after Table 3.2, 3.3, and 3.4.

3.3.2 Correlations between G_0 and CPT, SPT and c_u

3.3.2.1 Cone penetration (CPT) and standard penetration (SPT)

Relationships between the small-strain modulus G_0 and the corrected cone penetration tip resistance q_t have been proposed for clean quartz sands (Baldi et al. [11]), clays (Mayne & Rix [116]), and various soil types (Lunne et al. [108]). The correction of tip resistance due to pore water pressure effects is described in Lunne et al. [108].

For clays, Mayne & Rix [116] give the expression:

$$G_0 \text{ [MPa]} = 49.4 \frac{q_t^{0.695}}{e^{1.13}} \quad (3.24)$$

where q_t is the corrected tip resistance in units of MPa. The correlation by Mayne & Rix [116] and that by Lunne et al. [108] are shown in Figure 3.16.

Since G_0 is related to CPT tip resistance, which can be correlated to the undrained shear strength, G_0 should also be directly related to the undrained shear strength. Larson & Mulabdic [100] proved this for Scandinavian clays by formulating:

$$G_0 = \left(\frac{A}{\text{PI}} + B \right) c_u \quad (3.25)$$

where PI is the plasticity index, c_u is undrained shear strength in kPa, and A , B are empirical soil parameters. For Scandinavian clays they found a reasonable fit for $A = 208$, and $B = 250$.

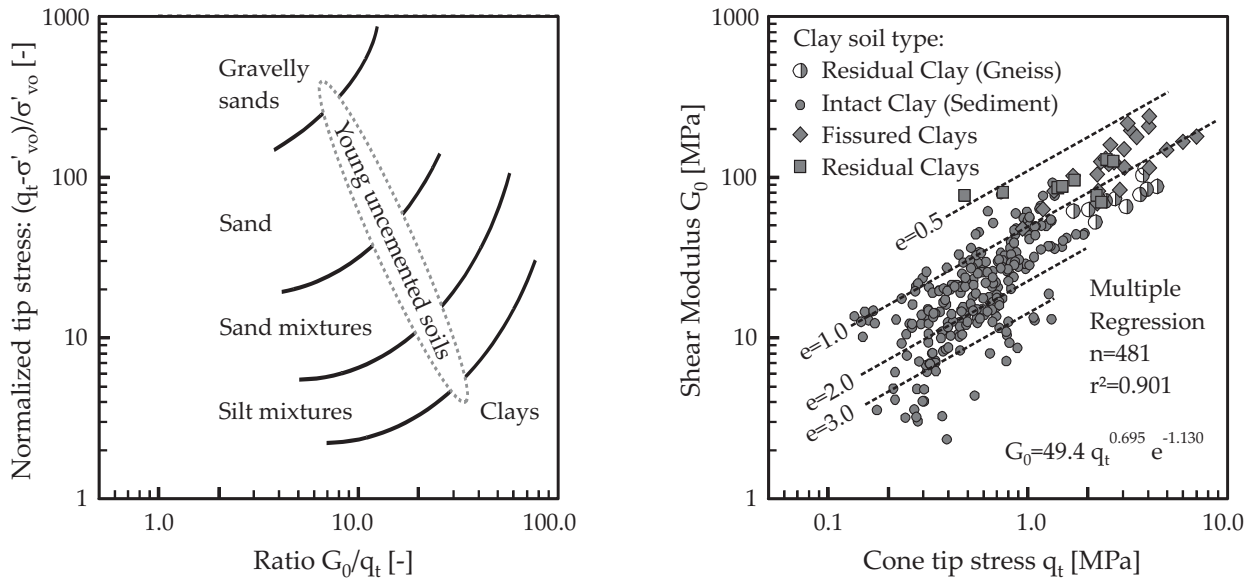


Figure 3.16: Correlation between CPT results and very small-strain stiffness after Lunne et al. [108] (left) and Mayne & Rix [116] (right).

Most correlations between standard penetration test (SPT) results and very small-strain stiffness take the form:

$$G_0 = A((N_1)_{60})^B \quad (3.26)$$

which was first proposed in Ohsaki & Iwasaki [132]. In Equation 3.26, $(N_1)_{60}$ is the number of blows per 0.3 m, and A and B are again empirical soil parameters. The relationship is generally limited to a maximum blow count of $(N_1)_{60} = 30$. For cohesive soils, Imai & Tonouchi [69] found a best fit to test data for $A = 15.56$ and $B = 0.68$ (G_0 in MPa units).

3.3.2.2 Estimating G_0 from conventional tests - Chart by Alpan

Alpan [3] published the chart shown in Figure 3.17 which, as he stated, relates *static* to *dynamic* soil stiffness (see axis labels E_s, E_d). Actually, this chart relates stiffness from conventional laboratory tests to very small-strain stiffness: The *dynamic* modulus is the initial, or very small-strain modulus E_0 , and the *static* modulus is the apparent elastic Young's modulus in conventional soil testing, e.g. at axial strains of $\varepsilon_a \approx 1 \times 10^{-3}$ in triaxial testing. For a soil with known Young's modulus in triaxial unloading-reloading, the Alpan chart can thus provide an estimate for its very small-strain modulus E_0 .

3.3.3 Correlations for the stiffness modulus reduction curve

In contrast to the numerous relationships that have been proposed for the shear modulus G_0 , only a few correlations are available for its reduction with strain amplitude. Some of these modulus reduction schemes rely on parameters that can be derived from test data

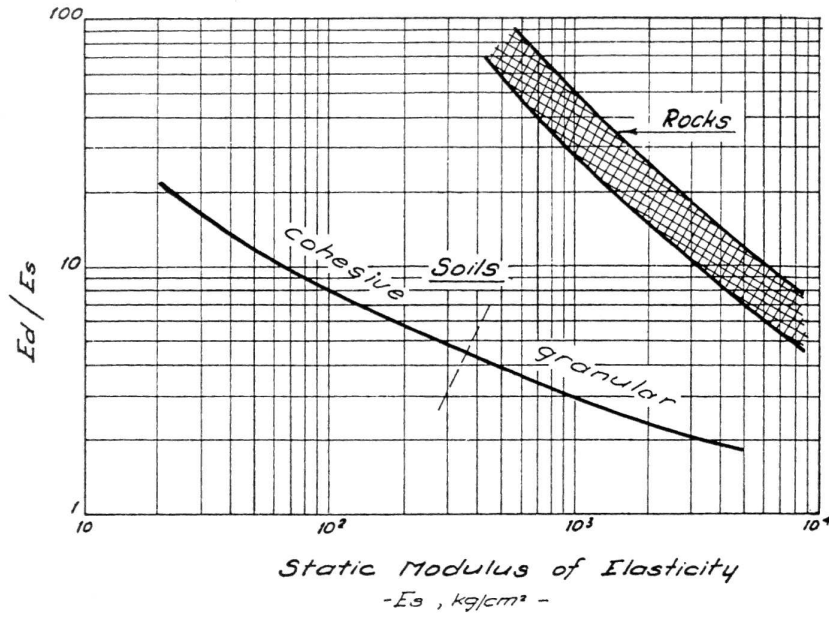


Figure 3.17: Correlation between very small-strain stiffness and stiffness at larger strains from conventional laboratory tests after Alpan ($10 \text{ kg/cm}^2 \approx 1 \text{ MPa}$).

directly, others use more complex fitting procedures. Only the former are discussed in this section. The latter are discussed in detail in Chapter 5.

From test data, sufficient agreement is found that the stress-strain curve for small strains can be adequately described by a simple hyperbolic law. An analogy to the hyperbolic law for larger strains by Kondner [94] (see Section 7) was proposed by Hardin & Drnevich [52]:

$$\frac{G}{G_0} = \frac{1}{1 + \left| \frac{\gamma}{\gamma_r} \right|} \quad (3.27)$$

where the threshold shear strain γ_r is quantified as:

$$\gamma_r = \frac{\tau_{max}}{G_0} \quad (3.28)$$

with τ_{max} being the shear stress at failure. Essentially, Equation 3.28 relates large (failure) strain to small-strain properties, which astonishingly often works well. More straightforward, and less prone to error is probably the use of a smaller threshold shear strain. Stokoe et al. [89] for example, suggest to use the shear strain $\gamma_r = \gamma_{0.5}$ at which the shear modulus G_0 is reduced to its half. Additionally they modify Equation 3.27 by introducing an additional exponent $\alpha = 0.92$:

$$\frac{G}{G_0} = \frac{1}{1 + \left(\frac{\gamma}{\gamma_r} \right)^\alpha} \quad (3.29)$$

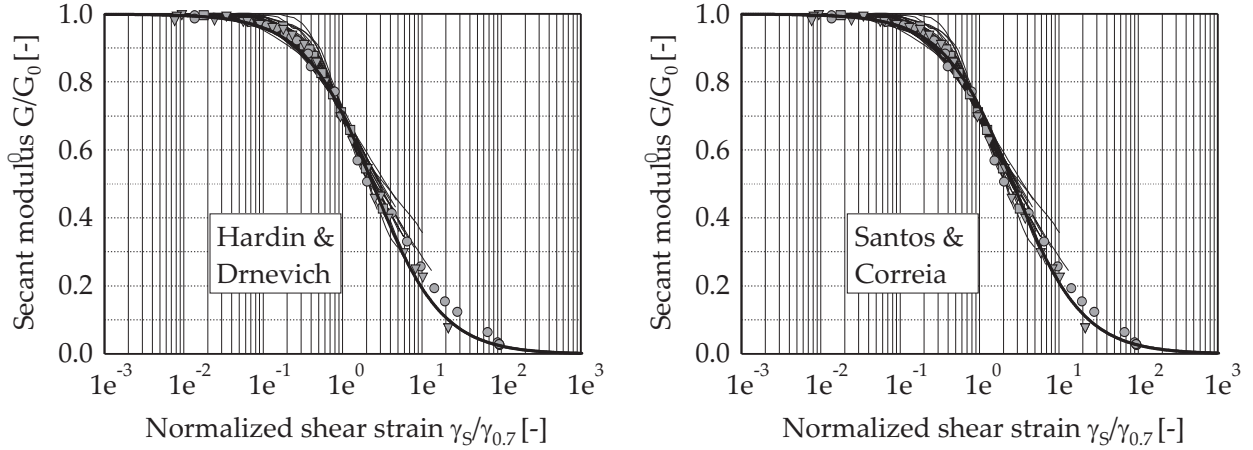


Figure 3.18: The original Hardin & Drnevich [52] relationship (left) and its modification by Santos & Correia [155] (right) compared to test data.

Using the threshold shear strain $\gamma_a = \gamma_{0.7}$, Santos & Correia [155] have put forward the following modified Hardin & Drnevich relationship:

$$\frac{G}{G_0} = \frac{1}{1 + a \left(\frac{\gamma}{\gamma_a} \right)}. \quad (3.30)$$

The constant a in Equation 3.30 is problematic though: For $a \neq \frac{3}{7}$ the relationship is inconsistent as the shear modulus G is not reduced exactly to $0.7G_0$ at shear strain $\gamma = \gamma_{0.7}$. This for example is the case for the best fit $a = 0.385$, Santos & Correia [155] found from a correlation using many test results. The modification by Santos & Correia combined with a constant of $a = \frac{3}{7}$ on the other hand is identical to the Hardin-Drnevich relationship. Looking at both reduction curves (Figure 3.18), their deviation is $< 3\%$ and thus negligible for practical purposes anyway. The approach by Santos & Correia gives a slight upshift of the reduction curve which is indeed desirable in comparison to the not truly hyperbolic test data collected by Santos & Correia [155] shown in Figure 3.18).

In the following, mostly the modified Hardin-Drnevich relationship (3.30) with $a = 0.385$ is used. For the original Hardin-Drnevich model, the reference shear strain $\gamma_a = \gamma_{0.7}^*$ is then taken at the shear strain where G decayed to $0.722G_0$. For the Santos & Correia upshift, $\gamma_a = \gamma_{0.7}$ where G decayed to $0.7G_0$ is to be selected. The exponent α proposed by Stokoe et al. is not adopted as it may sometimes flatten the shear modulus reduction curve too much in the small-strain range.

In Equation 3.28 the threshold shear strain γ_r is related to the shear stress at failure. In the Mohr-Coulomb failure criterion [123] the shear stress at failure can be expressed as follows:

$$\tau_{max} = \frac{1}{4} (2c(1 + \cos 2\varphi) + (\sigma'_1 + \sigma'_3) \sin 2\varphi). \quad (3.31)$$

Remembering that $\gamma_a = a\tau_{max}/G_0$, the threshold shear strains $\gamma_{0.7}$, and $\gamma_{0.7}^*$ of normally

consolidated soils can be calculated as:

$$\gamma_{0.7} = \frac{0.385}{4G_0} (2c(1 + \cos 2\varphi) + \sigma'_1(1 + K_0) \sin 2\varphi), \quad (3.32)$$

and

$$\gamma_{0.7} = \frac{3}{28G_0} (2c(1 + \cos 2\varphi) + \sigma'_1(1 + K_0) \sin 2\varphi), \quad (3.33)$$

respectively. If no small-strain experimental data is available, these values should also be crosschecked with the chart by Vucetic & Dobry [188] shown in Figure 3.9 and the correlation by Stokoe et al. [89] given in Section 3.2.4.

3.3.4 Summary

The stiffness of soils at very small strains is affected by a number of parameters. Its correct determination is not a trivial task: Test results on disturbed samples may give very different results than in-situ tests. In-situ testing methods use geophysical methods, which are not yet common in geotechnical engineering.

However, it has been shown that many of the factors which affect the shear modulus G_0 and its reduction can be regarded as being of minor importance. Neglecting these factors leads to the simple relationships shown in Table 3.4. and illustrated in Figure 3.15. Empirical relationships for estimating the shear modulus' reduction with strain are available as well. From a practical point of view, small-strain stiffness can thus be incorporated into routine design at minimum cost. The use of laboratory and/or in-situ testing data is still preferably though.

If no in-situ test data are available, laboratory small-strain stiffness data can be extrapolated to the field. In the case of common tube or rotary core sampled cemented soils, the actual soil stiffness in the field $G_{0,Field}$ should be expected to be considerably higher than that measured in the laboratory $G_{0,Lab}$ (Figure 3.10). The modulus reduction curve found in the laboratory can be extrapolated to the field by assuming [173]:

$$G_{\gamma,Field} = \frac{G_{0,Field}}{G_{0,Lab}} G_{\gamma,Lab}. \quad (3.34)$$

A numerical model that allows for the incorporation of small-strain stiffness into routine design is developed in the following chapters. The input parameters of this model will be exactly the ones quantified above: The shear modulus G_0 and the threshold shear strain $\gamma_{0.7}$ or $\gamma_{0.7}^*$.

Chapter 4

Small-strain stiffness at the soil particle level

The most important parameters that affect small-strain stiffness have been identified in the previous chapter. In summary, these are void ratio, confining stress, cementation and strain amplitude. The observed influence of these parameters on material stiffness are now interpreted at the soil particle level. However, it is not the aim of this chapter to derive a complete small-strain stiffness model from micromechanical considerations. It is aimed rather at providing a thorough understanding of the small-strain stiffness phenomenon.

The material, which we commonly refer to as soil is usually composed of air, water, and solid particles, which may vary in size, shape, and mineralogic composition. The mechanical properties of soil depend directly on the interaction of these phases with each other and with externally applied potentials such as stress and temperature. Some mechanical properties of soil, for example suction, cannot be understood without explicitly considering multi-phase physics. Others, that are purely determined by the net forces between particles, for example small-strain stiffness, can be sufficiently explained by the micromechanical considerations presented in this chapter.

4.1 Soil fabric and soil structure

The term soil fabric refers to the arrangement of particles, particle groups, and pores in a soil. Soil structure is made up of both, the fabric and the sum of inter-particle forces within the fabric. Soil structure thus takes both fabric and stability into account and is therefore a key feature in determining the engineering properties of a soil.

Sand has typically a single-grain fabric, which means that the particles behave as independent units in the overall soil structure. Possible forces between sand particles are largely electrostatic forces in the form of the Born repulsion forces as well as primary valence bonds in the presence of cementing agents. Born repulsion develops at contact points between particles to avoid the interpenetration of particles. Primary valence bonds are due to cementation and hence the chemical bonding of particles. Silica or carbonate cement is often found in aged sand deposits. Together with other diagenesis effects as for example densification, cementation leads to increased material stiffness (see Chapter 3) and strength. The penetration resistance of aged sand, for example, is reported to be twice as high as the penetration resistance of freshly deposited sand (Mesri et al. [117]). Figure 4.1 shows the bonded single-grain fabric of a Fontainebleau sandstone.

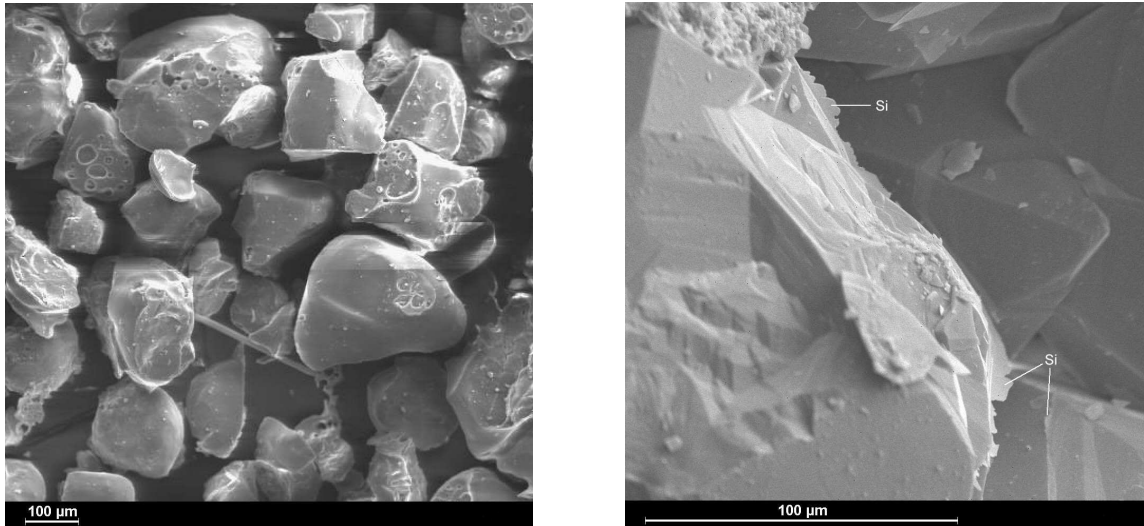


Figure 4.1: Scanning electron microscopy images of sand Particles: Single-grain sand fabric (left); Close-up of amorphous silica and quartz bonds in a sandstone (right). Photographs by IWF, Universität Marburg, and Tore Stendahl, NTNU, Trondheim, Norway.

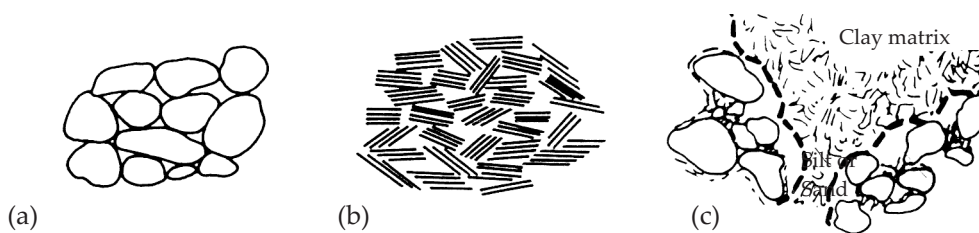


Figure 4.2: Particle arrangements after Mitchell [120]: (a) single-grain sand or silt fabric, (b) multi-grain clay fabric, (c) mixed fabric.

In contrast to sand, clay has typically a multi-grain fabric. If not an artefact from a preexisting rock, multi-grain clay fabrics develop due to high surface forces and chemical activity. Assemblages of clay particle groups or clusters can be arranged within clay fabric in several ways, i.e. edge-to-face or face-to-face. The particle arrangement within the clusters themselves depends mainly on the clay's mineralogy. Possible inter-particle and intercluster forces in clay, in addition to the aforementioned ones, include electrostatic forces in the form of ionic bonds, hydrogen bonds, and hydration forces, as well as capillary stresses.

Although sand and clay structures are different in many ways, their qualitative small-strain behavior is not (see Chapter 3). Both soil types are modeled as granular assemblies here, which represents the level of single-grain sand fabric, and multi-grain clay fabric. Figure 4.2 gives an illustration of the above introduced sand and clay fabrics and the more common case of mixed fabric.

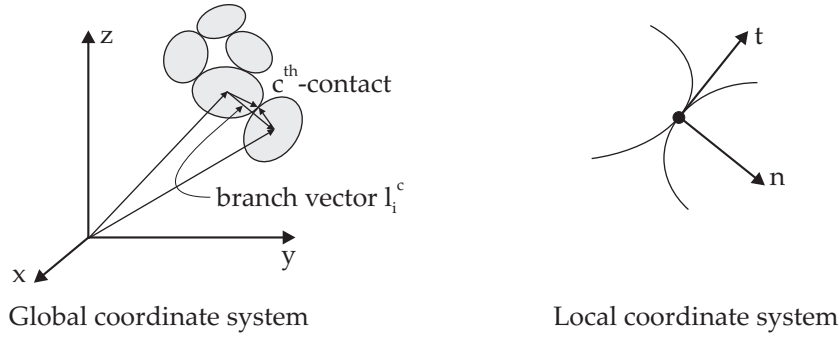


Figure 4.3: The c^{th} inter-particle contact in global and local coordinates.

4.2 Micromechanical considerations

Assuming the particle stiffness to be infinite, the global material stiffness of a granular material can be derived from its inter-particle contact properties (e.g. [27]):

$$C_{ijkl} = \frac{1}{V} \sum_{c=1}^M l_i^c \cdot k_{jl}^c \cdot l_k^c \quad (4.1)$$

where V is the representative volume of the granular assembly, M is the total contact number in the volume V , l_i^c is the branch vector as introduced in Figure 4.3, and k_{jl}^c is the contact stiffness tensor in the global coordinate system. In a local coordinate system the contact stiffness tensor can be written in the form:

$$k_{jl}^c = k_n^c \cdot n_j^c \cdot n_l^c + k_s^c \cdot s_j^c \cdot s_l^c + k_t^c \cdot t_j^c \cdot t_l^c \quad (4.2)$$

where k_n^c , k_s^c , and k_t^c are the local contact stiffnesses along directions \mathbf{n}^c , \mathbf{s}^c , and \mathbf{t}^c respectively. Several homogenization techniques have been proposed in literature to rewrite Equation 4.1 in an integral form. However, all these homogenization techniques involve the definition of density functions for directional contact frequency, branch lengths, and the definition of local stiffness properties. Postulating these density functions is not an easy task for a non-ideal particle assembly: The perturbation function of branch vector lengths for example should reflect particle gradation, shape and preferred particle orientation. As an alternative to explicitly introducing these density functions, numerical discrete element codes can be employed. At the cost of calculation time, these codes keep track of all inter-particle contacts.

Either way, using homogenization techniques or discrete element codes, deriving the global material stiffness from Equation 4.1 is an elaborate task. Unfortunately, not even the constitutive law for the inter-particle contacts is known exactly. Often the Hertz-Mindlin theory (see Section 4.5) is used in combination with correction factors, bonding, viscous components etc. Relating local inter-particle parameters to global soil parameters from laboratory or field testing is also difficult. Largely due to these reasons, micromechanical models are not yet used in engineering practice. Nevertheless, they can

often sufficiently explain experimentally observed material behavior. In the following sections, micromechanical considerations are used to explain the observed dependence of small-strain stiffness on confining stress, void ratio, cementation and strain amplitude.

4.2.1 The influence of strain amplitude

Assuming that small-strain stiffness is due to intermolecular and surface forces within the soil skeleton, as pointed out for example by Israelachvili [72], it can only be altered by rearranging these forces. If a simple Coulomb-type frictional law is assumed to exist inbetween the particles of a soil skeleton, the influence of strain amplitude on small-strain stiffness can be explained as follows: Initially, all inter-particle contacts are in a sticking mode. Due to a certain normal and tangential contact-elasticity, most contacts remain in the sticking mode for a finite strain amplitude. This finite strain amplitude can be considered to be equivalent to the quasi-elastic very small-strain regime. Further increase of the shear strain will then cause an increasing number of particles to slip. Assuming Coulomb friction, the local contact stiffness k_{jl}^c of all sliding contacts c reduces upon slipping. The global material stiffness, being the sum of all local contact stiffnesses, decays according to Equation 4.1. Strain reversals switch back the model's inter-particle contacts to sticking mode so that the maximum small-strain stiffness is recovered. The basic features of small-strain stiffness can therefore be readily simulated with a simple frictional inter-particle law.

Rearrangements of a soil's inter-particle forces can be visualized in chains of contact forces. The connection between chains of contact forces and soil stiffness has previously been pointed out by Kuwano & Jardine [96]. As long as there exists no clear directional chains of contact forces (very small strains), the intermolecular and surface forces are undisturbed. The more directional and concentrated chains of contact forces that are formed, the more that intermolecular and surface forces are distorted, which leads to a decrease in stiffness. To illustrate this, Figure 4.4 shows a biaxial test on a soil sample modeled within a 2D discrete element program, in which a simple frictional law between the particles is assumed. Inter-particle stiffness is modeled with a Hertz-Mindlin type law which will be discussed in more detail in the next section. An additional small bond between the particles is introduced upon the onset of loading in order to visualize sticking contacts. As long as the predefined bonding force is not exceeded, no relative movement between the bonded particles is allowed: The contact sticks. In this case the intermolecular and surface forces between the particles are undisturbed. In Figure 4.4, inter-particle contact forces are identified by lines pointing in the force direction. Line thickness represents the force magnitude. Intact bonds between particles are identified by small black lines that are orientated tangentially to the particle contacts.

Inter-particle force rearrangements, which are reflected in the force-chains shown in Figure 4.4 are related to the type of loading: Deviatoric loading distorts inter-particle forces more than isotropic loading. In case of *psammic* behavior (rigid grains), isotropic loading causes only an upscale and no rearrangement of existing inter-particle forces. Although soil particles are neither rigid nor unbreakable, the experimental data shown

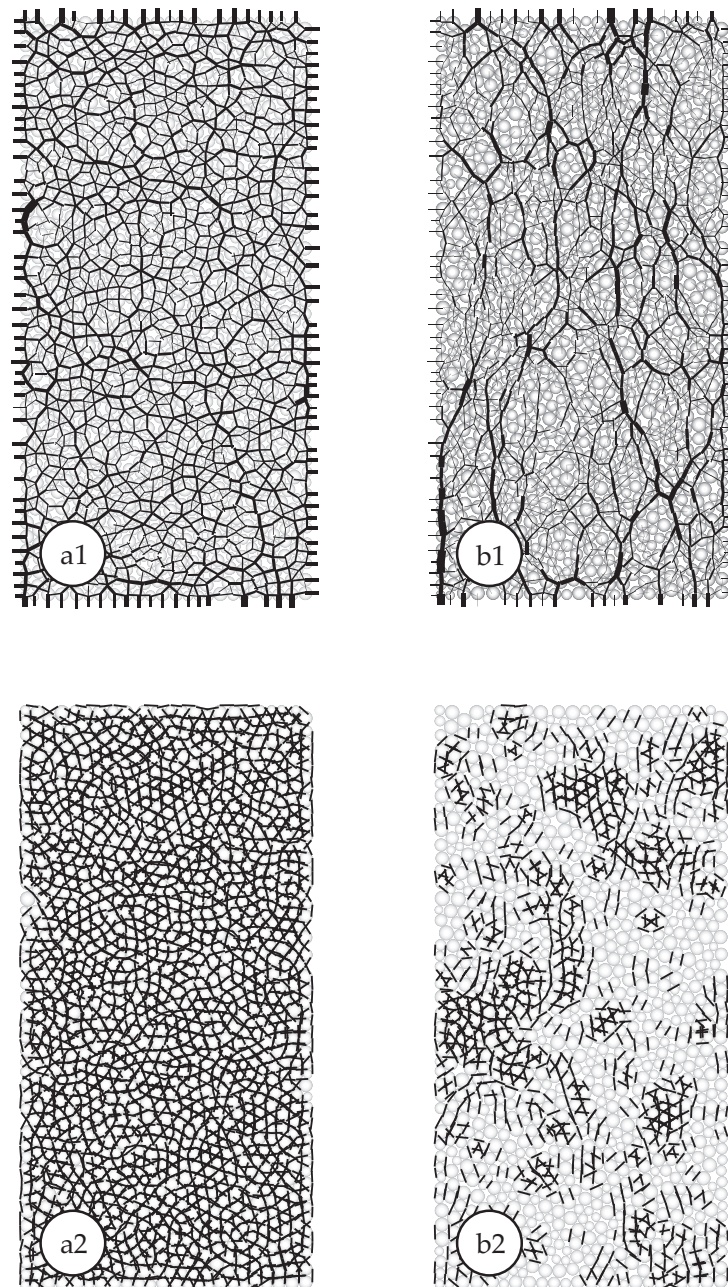


Figure 4.4: Disturbance of inter-particle forces in a biaxial test. A bonded discrete element model is first consolidated (a) and then biaxially sheared (b). From hydrostatic loading equally distributed chains of contact forces (a1) become concentrated during deviatoric loading (b1). At the same time, most of the initially sticking contacts (a2) slide so that the bonds break up (b2).

in Section 3.2.1 can therefore be explained.

4.2.2 The influence of confining stress and void ratio

The classical Hertz-Mindlin contact theory (Mindlin [118], Mindlin & Deresiewicz [119]) is employed to constitute the stiffness tensor k_{jl}^c introduced in Equation 4.1. The Hertz-Mindlin theory relates the contact stiffnesses of two equally sized elastic spheres to normal and tangential contact forces via their radii and elastic moduli. The elastic spheres are assumed to be smooth and perfectly rounded.

The original Hertz-Mindlin equation for normal contact tangent stiffness k_n reads:

$$k_n = \frac{2G_S}{1 - \nu_S} a, \quad (4.3)$$

where G_S , and ν_S are the elastic constants of the sphere material, and a is the radius of the circular contact area, which is calculated as:

$$a = \sqrt[3]{\frac{3NR(1 - \nu_S)}{8G_S}}. \quad (4.4)$$

The normal contact force N , the contact radius a , and the sphere radius R are illustrated in Figure 4.5. Contact shear stress distributions caused by different amounts of slip x_T inbetween the spheres are shown in Figure 4.5. The partial slip introduced in Figure 4.5 is a refinement of the previously discussed simple Coulomb-type frictional law. Energy dissipation and stiffness reduction start with the onset of partial slip. Johnson [85] gives as the resulting tangential contact stiffness:

$$k_s = k_t = k_n \frac{2(1 - \nu_S)}{2 - \nu_S} \sqrt[3]{1 - \frac{T}{N \tan \varphi_S}}, \quad (4.5)$$

where φ_S is the inter-particle friction angle, and T is the shear force in the inter-particle contact. Both normal and shear stiffness therefore increase with the normal contact force to the power of $m = \frac{1}{3}$.

The empirical power law by Hardin & Richard [54] that relates initial stiffness to confining pressure (Equation 3.5) can therefore be readily understood from a micromechanical point of view. The power law exponent observed in experiments is generally somewhat higher though. More sophisticated, and for soil particles probably more adequate, contact theories, yield these higher exponents. Rough surface contacts for example yield a power law exponent of $m \approx 0.5 - 0.6$ [197]. Meta-stable cone to sphere contacts yield a power law exponent of $m = 0.5$ [45], too. Higher power law exponents for large strains can be explained by slippage between the particles.

Local contact stiffness is not an explicit function of void ratio as can be seen in Equation 4.3, and 4.5. Therefore, the effect of void ratio is studied here by comparing two different cubical assemblies: simple cubic (SC) packing and face-centered cubic (FCC) packing of

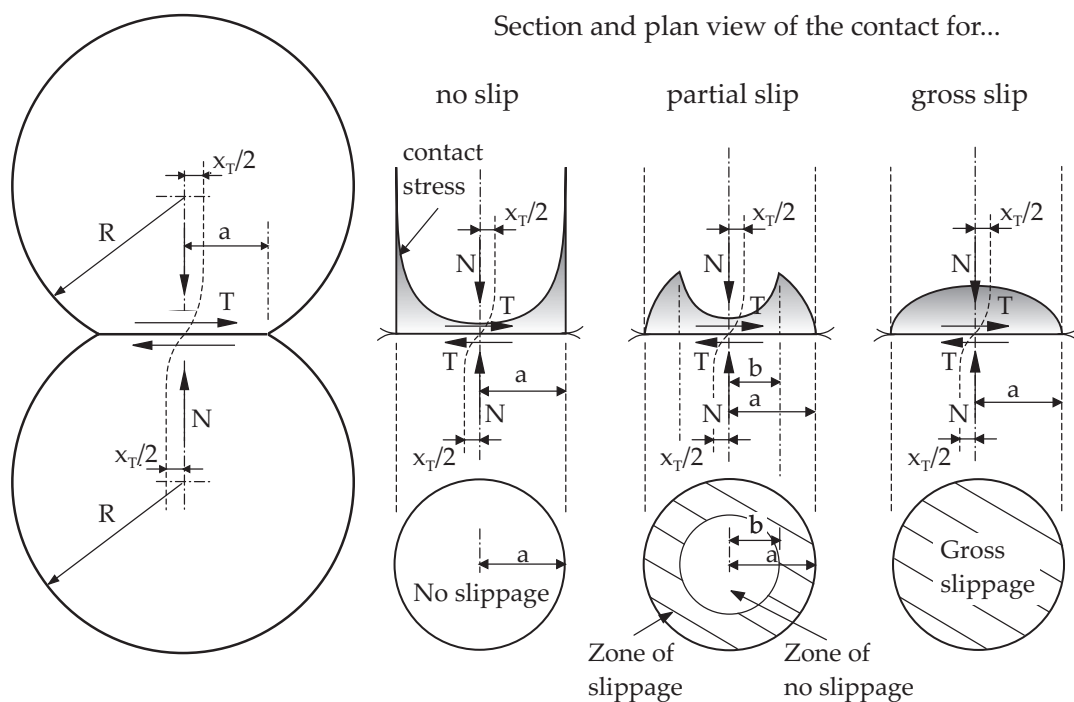


Figure 4.5: Two elastic and equally sized spheres in contact.

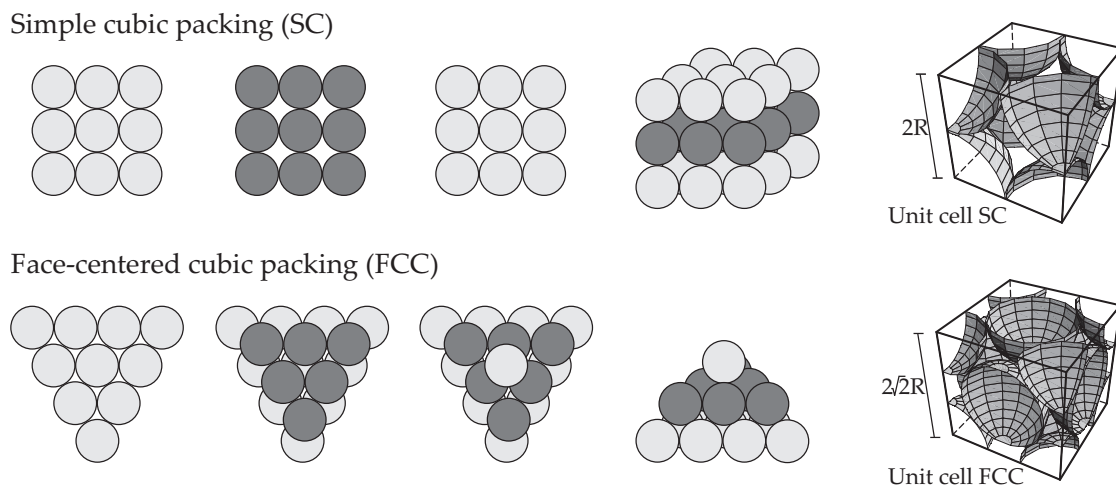


Figure 4.6: Simple cubic packing (SC) versus face-centered cubic packing (FCC).

equally sized spheres. Both assemblies are illustrated in Figure 4.6 together with their unit cell. SC packing has a coordination number of 6, and a void ratio of 0.91; FCC has a coordination number of 12, and a void ratio of 0.35.

The SC unit cell has 3 contacts in a volume of $8R^2$, where the FCC unit cell has 24 contacts in a volume of $16\sqrt{2}R^3$. Per unit volume, this results in $2\sqrt{2}$ more inter-particle contacts in the FCC packing than in the SC packing. The force per contact in isotropically loaded unit cells on the other hand, is $2\sqrt{2}$ times less in the FCC packing. From Equation 4.3, the bulk stiffness ratio between FCC and SC packing becomes:

$$\frac{(k)_{FCC}}{(k)_{SC}} = 2\sqrt{2} \left(\frac{1}{2\sqrt{2}} \right)^{\frac{1}{3}} = 2. \quad (4.6)$$

Assuming Poisson's ratio to be constant, the empirical relationship given by Hardin & Richart [54] presented in Equation 3.8, suggests a bulk stiffness increase of $\approx 65\%$ in the FCC packing. Compared to the empirical value, the above deduced stiffness increase of 100% is too high. The difference is probably due to the simplification of real soil structure in SC and FCC assemblies. Nevertheless, the stiffness increase is of the same magnitude. The number of contacts per particle and particle bracing can therefore be assumed to be the main factors, which lead to higher stiffness in real soils.

4.2.3 The influence of cementation

Figure 4.7 shows a cement coated contact of two spherical particles. Again, a simple Hertz contact between the spherical particles is assumed. The cementing agent shall have uniform thickness, the same material properties as the soil particles, and compatible deformations with the particles upon loading. As bonding increases the contact area, it is readily apparent from Equation 4.3, that bonding also increases contact stiffness. For spherical particles the cement coat thickness, t relates to cement contents by weight CC as follows:

$$(CC + 1)^{\frac{1}{3}} = 1 + \frac{t}{R}. \quad (4.7)$$

Using the geometrical relationship between coat thickness and cement contents, Fernandez & Santamarina [39] derived the following expressions for cementing before and after contact loading respectively:

$$(k_n)_{before} = \frac{G_S}{1 - \nu_S} \sqrt[3]{\frac{\left((CC + 1)^{\frac{2}{3}} - 1 \right)^{\frac{3}{2}}}{(CC + 1)^{\frac{1}{3}}} + \frac{3(1 - \nu_S)}{2} \frac{N}{4R^2 G_S}} \quad (4.8)$$

$$(k_n)_{after} = \frac{G_S}{1 - \nu_S} \sqrt[3]{(CC + 1)^{\frac{2}{3}} - 1 + \left(\frac{3(1 - \nu_S)}{2} \frac{N}{4R^2 G_S} \right)^{\frac{2}{3}}} \quad (4.9)$$

where k_n is the local normal contact stiffness as introduced in Equation 4.2. In both cases, cementation is causing a stiffness increase independent of confining pressure. With in-

creasing confining pressure, the relative importance of bonding decreases. If the number of particle contacts increases with decreasing void ratio, like for example in the FCC packing, the effect of cementation is more pronounced in the denser configuration.

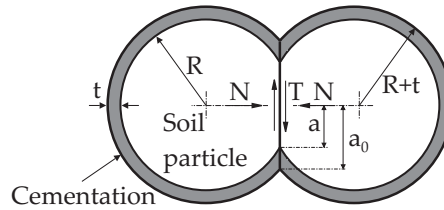


Figure 4.7: Cemented inter-particle contact of two spheres after Fernandez & Santamarina [39].

4.2.4 Summary

The influences of parameters that appear in almost all very small-strain stiffness relationship (see Table 3.2, 3.3, and 3.4) were studied at the inter-particle contact level. Most previously presented experimental findings were qualitatively reproduced. In order to obtain a quantitative reliable constitutive response of a micromechanical model, a number of conditions have to be fulfilled: First, the inter-particle contact needs to be defined adequately, second the soil grains and its structure have to be reasonably well abstracted and finally the problem of homogenization or calculation time must be solved. For the moment, a small-strain stiffness model aimed for practical use can hardly be formulated from a particle contact level. The following chapters therefore concentrate on continuum models. Existing continuum small-strain stiffness models are discussed in Chapter 5. A new small-strain model is developed in Chapter 6.

Chapter 5

Existing small-strain stiffness constitutive models

The first small-strain stiffness constitutive models that were intended for static soil analysis date from the late 1970's. This chapter gives an overview of the developments in the field of small-strain stiffness since then. It begins with a historical review followed by a discussion of the most well known models and modeling directions. Some of the models that will be introduced in this chapter should be classified rather as relationships because they lack a constitutive response in non-monotonic loading patterns. Nevertheless they are included in this chapter, since they have been extensively used in the past despite this shortcoming.

The models and modeling directions covered in more detail are:

- The Simpson Brick model
- Models known from soil dynamics
- The Jardine model
- Multi surface models
- Intergranular Strain

The order of the above list is chosen according to model complexity rather than according to the date they were proposed. Only continuum models are considered in this chapter. Although micromechanical concepts might be very helpful in the model abstraction process, they cannot yet be used in the analysis of boundary value problems.

5.1 A brief history of small strain modeling

The curves shown in Figure 3.4 were used in soil dynamics for many years before being compiled and published by Seed & Idris in 1970 [162]. They were not however applied to static problems until about ten years later. That was when the first small-strain models for static applications were introduced. Amongst them were models that use one or more kinematic yield surfaces, either in strain space as the model by Burland et al. published in 1979 [25] or stress space as the model by Mroz et al. [126] which dates

back to 1978. Limiting the number of kinematic yield surfaces to one for the purpose of modeling small-strain stiffness only, Al-Tabbaa [1], and Al-Tabbaa & Wood [2] created the class of *bubble* models in 1987. In 1990 Stallebrass [170] introduced an additional (kinematic) history surface for the bubble within the Cam-Clay framework and created the well known 3-SKH model. Parallel to these models with kinematic surfaces, a different approach was taken by Jardine et al. [79] in 1986. By fitting stiffness-strain curves, they directly calculated soil stiffness as a mathematical function of applied strain. In his 1992 Rankine lecture, Simpson [168] made the analogy between soil behavior and a man pulling bricks behind him. The analogy in fact can be used to explain the concept introduced by Mroz et al. [126], as well as many other models. Simpson's analogy together with his interpretation in strain space became well known by the term *Simpson brick model* and shall be the first to be discussed in detail.

Many refined models based on the ones mentioned above have been developed in subsequent years. Advances in finding mathematical descriptions of the stiffness-strain curve in the sense of Jardine [79] are for example documented by Gunn [48] in 1993 and by Tatsuoka [177] in 2000. The class of bubble models have mainly been enhanced by additional mechanisms, as for example the use of a second yield loci as found in the Milan Model published in 2002 [201]. However, most of these models still use a loading-unloading criterion similar to that of a one-brick Simpson brick model, as does the model by Papadimitriou et al. [134] and the Intergranular Strain concept, which is the small-strain extension of Hypoplasticity introduced by Niemunis & Herle in 1997 [129]. The Intergranular Strain concept makes use of a pre-defined interpolation function for the material's strain history dependent stiffness. For this reason, Intergranular Strain falls outside the mainstream modeling directions presented.

5.2 The Simpson Brick model

Simpson's brick model explains soil behavior on the basis of a man dragging some bricks behind him, each of them connected to a string of unique length. Some of these strings, or perhaps all of them, may slacken when the man heads in a new direction. Then, after continuously walking in the new direction, strings will be tensioned one by one again. An illustration of this analogy is presented in Figure 5.1.

Although these bricks could be interpreted as kinematic yield surfaces in stress space, Simpson favors the idea that the man is a point in strain space that represents a soil element. The bricks attached to his back represent quantified portions of the soil element. Bricks being dragged while the man moves, correspond to plastic strains, bricks with slackened strings correspond to elastic strains. Hence, fully elastic behavior is modeled whenever the man is moving without tensioning any strings. By selecting appropriate brick sizes and string lengths, an entire S-shaped stiffness-strain curve can be approximated as for example shown in Figure 5.1. Short strings represent the behavior of small-strains, long strings that of large strains. Strain history is automatically accounted for in the model by remembering the brick's positions in strain space. Although the original Simpson brick model is rarely found to be closely implemented as for example in

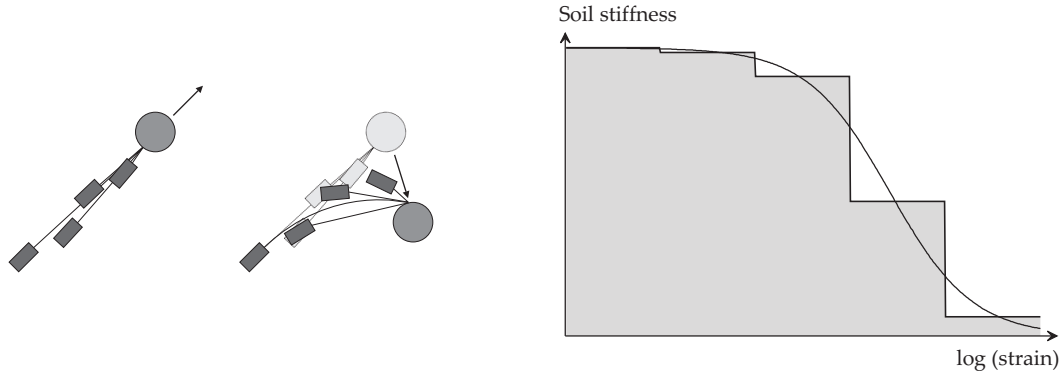


Figure 5.1: Simpson brick model with four bricks (left). Stiffness decay after load reversal is a discontinuous approximation of the real stiffness-strain curve (right).

the model by Länsivaara [105], its basic idea of history tracking has been widely used. Doing so, the number of bricks are often reduced to one only.

5.3 Models known from soil dynamics

Typical models used in dynamic soil analysis are mainly the bilinear, Ramberg-Osgood, and Hardin-Drnevich models. The characteristics of bilinear models were studied by Caughey [26] and incorporated in dynamic analysis for example by Idriss & Seed [68]. The Ramberg-Osgood model was first introduced by Ramberg & Osgood [145] and further developed by Jennings [81]. The Hardin-Drnevich model [52] is an extension of Kondner's [94] monotonic stress-strain relationship to the cyclic loading case. The hyperbolic law by Kondner is explored in more detail in Chapter 7. The Hardin-Drnevich model is probably the most frequently used model in soil dynamics.

In shear-strain γ shear-stress τ space these models are defined as follows:

$$\text{Bilinear:} \quad \tau = \begin{cases} G_0\gamma & \text{for } \gamma < \gamma_y \\ \tau_y + G_0(\gamma - \gamma_y) & \text{for } \gamma \geq \gamma_y \end{cases} \quad (5.1)$$

$$\text{Ramberg-Osgood:} \quad \gamma = \frac{\tau}{G_0} \left(1 + \alpha \left| \frac{\tau}{\tau_y} \right|^\kappa \right) \quad (5.2)$$

$$\text{Hardin-Drnevich:} \quad \tau = \frac{G_0\gamma}{1 + \left| \frac{\gamma}{\gamma_r} \right|} \quad (5.3)$$

where G_0 is the initial shear modulus, α , and $\kappa \geq 1$ are material constants, and τ_y , γ_y , and γ_r are user defined threshold values for shear- strain and stress respectively. Rewriting the Ramberg-Osgood, and Hardin-Drnevich models in terms of normalized secant

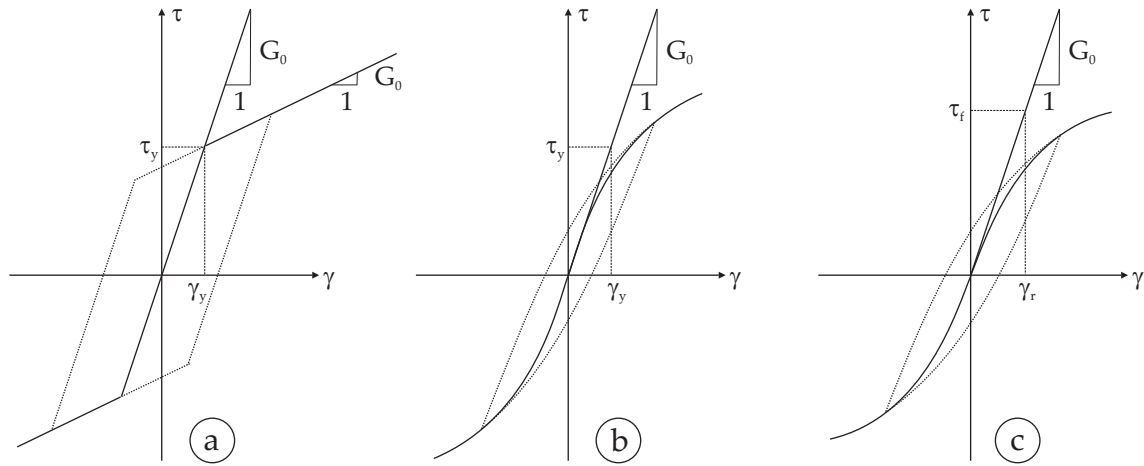


Figure 5.2: Skeleton curves in $\gamma - \tau$ -space of a) the bilinear model, b) the Ramberg-Osgood model, and c) the Hardin-Drnevich model.

stiffness, $\frac{G}{G_0}$ shows the similarity and basic difference in these two models:

$$\frac{G}{G_0} = \frac{1}{1 + \alpha \left| \frac{\tau}{\tau_y} \right|^\kappa} \quad (\text{Ramberg-Osgood}) \quad (5.4)$$

$$\frac{G}{G_0} = \frac{1}{1 + \left| \frac{\gamma}{\gamma_r} \right|} \quad (\text{Hardin-Drnevich}). \quad (5.5)$$

The Ramberg-Osgood defines stiffness decay as a function of stress whereas the Hardin-Drnevich model defines it as a function of strain. Other than that, the two formulations are very similar. The hysteresis effect described in Masing's second rule (see Section 3.2.7) can be easily incorporated in both models using the expression proposed in Hashiguchi [55]:

$$\varepsilon_0 - \varepsilon_R = f \left(\frac{\sigma_0 - \sigma_R}{L} \right) \quad (5.6)$$

with shape Factor $L = 1$ in primary loading and $L = 2$ in unloading and reloading. In Equation 5.6, $f(\sigma)$ represents the monotonic stress-strain relationship $\varepsilon = f(\sigma)$. The strain and stress levels ε_0 and σ_0 denote the last load reversal point in stress-strain space, where ε_R , and σ_R specify the actual strain and stress respectively. Figure 5.2 shows examples of hysteresis loops derived by the bilinear, Ramberg-Osgood and Hardin-Drnevich models.

The Ramberg-Osgood model has the probably unintended quality that it can be easily used in combination with stress space based elastoplastic models, as shown in Papadimitriou et al. [134]. For the coupling of the Ramberg-Osgood formulation to their elastoplastic model, Papadimitriou et al. defined two scalar valued functions χ for the

material's stress and strain history:

$$\chi_r = \sqrt{(\mathbf{r} - \mathbf{r}^{\text{lr}}) : (\mathbf{r} - \mathbf{r}^{\text{lr}})} \quad \text{and} \quad \chi_e = \sqrt{(\mathbf{e} - \mathbf{e}^{\text{lr}}) : (\mathbf{e} - \mathbf{e}^{\text{lr}})} \quad (5.7)$$

where \mathbf{r} and \mathbf{e} are deviatoric stress and strain ratio tensors respectively and superscript $()^{\text{lr}}$ denotes tensors that are associated to the last memorized load reversal point. A load reversal is assumed whenever the scalar valued function χ_e loses its monotony, e.g. $\chi_e \dot{\chi}_e < 0$. In terms of a one-brick Simpson model in strain space, a load reversal is thus assumed whenever the string between the man and the brick is slacking. Then the position of the brick is memorized and stiffness is calculated as a function of the distance to this memorized point in stress space, e.g. as the resulting stiffness of the Ramberg-Osgood formulation 5.4.

Small-strain stiffness models similar to the one published by Papadimitriou et al. can be found in Hueckel & Nova [65] or Pestana & Whittle [137]. The model of Hueckel & Nova mainly differs from the one by Papadimitriou et al. in the stress memory. The model by Hueckel & Nova memorizes not only one, but several load reversal points and does not explicitly use the Ramberg-Osgood formulation. Likewise, the hysteretic equations of the MIT-S1 model described in Pestana & Whittle [137] as:

$$\frac{2G/K}{2G_0/K_0} = \begin{cases} \frac{1}{1+\omega\chi_r} & \text{for unloading} \\ \frac{1}{1+\omega\chi_p\chi_r} & \text{for reloading} \end{cases} \quad (5.8)$$

are modified from the Ramberg-Osgood formulation. Here, ω is a material parameter and the scalar valued functions χ_p and χ_r give the volumetric and the deviatoric stress in respect to the last load reversal point $()^{\text{lr}}$:

$$\chi_p = \begin{cases} p/p^{\text{lr}} & \text{for } p < p^{\text{lr}} \\ p^{\text{lr}}/p & \text{for } p \geq p^{\text{lr}} \end{cases} \quad (5.9)$$

The deviatoric stress measure χ_r used in the MIT-S1 model is the same as the one defined in Equation 5.7. Another difference in the hysteretic equations of the MIT-S1 compared to the model by Papadimitriou et al. is the definition of load reversal points. The MIT-S1 model assumes load reversals whenever the volumetric strain history loses monotony. Only if the volumetric strain increment is zero (e.g. undrained loading), the MIT-S1 model checks for the monotony of deviatoric strains. Then, a load reversal is again assumed whenever $\chi_e \dot{\chi}_e < 0$.

Note that all of the above stress-strain laws are not continuous in strain (load reversals) so that by definition they do not qualify as *elastic* stress-strain laws. Nevertheless, strain on a closed stress cycle starting from a stress reversal point is recovered. In the following, the above stress-strain laws are therefore denominated *paraelastic* (Hueckel & Nova [65]).

5.4 The Jardine model

Jardine et al. [79] proposed a periodic logarithmic function to express the non-linear relationship between normalized secant Young's modulus E_u and axial strain ε_a in an

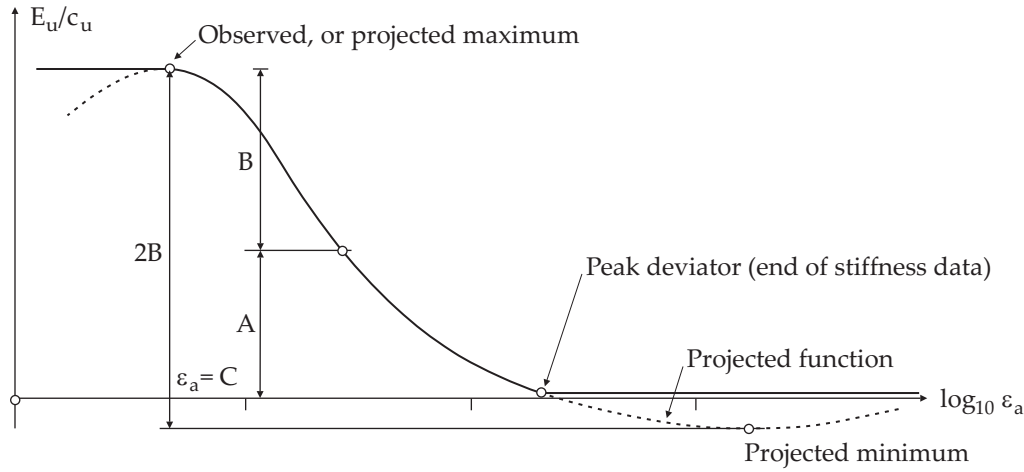


Figure 5.3: Jardine model - secant stiffness defined as a trigonometric function of strain (projected curve).

undrained triaxial test:

$$\frac{E_u}{c_u} = A + B \cos \left\{ \alpha \left[\log_{10} \left(\frac{\varepsilon_a}{C} \right) \right]^\gamma \right\}. \quad (5.10)$$

Today, this type of non-linear elastic stress-strain law is commonly known as the *Jardine model*. Its empirical model constants A , B , C , α , and γ can be determined from (small-strain) triaxial test data. The secant Young's modulus E_u is normalized with undrained shear strength c_u . Due to the Jardine model's trigonometric nature, it is mandatory to specify the exact strain range in which the non-linear stress-strain law is to be applied. When exceeding the upper or lower limit of the strain range specified, stiffness is set as constant (Figure 5.3).

The normalized tangent Young's modulus E_{ut} corresponding to the secant Young's modulus E_u can be derived by differentiating and rearranging Equation 5.10:

$$\frac{E_{ut}}{c_u} = A + B \cos(\alpha I^\gamma) - \frac{B\alpha\gamma I^{\gamma-1}}{2.303} \sin(\alpha I^\gamma), \quad (5.11)$$

where $I = \log_{10} \left(\frac{\varepsilon_a}{C} \right)$. Since most numerical procedures make use of the tangent modulus E_{ut} instead of the secant modulus E_u , Equation 5.11 represents the more commonly used form of the Jardine model. Jardine et al. [79] also mention in their original work the possibility of expanding the proposed nonlinear stress-strain law to bulk and shear moduli. Potts & Zdravkovic [138] propose the following notation for such an expansion:

$$\begin{aligned}
 \frac{3G}{p'} &= C_1 + C_2 \cos(c_1 X^{c_2}) - C_2 c_1 c_2 \frac{X^{c_2-1}}{2.303} \sin(c_1 X^{c_2}) \\
 \frac{K}{p'} &= C_4 + C_5 \cos(c_3 X^{c_4}) - C_5 c_3 c_4 \frac{X^{c_4-1}}{2.303} \sin(c_3 X^{c_4}) \quad \text{with} \\
 X &= \log_{10} \left(\frac{2\varepsilon_d}{3C_3} \right) = \log_{10} \left(\frac{2\sqrt{\frac{1}{2}[(\varepsilon_1 - \varepsilon_2)^2 - (\varepsilon_2 - \varepsilon_3)^2 - (\varepsilon_1 - \varepsilon_3)^2]}}{3C_3} \right), \quad \text{and} \\
 Y &= \log_{10} \left(\frac{\varepsilon_v}{C_6} \right) = \log_{10} \left(\frac{\varepsilon_1 + \varepsilon_2 + \varepsilon_3}{C_6} \right)
 \end{aligned} \tag{5.12}$$

where G is the shear modulus, K is the bulk modulus, p' is the mean effective stress, ε_i are the principal strains, and the number of material parameters ($C_1 \cdots C_6, c_1 \cdots c_4$) is increased to 10. In its expanded version, the Jardine model implicitly varies Poisson's ratio as a function of strain. When selecting the model's parameters the user needs to be aware of this in order to keep Poisson's ratio within its physical limits. Since the Jardine model is often used in Great Britain, model parameters for many British clays are available in the literature.

5.5 Multi (or Infinite) surface models

The first multi surface models were independently proposed by Mroz [125], and by Iwan [73]. Back then, these models were developed to model the hysteretic Bauschinger effect in metals. Later, multi surface models were mainly developed for soils, starting with the model by Prevost [142], and this by Mroz et al. [126]. The common idea of all these early models is to have a set of similar, nested yield loci f_n that are kinematically (and optionally volumetrically) hardened:

$$\begin{aligned}
 f_n &= \hat{f}((\hat{\sigma}_{ij})_n) - r_n \bar{f}(q_{*,n}) \quad \text{with} \\
 (\hat{\sigma}_{ij})_n &= \sigma_{ij} - (\alpha_{ij})_n
 \end{aligned} \tag{5.13}$$

where r_n is the ratio of the n^{th} yield surface to the outermost, or distinct yield surface, $(\alpha_{ij})_n$ gives the internal backstress of the n^{th} yield surface, and $q_{*,n}$ is a suitable set of scalar internal variables.

One of the most important features of multi-surface models is their ability to capture recent stress history in their internal variables (mainly backstress). Small-strain stiffness models based on the multi-surface concept associate small-strain stiffness with the innermost yield surface. By defining an appropriate set of hardening laws for all yield surfaces, such multi-surface models can give realistic predictions over a wide strain range.

A special subclass of kinematic multi-surface small-strain stiffness models is the class of *bubble* models (Al-Tabbaa [1], [2]). Bubble models have only one small kinematic yield surface (*bubble*), with elastic stiffness equal to the soil's small-strain stiffness. Increasing the number of kinematic yield surfaces to two, Stallebrass & Taylor [171] extended the bubble model by Al-Tabbaa & Wood [2] to the 3-SKH model. Although the 3-SKH model might be considered sufficiently complex, the number of yield surfaces could also theoretically be increased to infinite.

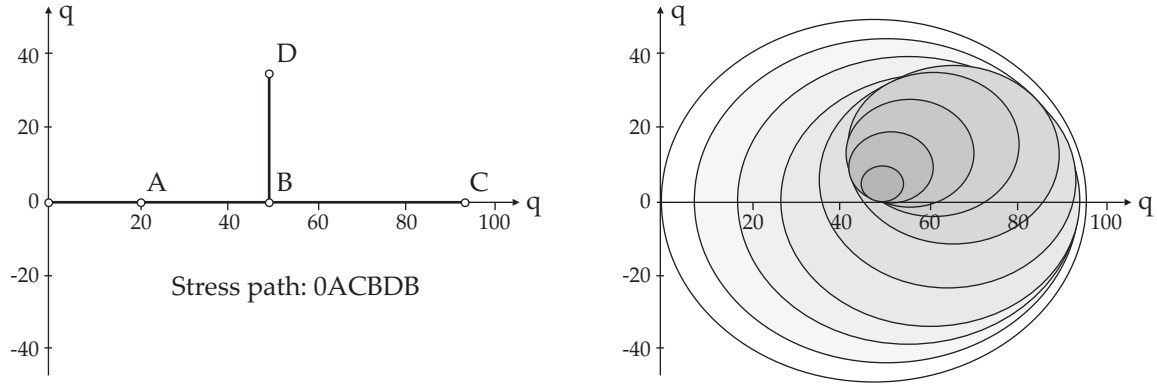


Figure 5.4: Position of 10 yield surfaces after stress path 0ACBDB. The inner surfaces have been dragged by the stress point. The outermost yield surface has never been reached because of volumetric hardening: Plastic volumetric strains on inner yield surfaces increase the size of all yield surfaces.

An illustration of the multi-surface concept is given in Figure 5.4. Here the evolution of 10 yield surfaces for a given load path is shown, using a discrete form of Houlsby's [62] continuous hyperplastic formulation. Note that this formulation abandons the concept of nested and non-overlapping yield surfaces, which goes back originally to Prevost [142].

5.6 Intergranular Strain for the Hypoplastic model

In 1997 Niemunis & Herle [129] introduced a new tensorial state variable δ to the hypoplastic theory. The new state variable has been named Intergranular Strain since it is meant to account for intermolecular and surface forces within the soil skeleton. The normalized magnitude of Intergranular Strain is defined as:

$$\rho = \frac{\|\delta\|}{R} \quad (5.14)$$

where R is a material constant associated with the very small-strain range. Evolution of Intergranular Strain is controlled by the loading direction; loading history is memorized as Intergranular Strain. Again, a one-brick like loading-unloading criterion is used:

$$\dot{\delta} = \begin{cases} (1 - \hat{\delta}\hat{\delta}^{\beta_r}) : \mathbf{D} & \text{for } \hat{\delta} : \mathbf{D} > 0 \\ \mathbf{D} & \text{for } \hat{\delta} : \mathbf{D} \leq 0 \end{cases} \quad (5.15)$$

where \mathbf{D} is the stretch tensor and β_r is a material parameter that controls the evolution of Intergranular Strain. At the same time, β_r controls the nonlinearity of the resulting stiffness-strain curve. Numerically integrating Equation 5.15 over time gives continuous Intergranular Strain ρ with $0 \leq \rho \leq 1$. For $\rho = 0$ stiffness is increased in all loading directions; for $\rho = 1$ stiffness is a function of loading direction. Minimum stiffness is obtained

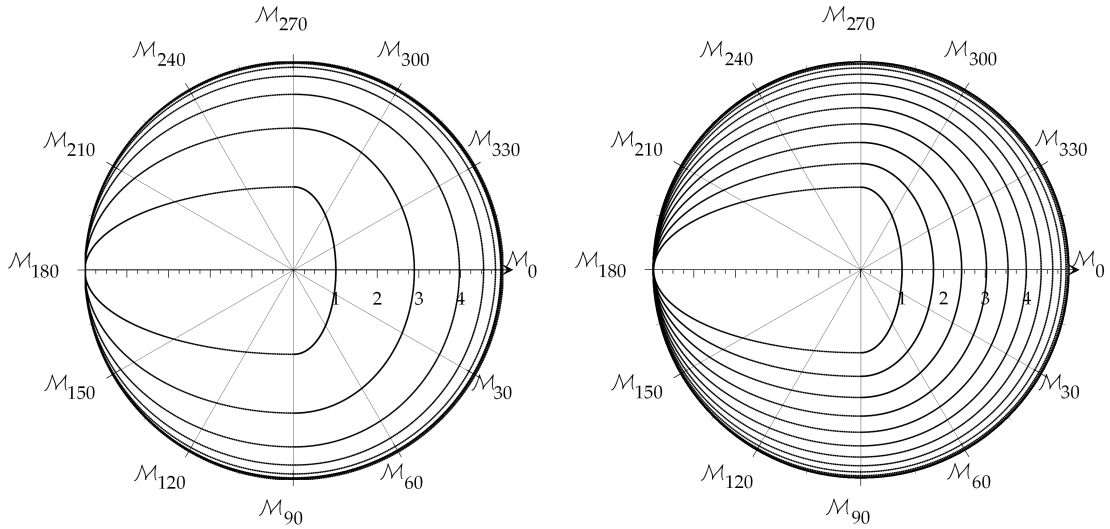


Figure 5.5: Interpolated stiffness \mathcal{M} as a function of angular change in the loading path according to Equation 5.16 with $\mathcal{L} = \mathbf{1}$, $\mathbf{N} = \mathbf{0}$, $m_R = 5$, and $m_T = 2$. Response curves are drawn at Intergranular Strains of $\rho = 0$ to 1 in steps of 0.1 for $\chi = 6.0$ on the left and $\chi = 2.0$ on the right respectively.

for monotonic loading, neutral loading gives a somewhat increased stiffness defined by the multiplier m_T whereas reversed loading gives maximum stiffness by applying the multiplier m_R . Loading directions in between are interpolated according to:

$$\mathcal{M} = [\rho^\chi m_T + (1 - \rho^\chi) m_R] \mathcal{L} + \begin{cases} \rho^\chi (1 - m_T) \mathcal{L} : \hat{\boldsymbol{\delta}} \hat{\boldsymbol{\delta}} + \rho^\chi \mathbf{N} \hat{\boldsymbol{\delta}} & \text{for } \hat{\boldsymbol{\delta}} : \mathbf{D} > 0 \\ \rho^\chi (m_R - m_T) \mathcal{L} : \hat{\boldsymbol{\delta}} \hat{\boldsymbol{\delta}} & \text{for } \hat{\boldsymbol{\delta}} : \mathbf{D} \leq 0 \end{cases} \quad (5.16)$$

where \mathcal{M} is the interpolated stiffness and $\hat{\boldsymbol{\delta}}$ is the direction of Intergranular Strain defined as $\hat{\boldsymbol{\delta}} = \boldsymbol{\delta} / \|\boldsymbol{\delta}\|$. Material parameters m_R , m_T and χ affect the interpolation, where χ purely increases the impact of ρ on the interpolation and so together with β_R controls the non-linear stiffness decay. The hypoplastic operators \mathcal{L} and \mathbf{N} represent the linear and the nonlinear terms in the original hypoplastic equation respectively [93]. Assuming a straight monotonic loading history in a plane problem, the directional dependency of \mathcal{M} on the loading direction can be visualized as shown in Figure 5.5. For increasing Intergranular Strain the directional dependency grows to its maximum at $\rho = 1$.

The high number of parameters and also the model abstraction might pose a serious problem for routine application of Intergranular Strain. Engineers working in practise may simply not understand the meaning of the parameters they should provide. Different aspects of the practical usability of all the models introduced so far are discussed in more detail in the next section.

5.7 A critical review of small-strain stiffness models regarding their use in routine design

All the small-strain models discussed in this chapter can be divided into three subclasses: (i) Non-linear (para-)elastic stress-strain laws, (e.g. models from soil dynamics, Jardine model), (ii) Kinematic hardening elastoplastic models formulated in stress space, (e.g. multi-surface models) and (iii) Other concepts that might include strain space based formulations, (e.g. Simpson Brick model, Intergranular Strain).

Non-linear paelastic stress-strain laws are generally deduced for a specific loading path. Prior to application in boundary value problems, they need to be generalized. Without such a generalization, the above introduced non-linear stress-strain laws cannot be recommended for use in practical applications. In combination with an elastoplastic approach, they may prove to be very suitable to use in small-strain stiffness modeling. The Hardin-Drnevich model particularly qualifies for such applications as it combines minimum material parameter input with reasonable modeling qualities (see Chapter 3). In this respect, the Jardine model seems less adequate.

Kinematic multi-surface elastoplastic models, for example the 3-SKH model, can provide reasonable analysis results while the computational costs remain moderate. The main obstacle in using these models in practical applications is probably the material parameter selection process. The recent implementation of the 3-SKH model by Gramatikopoulou [46], expects for example, user input for a) the ratio of the size of the history surface to that of the outermost surface, b) the ratio of the size of the yield surface to that of the history surface, and c) the exponent in the hardening function. Without relating these parameters to test data or providing trustworthy correlations, such models cannot be recommended for routine design. On the other hand, providing such correlations might be an elaborate or even impossible task.

The remaining concepts discussed in this chapter lack also some substantial features of real soil behavior (Simpson Brick model) or they afford too many (abstract) user parameters (Intergranular Strain) to allow them to be recommended for use in routine design. However, it should be noted that many parameters in the Intergranular Strain concept can be set to default values. Determination of the full set of Hypoplastic material parameters is still not an easy task to undertake.

Chapter 6

The Small-Strain Overlay model

All isotropic hardening, and most kinematic hardening elastoplastic models use yield loci of finite size. Strategies to implement small-strain stiffness in just one very small elastic domain (bubble models), or in many yield loci (multi-surface plasticity), have been discussed in the previous chapter. However, models that are used in engineering practice today, rarely have more than one elastic domain. The Cam-Clay, or the Hardening Soil model are just two examples of such models. It is impossible for very small-strain stiffness to be associated with the entire elastic domain in these models as they would respond too stiff in larger unloading-reloading cycles as a consequence. Therefore, their elastic stiffness is generally taken as secant stiffness of larger strain unloading-reloading loops. Small-strain stiffness is neglected. Here, the Small-Strain Overlay model which will be developed in this chapter, comes into play.

The Small-Strain Overlay model is, similar to some of the models discussed in the previous chapter, a paraelastic approach. The overlay model can be used in combination with elastoplastic formulations: If it detects small or very small-strain amplitudes, it increases the stiffness of the elastoplastic model accordingly. For larger strain amplitudes, the overlay model is inactive, but still monitors loading history.

In order to guarantee the new model's compatibility with many existing constitutive models, it was decided to keep its output isotropic. Its objective multi-axial formulation though accounts for strain induced anisotropy. In this chapter, the small-strain stiffness overlay model is first formulated, and secondly validated.

6.1 Model formulation

6.1.1 Material history and history mapping

As pointed out in Chapter 3 and 4, decay of small-strain soil stiffness with straining can be associated with inter-particle forces within the soil skeleton. Once the direction of loading is reversed, the stiffness regains a maximum recoverable value. Then, while loading in the reversed direction is continued, the stiffness decreases again. From a modeling point of view, it is therefore essential to keep track of the material's strain history. It has already been mentioned that deviatoric loading has a higher impact on the re-arrangement of inter-particle force than hydrostatic loading. Hydrostatic loading mainly increases force magnitude, whereas deviatoric loading additionally causes the directional rearrangement of forces. In order to simplify the model and its calibration,

effects of hydrostatic strain and strain history are neglected in the following. Hence, the model presented relies completely on the deviatoric strain history.

A criterion has to be defined for whether the actual strain rate is to be considered monotonic or not. The criterion has to distinguish whether the actual strain rate points in the same direction of the previous applied loading or not. In order to have a realistic 3D model response, this criterion should not only rely on a scalar valued test variable, i.e. length measured in the deviatoric plane. Hence, the criterion proposed here considers all three principal deviatoric strain directions separately, which resembles three independent brick models. When there is no principal strain rotation, the criterion reduces to two independent brick-models.

In order to account for principal strain rotations, the strain history is stored in general strain space. Transformed to the principal system of the actual strain increment, it is then interpreted as a 2^{nd} order surface. To avoid any possible singularities of the 2^{nd} order surface, a volumetric 1 strain is superimposed onto the deviatoric history strain. A geometrical interpretation of 2^{nd} order surfaces in some basic tests is shown in Figure 6.1. Here, the small deviatoric strains have been amplified to the power of $1e^3$ in order to visualize the distortion of the volumetric 1 strain component, which is a perfect sphere in this interpretation.

In a mathematical framework, determination of the actual strain history is as follows. Let H_{kl} be a strain tensor that memorizes the deviatoric strain history. The actual deviatoric strain rate is denoted as \dot{e}_{kl} . By solving the Eigenvalue problem:

$$(\dot{e}_{kl} - \lambda^{(m)}\delta_{kl}) S_l^{(m)} = 0 \quad (6.1)$$

a set of orthogonal Eigenvectors S_{lm} for \dot{e}_{kl} is found. Unlike the transformed deviatoric strain increment

$$\underline{\dot{e}}_{kl} = S_{km}\dot{e}_{mn}S_{nl}, \quad (6.2)$$

the transformed strain history

$$\underline{H}_{kl} = S_{km}H_{mn}S_{nl}, \quad (6.3)$$

typically is not diagonal. However, extending strain history by a volumetric 1 strain makes it a positive definite symmetric tensor. Its deviation from the volumetric 1 sphere in the principal directions is given by the diagonal terms of \underline{H}_{kl}^i . Each principal direction is checked for possible reversed loading separately: Reversed loading is assumed whenever the sign of a diagonal term does not equal that of the corresponding Eigenvalue λ . To reset strain history in reversed loading directions, a diagonal transformation matrix \underline{T}_{kl} is defined as:

$$\begin{aligned} \underline{T}_{11} &= \frac{1}{\sqrt{H_{11}+1}} (1 + u(\lambda^{(1)}H_{11})(\sqrt{H_{11}+1} - 1)) \\ \underline{T}_{22} &= \frac{1}{\sqrt{H_{22}+1}} (1 + u(\lambda^{(2)}H_{22})(\sqrt{H_{22}+1} - 1)) \\ \underline{T}_{33} &= \frac{1}{\sqrt{H_{33}+1}} (1 + u(\lambda^{(3)}H_{33})(\sqrt{H_{33}+1} - 1)) \end{aligned} \quad (6.4)$$

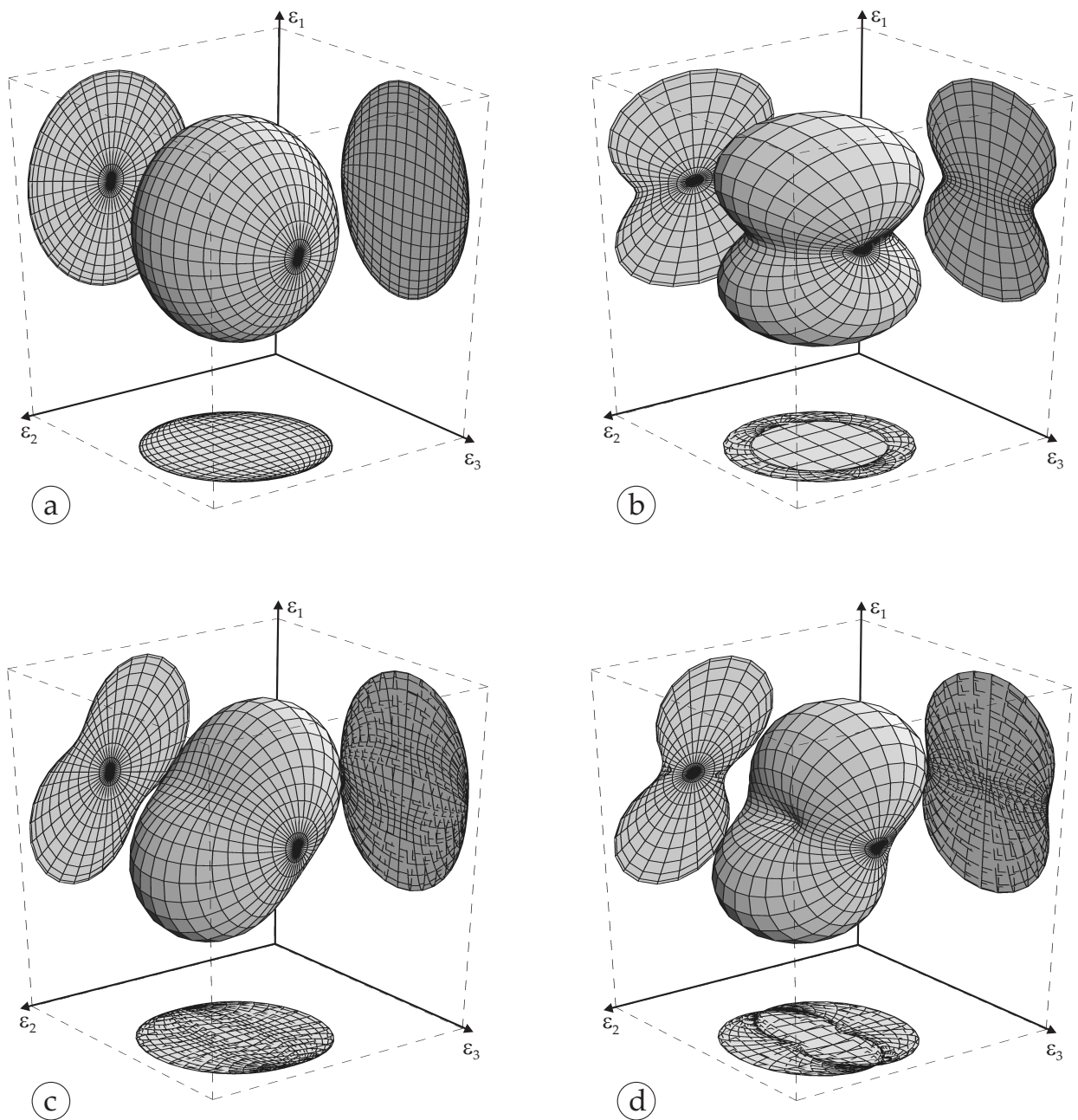


Figure 6.1: Strain history interpreted as 2nd order surface in strain space. From left to right: (a) hydrostatic loading, (b) triaxial extension, (c) simple shear, (d) simple shear after triaxial extension.

where $u(x)$ is the Heaviside step function, defined as:

$$u(x) = \begin{cases} 0 & \text{for } x < 0 \\ 1 & \text{for } x \geq 0 \end{cases} \quad (6.5)$$

The updated strain history \underline{H}_{kl}^* is then calculated as:

$$\underline{H}_{kl}^* = \underline{T}_{km}(\underline{H}_{mn} + \delta_{mn})\underline{T}_{nl} - \delta_{kl}. \quad (6.6)$$

From the updated strain history a scalar valued shear strain measure γ_{Hist} is defined next:

$$\gamma_{Hist} = \sqrt{3} \frac{\|\dot{\underline{e}}_{km} \underline{H}_{ml}^*\|}{\|\dot{\underline{e}}_{kl}\|} \quad (6.7)$$

where $\|\dots\|$ denotes the Hilbert-Schmidt norm $\|A\| = \sqrt{a_{ij}a_{ij}}$, which can be proven to conserve objectivity. In a geometric context, Equation 6.7 is the projection of the strain history onto the actual loading direction. The shear strain measure γ_{Hist} can then subsequently be used to define an isotropic material stiffness as shown in the next section. In an incremental form, the model formulation is summarized in Box 6.1.

6.1.2 From strain history to stiffness

The modified Hardin-Drnevich relationship introduced in Chapter 3 is used next in relating scalar valued strain amplitudes γ_{Hist} to material stiffness. Stiffness is described by two independent elastic moduli. However, it should be noted that a material with non-linear strain dependent stiffness as introduced here, is neither an elastic nor a hypoelastic material. Definitions of these material types and the consequences of being neither of these types is discussed in Section 6.3.

Shear modulus

As an alternative to the formulation by Jardine [78] [79] or the Ramberg-Osgood formulation [145], the modified Hardin-Drnevich [52] relationship is used here to relate deviatoric strain history to shear stiffness:

$$G = \frac{G_0}{1 + a \frac{\gamma_{Hist}}{\gamma_{0.7}}}, \quad (6.8)$$

where G is the actual secant shear modulus, G_0 is the initial shear modulus at very small-strains, and γ_{Hist} is the monotonic shear strain defined above. The parameter a and the threshold shear strain $\gamma_{0.7}$ is discussed in more detail in Section 3.3.3. In numerical applications, the secant modulus given in Equation 6.8 must be converted to a tangent modulus:

$$G = G_0 \left(\frac{\gamma_{0.7}}{\gamma_{0.7} + a\gamma_{Hist}} \right)^2. \quad (6.9)$$

In an incremental formulation, the actual elastic tangent shear modulus is best calculated by integrating the stiffness modulus reduction curve over the actual shear strain increment. In this way, large strain increments will not miss out small-strain stiffness:

$$G^{i+1} = \frac{G_0}{\gamma_{Hist}^{i+1} - \gamma_{Hist}^i} \left(\frac{\gamma_{Hist}^{i+1}}{1 + \frac{0.385\gamma_{Hist}^{i+1}}{\gamma_{0.7}}} - \frac{\gamma_{Hist}^i}{1 + \frac{0.385\gamma_{Hist}^i}{\gamma_{0.7}}} \right), \quad (6.10)$$

where i and $i + 1$ denote quantities of the previous and the actual calculation step respectively.

A complete numerical implementation of the Small-Strain Overlay model that integrates over the stiffness reduction curve is shown in Appendix A. Here, a lower cut-off of the model's stiffness reduction curve is introduced. The cut-off should be activated in combination with hardening plasticity formulations as otherwise, material stiffness for larger strains would become too small (see also Section 7.3.1).

Bulk modulus

Assuming Poisson's ratio to be constant (see Section 3.3) the bulk modulus can be calculated from the actual shear modulus as:

$$K = G \frac{2(1 + \nu)}{3(1 - 2\nu)}. \quad (6.11)$$

6.1.3 Initial loading and reloading

To systematically describe the behavior of brass under cyclic loading, Masing [111] proposed the following two rules (see also Section 3.2.7):

1. The shear modulus in unloading is equal to the initial tangent modulus for the initial loading curve.
2. The shape of the unloading and reloading curve is equal to the initial loading curve, except that its scale is enlarged by a factor of two.

Given that a functional form exists that can describe the initial loading curve, the above rules can likewise be applied to construct the hysteresis loops of soils for symmetrical or periodic loadings. However, if the loading is irregular, i.a. not symmetrical or periodic, two additional rules are commonly added to the original Masing rules:

3. Unloading and reloading curves should follow the initial curve in case the previous maximum shear strain is exceeded.
4. If the current loading or unloading curve intersects a previous one, it should follow the previous curve.

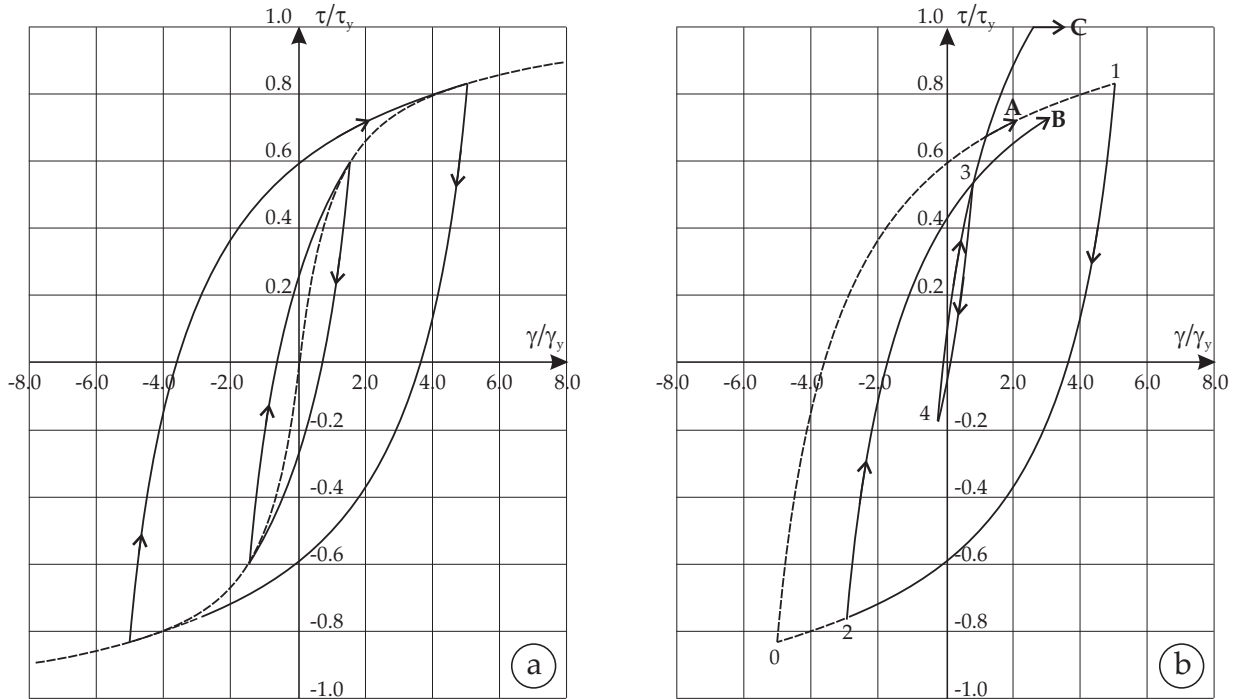


Figure 6.2: Hysteresis loops in symmetric (a) and irregular (b) loading according to the extended Masing rules (after Pyke [143]).

All four rules together are also referred to as the extended Masing rules. A discussion of several possible extensions replacing the fourth of the above rules, which goes back to Rosenblueth & Herrera [152], is given in Pyke [143]. Jennings [81], [82] for example proposes that the upper and lower bounds of the stress-strain relationship could be given by the reloading and unloading curves corresponding to the previous minimum and maximum strain amplitudes. Richart [149] on the other hand, simply limits the shear stress to a value no greater than the shear strength.

The Masing rule extensions by Rosenblueth & Herrera, Jennings and Richart are illustrated in Figure 6.2 for a one-dimensional simple shear problem. If point 2 is the previous minimum strain amplitude and curve 3 is the greatest previous reloading curve, on reloading from point 4, the solutions suggested by Rosenblueth & Herrera and that proposed by Jennings would follow path A. If, however, the dashed curve 0-1 is the greatest previous reloading curve, the solution used by Jennings follows stress path B. The solution used by Richart always follows path C.

The Small-Strain Overlay model adopts the first Masing rule by assuming $G_0 = \text{constant}$ in Equation 6.8. The second rule is obeyed by assuming a shape factor of 2 in the relationship given by Hashiguchi [55] (see Equation 5.6) i.e. $(\gamma_{0.7})_{ur} = 2\gamma_{0.7}$ where $(\gamma_{0.7})_{ur}$ is the threshold shear strain in unloading and reloading. The third and fourth rule request an internal memory of previous changes in the stress-strain path. For all of the above introduced Masing rule extensions, the memory i.a. requires loci in stress space.

A possible scheme of material memory rules is given in Hueckel & Nova [65]. However, an internal memory in stress space is not a practicable constitutive ingredient to the Small-Strain Overlay model, which is not intended to be used as a stand-alone model. In combination with an elastoplastic model, the memory would be highly influenced by plastic yielding, so that the response of the overlay model could only be determined in an iterative scheme. The yield loci of an combined elastoplastic model, e.g. the later discussed Hardening Soil model, can basically enforce the third Masing rule.

The material memory required to enforce the second Masing rule can on the other hand be defined in strain space by memorizing the minimum stiffness in loading history G_{\min} : For a given strain increment, it is always assumed first that the material is unloaded or reloaded. If then

$$G = \frac{G_0}{1 + a_{(\gamma_{0.7})_{ur}}^{\gamma_{Hist}}} \geq G_{\min}, \quad (6.12)$$

holds, the assumption is verified. Otherwise, primary loading is indicated.

A more convenient description of the minimum stiffness in the loading history can be given by normalized shear moduli. The elastic stiffness G_{ur} of a combined elastoplastic model can serve as a normalization measure. The small-strain stiffness multiplier G_m is defined as:

$$G_m = \frac{G_{\min}}{G_{ur}}. \quad (6.13)$$

If the Small-Strain Overlay model is combined with an elastoplastic model that hardens from the onset of primary loading, the above described implementation of Masing's second rule could be accomplished differently. Hardening plasticity can readily account for more rapidly decaying small-strain stiffness during initial loading. If the reloading threshold shear strain is also used in initial loading, material hardening of the elastoplastic model should equal the difference between initial loading and reloading as shown in Figure 6.3. This requires an elastoplastic model that would allow an adaption to its hardening laws in the small-strain range. One possibility, how such a modification can be accomplished is shown in the next chapter.

6.1.4 Effects of mean stress, void ratio, and OCR

Many of the influences on small-strain stiffness discussed in Chapter 3 can be easily incorporated into the Small-Strain Overlay model. The incorporation of mean stress, void ratio, or OCR effects for example, can be obtained by deploying the given correlations to the model's parameters G_0 and $\gamma_{0.7}$. User input is necessary for a set of parameters at well defined reference void ratio, reference mean stress, etc. A detailed example of the incorporation of mean stress dependency into the Small-Strain Overlay model is given in the next chapter. What follows in the next section is a verification of the basic model with fixed input parameters. An exception is made only when cyclic mobility is considered. Here, a power law of the form:

$$G_0 = G_0^{\text{ref}} \left(\frac{p'}{p^{\text{ref}}} \right)^m \quad (6.14)$$

scales the initial shear modulus. The shear modulus G_0^{ref} is specified at the reference mean stress p^{ref} .

6.2 A first model validation in element tests

For its first verification and validation, the Small-Strain Overlay model is not combined with any elastoplastic model. Triaxial loading paths render the overlay model's three-brick criterion for load reversals to a one-brick model. Applying the Small-Strain Overlay model in triaxial conditions can therefore be considered as code verification and validation of the modified Hardin-Drnevich relationship only. The Hardin-Drnevich relationship, however, can be assumed to be sufficiently validated for its use in a constitutive model (see for example Section 3.3.3). Not many triaxial test data are therefore presented here. Unfortunately, there are no biaxial, true triaxial, or hollow cylinder data known to the author, which could be used in the validation of the model's strain history mapping. Numerical simulations of a biaxial test published in [129] are used instead.

6.2.1 Triaxial tests

Almost all available stiffness-strain curves are derived in triaxial extension or compression. Figures 6.4 and 6.5 present triaxial test results by Rivera & Bard [16] and Richardson [148] for dense sand and reconstituted London clay respectively. The tests by Rivera & Bard comprise static and cyclic (repeated) triaxial loading. The test by Richardson gives shear stiffness for different loading histories: four samples were consolidated to point A (Figure 6.5 right), from where on the samples were brought to point O on different paths (AOX, (AO)BOX, (AO)COX, and (AO)DOX). Finally, the stiffness on the path from point O to X was studied as shown in Figure 6.5. In both experiments it turns out that the model's ability to capture differences between initial or monotonic loading and reloading is essential. As shown on the right hand side of Figure 6.4, Masing's rule is fulfilled. In Richardson's experiment, the differences in paths AOX and COX could not be simulated by the Small-Strain Overlay model as it does neither account for the higher pre-consolidation pressure in path AOX, nor for the decreased void ratio. For larger strains, stiffness is too small in all loading paths. In the small-strain range, however, both materials tested, could be simulated reasonably well with the Small-Strain Overlay model.

6.2.2 Biaxial test

Figure 6.6 illustrates stiffness reduction curves in strain controlled plane strain biaxial loading. First, equal strain increments are applied in both axial directions. From there on, three different loading paths are examined: (1) Monotonic loading - strain is equally increased in both directions; (2) Loading to the side - strain is equally increased in both directions, but one of them is reversed; (3) Reversed loading - both loading directions are reversed. As no small-strain biaxial laboratory test data are presently available, the

Box 6.1: Algorithmic setting for the Small-Strain Overlay model.

1. Initialize strain history. Default setting is $H_{kl}^0 = 0$.
 2. Adapt G_0^{ref} and $\gamma_{0.7}^{\text{ref}}$ to the actual material state (optionally):
 $G_0 = f(G_0^{\text{ref}}, p, e, \dots)$ and $\gamma_{0.7} = f(\gamma_{0.7}^{\text{ref}}, p, e, \dots)$
 3. Calculate shear strain γ_{Hist} :
 - a) Transform H_{kl}^i to the strain increment's Eigensystem:
 $\underline{H}_{kl}^i = S_{km} H_{mn}^i S_{nl}$ where $(\Delta e_{kl}^{i+1} - \lambda^{(m)} \delta_{kl}) S_l^{(m)} = 0$
 - b) Calculate monotonic shear strain at time i :
 $\gamma_{Hist}^i = \sqrt{3} \frac{\|\Delta e_{km}^{i+1} H_{ml}^i\|}{\|\Delta e_{kl}^{i+1}\|}$
 - c) Calculate transformation matrix \underline{T}_{kl}^i :

$$\underline{T}_{11} = \frac{1}{\sqrt{H_{11}+1}} (1 + u(\lambda^{(1)} H_{11})) (\sqrt{H_{11}+1} - 1)$$

$$\underline{T}_{22} = \frac{1}{\sqrt{H_{22}+1}} (1 + u(\lambda^{(2)} H_{22})) (\sqrt{H_{22}+1} - 1)$$

$$\underline{T}_{33} = \frac{1}{\sqrt{H_{33}+1}} (1 + u(\lambda^{(3)} H_{33})) (\sqrt{H_{33}+1} - 1)$$

$$\underline{T}_{ij} = 0 \text{ for } i \neq j$$
 where $u(x) = \begin{cases} 0 & \text{for } x < 0 \\ 1 & \text{for } x \geq 0 \end{cases}$
 - d) Update strain history:
 $\underline{H}_{kl}^{i+1} = \underline{T}_{km}^i (\underline{H}_{mn}^i + \delta_{mn}) \underline{T}_{nl}^i + \Delta e_{kl}^{i+1} - \delta_{kl}$
 - e) Calculate monotonic shear strain at time $i+1$:
 $\gamma_{Hist}^{i+1} = \sqrt{3} \frac{\|\Delta e_{km}^{i+1} H_{ml}^{i+1}\|}{\|\Delta e_{kl}^{i+1}\|}$
 4. Calculate tangent stiffness G^{i+1} (unloading/ reloading):

$$G^{i+1} = \frac{G_0}{\gamma_{Hist}^{i+1} - \gamma_{Hist}^i} \left(\frac{\gamma_{Hist}^{i+1}}{1 + \frac{0.385 \gamma_{Hist}^{i+1}}{2\gamma_{0.7}}} - \frac{\gamma_{Hist}^i}{1 + \frac{0.385 \gamma_{Hist}^i}{2\gamma_{0.7}}} \right)$$
 5. IF $G^{i+1} < \text{Min}\{G^1, G^2, \dots, G^i\}$ THEN (primary loading):
 - a) Set $\gamma_{0.7} = \gamma_{0.7}/2$
 - b) Recalculate stiffness (4)
- END IF

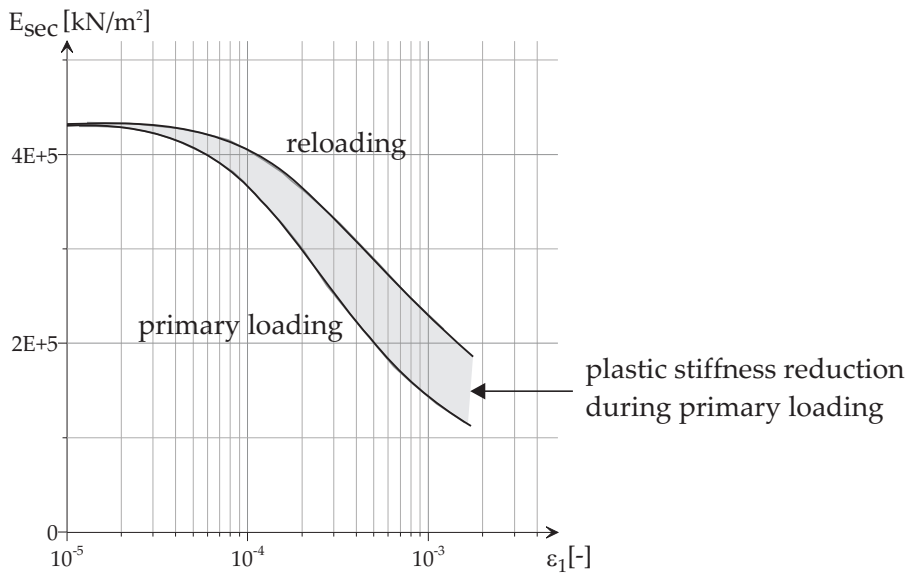


Figure 6.3: Stiffness reduction in initial- or primary loading and in reloading.

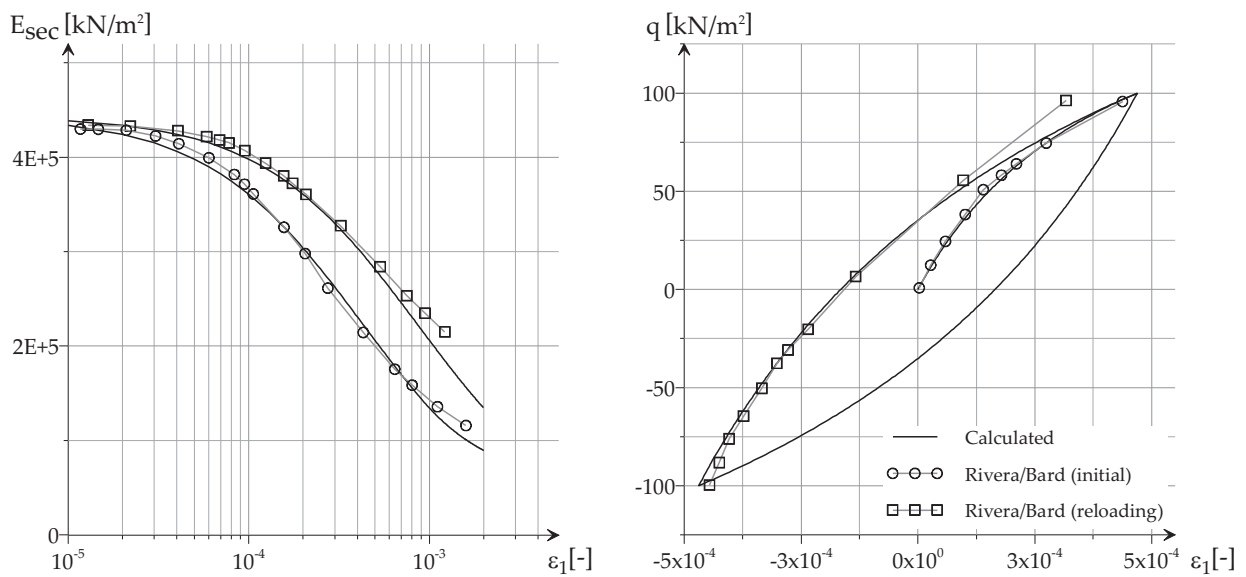


Figure 6.4: Standard drained triaxial test by Rivera & Bard (after Biarez & Hicher [16]) and simulation with the Small-Strain Overlay model ($G_0 = 185\text{MPa}$, $\nu = 0.20$, $\gamma_{0.7} = 2e^{-4}$).

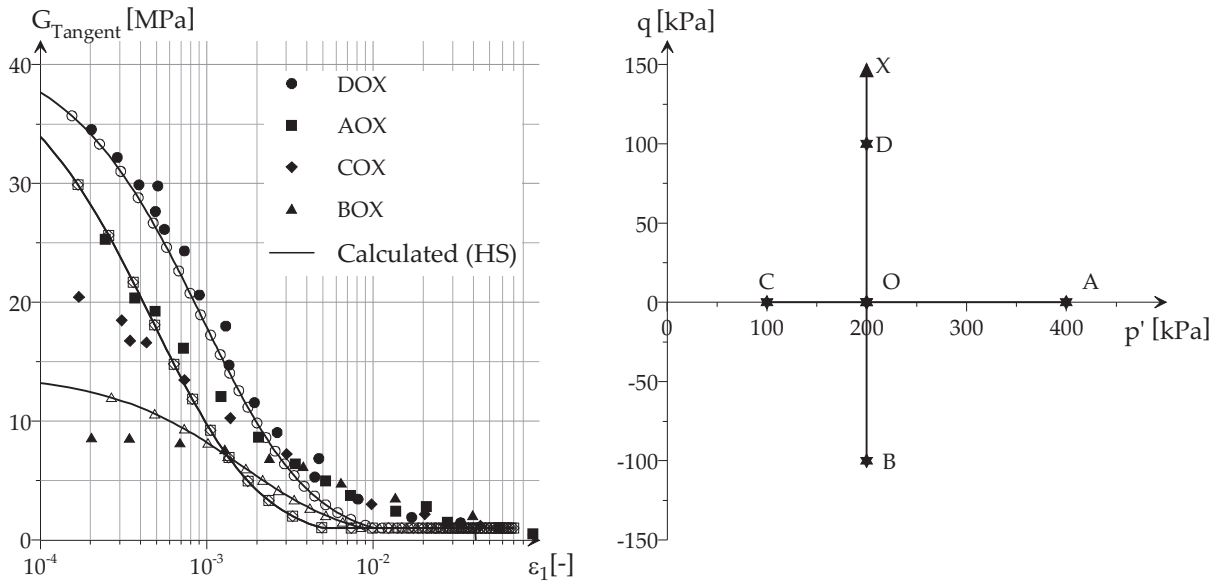


Figure 6.5: Triaxial test by Richardson [148] and its simulation with the Small-Strain Overlay model ($G_0^{ref} = 42$ MPa, $\nu = 0.20$, $\gamma_{0.7} = 5.5e^{-4}$) Left: path dependent shear stiffness. Right: loading paths in q - p space.

model response of the Small-Strain Overlay model is compared to that of the Intergranular Strain concept.

Both, the model proposed here and the Hypoplastic model with Intergranular Strain show a similar behavior. The least stiffness is obtained during monotonic loading; highest stiffness is obtained for a full load reversal, which in the case of biaxial loading is a reversal in both loading directions. Reversing only one biaxial loading direction and keeping the other constant, results in a somewhat increased stiffness which lies between the minimum and the maximum stiffness. Here the Small-Strain Overlay model clearly shows its ability to capture deviatoric strain history. Loading to the side yields less stiffness than reversed loading.

6.2.3 Strain response envelopes

Strain response envelopes were originally introduced by Lewin & Burland [101] and later used by Gudehus [47] as a tool to evaluate constitutive models. In their simplest form, response envelopes for axisymmetric stress states are constructed by applying stress increments of fixed magnitude but at different directions to a triaxial probe with an initially predefined stress state. Connecting the single strain-responses of all tested stress directions yields the strain response envelope.

Doanh [32] experimentally derived three strain response envelopes for Hostun sand, for different initial stress states. A first response envelope is obtained after isotropic consolidation to 100 kPa. A second envelope is obtained at an intermediate stress state,

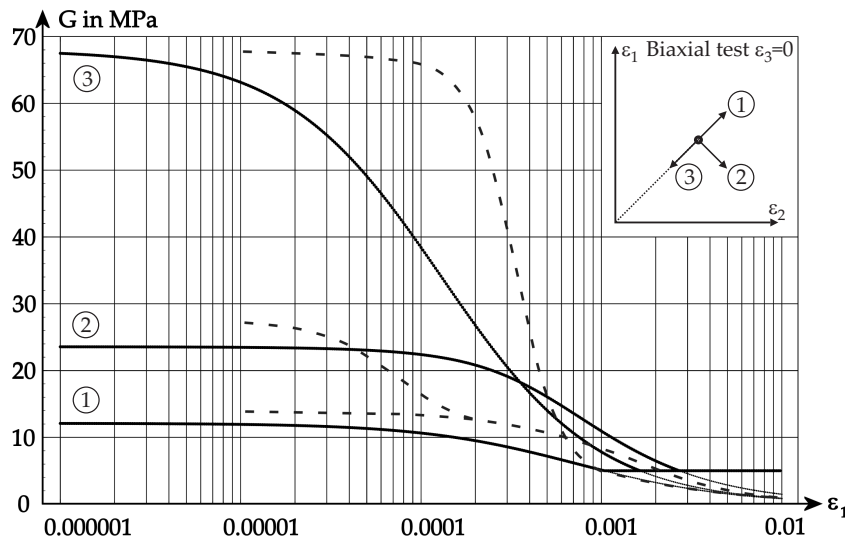


Figure 6.6: Stiffness-strain decay in a biaxial test on sand. Comparison of the tangent stiffness generated by the Small-Strain Overlay model to that, generated by a Hypoplastic model with Intergranular Strain range.

which is reached by isotropic consolidation to 100 kPa and application of 100 kPa vertical stress afterwards. The magnitude of the then applied stress increments is 10 kPa. Experimentally tested stress increment directions are shown in Figure 6.7. Only the intermediate stress state is considered here.

Doanh's strain response envelopes are derived in the triaxial plane. In the triaxial plane however, the unloading-reloading criterion of the Small-Strain Overlay model reduces to a one brick criterion. A sharp stiffness jump is obtained whenever the deviatoric strain increment reverses its direction. In order to avoid sharp stiffness jumps around hydrostatic loading, an alternative to the above model formulation is explored in Figure 6.7. Assuming Poisson's ratio not to be constant, but varying from $\nu = 0.05 \dots 0.25$ in the case of the sand tested, smooth stiffness transitions could be obtained: The bulk modulus is assumed constant as long as Poisson's ratio is within an admissible range, i.e. $\nu \geq \nu_{\min}$. In the experiment, the bulk modulus is therefore unaffected by the non-linear small-strain shear stiffness decrease. However, as such large variations in Poisson's ratio within the small strain range is not supported by experimental evidence, it is not further considered in this thesis.

In Figure 6.7 experimentally derived strain responses are compared to these derived by the Small-Strain Overlay model. Strain responses after load reversals are modeled reasonably well except for those which involve more soil plasticity. However, a combination of the Overlay model with an elastoplastic model can also reproduce monotonic and almost monotonic strain responses.

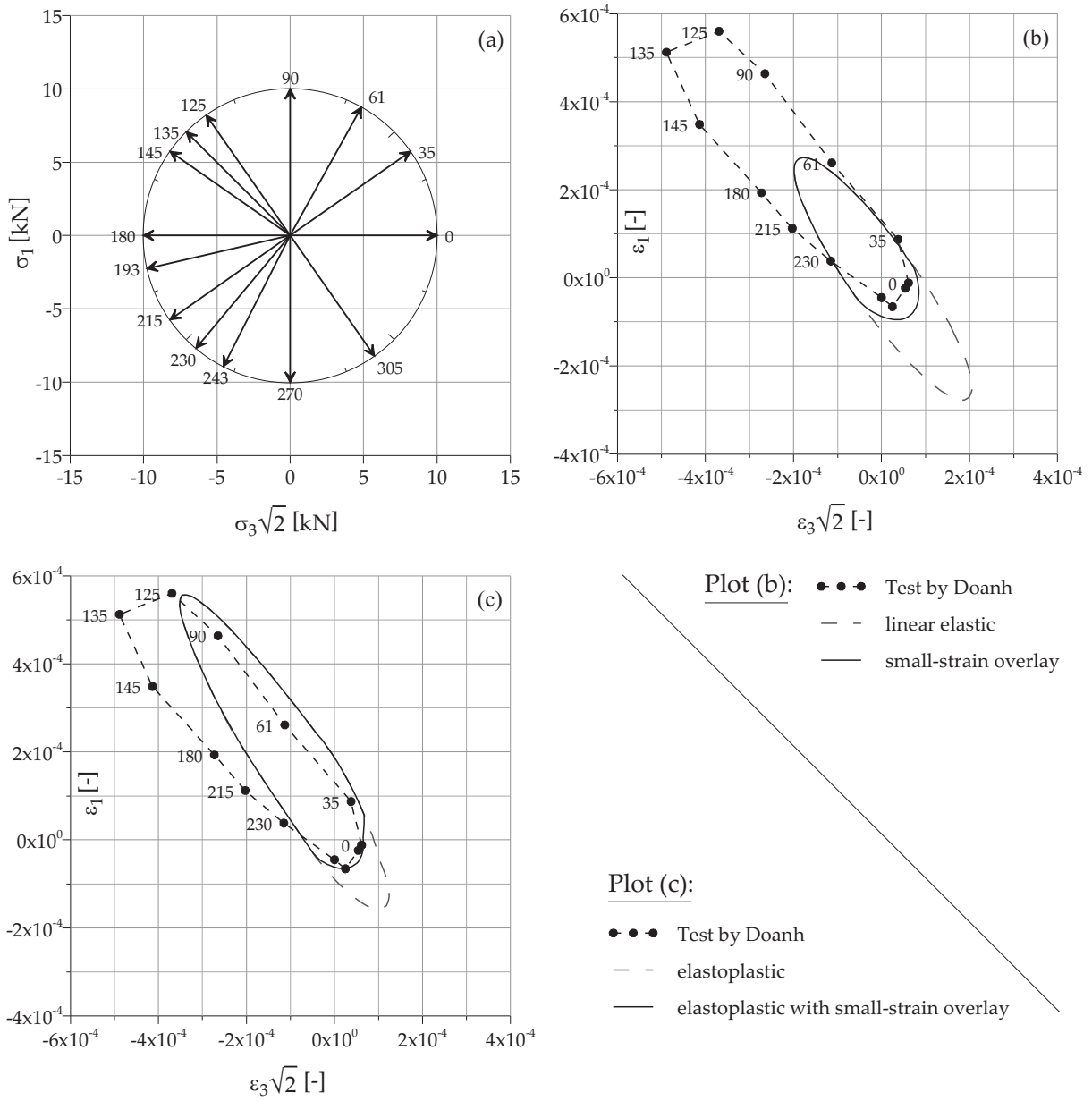


Figure 6.7: Strain response envelopes experimentally derived by Doanh [32] and their simulation with the Small-Strain Overlay model: (a) strain increment directions, (b) Small-Strain Overlay model, (c) Small-Strain Overlay combined with hardening plasticity.

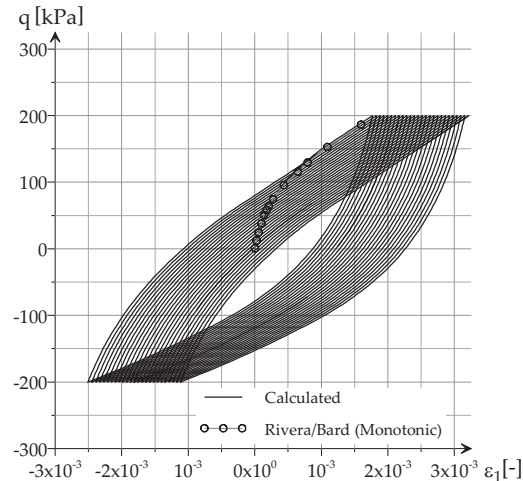


Figure 6.8: Strain accumulation in closed cycles due to mean stress dependent elastic stiffness.

6.2.4 Cyclic mobility

Extending the basic Small-Strain Overlay model with pressure or void ratio dependent formulations leads to unrecoverable deformations in cyclic loading (Figure 6.8). Such a possible extension is for example, the adaption of the model's initial shear modulus G_0 to mean pressure as shown above. In a drained problem, the unrecoverable deformations may lead to small, but constant ratcheting. In an undrained problem, cyclic mobility will eventually be reached. This behavior, although close to experimental evidence, needs to be considered for combining the overlay model with any elastoplastic model. Void ratio dependent dilatancy concepts can stabilize the observed ratcheting. In case the Small-Strain Overlay model is not used explicitly in cyclic modeling, or if only a few cycles are modeled, the aspect of cyclic mobility can be neglected.

6.3 Thermodynamic considerations

Elastic materials are not dependent on their stress or strain history. Thus the stress in an elastic material at time t depends only on the local configuration at time t , and not on the past stress or strain history. Hypo-elastic materials, although history dependent, assume the stress rate to be linear and isotropic in stretching. Hyperelastic materials conserve energy in closed cycles, which means that hyperelasticity can only be applied to either perfect materials at uniform temperature or uniform specific entropy, or to simple materials in thermal equilibrium at uniform temperature or uniform specific entropy. For a definition of perfect materials and simple materials see for example Truesdell & Noll [181]. The material introduced here belongs to neither of these classes of elastic material. For a rigorous mechanical description, a more complex theory has to be applied, for example Coleman's general thermodynamics of simple materials. In this theory, attention

is also paid to the Clausius-Duhem inequality. In a local form, this inequality can be expressed as [181]:

$$\dot{\eta} \geq \frac{1}{\rho\theta} \operatorname{div} \mathbf{h} - \frac{1}{\rho\theta^2} \mathbf{h} \operatorname{grad} \theta + \frac{q}{\theta} \quad (6.15)$$

where η denotes specific entropy, ρ mass density, θ temperature, q heat absorption, and \mathbf{h} is the heat flux vector.

Constitutive equations have then not only to be defined for stress, but also for specific entropy, internal energy, and heat flux. This, however, is not within the scope of the Small-Strain Overlay model, which simulates near elastic material behavior with a relatively small change in specific entropy compared to the overall entropy change during plastic loading of the background model. Nevertheless, a rigorously formulated constitutive model should obey thermodynamic principles. The model has not, however, been demonstrated to obey such principles, although its constitutive parts have been chosen to represent soil behavior realistically.

An example of the potential problems due to the non-rigorous thermodynamic formulation of the Small-Strain Overlay model is given next. Considered are isothermal processes, starting from a state of equilibrium only. For such processes, the theorem on isothermal cyclic processes hold (e.g. Truesdell & Noll [181]: *In every isothermal process starting from a state of equilibrium, the total stress work around a closed path is non-negative.*

Partly as a consequence of not having implemented the entire set of Masing rules in the Small-Strain Overlay model, the irregular cyclic loading situation shown on the left hand side of Figure 6.9 may violate the theorem on isothermal cyclic loading processes. The same loading situation, however, with less negative stress work release during unloading does not violate the above theorem (Figure 6.9 right hand side). The unloading stiffness in the second case is calculated as follows:

Let t_0 be the time at the onset of loading. For any time $t_1 > t_0$ the total stress work associated with the overlay model is given by:

$$W(t_1) = \int_{t_0}^{t_1} (\sigma_{kl})^{\text{ol}} (\varepsilon_{kl})^{\text{ol}} dt \quad (6.16)$$

The stiffness of a linear elastic material with

- Poisson's ratio identical to that of the overlay model
- Loading history identical to that of the overlay model
- Elastic energy identical to the stress work $W(t_1)$

calculates as:

$$C_{ijkl}^{\text{el}}(t_1) = (\sigma_{ij})^{\text{ol}}(t_1) (\varepsilon_{kl})^{\text{ol}}(t_1)^{-1}. \quad (6.17)$$

The shear modulus $G^{\text{el}}(t_1)$ of the iso-energetic linear elastic material can thus be explicitly determined. In order to avoid negative stress work in a closed path simulated by the

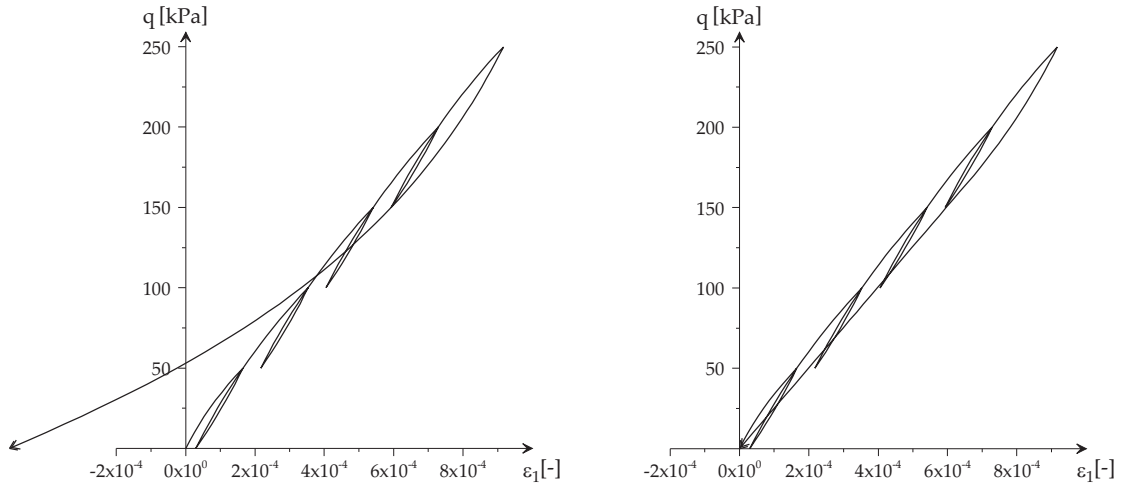


Figure 6.9: Stress work in the Small-Strain Overlay model.

overlay model, its stiffness $G^{ol}(t)$ in unloading should at all times $t > t_0$ be greater than or equal to that of the corresponding linear elastic material:

$$G^{ol}(t) \geq G^{el}(t) \quad \forall t > t_0 \quad \text{with } \dot{W}(t) < 0. \quad (6.18)$$

In this way, it is ensured that the total negative stress work during unloading is not less than that of a linear elastic material with identical internally stored strain energy at the onset of unloading. Furthermore, as the positive stress work of the materials before unloading are equal, the total stress work in a closed path cannot be negative.

Chapter 7

HS-Small, a small-strain extension of the Hardening Soil model

In this chapter, the Small-Strain Overlay model is combined with an existing double-hardening elastoplastic model. As the main focus of this thesis is with the development of a model for routine design, the combination is made with the Hardening Soil (HS) model as implemented in the finite element code PLAXIS V8. The small-strain enhanced version of the HS model resulting from the combination is referred to as the HS-Small model. Compared to the HS model, the HS-Small model additionally offers a Matsuoka-Nakai [113] [114] failure criterion (optional) and a refined flow rule (mandatory). Following a brief introduction to the basic equations of infinitesimal elastoplasticity, both models' constitutive equations are developed within this chapter.

Because of the availability of two yield criteria, it is generally distinguished between the *HS-Small(MC)* model with Mohr-Coulomb failure criterion, and the *HS-Small(MN)* with Matsuoka-Nakai failure criterion. The terminology HS-Small is used whenever the actual type of yield criterion is not of interest for a particular discussion. The term HS-Small is thus a collective term for HS-Small(MC) and HS-Small(MN).

Within this chapter, all stresses are effective although not explicitly indicated by a prime. In triaxial conditions, $\sigma_1 = \sigma_{\text{axial}}$, denotes axial strain and $\sigma_2 = \sigma_3 = \sigma_{\text{lateral}}$, denotes lateral strain. In the following, it is generally assumed $\sigma_{\text{axial}}/\sigma_{\text{lateral}} \geq 1$. The reader can easily verify all triaxial equations to hold likewise in triaxial extension ($\sigma_{\text{axial}}/\sigma_{\text{lateral}} < 1$) by substituting σ_1 with σ_3 and vice versa.

7.1 Constitutive relations for infinitesimal plasticity

Elastoplastic materials can be described by means of the following set of constitutive equations (e.g. Hill [58], Drucker [34], or Hughes [66]):

$$\varepsilon_{ij} = \varepsilon_{ij}^e + \varepsilon_{ij}^p \quad (7.1)$$

$$\sigma_{ij} = D_{ijkl} \varepsilon_{kl}^e \quad (7.2)$$

$$d\varepsilon_{ij}^p = d\lambda \frac{\partial g}{\partial \sigma_{ij}} \quad (7.3)$$

$$dq_* = d\lambda h_*(\sigma_{ij}, q_*) \quad (7.4)$$

where ε_{ij} , ε_{ij}^e , and ε_{ij}^p denote the total, elastic, and plastic strain tensor respectively, σ_{ij} is the Cauchy stress tensor, q_* is a suitable set of scalar or tensorial internal material

variables, and D_{ijkl} is a fourth-order tensor describing the material's elastic stiffness. The asterisk in place of indices in q_* replaces n indices of tensorial functions which vanish for scalar functions.

From top to bottom, Equation 7.1 gives the additive decomposition of total strains in an elastic and a plastic part, which is generally assumed in elastoplasticity. Equation 7.2 expresses the elastic stress-strain relationship by means of a Hooke's law with the elastic stiffness fourth-order tensor D_{ijkl} . Equation 7.3 gives the flow rule for the plastic strain. Depending on the choice of the plastic potential function $g = g(\sigma_{ij}, q_*)$ in respect to the yield function $f = f(\sigma_{ij}, q_*)$, the flow rule is either associated $f = g$, or non-associated $f \neq g$. The hardening laws expressed in Equation 7.4 complete the basic set of constitutive equations by introducing a set of evolution functions h_* for the internal variables. In the last equation, $d\lambda$ represents the plastic multiplier that is to be determined with the aid of the Karush-Kuhn-Tucker conditions:

$$f(\sigma_{ij}, q_*) \leq 0 \quad (7.5)$$

$$d\lambda \geq 0 \quad (7.6)$$

$$fd\lambda = 0 \quad (7.7)$$

The Karush-Kuhn-Tucker, must simultaneously hold up in any process of loading and hence, distinguish between elastic and plastic loading processes. The yield function $f(\sigma_{ij}, q_*)$ encloses the elastic material domain. The material is elastic whenever $f < 0$ holds. In this case Equation 7.7 yields $d\lambda = 0$. Plastic flow is characterized by $f = 0$ and $d\lambda > 0$, while neutral loading is obtained for $f = d\lambda = 0$. From the Karush-Kuhn-Tucker conditions, the consistency condition for plastic flow can be derived as follows:

$$df = \frac{\partial f}{\partial \sigma_{ij}} d\sigma_{ij} + \frac{\partial f}{\partial q_*} dq_* = 0. \quad (7.8)$$

Combining the consistency condition introduced above with the basic set of constitutive equations (Equation 7.1 to 7.4), the plastic multiplier $d\lambda$ can be calculated as:

$$d\lambda = \frac{\frac{\partial f}{\partial \sigma_{ij}} D_{ijkl} d\varepsilon_{kl}}{\frac{\partial f}{\partial \sigma_{ij}} D_{ijkl} \frac{\partial g}{\partial \sigma_{kl}} + h} \quad \text{with} \quad h = -\frac{\partial f}{\partial q_*} h_*. \quad (7.9)$$

If all derivatives in Equation 7.9 are constant or linear functions in stress and the internal variables, the plastic multiplier may be found analytically. However, commonly used yield functions and plastic potentials do not satisfy these requirements. Calculation of the plastic multiplier and at the same time the integration of the constitutive equations therefore requires an efficient iterative scheme.

Many constitutive laws can be formulated within the framework of elastoplasticity presented above. These laws differ only in their yield function, plastic potential, and evolution laws for the internal variables. When functions of strain are applied the above formulation can also be recast in strain space in terms of $\{ \varepsilon_{ij}, \varepsilon_{ij}^p \}$, by eliminating σ_{ij} with the help of Equation 7.1 and Equation 7.2.

The implications of large strains are not considered explicitly in this thesis. However, it should be noted that conserving objectivity, for example by the consideration of a Jaumann term in the stress-rate, will not alter the following model description.

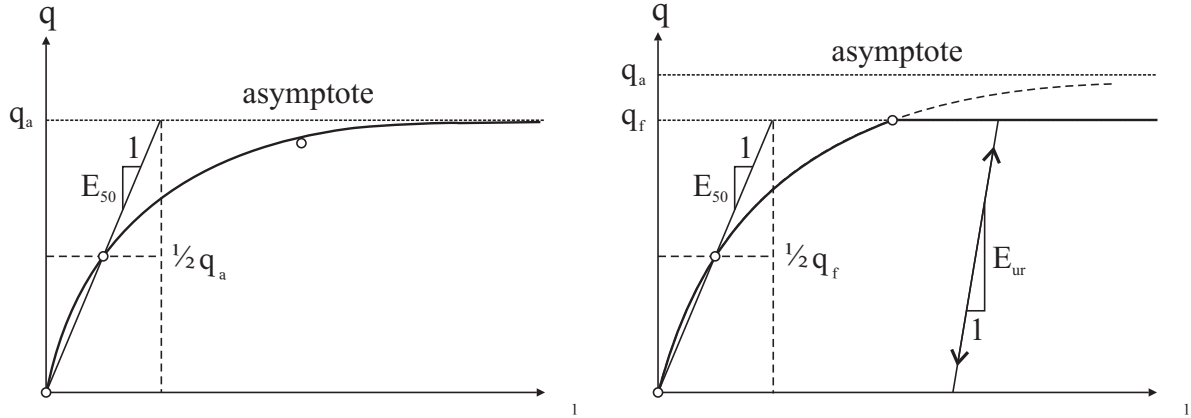


Figure 7.1: Hyperbolic stress-strain law by Kondner & Zelasko (left) and its modification after Duncan & Chang (right).

7.2 The Hardening Soil model

The original HS model was developed by Schanz [157] and Schanz et al. [158] on the basis of the Double Hardening model by Vermeer [183]. Thus, the HS model also comprises ideas by Kondner [94], Duncan & Chang [36], Ohde [131] or Janbu [77], and Rowe [153]. Standard lab tests, such as triaxial and oedometer tests provide the model's basic characteristics.

In drained triaxial primary loading, the experimentally observed relation between axial strain and deviatoric stress in soils can be well approximated by a hyperbolic function. Kondner & Zelasko [94] described the hyperbolic stress-strain relation for drained triaxial loading as follows:

$$\varepsilon_1 = \varepsilon_{50} \frac{q}{q_a - q} \quad \text{with } q_a = \frac{2 \sin \varphi}{1 - \sin \varphi} (\sigma_3 + c \cot \varphi) \quad \text{and } \varepsilon_{50} = \frac{q_{50}}{E_{50}} = \frac{q_a}{2E_{50}} \quad (7.10)$$

Duncan & Chang [36] based their hypoelastic model on the above formulation by Kondner & Zelasko, additionally introducing the deviatoric measure q_f in the form:

$$\varepsilon_1 = \varepsilon_{50} \frac{q}{q_a - q} \quad \text{for } q < q_f = \frac{2 \sin \varphi}{1 - \sin \varphi} (\sigma_3 + c \cot \varphi) \quad \text{and } q_a = \frac{q_f}{R_f} \geq q_f \quad (7.11)$$

The conceptual difference in the formulations by Kondner & Zelasko and that by Duncan & Chang is illustrated in Figure 7.1. Extending the hypoelastic Duncan-Chang model to an elastoplastic formulation, Schanz [157] proposed the following yield function:

$$f^s = \frac{q_a}{E_{50}} \frac{q}{q_a - q} - \frac{2q}{E_{ur}} - \gamma^{ps} \quad (7.12)$$

where γ^{ps} is an internal material variable for the accumulated plastic deviatoric strain, $q = \sigma_1 - \sigma_3$ is defined for triaxial loading, and q_a is the asymptotic deviatoric strain

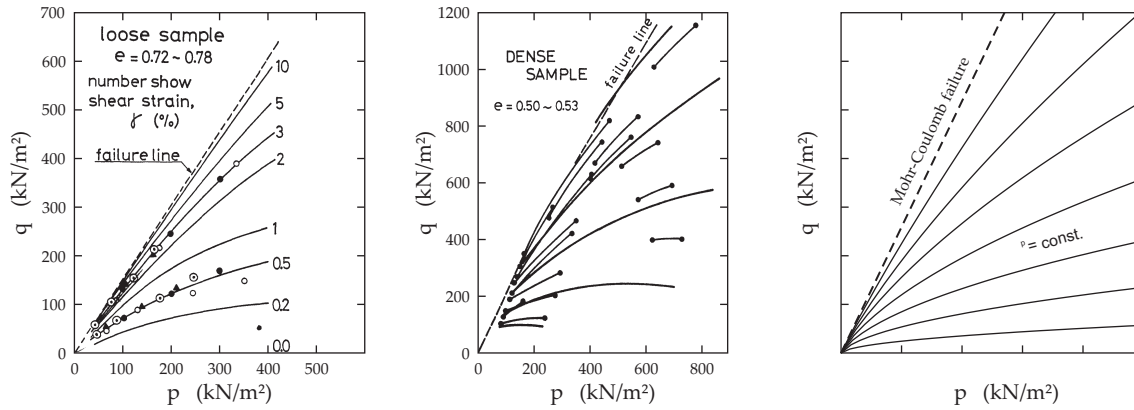


Figure 7.2: Experimentally derived shear strain contours versus HS yield loci. Left: Shear strain contours of loose Fuji River sand [71]. Middle: Shear strain contours of dense Fuji River sand [178]. Right: Yield loci of the HS model for stress independent stiffness ($m=0$).

as defined in the original Duncan-Chang model (Equation 7.11). As the stress-strain relation of soils in unloading and reloading can be approximated by a linear function, isotropic elasticity inside the yield function is another assumption of the HS model: The elastic unloading-reloading stiffness E_{ur} relates elastic stress to elastic strain.

For constant volumetric strain, the equivalence of Equation 7.12 with the approach by Duncan & Chang is given by defining:

$$\gamma^{ps} = \varepsilon_1^p - \varepsilon_2^p - \varepsilon_3^p \quad \text{and thus} \quad \gamma^{ps} = 2\varepsilon_1^p \quad (7.13)$$

as then the following relation holds:

$$\varepsilon_1 = \varepsilon_1^e + \varepsilon_1^p = \frac{q}{E_{ur}} - \frac{1}{2}f^s = \frac{q_a}{2E_{50}} \frac{q}{q_a - q} = \frac{q_{50}}{E_{50}} \frac{q}{q_a - q} = \varepsilon_{50} \frac{q}{q_a - q}. \quad (7.14)$$

In accordance with the basic idea of Vermeer [185], the defined yield loci are ‘lines’ of constant plastic shear strain in p - q space. The striking similarity between experimentally derived shear strain contours and the yield loci defined by Equation 7.12 is depicted in Figure 7.2. All the shear strain contours shown in Figure 7.2 (left and middle) were experimentally derived by Tatsuoka & Ishihara [178], and Ishihara et al. [71]. Their triaxial testing procedure was as follows: They first sheared a given sample at mean stress p_1 to shear stress q_1 . After reducing shear stress (unloading) and increasing mean stress to p_2 , they sheared the sample again until it yielded at shear stress q_2 . This procedure was repeated many times so that the regression line through the n -tuple of points $\{(p_1, q_1), (p_2, q_2), \dots, (p_n, q_n)\}$, called the shear strain contour, marks a line of constant shear strain in p - q space.

When translating Equation 7.12 to principal stress space, the resulting cone-type yield

function can only be formulated in stages:

$$\begin{aligned} f_{12}^s &= \frac{2q_a}{E_i} \frac{(\sigma_1 - \sigma_2)}{q_a - (\sigma_1 - \sigma_2)} - \frac{2(\sigma_1 - \sigma_2)}{E_{ur}} - \gamma^{ps}, \text{ and} \\ f_{13}^s &= \frac{2q_a}{E_i} \frac{(\sigma_1 - \sigma_3)}{q_a - (\sigma_1 - \sigma_3)} - \frac{2(\sigma_1 - \sigma_3)}{E_{ur}} - \gamma^{ps}. \end{aligned} \quad (7.15)$$

The transition from E_{50} to E_i is made because of a second yield surface that will be introduced later in this section. The second yield surface will affect material stiffness such that, the meaning of E_i in the full HS model is not as closely related to the hyperbolic model by Kondner & Zelasko as the one of E_{50} .

Associated plasticity is an unrealistic assumption for most geotechnical materials. Thus, an additional plastic potential of the form:

$$\begin{aligned} g_{12}^s &= \frac{(\sigma_1 - \sigma_2)}{2} - \frac{\sigma_1 + \sigma_2}{2} \sin \psi_m, \text{ and} \\ g_{13}^s &= \frac{(\sigma_1 - \sigma_3)}{2} - \frac{\sigma_1 + \sigma_3}{2} \sin \psi_m \end{aligned} \quad (7.16)$$

is introduced. The mobilized dilatancy angle ψ_m in the above equation is defined according to Rowe's stress dilatancy theory [153]:

$$\sin \psi_m = \frac{\sin \varphi_m - \sin \varphi_{cs}}{1 - \sin \varphi_m \sin \varphi_{cs}} \quad (7.17)$$

where, φ_{cs} is the critical state friction angle and the mobilized friction angle φ_m is calculated as follows:

$$\sin \varphi_m = \frac{\sigma_1 - \sigma_3}{\sigma_1 + \sigma_3 + 2c \cot \varphi}. \quad (7.18)$$

The stiffness moduli E_i and E_{ur} are scaled for their stress dependency with an Ohde [131] or Janbu [77] power law:

$$\begin{aligned} E_i &= E_i^{\text{ref}} \left(\frac{\sigma_3 + c \cot \varphi}{p^{\text{ref}} + c \cot \varphi} \right)^m, \text{ and} \\ E_{ur} &= E_{ur}^{\text{ref}} \left(\frac{\sigma_3 + c \cot \varphi}{p^{\text{ref}} + c \cot \varphi} \right)^m \end{aligned} \quad (7.19)$$

where E_i^{ref} and E_{ur}^{ref} are the material stiffness moduli at the reference pressure p^{ref} , and m is the exponent of the power law. In Equation 7.19 the minor principal stress σ_3 is used as an indicator of the actual stress state in the material instead of the mean stress $p = \frac{\sigma_{ii}}{3}$.

The cone-type yield loci of the HS model mainly accounts for plastic deviatoric strains, or shear hardening. A second cap-type yield surface is introduced next. The cap-type yield surface accounts for plastic volumetric strains, or volumetric hardening. Volumetric hardening corrects too stiff primary oedometric or isotropic loading, obtained in pure shear hardening models. The HS model's cap-type yield surface is defined as follows:

$$f^c = \frac{\tilde{q}^2}{\alpha^2} - p^2 - p_p^2 \quad (7.20)$$

where $p = \frac{\sigma_{ii}}{3}$ is the mean stress, α is an internal material constant, controlling the steepness of the cap in p-q space as shown in Figure 7.4, p_p is an internal material variable for pre-consolidation stress, and \tilde{q} is a special stress measure, defined as:

$$\tilde{q} = \sigma_1 + (\delta^{-1} - 1)\sigma_2 - \delta^{-1}\sigma_3 \quad \text{with} \quad \delta = \frac{3 - \sin \varphi}{3 + \sin \varphi}. \quad (7.21)$$

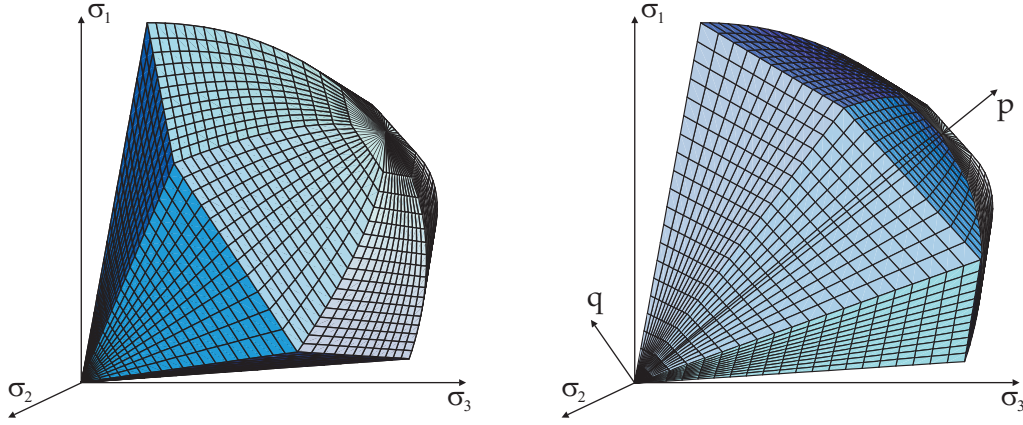


Figure 7.3: Yield surfaces of the HS model for cohesionless soil. Left: Cap and cone-type yield surfaces in principal stress space with the cone being in its ultimate Mohr-Coulomb failure criterion position. Right: p-q slice through the yield surfaces.

The definition of the special stress measure \tilde{q} is necessary to adopt the cap-type yield surface's deviatoric shape to this of the cone-type yield surface as shown in Figure 7.3. The plastic potential for the cap-type yield surface is chosen equal to its yield surface ($g^c = f^c$), so that plastic strain on the cap-type yield surface is associated, in contrast to plastic strain, on the cone-type yield surface.

A total of two state variables are used within the HS model's yield and potential functions: The plastic deviatoric strain γ^{ps} , and the pre-consolidation stress p_p . Their evolution laws are defined as follows:

$$\begin{aligned} d\gamma^{ps} &= d\lambda^s h_{\gamma^{ps}} & \text{with } h_{\gamma^{ps}} &= \left(\frac{\partial g}{\partial \sigma_1} - \frac{\partial g}{\partial \sigma_2} - \frac{\partial g}{\partial \sigma_3} \right)^m = 1 \\ dp_p &= d\lambda^c h_{p_p} & \text{with } h_{p_p} &= 2H \left(\frac{\sigma_3 + c \cot \varphi}{p^{\text{ref}} + c \cot \varphi} \right)^m p \end{aligned} \quad (7.22)$$

where m represents the power law exponent, and H relates plastic volumetric strain $\varepsilon_v^p = \varepsilon_1^p + \varepsilon_2^p + \varepsilon_3^p$ to pre-consolidation stress p_p as follows:

$$dp_p = H \left(\frac{\sigma_3 + c \cot \varphi}{p^{\text{ref}} + c \cot \varphi} \right)^m d\varepsilon_v^p. \quad (7.23)$$

In decomposing volumetric strain in elastic and plastic contributions, H can be rewritten as a function of the bulk stiffness in unloading-reloading, K_s and the bulk stiffness in primary loading, K_c as:

$$H = \frac{K_s K_c}{K_s - K_c} = \frac{1}{\frac{K_s}{K_c} - 1} K_s. \quad (7.24)$$

where due to the assumption of isotropic elasticity, the elastic bulk stiffness K_s relates to $E_{\text{ur}}^{\text{ref}}$ as follows:

$$K_s = \frac{E_{\text{ur}}^{\text{ref}}}{3(1 - 2\nu)}. \quad (7.25)$$

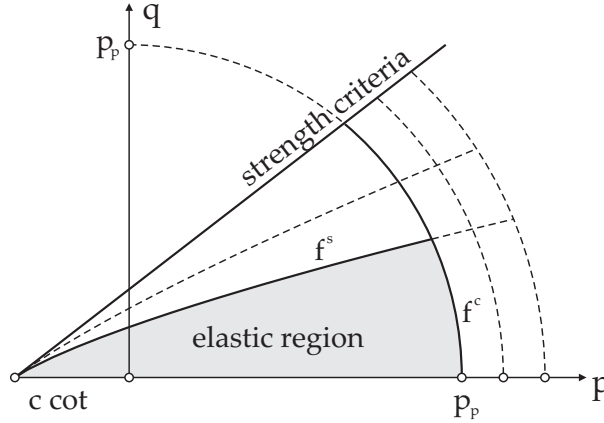


Figure 7.4: Evolution of the HS models' cap and cone-type yield surfaces in p - q space.

The model parameter H can therefore be determined by the bulk stiffness ratio K_s/K_c . As the physical meaning of the latter is more evident, it is often used to quantify H . An illustration of yield surface evolution in $p - q$ space is given in Figure 7.4. Note that by the above definition of $d\gamma^{ps} = d\lambda^s$, it is always assured that for zero volumetric strain, $d\gamma^{ps} = 2\varepsilon_1$ as required in Equation 7.13.

In order to formally complete the model description in the framework of infinitesimal elastoplasticity, the elastic stiffness tensor D_{ijkl} must be defined. The HS model assumes isotropic elasticity inside the yield loci, so that D_{ijkl} is assembled from the user defined stiffness E_{ur} and Poisson's ratio, ν_{ur} as follows:

$$D_{ijkl} = \frac{E_{ur}}{(1 + \nu_{ur})(1 - 2\nu_{ur})} ((1 - 2\nu_{ur})\delta_{ik}\delta_{jl} + \nu_{ur}\delta_{jk}\delta_{il}). \quad (7.26)$$

A summary of the HS model's governing equations and parameters is presented in Box 7.1 and Table 7.1 respectively. In Table 7.1, a differentiation is made between user input and internal parameters because some model parameters cannot be quantified as results of standard triaxial and oedometer tests directly.

Internal model parameters are the stiffness measures E_i^{ref} and H , and the cap-type yield surface's steepness α . These internal parameters mainly relate to the user input parameters E_{50}^{ref} , $E_{\text{oed}}^{\text{ref}}$, and K_0^{nc} respectively, where $E_{\text{oed}}^{\text{ref}}$ is the tangent stiffness at $\sigma_1 = p^{\text{ref}}$ in K_0 (oedometer) loading, and K_0^{nc} is the stress ratio of horizontal effective stress to vertical effective stress in a normally consolidated state.

In double hardening situations, i.e. both yield loci are hardened simultaneously, analytical back-calculation of internal model parameters is impossible. Therefore, the internal parameters are solved for in an iterative scheme so that the HS model simulates the user input E_{50}^{ref} in triaxial element tests and both, $E_{\text{oed}}^{\text{ref}}$, and K_0^{nc} in oedometer element tests, to within a tolerated error.

Box 7.1: Governing equations of the Hardening Soil model.

1. Elastic stiffness tensor:

$$D_{ijkl} = \frac{E_{ur}}{(1+\nu_{ur})(1-2\nu_{ur})} ((1 - 2\nu_{ur})\delta_{ik}\delta_{jl} + \nu_{ur}\delta_{jk}\delta_{il})$$
2. Yield functions:

$$f_{12}^s = \frac{2q_a}{E_i} \frac{(\sigma_1 - \sigma_2)}{q_a - (\sigma_1 - \sigma_2)} - \frac{2(\sigma_1 - \sigma_2)}{E_{ur}} - \gamma^{ps}$$

$$f_{13}^s = \frac{2q_a}{E_i} \frac{(\sigma_1 - \sigma_3)}{q_a - (\sigma_1 - \sigma_3)} - \frac{2(\sigma_1 - \sigma_3)}{E_{ur}} - \gamma^{ps} \text{ and}$$

$$f^c = \frac{\tilde{q}^2}{\alpha^2} - p^2 - p_p^2 \text{ where}$$

$$\tilde{q} = \sigma_1 + (\delta^{-1} - 1)\sigma_2 - \delta^{-1}\sigma_3 \text{ with } \delta = \frac{3 - \sin \varphi}{3 + \sin \varphi}$$
3. Plastic potentials:

$$g_{12}^s = \frac{(\sigma_1 - \sigma_2)}{2} - \frac{\sigma_1 + \sigma_2}{2} \sin \psi_m$$

$$g_{13}^s = \frac{(\sigma_1 - \sigma_3)}{2} - \frac{\sigma_1 + \sigma_3}{2} \sin \psi_m \text{ and}$$

$$g^c = \frac{\tilde{q}^2}{\alpha^2} - p^2 - p_p^2 \text{ where}$$

$$\tilde{q} = \sigma_1 + (\delta^{-1} - 1)\sigma_2 - \delta^{-1}\sigma_3 \text{ with } \delta = \frac{3 - \sin \varphi}{3 + \sin \varphi}$$
4. Mobilized dilatancy (modified Rowe):

$$\sin \psi_m = \frac{\sin \varphi_m - \sin \varphi_{cs}}{1 - \sin \varphi_m \sin \varphi_{cs}} \geq 0, \text{ where}$$

$$\sin \varphi_{cs} = \frac{\sin \varphi - \sin \psi}{1 - \sin \varphi \sin \psi}$$
5. Hardening laws:

$$d\gamma^{ps} = d\lambda^s h_{\gamma^{ps}} \text{ with } h_{\gamma^{ps}} = \left(\frac{\partial g}{\partial \sigma_1} - \frac{\partial g}{\partial \sigma_2} - \frac{\partial g}{\partial \sigma_3} \right) = 1$$

$$dp_p = d\lambda^c h_{p_p} \text{ with } h_{p_p} = 2H \left(\frac{\sigma_3 + c \cot \varphi}{p^{\text{ref}} + c \cot \varphi} \right)^m p, \text{ where}$$

$$H = \frac{K_s K_c}{K_s - K_c} \text{ and } K_s = \frac{E_{ur}^{\text{ref}}}{3(1 - 2\nu)}$$
6. Stress dependent stiffness:

$$E_i = E_i^{\text{ref}} \left(\frac{\sigma_3 + c \cot \varphi}{p^{\text{ref}} + c \cot \varphi} \right)^m$$

$$E_{ur} = E_{ur}^{\text{ref}} \left(\frac{\sigma_3 + c \cot \varphi}{p^{\text{ref}} + c \cot \varphi} \right)^m$$

7.3 The HS-Small model

The HS model is next combined with the Small-Strain Overlay model which was introduced in Chapter 6. Although probably the most important new feature of the resulting HS-Small model is the Small-Strain Overlay model, two existing model mechanisms are also modified. These are the HS model's flow rule, and failure criterion (Figure 7.5). While the incorporation of the Small-Strain Overlay model in the HS-Small model is straight forward, the application of a new failure criterion is not. It requires the more generalized model description developed at the end of this section.

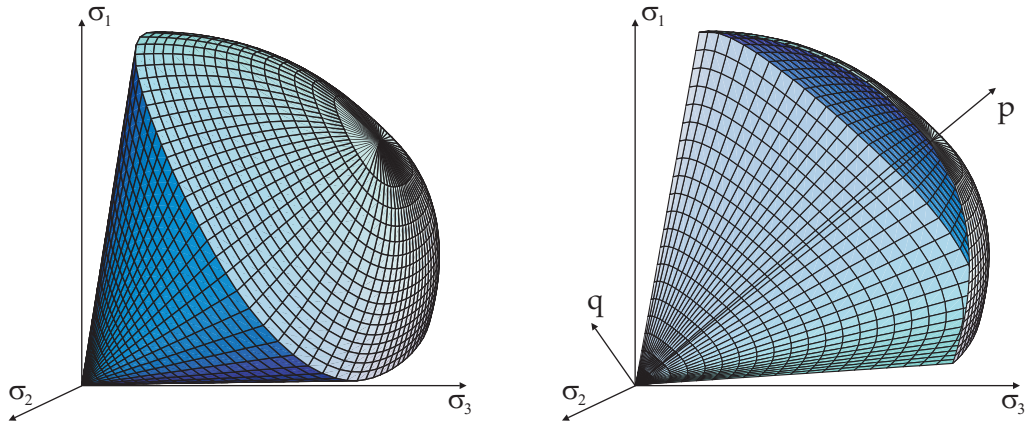


Figure 7.5: Yield surfaces of the HS-Small model for cohesionless soil. Left: Cap- and cone-type yield surfaces in principal stress space with the cone being in its ultimate Matsuoka-Nakai failure criterion position. Right: p-q slice through the yield surfaces.

7.3.1 Small-Strain formulation

The Small-Strain Overlay model primarily renders the HS model's isotropic elastic stiffness dependant on strain history. Additionally, it attenuates plastic straining under initial loading when necessary, to preserve the material's small-strain stiffness. For its application within the HS-Small model, the Small-Strain Overlay model's Poisson's ratio is set to $\nu = \nu_{ur} = const.$ so that the basic elastic relationships:

$$\begin{aligned} G &= \frac{E}{2(1+\nu)} \\ K &= \frac{E}{3(1-2\nu)} \end{aligned} \quad (7.27)$$

hold. Two additional material parameters are needed to control the stress and strain history dependent stiffness of the HS-Small model. These are the initial shear modulus G_0^{ref} defined for the reference pressure p^{ref} and the shear strain $\gamma_{0.7}$, at which the shear modulus has decayed to 70 percent of its initial value. The shear modulus G_0 is calculated from:

$$G_0 = G_0^{\text{ref}} \left(\frac{\sigma_3 + c \cot \varphi}{p^{\text{ref}} + c \cot \varphi} \right)^m, \quad (7.28)$$

where m is the power law exponent that scales also the other stiffness parameters of the HS-Small model (see Equation 7.19). The threshold shear strain $\gamma_{0.7}$ is taken independent of mean stress.

A lower cut-off in the hyperbolic small-strain stiffness reduction curve is introduced at the shear strain γ_c where tangent stiffness is reduced to the unloading-reloading stiffness G_{ur} in larger strain cycles. The unloading-reloading shear modulus G_{ur} relates to the HS model parameter E_{ur} as follows:

$$G_{ur} = \frac{E_{ur}}{2(1 + \nu_{ur})}. \quad (7.29)$$

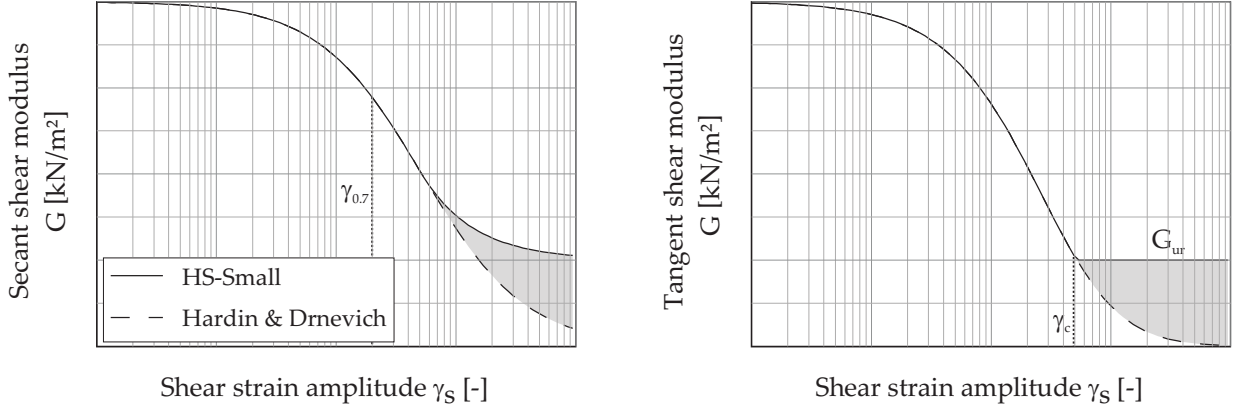


Figure 7.6: Cut-off in the tangent stiffness degradation curve as used in the HS-Small model.

The shear strain γ_c is then obtained from the modified Hardin-Drnevich relationship, which for the tangent stiffness G_{ur} yields:

$$G_{ur} = G_0 \left(\frac{a\gamma_c}{\gamma_{0.7} \left(1 - a\frac{\gamma_c}{\gamma_{0.7}}\right)^2} + \frac{1}{1 - a\frac{\gamma_c}{\gamma_{0.7}}} \right) = G_0 \left(\frac{\gamma_{0.7}}{\gamma_{0.7} + a\gamma_c} \right)^2 \quad (7.30)$$

and hence:

$$\gamma_c = \frac{\gamma_{0.7}}{a} \left(\sqrt{\frac{G_0}{G_{ur}}} - 1 \right). \quad (7.31)$$

The resulting small-strain stiffness behavior of the HS-Small model is illustrated in Figure 7.6. Its isotropic elasticity tensor is calculated as:

$$D_{ijkl} = \frac{2G}{1 - 2\nu_{ur}} \left((1 - 2\nu_{ur})\delta_{ik}\delta_{jl} + \nu_{ur}\delta_{jk}\delta_{il} \right) \quad \text{with} \quad G = G_0 \left(\frac{\gamma_{0.7}}{\gamma_{0.7} + a\gamma_{Hist}} \right)^2. \quad (7.32)$$

The stiffness tensor given by Equation 7.32 is not a truly elastic, but a paelastic one (Hueckel & Nova [65]). Nevertheless, the terminology *elastic* stiffness is maintained for the use of the above defined stiffness in the HS-Small model as a reminder that it applies to all stress states, within as well as on the yield surface, similar to the elastic stiffness known from traditional elastoplastic models.

By default, the HS model is hardened under initial loading. Without altering its hardening laws, plastic straining will reduce the HS-Small model's small-strain stiffness. In order to preserve the stiffness defined by the material parameters G_0 and $\gamma_{0.7}$, the HS-Small hardening laws are rewritten as:

$$\begin{aligned} d\gamma^{ps} &= d\lambda^s h_i h_{\gamma^{ps}} & \text{with } h_{\gamma^{ps}} & \text{as defined in Equation 7.22} \\ dp_p &= d\lambda^c h_i h_{pp} & \text{with } h_{pp} & \text{as defined in Equation 7.22} \end{aligned} \quad (7.33)$$

where h_i approximates plastic hardening under initial small-strain loading. In reasonably well agreement with initial modulus reduction curves, h_i is defined as:

$$h_i := G_m^{1 + \frac{E_{ur}}{E_i}} \quad (7.34)$$

where G_m is the stiffness multiplier defined in Section 6.1.3. Note, that in combination with the HS model, the threshold shear strain $\gamma_{0.7}$ in the Small-Strain Overlay model is always doubled for reloading. If a primary loading condition exists, this will be accounted for by plastic hardening of the yield locus. For further details on the distinction between initial and reloading, it is referred to Section 6.1.3.

7.3.2 Mobilized dilatancy

A main drawback of Rowe's [153] approach to model mobilized dilatancy angles, is the highly contractive behavior at low mobilized friction angles. In the original HS model the mobilized dilatancy angle, $\sin \psi_m$ is therefore set to be greater or equal to zero overriding Rowe's original equation (7.17):

$$\sin \psi_m = \frac{\sin \varphi_m - \sin \varphi_{cs}}{1 - \sin \varphi_m \sin \varphi_{cs}} \geq 0. \quad (7.35)$$

Unfortunately, the dilatancy cut off introduced in Equation 7.17 typically yields too little plastic volumetric contraction. Recently, several formulations have been proposed to resolve this problem.

Wehnert [191] proposed a non-zero lower cut-off value, similar to Equation 7.35, for the allowable contraction in loose sands:

$$\sin \psi_m = \frac{\sin \varphi_m - \sin \varphi_{cs}}{1 - \sin \varphi_m \sin \varphi_{cs}} \geq 0.07 \quad (7.36)$$

Even though the method by Wehnert is efficient, the lower cut-off value effectively represents an additional material parameter. Soreide [169] proposed to scale Rowe's equation as a function of mobilized friction:

$$\sin \psi_m = \left(\frac{\sin \varphi_m - \sin \varphi_{cs}}{1 - \sin \varphi_m \sin \varphi_{cs}} \right) \left(\frac{\sin \varphi_m}{\sin \varphi} \right). \quad (7.37)$$

From a quantitative point of view, the methods by Wehnert, and Soreide seem to be very much alike as shown in Figure 7.7 and again in the model validation (Chapter 8). Soreide additionally claims numerical benefits from his formulation: The likelihood of stress return towards the apex is less when using big step sizes in the return mapping (see Section 7.4 for further details on return mapping). However, having well defined initial stresses and a suitable return mapping scheme this advantage should not be overrated.

In contrast to the Rowe trouble shooting strategies by Wehnert and Soreide, the modified flow rule of the HS-Small model makes use of critical state soil mechanics. Li & Dafalias [103] proposed to treat dilatancy as a state-dependent quantity within the

framework of critical state soil mechanics. They defined dilatancy D , the ratio of plastic volumetric strain increment to plastic deviatoric strain increment in triaxial space, as:

$$D = \frac{d_0}{M}(Me^{m\psi} - \eta), \quad (7.38)$$

where d_0 , and m are two material parameters, M is the critical stress ratio, $\eta = \frac{q}{p}$ is the actual stress ratio, and ψ is the state parameter defined by Been & Jefferies [13]. The state parameter ψ is a scalar quantity that measures the difference between the actual and the critical void ratio at the same mean stress p . Equation 7.38 reduces to the Cam-Clay dilatancy (Roscoe & Schofield [151]) by specifying $m = 0$, and $d_0 = M$.

Using the original formulation by Li & Dafalias in the HS-Small model would require four additional material input parameters. These are the parameters d_0 , and m introduced in Equation 7.38, and two parameters which define the critical state line in $e - \ln p$ space. The critical state line can for example, be defined by an initial void ratio e_0 and its slope λ . Unfortunately, the parameters d_0 , and m can be obtained in numerical fitting procedures only. Altogether, the input to the original approach by Li & Dafalias seems too demanding for a model that is meant to be used in practical engineering applications. Therefore, the formulation by Li & Dafalias is simplified by a) calculating the state parameter, ψ based on constant void ratio, and b) providing default parameters for $\lambda * m$, and d_0 . With these simplifications, Equation 7.38 can be rewritten as:

$$\tan \psi_m = (Me^{\frac{1}{15} \ln(p_{cs}/p)} - \eta)/10, \quad (7.39)$$

where

$$\frac{p_{cs}}{p} = \frac{\eta \sin \varphi_{cs}(1 - \sin \varphi_m)}{M \sin \varphi_m(1 - \sin \varphi_{cs})} \quad (7.40)$$

and $\lambda * m = -\frac{1}{15}$, and $d_0 = \frac{M}{10}$. These default parameters are in good agreement to the ones presented in Li & Dafalias [103]. As the default parameters cannot be guaranteed to work in dilatant conditions, they are used for contraction only. Whenever dilatant material behavior is detected, the HS-Small model falls back to the original Rowe equation.

Figure 7.7 compares the mobilized dilatancy angles of all flow rules discussed above. The comparison of mobilized dilatancy angles is supplemented by test data in Chapter 8. However, it can already be noted that not one of the discussed approaches is considered fully satisfactory. In future work, the HS-Small model could perhaps fully adopt the approach by Li & Dafalias, therefore extending its use to dilatant behavior in a void ratio dependent formulation (see Chapter 10).

7.3.3 Yield surface and plastic potential - HS-Small(MN) only

The Mohr-Coulomb failure criterion [123] for soils, which is implemented in the original HS model, is one of the earliest and most trusted failure criteria. It is experimentally verified in triaxial compression and extension and is of striking simplicity. However, the Mohr-Coulomb criterion is very conservative for intermediate principal stress states

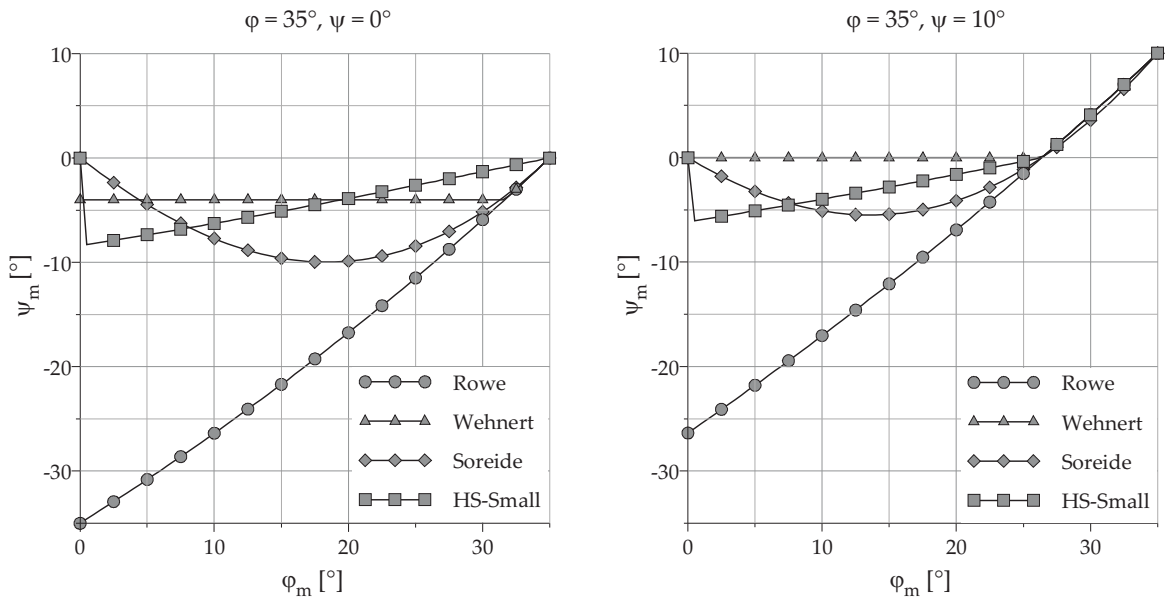


Figure 7.7: Mobilized dilatancy angle versus mobilized friction angle. Results from the original Rowe equation, its modification by Wehnert, and Soreide, and the modified Li & Dafalias formulation.

between triaxial compression and extension. Figure 7.8, for example, shows experimental results for reconstituted Osaka alluvial clay. Similar findings for sand and sandstone have been for example reported by Lade [97], Ramamurthy & Rawat [144], Sutherland & Mesdary [176], and Yamada & Ishihara [196].

Matsuoka & Nakai [113], [114] (MN) proposed a failure criterion that is in better agreement with the experimental surface shown in Figure 7.8. They propose the concept of a *Spatial Mobilized Plane (SMP)*, which defines the plane of maximum spatial, averaged particle mobilization in principal stress space. The SMP is geometrically constructed by deriving the mobilized (Mohr-Coulomb) friction angles for each principal stress pair separately (Figure 7.9, left) and sketching the respective mobilized planes in principal stress space (Figure 7.9, right). Matsuoka & Nakai derive their failure criterion by limiting the averaged ratio of spatial normal stress to averaged spatial shear stress on this plane. Their failure stress ratio can be expressed as a simple function of the first, second, and third stress invariant, I_1 , I_2 , and I_3 as shown in Equation 7.41. With the SMP concept, the Matsuoka-Nakai criterion automatically retains the well established material strength of the Mohr-Coulomb criterion in triaxial compression and extension.

The likewise well-known failure criterion by Lade & Duncan [99] (Lade) appears compared to the Mohr-Coulomb criterion and the Matsuoka-Nakai criterion rather optimistic in plane strain conditions and triaxial extension. Therefore, it has not (unlike the Matsuoka-Nakai criterion), been considered as an option for the HS-Small model, though it is mentioned here for the sake of completeness. It should also be mentioned that using bifurcation analysis, progressive failures would most likely 'correct' for the

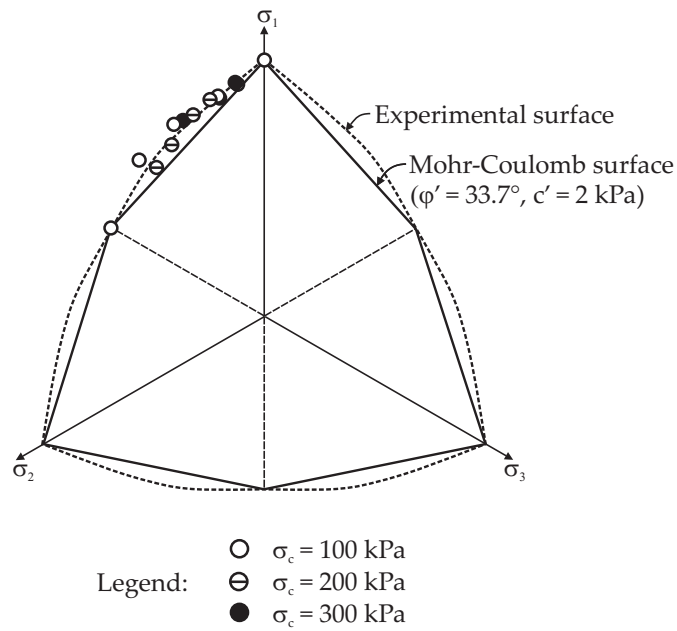


Figure 7.8: Test results by Shibata & Karube [163] on reconstituted Osaka alluvial clay.

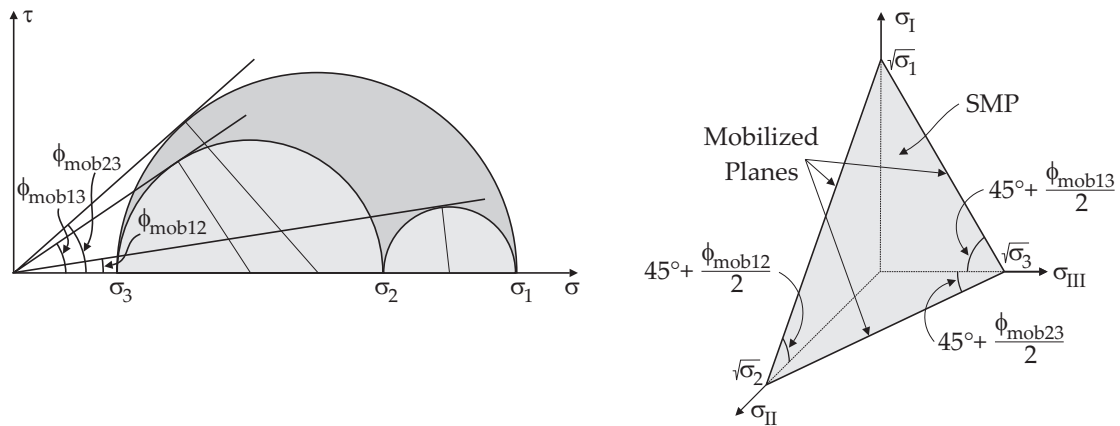


Figure 7.9: The SMP concept of Matsuoka & Nakai. Left: Three mobilized planes where the maximum shear stress to normal stress ratio is reached for the respective principal stresses. Right: SMP in principal stress space.

Lade criterion's overly optimistic, ultimate material strength estimate.

Both failure criteria, Matsuoka-Nakai, and Lade, are functions of the first, second, and third stress invariants, I_1 , I_2 , and I_3 respectively:

$$\begin{aligned} f_{\text{Lade}} &= \frac{I_1^3}{I_3} - c_1 = 0 & \text{with} & \quad c_1 = \frac{(-3 + \sin \varphi)^3}{(-1 - \sin \varphi)(-1 + \sin \varphi)^2} \\ f_{\text{MN}} &= \frac{I_1 I_2}{I_3} - c_2 = 0 & \text{with} & \quad c_2 = \frac{9 - \sin^2 \varphi}{-1 + \sin^2 \varphi} \end{aligned} \quad (7.41)$$

where

$$\begin{aligned} I_1 &= \sigma_{ii} \\ I_2 &= \frac{1}{2}(\sigma_{ij}\sigma_{ij} - \sigma_{ii}\sigma_{jj}) \\ I_3 &= \frac{1}{6}(\sigma_{ii}\sigma_{jj}\sigma_{kk} + 2\sigma_{ij}\sigma_{jk}\sigma_{ki} - 3\sigma_{ij}\sigma_{ji}\sigma_{kk}). \end{aligned} \quad (7.42)$$

In principal stress, the stress invariants simplify to:

$$\begin{aligned} I_1 &= \sigma_1 + \sigma_2 + \sigma_3 \\ I_2 &= -\sigma_1\sigma_2 - \sigma_2\sigma_3 - \sigma_3\sigma_1 \\ I_3 &= \sigma_1\sigma_2\sigma_3. \end{aligned} \quad (7.43)$$

The constants c_1 and c_2 in Equation 7.41 are defined so that both failure criteria are identical to the Mohr-Coulomb criterion in triaxial compression.

The HS-Small model optionally uses a Matsuoka-Nakai yield surface and criterion instead of the original HS model's Mohr-Coulomb criterion. In the HS-Small(MN) model the non-associated Mohr-Coulomb potential is substituted by a Drucker-Prager [35] potential. The cap-type yield function remains unchanged, only its potential is adjusted to the new deviatoric flow of the cone-type yield surface.

The true triaxial experiments by Yamada & Ishihara [196] shown in Figure 7.10 not only support the failure hypothesis by Matsuoka & Nakai but at the same time proof that the Drucker-Prager potential's radial deviatoric flow direction is a reasonable assumption for low mobilized friction angles. For higher mobilized friction angles, flow directions increasingly tend towards an associated deviatoric flow, the solid curve in Figure 7.10 represent the Matsuoka-Nakai failure criterion ($\varphi = 30^\circ$). However, in the example presented in Figure 7.10, the error in assuming radial flow for high mobilized friction angles is of the same magnitude or less than that made in assuming deviatoric associated flow. A more detailed discussion of the test results by Yamada & Ishihara is given in Müllerschön [127], a summary of true triaxial test results of several researchers is given in Biarez & Hicher [16].

Replacing the Mohr-Coulomb yield surface and plastic potential by smooth surfaces is also an advantage from a numerical point of view. Other than the Mohr-Coulomb criterion, these have well defined gradients at all points except the apex. Therefore, they allow for a more rigorous numerical formulation. The singular intersections of the Mohr-Coulomb surface (Figure 7.3) on the other hand require a Koiter [91] algorithm which will be explored in more detail in Section 7.4.4.

When using a Drucker-Prager plastic potential, from a numerical point of view it is beneficial to formulate the yield criterion, Lode angle dependent. This will become more obvious later in this Chapter when discussing the cap-type yield surface of the

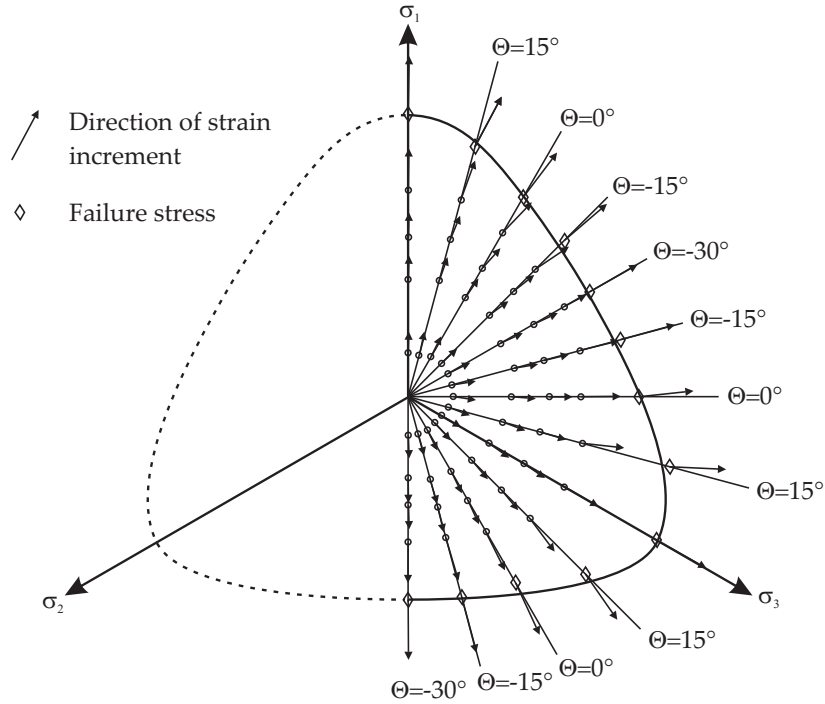


Figure 7.10: Experimentally derived shear strain increment vectors projected on the octahedral plane (after Nakai & Matsuoka [128]).

HS-Small(MN) model or its return mapping. As the Lode dependent formulation of the original Matsuoka-Nakai yield criterion is bulky, several other simplified Lode dependent yield criterion were also proposed in the literature.

The Lode angle θ [106] in this thesis is defined as:

$$\theta = \frac{1}{3} \arcsin\left(\frac{3\sqrt{3}J_3}{2J_2^{3/2}}\right) \quad (7.44)$$

where J_2 and J_3 are the second and third deviatoric stress invariants. These are defined for the deviatoric stress tensor, $\sigma_{ij}^* = \sigma_{ij} - \frac{1}{3}\sigma_{ii}$ analog to Equation 7.42, substituting σ by σ^* . In principal stress space, J_2 and J_3 can be expressed as:

$$\begin{aligned} J_2 &= \frac{1}{6}((\sigma_1 - \sigma_2)^2 + (\sigma_2 - \sigma_3)^2 + (\sigma_3 - \sigma_1)^2) \\ J_3 &= \frac{1}{27}(2\sigma_1 - \sigma_2 - \sigma_3)(2\sigma_2 - \sigma_3 - \sigma_1)(2\sigma_3 - \sigma_1 - \sigma_2). \end{aligned} \quad (7.45)$$

The Lode angle in triaxial compression and extension is evaluated as $\theta = \frac{\pi}{6}$ and $\theta = -\frac{\pi}{6}$ respectively. In the literature, Lode angles are sometimes defined in an $\arccos()$ function, which implies a radial shift of $\frac{\pi}{6}$. All Lode dependent relationships presented in this section can be easily adapted to the alternatively defined Lode angle as well.

The Lode dependent formulation of the Matsuoka-Nakai criterion is known as LMN

dependence [12]:

$$\begin{aligned} \chi(\theta) &= \frac{\sqrt{3}\delta}{2\sqrt{\delta^2-\delta+1}} \frac{1}{\cos \vartheta} \\ \text{with } \begin{cases} \vartheta &= \frac{1}{6} \arccos\left(-1 + \frac{27\delta^2(1-\delta)^2}{2(\delta^2-\delta+1)} \sin^2(3\theta)\right) & \text{for } \theta \leq 0 \\ \vartheta &= \frac{\pi}{3} - \frac{1}{6} \arccos\left(-1 + \frac{27\delta^2(1-\delta)^2}{2(\delta^2-\delta+1)} \sin^2(3\theta)\right) & \text{for } \theta > 0 \end{cases} \\ \text{and } \delta &= \frac{3-\sin \varphi}{3+\sin \varphi} \end{aligned} \quad (7.46)$$

Unfortunately, the derivatives of the LMN dependence are bulky compared to those of other Lode dependent strength criteria proposed in the literature. Here the criteria by Argyris [6], Papadimitriou & Bouckovalas (PB) [133], and Wang [102] shall be mentioned:

$$\text{Argyris: } \chi(\theta) = \frac{2\delta}{(1+\delta) - (1-\delta) \sin(3\theta)} \quad (7.47)$$

$$\text{PB: } \chi(\theta) = \frac{4\delta}{(1+\delta) - (1-\delta) \sin(3\theta)} - \frac{1}{2}((1+\delta) + (1-\delta) \sin(3\theta)) \quad (7.48)$$

$$\text{Wang: } \chi(\theta) = \frac{\sqrt{(1+\delta^2)^2 + 4\delta(1-\delta^2) \sin(3\theta)} - (1+\delta^2)}{2(1-\delta) \sin(3\theta)} \quad (7.49)$$

Results of all the above strength criteria are plotted in Figures 7.11, 7.12, and 7.13 for triaxial compression friction angles φ of 20° , 30° , and 40° respectively. Obviously the less complex formulations 7.47 to 7.49 tradeoff convexity at high friction angles for their simplicity. The Matsuoka-Nakai (MN), and Lade yield surfaces stay convex even at high friction angles and hence, fulfill Drucker's convexity postulate [33].

Due to the Drucker-Prager plastic potential of the HS-Small(MN) model, the Lode angle is constant during return mapping (see Section 7.4). This favors the use of the LMN dependence in the HS-Small(MN) model. The less complex and very similar criteria by Wang or Papadimitriou & Bouckovalas would seem more appropriate in case the condition $\frac{\partial \theta}{\partial \sigma_i} = 0$, does not hold while higher order derivatives are needed in the algorithmic setting.

7.3.4 Generalized model formulation - HS-Small(MN) only

The original formulation of the HS model is closely related to triaxial stress conditions. In order to apply the Matsuoka-Nakai yield criterion, the basic yield function (7.12) is reformulated in terms of mobilized friction φ_m . The Mohr-Coulomb criterion in triaxial conditions yields:

$$\sin \varphi_m = \frac{\sigma_1 - \sigma_3}{\sigma_1 + \sigma_3 + 2c \cot \varphi} \Leftrightarrow q = \sin \varphi_m (\sigma_1 + \sigma_3 + 2c \cot \varphi) \quad (7.50)$$

and

$$q_f = \frac{2 \sin \varphi}{1 - \sin \varphi} (\sigma_3 + c \cot \varphi) \quad (7.51)$$

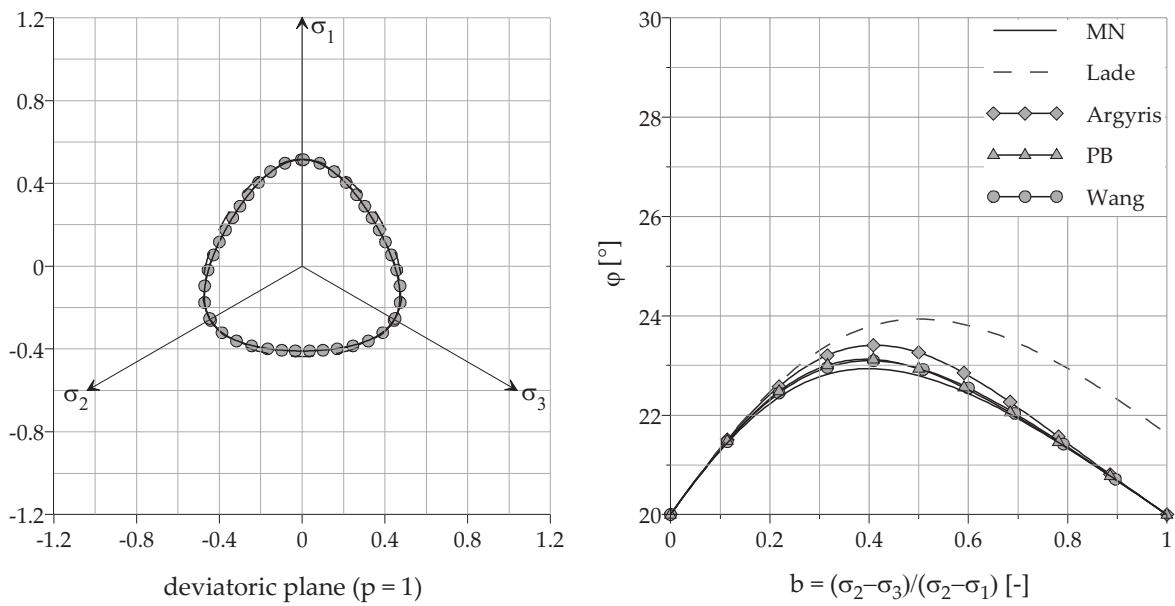


Figure 7.11: Different failure criteria for a friction angle of $\varphi = 20^\circ$ in triaxial compression. Left: Deviatoric shape of the yield criteria. Right: Friction angle as a function of the intermediate stress parameter b .

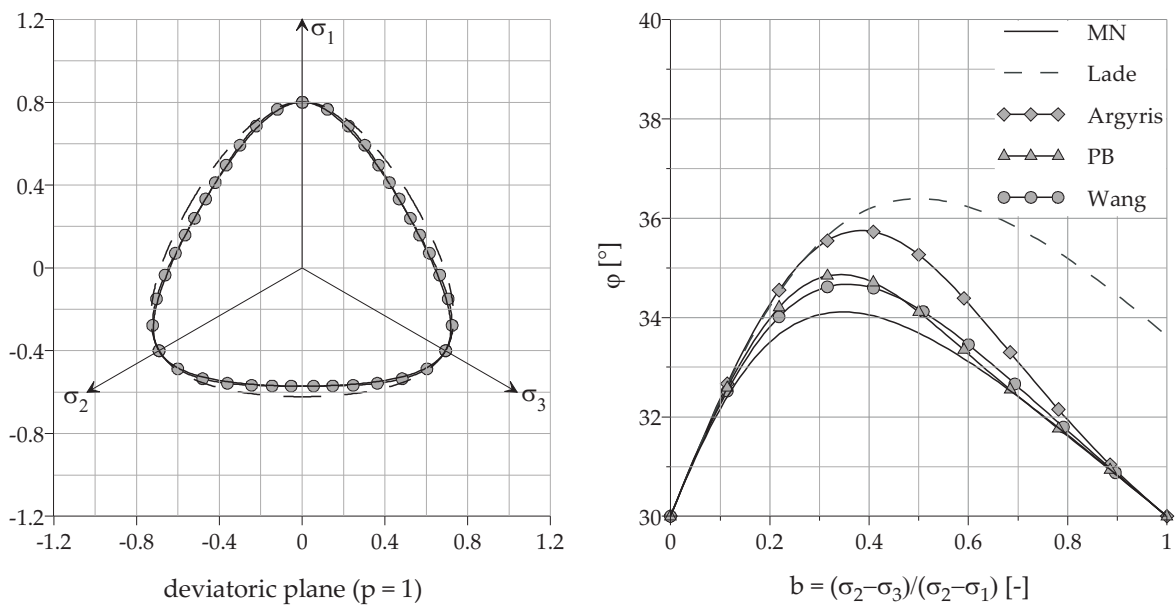


Figure 7.12: Different failure criteria for a friction angle of $\varphi = 30^\circ$ in triaxial compression. Left: Deviatoric shape of the yield criteria. Right: Friction angle as a function of the intermediate stress parameter b .

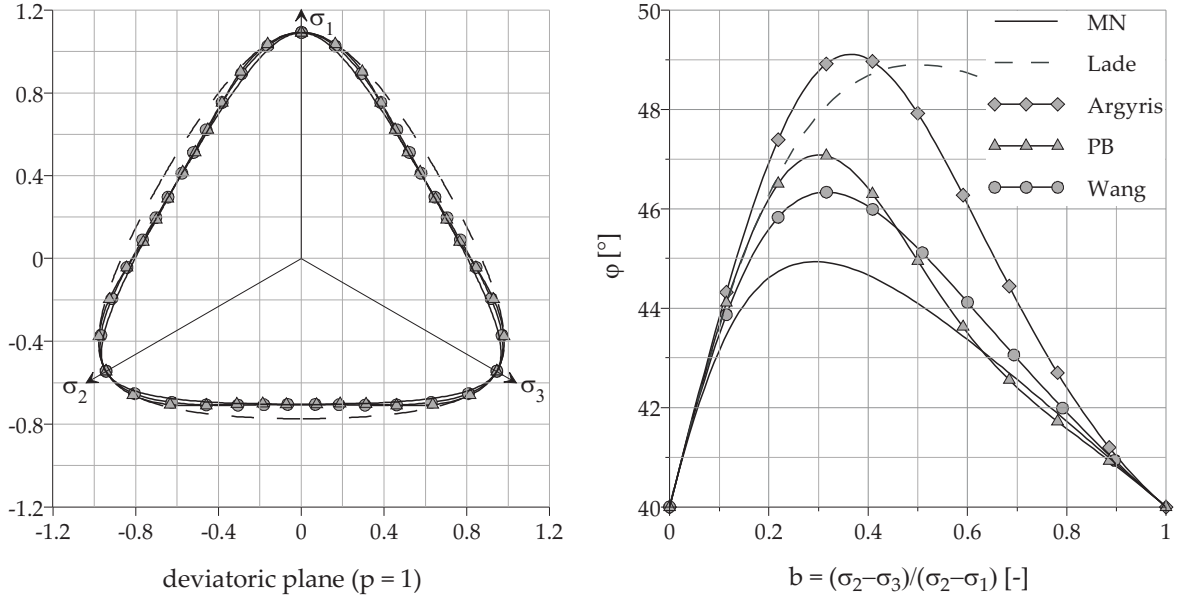


Figure 7.13: Different failure criteria for a friction angle of $\varphi = 40^\circ$ in triaxial compression. Left: Deviatoric shape of the yield criteria. Right: Friction angle as a function of the intermediate stress parameter b .

and thus:

$$\frac{q}{q_a} = R_f \left(\frac{1 - \sin \varphi}{\sin \varphi} \right) \left(\frac{\sin \varphi_m}{1 - \sin \varphi_m} \right). \quad (7.52)$$

With the objective shear strain measure:

$$\gamma_s = \sqrt{\frac{1}{2}((\varepsilon_1 - \varepsilon_2)^2 + (\varepsilon_2 - \varepsilon_3)^2 + (\varepsilon_3 - \varepsilon_1)^2)} \quad (7.53)$$

which reduces to $\gamma_s = \varepsilon_1 - \varepsilon_3$ in triaxial conditions, one obtains $\gamma_s = \frac{3}{2}\varepsilon_1$ for zero volumetric strain. Adopting the original HS model's yield function (Equation 7.12) to shear strain γ_s and considering Equation 7.52 results in:

$$f^s = \frac{3}{2} \frac{q}{E_i} \frac{\left(\frac{1 - \sin \varphi_m}{\sin \varphi_m} \right)}{\left(\frac{1 - \sin \varphi_m}{\sin \varphi_m} \right) - R_f \left(\frac{1 - \sin \varphi}{\sin \varphi} \right)} - \frac{3}{2} \frac{q}{E_{ur}} - \gamma_s^{ps} \quad (7.54)$$

where $\sin \varphi_m$ is the mobilized friction angle in triaxial compression. In mobilized friction, the Matsuoka-Nakai yield criterion defined in Equation 7.41, can be written as:

$$\sin^2 \varphi_m \equiv \frac{9 - \frac{I_1 I_2}{I_3}}{1 - \frac{I_1 I_2}{I_3}}. \quad (7.55)$$

This definition yields deviatoric isolines of mobilized friction that are similar to the shape of the Matsuoka-Nakai yield criterion. Alternatively, Equation 7.55 can be expressed in

the LMN dependency $\chi = \chi(\theta)$ as:

$$\sin \varphi_m = \frac{3q}{6\chi(p + c \cot \varphi) + q} \quad (7.56)$$

The plastic potential to the cone-type yield surface is defined as:

$$g^s = (p + c \cot \varphi) \frac{6 \sin \psi_m}{3 - \sin \psi_m} \quad (7.57)$$

Due to the cone-type yield surface's new shape, the cap-type yield surface is also to be reformulated. The special stress measure defined in Equation 7.21 is now replaced by the Roscoe invariant $q = \sqrt{3J_2}$. At the same time the Lode angle dependency of the cone-type yield surface is translated to the cap by scaling its steepness:

$$f^c = \frac{q^2}{(\chi\alpha)^2} - p^2 - p_p^2 \quad (7.58)$$

The cap-type yield surface uses the non-associated plastic potential

$$g^c = \frac{q^2}{(\tilde{\chi}\alpha)^2} - p^2 - p_p^2 \quad (7.59)$$

where $\tilde{\chi} = \chi(\theta_{\sigma_{T_{trial}}})$. The cap's deviatoric plastic flow direction is thus consistent with the cone's radial Drucker-Prager potential.

Although the HS-Small model should respond slightly different under general (plastic) loading conditions, its triaxial behavior should be equal to the HS model. The HS-Small evolution laws are therefore adapted to the objective shear strain measure as follows:

$$\begin{aligned} d\gamma_s^{ps} &= d\lambda^s h_i h_{\gamma_s^{ps}} & \text{with } h_{\gamma_s^{ps}} &= \sqrt{\frac{1}{2} \left(\left(\frac{\partial g}{\partial \sigma_1} - \frac{\partial g}{\partial \sigma_2} \right)^2 + \left(\frac{\partial g}{\partial \sigma_2} - \frac{\partial g}{\partial \sigma_3} \right)^2 + \left(\frac{\partial g}{\partial \sigma_3} - \frac{\partial g}{\partial \sigma_1} \right)^2 \right)} = \frac{3}{2} \\ dp_p &= d\lambda^c h_i h_{p_p} & \text{with } h_{p_p} &= 2H \left(\frac{\sigma_3 + c \cot \varphi}{p^{\text{ref}} + c \cot \varphi} \right)^m p \end{aligned} \quad (7.60)$$

The evolution laws finally round up the formulation of the HS-Small model, which is summarized for the HS-Small(MN) model in Box 7.2. A complete list of model parameters can be found in Table 7.1. The integration of the constitutive equations is discussed in the next section.

7.4 Local integration of the constitutive equations

In the context of finite element analysis, integration of the constitutive equations (Section 7.1) is carried out within a finite set of integration points. The integration points' spatial coordinates are defined by the element mesh's geometry and the element type. In case of commonly used isoparametric elements, the integration points generally are Gauss (quadrature) points. By balancing internal and external loads within the finite

Box 7.2: Governing equations of the HS-Small(MN) model.

1. (Para-)Elastic stiffness tensor:

$$D_{ijkl} = \frac{2G}{1-2\nu_{ur}} ((1-2\nu_{ur})\delta_{ik}\delta_{jl} + \nu_{ur}\delta_{jk}\delta_{il}) \text{ where}$$

$$G = \begin{cases} G_0 \left(\frac{\gamma_{0.7}}{\gamma_{0.7} + a\gamma_{Hist}} \right)^2 & \text{for } \gamma_s < \gamma_c \\ \frac{E_{ur}}{2(1+\nu_{ur})} & \text{for } \gamma_s \geq \gamma_c \end{cases}$$

2. Yield functions:

$$f^s = \frac{3}{2} \frac{q}{E_i} \frac{\left(\frac{1-\sin\varphi_m}{\sin\varphi_m} \right)}{\left(\frac{1-\sin\varphi_m}{\sin\varphi_m} \right) - R_f \left(\frac{1-\sin\varphi}{\sin\varphi} \right)} - \frac{3}{2} \frac{q}{E_{ur}} - \gamma_s^{ps}$$

$$f^c = \frac{q^2}{(\tilde{\chi}\alpha)^2} - p^2 - p_p^2 \text{ where}$$

$$\sin^2 \varphi_m = \frac{9 - \frac{I_1 I_2}{I_3}}{1 - \frac{I_1 I_2}{I_3}}$$

3. Plastic potentials:

$$g^s = q - (p + c \cot \varphi) \frac{6 \sin \psi_m}{3 - \sin \psi_m}$$

$$g^c = \frac{q^2}{(\tilde{\chi}\alpha)^2} - p^2 - p_p^2 \text{ where}$$

$$\tilde{\chi} = \chi(\theta_{\sigma_{T_{rial}}})$$

4. Mobilized dilatancy (modified Rowe):

$$\sin \psi_m = \begin{cases} \frac{\sin \varphi_m - \sin \varphi_{cs}}{1 - \sin \varphi_m \sin \varphi_{cs}} & \text{for } \sin \varphi_m - \sin \varphi_{cs} \geq 0 \\ \frac{1}{10} (M e^{\frac{1}{15} \ln(p_{cs}/p)} - \eta) & \text{for } \sin \varphi_m - \sin \varphi_{cs} < 0 \end{cases}$$

$$\sin \varphi_{cs} = \frac{\sin \varphi - \sin \psi}{1 - \sin \varphi \sin \psi} \text{ and } \frac{p_{cs}}{p} = \frac{\eta \sin \varphi_{cs} (1 - \sin \varphi_m)}{M \sin \varphi_m (1 - \sin \varphi_{cs})}$$

5. Hardening laws:

$$d\gamma_s^{ps} = d\lambda^s h_{\gamma_s^{ps}} \text{ with } h_{\gamma_s^{ps}} = \frac{3}{2}$$

$$dp_p = d\lambda^c h_{p_p} \text{ with } h_{p_p} = 2H \left(\frac{\sigma_3 + c \cot \varphi}{p^{ref} + c \cot \varphi} \right)^m p$$

$$H = \frac{K_s K_c}{K_s - K_c} \text{ and } K_s = \frac{E_{ur}^{ref}}{3(1-2\nu)}$$

6. Stress dependent stiffness:

$$E_i = E_i^{ref} \left(\frac{\sigma_3 + c \cot \varphi}{p^{ref} + c \cot \varphi} \right)^m$$

$$E_{ur} = E_{ur}^{ref} \left(\frac{\sigma_3 + c \cot \varphi}{p^{ref} + c \cot \varphi} \right)^m$$

$$G_0 = G_0^{ref} \left(\frac{\sigma_3 + c \cot \varphi}{p^{ref} + c \cot \varphi} \right)^m$$

7. Lode Matsuoka-Nakai dependency:

$$\chi(\theta) = \frac{\sqrt{3}\delta}{2\sqrt{\delta^2 - \delta + 1}} \frac{1}{\cos \vartheta} \text{ with}$$

$$\vartheta(\theta) = \begin{cases} \frac{1}{6} \arccos\left(-1 + \frac{27\delta^2(1-\delta)^2}{2(\delta^2 - \delta + 1)} \sin^2(3\theta)\right) & \text{for } \theta \leq 0 \\ \frac{\pi}{3} - \frac{1}{6} \arccos\left(-1 + \frac{27\delta^2(1-\delta)^2}{2(\delta^2 - \delta + 1)} \sin^2(3\theta)\right) & \text{for } \theta > 0 \end{cases}$$

$$\delta = \frac{3 - \sin \varphi}{3 + \sin \varphi}$$

Table 7.1: Parameters for the HS and the HS-Small models

Parameter	Symbol	Unit	HS	HS-Small
<i>I. User defined parameters</i>				
Triaxial secant stiffness	E_{50}^{ref}	$\left[\frac{kN}{m^2}\right]$	✓	✓
Oedometric tangent stiffness	$E_{\text{oed}}^{\text{ref}}$	$\left[\frac{kN}{m^2}\right]$	✓	✓
Unloading/ reloading stiffness	$E_{\text{ur}}^{\text{ref}}$	$\left[\frac{kN}{m^2}\right]$	✓	✓
Power of stress dependency	m	$[-]$	✓	✓
Cohesion (effective)	c	$\left[\frac{kN}{m^2}\right]$	✓	✓
Friction angle (effective)	φ	$[^\circ]$	✓	✓
Dilatancy angle	ψ	$[^\circ]$	✓	✓
Poisson's ratio	ν_{ur}	$[-]$	✓	✓
Reference stress for stiffness	p^{ref}	$\left[\frac{kN}{m^2}\right]$	✓	✓
K_0 -value (normal consolidation)	K_0^{nc}	$[-]$	✓	✓
Failure ratio	R_f	$[-]$	✓	✓
Tensile strength	σ_{Tension}	$\left[\frac{kN}{m^2}\right]$	✓	✓
Small strain Stiffness	E_0^{ref}	$\left[\frac{kN}{m^2}\right]$	-	✓
Threshold shear strain	$\gamma_{0.7}$	$[-]$	-	✓
<i>II. Internal parameters</i>				
Initial secant stiffness	E_i^{ref}	$\left[\frac{kN}{m^2}\right]$	✓	✓
Cap parameter (steepness)	α	$[-]$	✓	✓
Cap parameter (stiffness ratio)	K_s/K_c	$[-]$	✓	✓
<i>III. State parameters</i>				
Plastic deviatoric strain	γ^{ps}	$[-]$	✓	-
Plastic shear strain	γ_s^{ps}	$[-]$	-	✓
Pre-consolidation pressure	p_p	$\left[\frac{kN}{m^2}\right]$	✓	✓
Deviatoric strain history	H_{ij}	$[-]$	-	✓

element mesh, the global iterative procedure supplies strain increments for each integration point. Supplying constitutive stresses for the given strain increments is the task of the constitutive model. The process of finding an admissible stress state and its corresponding internal variables for each integration point is called local integration.

In this section the local integration of the HS-Small model is discussed. The algorithm chosen for this purpose is a member of the class of generalized midpoint algorithms that were originally introduced by Simo & Hughes [166] as closest point projection algorithm. The global integration is here not discussed in more detail since only standard finite element procedures are deployed. These are documented in many books, for example those by Hughes [66] or Belytschko [15].

The following abbreviations are used in the algorithmic formulations:

$$\begin{aligned} {}^{n+1}n_{ij} &= \left. \frac{\partial f}{\partial \sigma_{ij}} \right|_{n+1} \\ {}^{n+1}m_{ij} &= \left. \frac{\partial g}{\partial \sigma_{ij}} \right|_{n+1} \\ {}^{n+1}\xi_* &= \left. \frac{\partial f}{\partial q_*} \right|_{n+1} \end{aligned} \quad (7.61)$$

where again the asterisk denotes n indices or vanishes for scalar functions.

7.4.1 Return mapping onto the yield surface

Local integration of the constitutive equations can be geometrically interpreted as the projection of an elastic trial stress onto the updated yield surface. Numerical schemes for stress return onto the yield surface are therefore known as return mapping algorithms. The elastic predictor or trial stress ${}^{Trial}\sigma_{ij}$ that functions as the mapping object is initially obtained by freezing plastic flow. The flow rule then defines the mapping *direction* back onto the yield surface. The point in *time* when the flow rule is evaluated is set by the time integration scheme. The class of generalized midpoint algorithms contains all possible evaluation times. Using Vermeer's [184] notation, the class of generalized midpoint algorithms can be expressed as:

$${}^{n+1}\sigma_{ij} = D_{ijkl} ({}^{n+1}\varepsilon_{kl} - {}^{n+1}\varepsilon_{kl}^p) \quad (7.62)$$

$${}^{n+1}\varepsilon_{kl}^p = {}^n\varepsilon_{kl}^p + \lambda^{n+\alpha} m_{ij} \quad (7.63)$$

$${}^{n+1}q_* = {}^nq_* + \lambda^{n+\alpha} h_* \quad (7.64)$$

$$F_{n+1} = 0 \quad (7.65)$$

where

$${}^{n+\alpha} m_{ij} = m_{ij} \left((1 - \omega) {}^n\sigma_{ij} + \omega {}^{n+1}\sigma_{ij}, (1 - \omega) {}^nq_* + \omega {}^{n+1}q_* \right) \quad \text{and} \quad (7.66)$$

$${}^{n+\alpha} h_* = h_* \left((1 - \omega) {}^n\sigma_{ij} + \omega {}^{n+1}\sigma_{ij}, (1 - \omega) {}^nq_* + \omega {}^{n+1}q_* \right) \quad (7.67)$$

and the superscripts n and $n + 1$ denote two subsequent steps in the integration procedure and $0 \leq \omega \leq 1$, defines the time when the flow rule is evaluated. For $\omega = 0$ the flow rule is evaluated at the initial stress or, if this is elastic, at the intersection with the yield

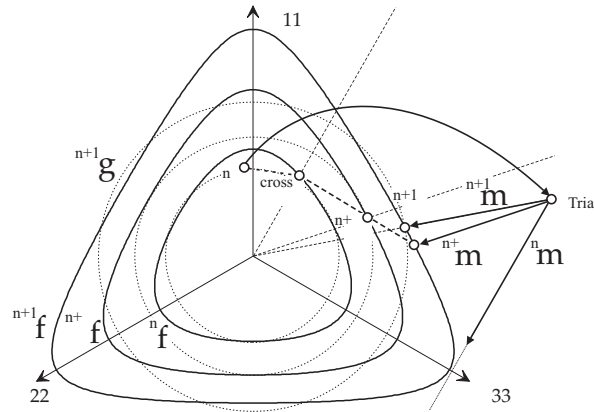


Figure 7.14: Deviatoric return mapping using the generalized midpoint algorithm with different ω values. The chosen yield surface (Matsuoka-Nakai) and plastic potential (Drucker-Prager) correspond to the HS-Small(MN) model.

surface. Hence, $\omega = 0$ corresponds to an explicit Forward Euler approach. Similarly, the generalized midpoint algorithm corresponds to an implicit Backward Euler scheme for $\omega = 1$ and to a Crank-Nicholson scheme for $\omega = \frac{1}{2}$.

Figure 7.14 illustrates different possible results of applying these integration schemes to the deviatoric return mapping in the HS-Small(MN) model. Obviously, the Forward Euler approach could not converge for the rather large excursion outside the yield surface. The implicit and midpoint schemes would both converge in the example given, the implicit one with less accuracy than the midpoint scheme (first order only). However, the implicit scheme has several advantages over the midpoint scheme. There is no need to calculate the intersection with the yield surface in the implicit scheme, its solution is sought by evaluating the flow rule at the final stress. By implicitly assuming that such a stress state exists, the Backward Euler algorithm is guaranteed to provide a solution. Another important advantage of the implicit algorithm lies in the fact that it can be linearized in a closed form. From linearization, consistent elastoplastic tangent moduli can be obtained that preserve quadratic convergence in the global equilibrium iterations, if a Newton-Raphson scheme is used.

In the following, an implicit closest point projection algorithm for $\omega = 1$ is introduced. The consistent algorithmic tangent moduli for a single yield surface is discussed as well. The algorithmic setting presented, is based on works of Jeremic & Sture [83]. The implications of multiple yield surfaces is discussed in Section 7.4.4.

7.4.2 The closest point projection algorithm

Let the load step $n \rightarrow (n+1)$ be a plastic load step so that $\lambda > 0$. With the strain increment ${}^{n+1}d\varepsilon$ the elastic trial stress calculates for this load step as:

$${}^{Trial}\sigma_{ij} = {}^n\sigma_{ij} + D_{ijkl} {}^{n+1}d\varepsilon_{kl}. \quad (7.68)$$

The implicit form of the general midpoint algorithm (Equation 7.62) can now be rewritten as:

$${}^{n+1}\sigma_{ij} = {}^{Trial}\sigma_{ij} - \lambda D_{ijkl} {}^{n+1}m_{kl} \quad (7.69)$$

where ${}^{n+1}m_{kl}$ is the derivative of the plastic potential for the implicitly assumed stress at the end of the load step. A algorithmic solution for this equation can be found by defining the tensor of residuals:

$$r_{ij} = \sigma_{ij} - ({}^{Trial}\sigma_{ij} - \lambda D_{ijkl} {}^{n+1}m_{kl}) \quad (7.70)$$

and enforcing $r_{ij} = 0$ for the final stress $\sigma_{ij} = {}^{n+1}\sigma_{ij}$ in the linearized form of Equation 7.70:

$$r_{ij} + d\sigma_{ij} + \lambda D_{ijkl} {}^{n+1}m_{kl} + \lambda D_{ijkl} \left. \frac{\partial m_{kl}}{\partial \sigma_{mn}} \right|_{n+1} d\sigma_{mn} + \lambda D_{ijkl} \left. \frac{\partial m_{kl}}{\partial q_*} \right|_{n+1} dq_* = 0. \quad (7.71)$$

By algebraic manipulation the above equation can be solved to $d\sigma_{ij}$:

$$d\sigma_{mn} = - (r_{ij} + d\lambda D_{ijkl} {}^{n+1}\Theta_{kl}) \Xi_{ijmn} \quad \text{with} \quad (7.72)$$

$$\Xi_{ijmn} = \left(\delta_{im}\delta_{nj} + \lambda D_{ijkl} \left. \frac{\partial m_{kl}}{\partial \sigma_{mn}} \right|_{n+1} \right)^{-1} \quad \text{and} \quad (7.73)$$

$$\Theta_{kl} = {}^{n+1}m_{kl} + \lambda \left. \frac{\partial m_{kl}}{\partial q_*} \right|_{n+1} h_* \quad (7.74)$$

and applied to the linearized yield function:

$${}^{n+1}f + {}^{n+1}n_{mn}d\sigma_{mn} + {}^{n+1}\xi dq_* = 0 \quad (7.75)$$

which is derived by a first order Taylor expansion around the final stress state ${}^{n+1}f = 0$. Solving the above equation for $d\lambda$, the solution for the iterative update of the plastic multiplier is readily found as:

$$d\lambda = \frac{{}^{n+1}f - r_{ij}\Xi_{ijmn} {}^{n+1}n_{mn}}{D_{ijkl}\Theta_{kl}\Xi_{ijmn} {}^{n+1}n_{mn} - {}^{n+1}\xi_* h_*} \quad (7.76)$$

where again the conventions defined in Equation 7.61 have been used.

In order to successfully apply the closest point projection as an iterative procedure, a suitable starting point is necessary. A good guess for the starting point can typically be found by using the normal to the elastic trial point [83]:

$${}^{Trial}f + {}^{Trial}n_{mn}d\sigma_{mn} + {}^{Trial}\xi dq_* = 0, \quad (7.77)$$

and assuming that any stress relaxation from the trial stress is due to plastic straining and thus:

$$d{}^{Trial}\sigma_{mn} = -D_{mnpq}d\lambda^{(0)} ({}^{Trial}m_{pq}). \quad (7.78)$$

Solving the above equations for $d\lambda$

$$d\lambda^{(0)} = \frac{^{Trial}f}{^{Trial}n_{nm}D_{nmpq} - ^{Trial}m_{pq} \xi_* h_*} \quad (7.79)$$

the starting point $\sigma_{mn}^{(0)}$ is calculated as:

$$\sigma_{mn}^{(0)} = ^{Trial}\sigma_{mn} - d\lambda^{(0)} D_{mnpq} ^{Trial}m_{pq}. \quad (7.80)$$

The algorithmic setting for the closest point projection algorithmic can now be summarized as follows (Box 7.3):

7.4.3 The consistent algorithmic tangent stiffness tensor

When the Newton-Raphson scheme is used for solving the global equilibrium equations, only the consistent tangent stiffness can preserve its quadratic convergence. Using other stiffness tensors, for example the traditional tangent stiffness obtained by a Forward Euler method ($\omega = 0$), the quadratic convergence is lost.

The consistent elastoplastic algorithmic tangent stiffness was originally introduced by Hughes & Taylor [67] for viscoplastic materials. Simo & Taylor [167] and Runesson & Samuelsson [154] later adopted it for elastoplastic materials.

In any case the consistent elastoplastic stiffness is obtained by enforcing the consistency condition on the discrete algorithmic problem instead of the continuum problem, which would result in the continuum elastoplastic tangent. Enforcing the consistency condition at the final converged stress position $^{n+1}\sigma_{ij}$ yields :

$$\begin{aligned} d^{n+1}f &= \left. \frac{\partial f}{\partial \sigma_{ij}} \right|_{n+1} d\sigma_{ij} + \left. \frac{\partial f}{\partial q_*} \right|_{n+1} dq_* \\ &= ^{n+1}n_{ij}d\sigma_{ij} + ^{n+1}\xi_*dq_* = 0. \end{aligned} \quad (7.81)$$

The unknown stress increment $d\sigma_{ij}$ is found by linearization or differentiation of the implicit Backward Euler equation (7.69) to:

$$d\sigma_{ij} = D_{ijkl}d\varepsilon_{kl} - d\lambda D_{ijkl} ^{n+1}m_{kl} - \lambda D_{ijkl} \left. \frac{\partial m_{kl}}{\partial \sigma_{mn}} \right|_{n+1} d\sigma_{mn} - \lambda D_{ijkl} \left. \frac{\partial m_{kl}}{\partial q_*} \right|_{n+1} dq_* \quad (7.82)$$

and isolation through simple algebraic manipulations:

$$d\sigma_{mn} = \Xi_{ijmn} D_{ijkl} (d\varepsilon_{kl} - d\lambda \Theta_{kl}) \quad (7.83)$$

where Ξ and Θ are defined in Equation 7.73 and 7.74 respectively. Finally substituting 7.83 into 7.81 gives an expression for the consistent elastoplastic tangent:

$$d\sigma_{pq} = D_{pqmn}^{ep} d\varepsilon_{mn} \quad \text{with} \quad (7.84)$$

$$D_{pqmn}^{ep} = (\Xi_{rspq} D_{rsmn}) \frac{(\Xi_{rspq} D_{rskl}) \Theta_{kl} ^{n+1}n_{ij} (\Xi_{rsij} D_{rsmn})}{^{n+1}n_{ot} (\Xi_{rsot} D_{rspq}) \Theta_{pq} + ^{n+1}\xi_* h_*} \quad (7.85)$$

Box 7.3: Closest point projection algorithm.

1. Initialize: $k = 0$; ${}^{n+1}q^{(0)} = {}^n q$; $d\lambda^{(0)} = 0$.

2. Calculate trial stress and yield function

$$\begin{aligned} {}^{Trial}\sigma_{ij} &= {}^n \sigma_{ij} + D_{ijkl} {}^{n+1}d\varepsilon_{kl} \\ {}^{Trial}f^{(0)} &= f({}^{Trial}\sigma_{ij}^{(0)}, {}^{Trial}q^{(0)}) \end{aligned}$$

3. IF ${}^{n+1}f^{(0)} \leq 0$ THEN EXIT.

4. Calculate starting point and update state variables

$$\begin{aligned} d\lambda^{(0)} &= \frac{{}^{Trial}f}{{}^{Trial}h_{nm} D_{nmpq} - {}^{Trial}m_{pq} - {}^{Trial}\xi_* h_*} \\ {}^{n+1}\sigma_{mn}^{(0)} &= {}^{Trial}\sigma_{mn} - d\lambda^{(0)} D_{mnpq} {}^{Trial}m_{pq} \\ {}^{n+1}q_*^{(0)} &= {}^n q_* + d\lambda^{(0)} h_* \end{aligned}$$

5. DO WHILE ${}^{n+1}f^{(k)} \geq TOL$

a) Calculate yield function ${}^{n+1}f^{(k)}$

$${}^{n+1}f^{(k)} = f({}^{n+1}\sigma_{ij}^{(k)}, {}^{n+1}q^{(k)})$$

b) Calculate derivatives ${}^{n+1}n_{kl}^{(k)}$, ${}^{n+1}m_{kl}^{(k)}$, $\left. \frac{\partial m_{kl}}{\partial \sigma_{mn}} \right|_{n+1}^{(k)}$, and $\left. \frac{\partial m_{kl}}{\partial q_*} \right|_{n+1}^{(k)}$

c) Update plastic multiplier $d\lambda^{(k+1)}$

$$d\lambda^{(k+1)} = d\lambda^{(k)} + \left(\frac{{}^{n+1}f - r_{ij} \Xi_{ijmn} {}^{n+1}n_{mn}}{D_{ijkl} \Theta_{kl} \Xi_{ijmn} {}^{n+1}n_{mn} - {}^{n+1}\xi_* h_*} \right)^{(k)}$$

d) Update stress and state variables

$$\begin{aligned} {}^{n+1}\sigma_{mn}^{(k+1)} &= {}^{Trial}\sigma_{mn} - d\lambda^{(k+1)} D_{mnpq} {}^{n+1}m_{pq}^{(k)} \\ {}^{n+1}q_*^{(k+1)} &= {}^n q_* + d\lambda^{(k+1)} h_* \end{aligned}$$

e) SET $k = k + 1$

END DO

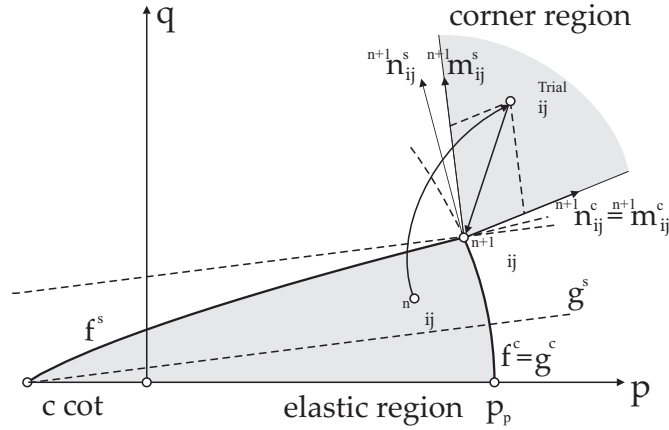


Figure 7.15: Corner problem at the intersection of cone- and cap-type yield surface.

When using an implicit return mapping scheme as the one presented in the previous section, it is only a small effort to calculate the consistent elastoplastic tangent. However, the main drawback associated with the implicit closest point projection algorithm and the calculation of the consistent tangent is their need for the plastic potential's second order gradients. This may prove exceedingly laborious for more complex plastic potentials, but is straightforward in the HS-Small model.

7.4.4 Corner and apex problems

Corner problems arise at non-smooth intersections of yield surfaces, if not a single surface criterion is used (e.g. Ehlers [38]). By substituting the Mohr-Coulomb yield surface of the original HS model, by the smooth Matsuoka-Nakai criterion, some singularities are eliminated in the HS-Small(MN) model. Yet, the intersection of cone and cap-type yield surface still causes a corner problem.

Koiter [91], additively decomposes plastic strain rates in such a corner problem as follows:

$$d\varepsilon_{ij}^p = d\lambda_{cone}^{cone} m_{ij}(\sigma_{ij}, q_*) + d\lambda_{cap}^{cap} m_{ij}(\sigma_{ij}, q_*). \quad (7.86)$$

The two vector cone-cap return problem is illustrated in Figure 7.15. Return mapping in corner regions is slightly more tricky than regular return mapping to one yield surface. Yet, the concepts explained above remain the same. Appendix B gives the updated algorithm for two surface closest point projection.

Another difficulty in corner problems is the estimate of the corner gray region. If the Lode angle is frozen during return mapping (Drucker-Prager potential), and there is no hardening (cone in final position), a two-dimensional analysis can be conducted as shown in Figure 7.15. Otherwise, a strategy that determines to which surface the trial stress is to be returned, is required. The strategy proposed by Bonnier [18] shown in Appendix C is used in the HS-Small implementation.

Chapter 8

Validation and verification of the HS-Small model

The HS-Small model is validated by comparing numerically simulated experimental data to real (measured) data. Model validation is divided into two main parts: Element tests and boundary value problems.

The element tests section strictly speaking also contains partly code verification. Iteratively derived stiffness decay curves are checked against the closed form model by Hardin & Drnevich in the version of Santos & Correia. This is necessary due to the hardening plasticity's impact on total elastoplastic stiffness. For clarification of the differences implied by the terms validation and verification see also Figure 1.2.

All element tests are calculated on the Gauß-Point level. All boundary value problems are analyzed using the finite element code PLAXIS V 8.2 [21]. As the HS-Small model was implemented in the calculation kernel of this code, standard interface definitions and calculation settings could be used. The help and cooperation of Plaxis B.V, especially the help of Dr. Paul Bonnier, during model implementation is greatly acknowledged here. All calculations are performed with triangular elements (6 nodes, 3 integration points) and default settings in the iteration controls of the finite element code PLAXIS.

8.1 Element tests

The element test section as the first part of the verification and validation process of the HS-Small model makes use of triaxial, biaxial and oedometer test data readily available in the literature. Materials considered include dense sand, medium dense to loose sand, and reconstituted Kaolin clay.

Most test data on sand presented in this section are taken from the database compiled by Desrues et al. [31]. This database contains many well documented experiments on Hostun-'RF'-Sand (Hostun sand), an industrial sand quarried near the village of Hostun, Drôme, Rhône-Alpes, France. Hostun sand results from the specification of its sieving process (Flavigny et al. [41]) uniformly graded. Its coefficient of uniformity is $U = \frac{D_{60}}{D_{10}} = 1.70$, where its medium grain size is $D_{50} = 0.35mm$. The minimum and maximum void ratio are experimentally derived as $e_{min} = 0.63$ and $e_{max} = 1.00$. The experimental database distinguishes between dense and loose Hostun sand, based on its initial void ratio e . For initial void ratios in the range of $e = 0.63...0.68$ the sand is classified as dense, whereas in the range of $e = 0.85...0.92$, it is classified as loose. The corresponding

density index, $I_D = \frac{e_{max} - e}{e_{max} - e_{min}}$ calculates to $I_D = 0.87 \dots 1.00$ and $I_D = 0.22 \dots 0.40$ for the dense and loose sand respectively. According to DIN EN ISO 14688-2:2004 [43] the sand should therefore rather be classified very dense and loose to medium dense respectively. However, for the sake of consistency with the database used, its classification as dense and loose is adopted here, too. Beyond the data available in the database by Desrues, test data from the book by Biarez & Hicher [16] is used. In excess of conventional lab data, Biarez & Hicher provide also some small-strain stiffness data in their book.

The Kaolin clay test presented in this section is also taken from the data collection by Biarez & Hicher [16]. Its plasticity index is specified as, $PI = 30$, its liquid limit is $w_l = 70$. Only normally consolidated samples are considered. Unfortunately the test data provided for drained and undrained tests are obtained at very different confining pressures (and hence void ratios). Drained test data are available at confining pressures up to 800 kPa whereas those for undrained tests are available only for confining pressures above 2000 kPa. Here the HS as well as the HS-Small model, both have the shortcoming that the material's void ratio is not considered in the model formulation.

Two separate material data sets have been defined for Hostun sand. In Table D.1, Sand(D) and Sand(L) denote dense Hostun sand and loose Hostun sand respectively. The clay data in Table D.1 describes normally consolidated Kaolin clay at low confining pressures. The undrained Kaolin tests given in Biarez & Hicher [16] are not considered in the following due to their high confining pressures. If not indicated otherwise, the material parameter sets given in Table D.1 are used exclusively in all element tests presented in this section.

Oedometer, or K_0 compression test data for loose and dense Hostun sand are shown in Figure 8.1. The HS as well as the HS-Small model can simulate these tests reasonably well. As expected, the HS-Small model gives a somewhat stiffer response than the original HS model in both tests. The difference is emphasized more for the dense sample due to its higher threshold shear strain $\gamma_{0.7}$. Since both models, HS and HS-Small, cannot predict the accumulation of plastic strain within closed cycles correctly, both models give overall, less deformation compared to the experiment. This effect is more pronounced for the loose sample, which accumulates more plastic strain in closed cycles.

Tracing of the unloading-reloading cycles is nevertheless improved by the HS-Small model, which gives a small amount of hysteresis as also seen in the experiment. From the unloading-reloading loops it can be concluded that the power law exponent $m = 0.55$ chosen for dense Hostun sand is rather high. However, the chosen exponent is also attributed to the triaxial test data shown next.

Drained triaxial test data is shown in Figure 8.2, 8.3, and 8.4 for dense Hostun sand, loose Hostun sand, and normally consolidated Kaolin clay respectively. For the sand tests little experimental small-strain data are available. For the Kaolin clay there is no $p-q$ test data available at these confining pressures where small-strain data are available.

From the right hand side of Figures 8.2, 8.3, and 8.4 it can be concluded that the incrementally (HS-Small) and analytically derived (Santos & Correia) stiffness decay curves match up pretty well. The need for the modification of the HS hardening laws is also illustrated in Figures 8.2, 8.3, and 8.4: A pure combination of the HS model with the Small-Strain Overlay model without modification of the HS hardening laws (HS + Small-

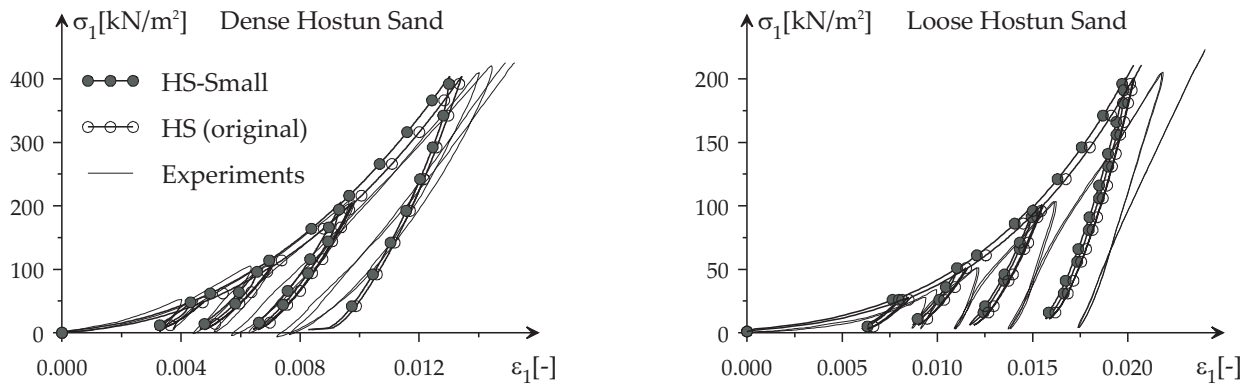


Figure 8.1: Oedometer test on dense (left) and loose (right) Hostun sand.

Strain Overlay) yields too low small-strain stiffness. Here, plasticity is over-dominating the initial elastoplastic stiffness.

It can be noted that there is a small numerical discrepancy between the material input parameter $\gamma_{0.7}$ and the computed shear strain (HS-Small), at which small-strain stiffness is decreased to 70% of its initial value. For practical applications this discrepancy can be easily neglected since it is probably well below the experimental precision and repeatability. Alternatively, the internal model parameter h_i (see Section 7.3.1), could be fitted in an iterative procedure by including it with the internal parameter conversion discussed in Chapter 7. In either case, a perfect match between the HS-Small decay curves and the analytically derived curves is obtained for zero plastic straining. Then, the elastoplastic model degenerates to the Small-Strain Overlay model as presented in Chapter 6.

Altogether, the simulated triaxial tests match the test data presented, reasonably well. It turns out that the modified flow rule has a vanishing effect on the volumetric behavior in drained tests. This will be proven to be different for undrained tests later in this section.

The implementation of the Small-Strain Overlay model into the HS-Small model does not overly affect the overall stress-strain curve. There is no over-pronounced shift or bump in the stress-strain curve. Combining the Small-Strain Overlay model with a bubble model, or any other model that has an initial elastic range would probably not give such smooth results.

In oedometer and triaxial tests the intermediate stress parameter b always equals 0. Both failure criteria used in the HS-Small model, Mohr-Coulomb (MC) and Matsuoka-Nakai (MN), are coincident in this case. For this reason, there has so far been no distinction made towards the HS-Small model's failure criteria in the validation process. In biaxial tests (plane strain), however, the non-zero intermediate stress parameter increases the material strength estimate of the Matsuoka-Nakai criterion compared to that of the Mohr-Coulomb criterion.

Figures 8.5, and 8.6 show biaxial test results for dense and loose Hostun sand respectively. As expected, the HS-Small model with the Matsuoka-Nakai yield criterion

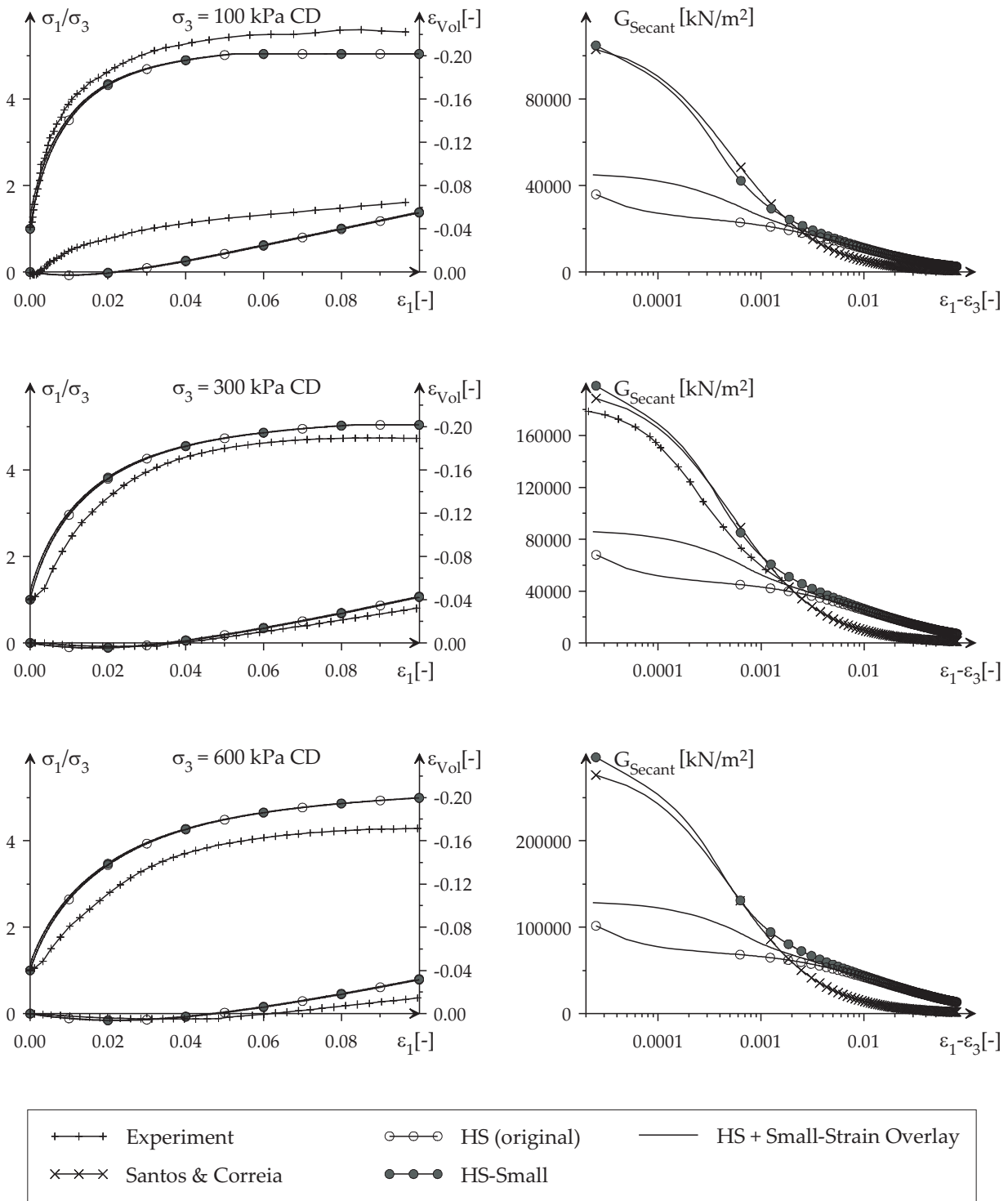


Figure 8.2: Drained triaxial tests on dense Hostun sand at confining pressures of 100, 300, and 600 kPa. Left: Stress-strain data. Right: Shear modulus reduction.

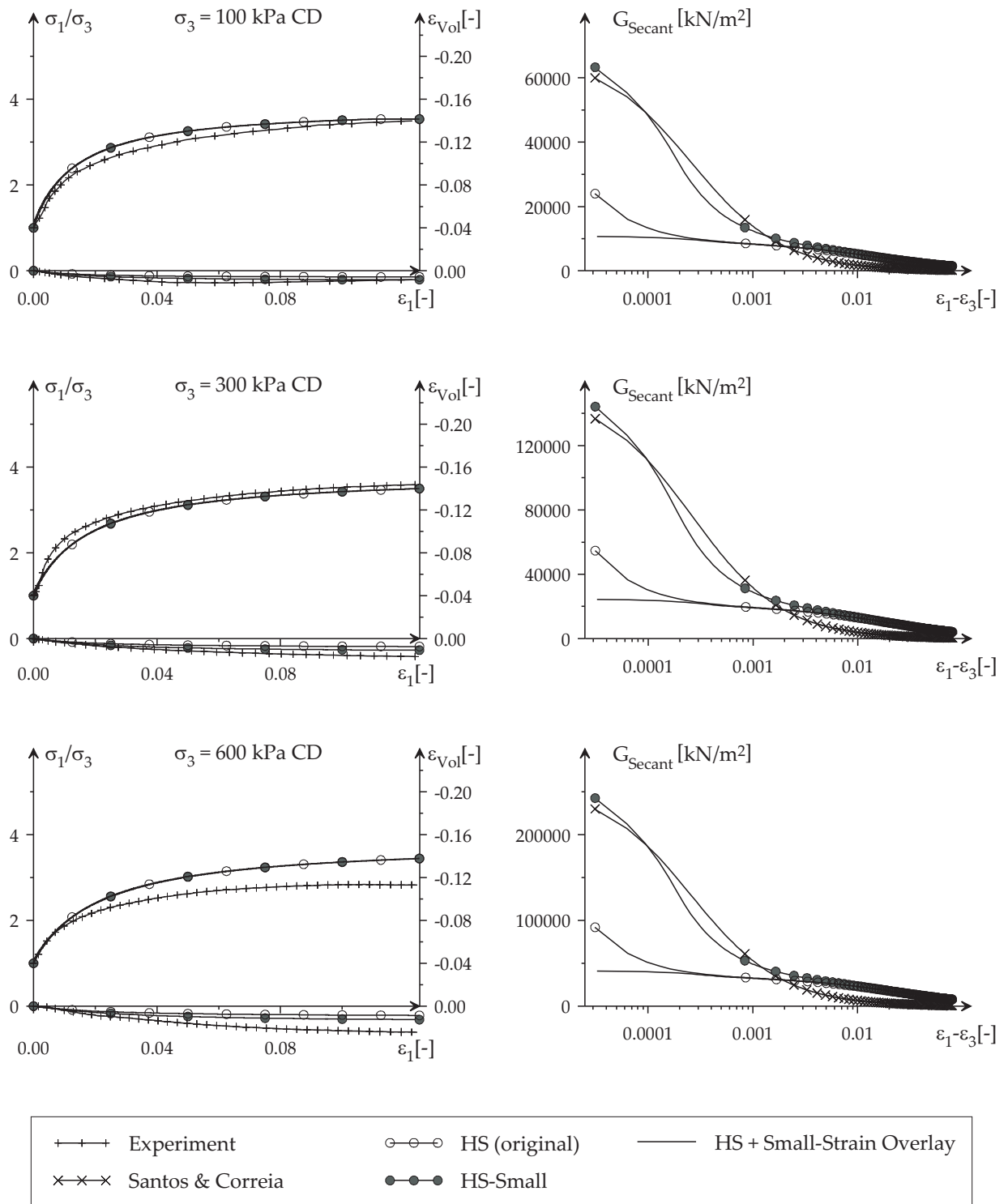


Figure 8.3: Drained triaxial tests on loose Hostun sand at confining pressures of 100, 300, and 600 kPa. Left: Stress-strain data. Right: Shear modulus reduction.

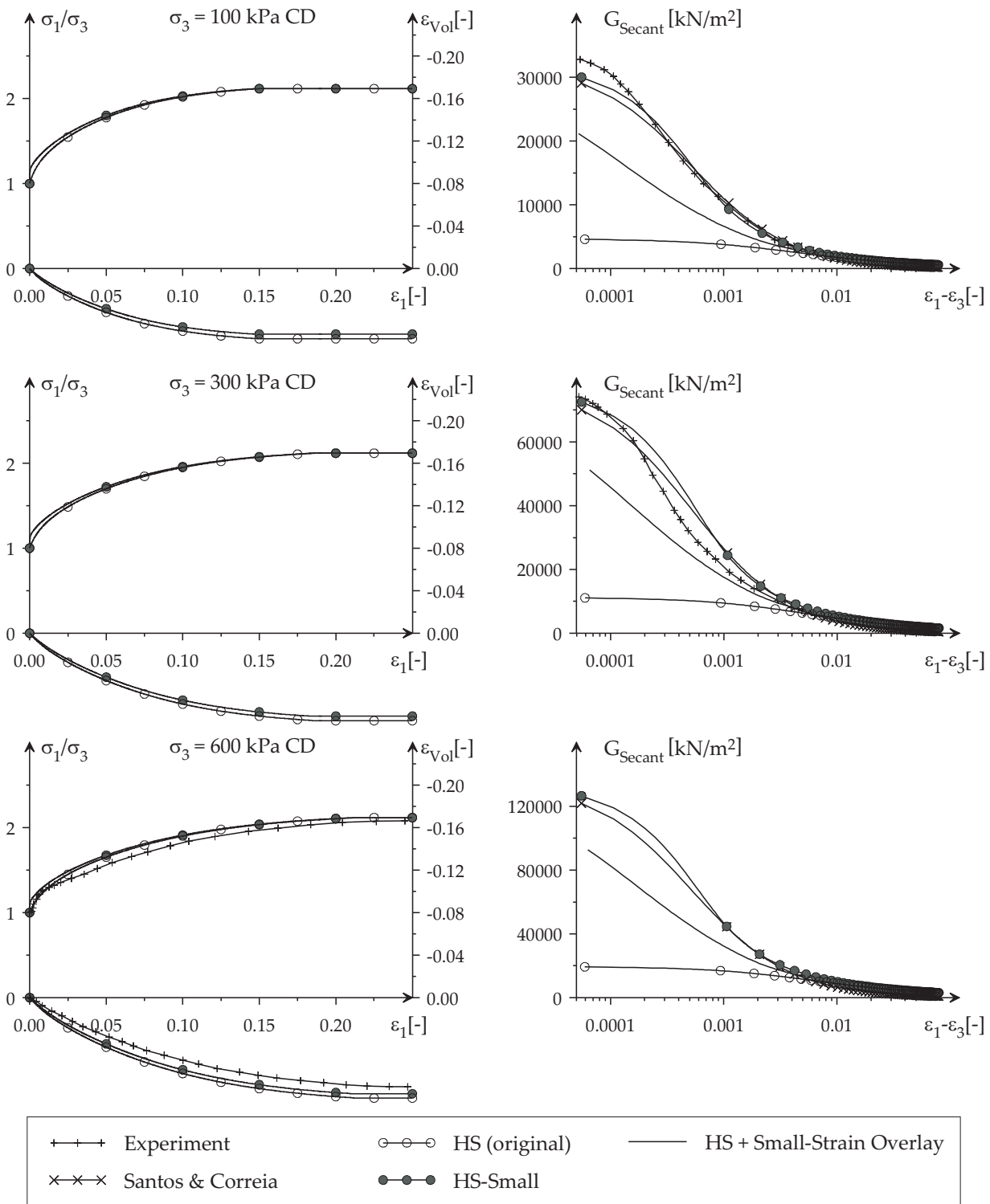


Figure 8.4: Drained triaxial tests on reconstituted Kaolinite clay at confining pressures of 100, 300, and 600 kPa. Left: Stress-strain data. Right: Shear modulus reduction.

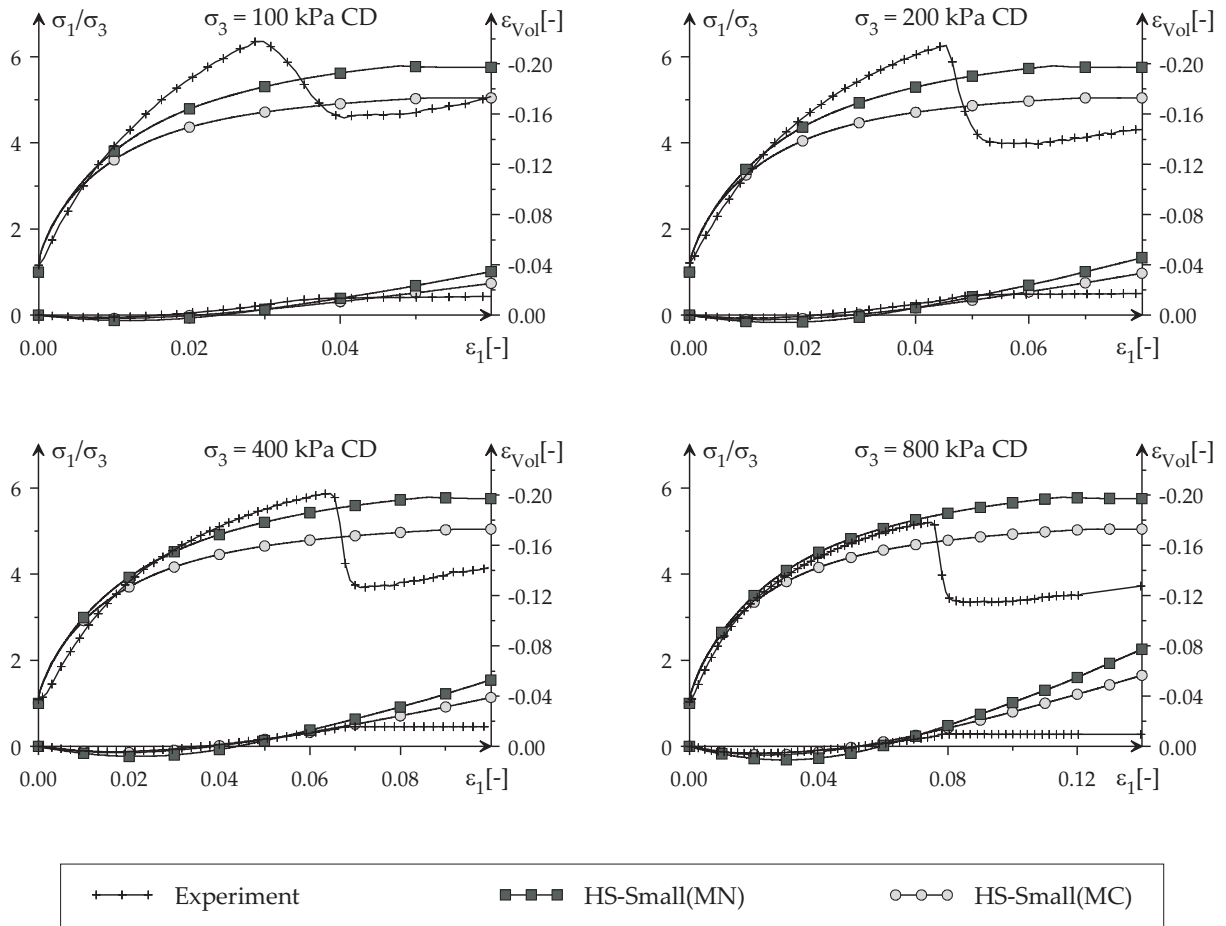


Figure 8.5: Drained biaxial tests on dense Hostun sand at confining pressures of 100, 200, 400, and 800 kPa.

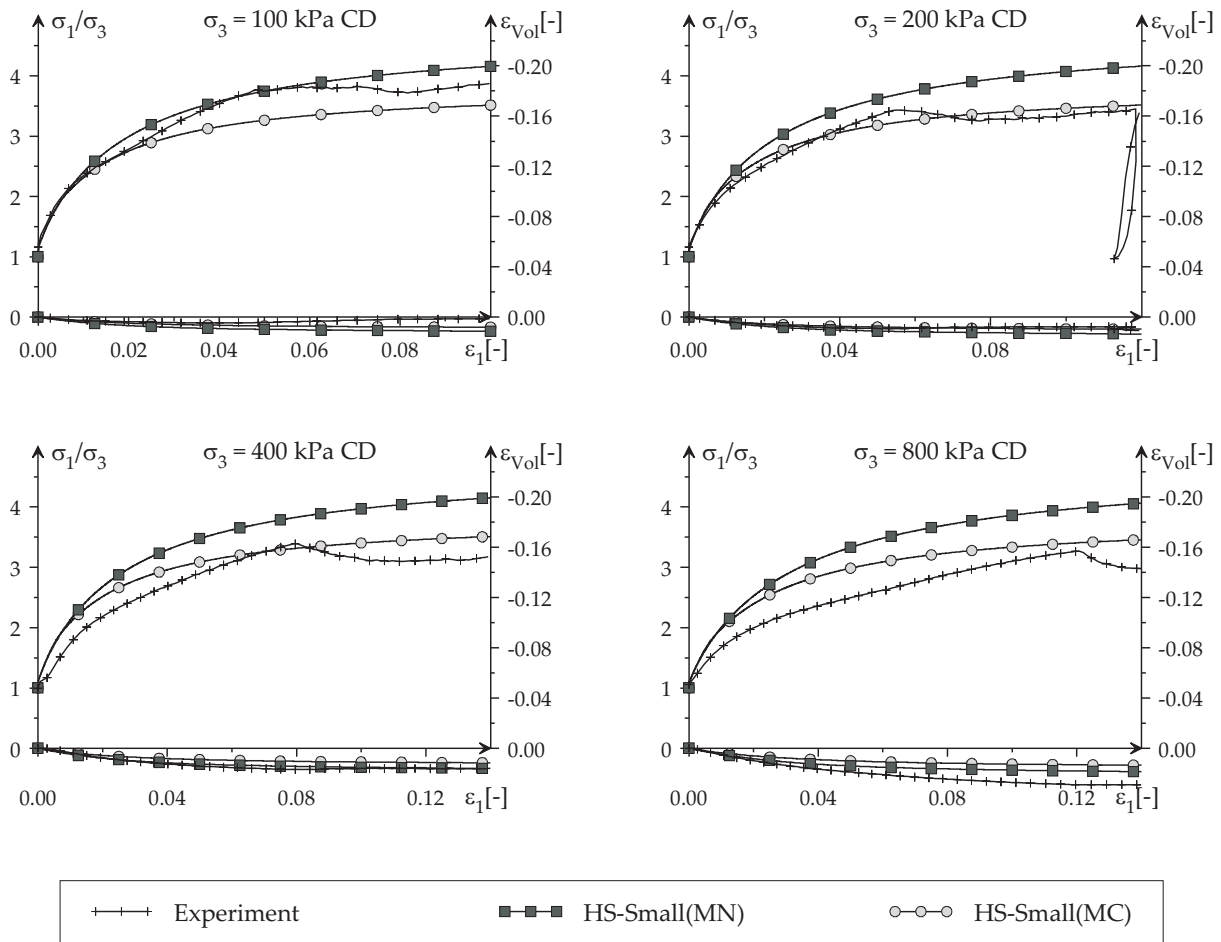


Figure 8.6: Drained biaxial tests on loose Hostun sand at confining pressures of 100, 200, 400, and 800 kPa.

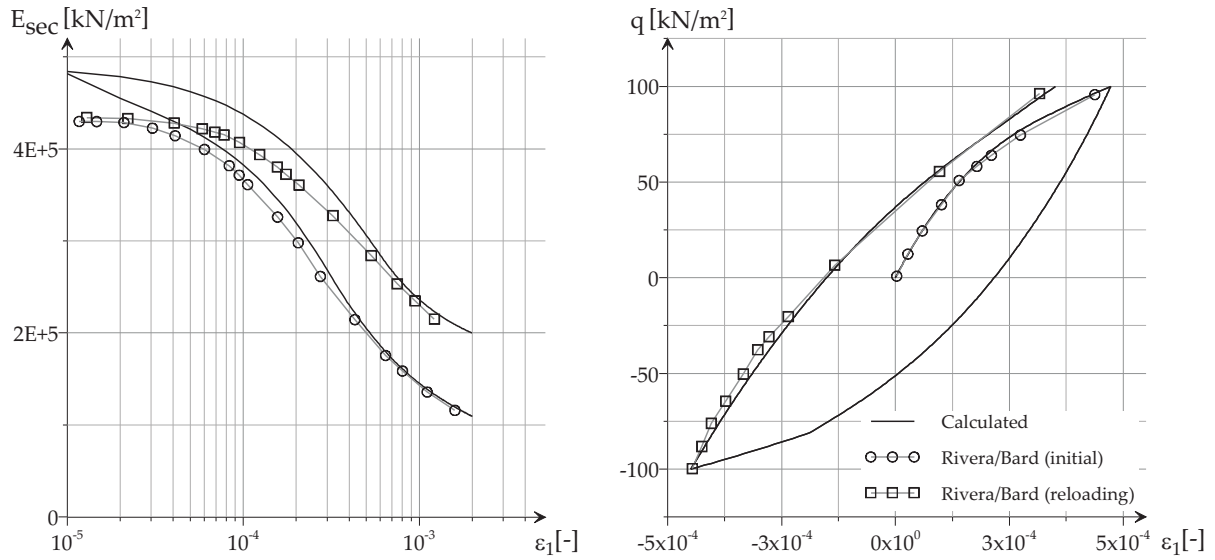


Figure 8.7: Hysteresis loop in a drained triaxial test on dense Hostun sand.

(HS-Small(MN)) always predicts higher peak strengths than the model with the Mohr-Coulomb yield criterion (HS-Small(MC)). The test data fully validates the Matsuoka-Nakai approach for dense sand whereas for loose sand the strength is slightly over-predicted. Here it seems that bifurcations set in even before the limit state according to the Matsuoka-Nakai criterion is reached.

The element tests presented in Figures 8.7, 8.8, and 8.9 recapitulate some of the tests already presented and introduced in Chapter 6. Now, the HS-Small and the original HS model are evaluated in these tests instead of the pure Small-Strain Overlay model.

The initial stiffness in Figure 8.7 is slightly over-predicted since the standard material set for dense Hostun sand given in Table D.1 is used. The calculated hysteresis loop is not closed anymore because of too much unloading plasticity. Here, as for other cyclic phenomena as well, kinematic hardening formulations should be used rather than purely isotropic hardening models. Nevertheless, the hysteresis loop is simulated not too badly by the (isotropic hardening) HS-Small model.

Figures 8.8, and 8.9 show numerical simulations of the tests by Richardson [148] on reconstituted London clay. The London clay could be reasonably modeled with the data set defined for Kaolin clay by slightly reducing the initial stiffness to $G_0^{\text{ref}} = 26$ MPa and increasing the unloading-reloading stiffness to $E_{\text{ur}}^{\text{ref}} = 21$ MPa ($E_{50}^{\text{ref}} = E_{\text{oed}}^{\text{ref}} = 7$ MPa). Again, there is no difference between the Matsuoka-Nakai and the Mohr-Coulomb flavor of the HS-Small model as $b = 0$. The improvement achieved by using the HS-Small model is obvious. However, a pronounced distinction between stress paths AOX and COX is missing. The HS-Small model tracks the difference in these stress paths by means of different overconsolidation pressures p_p only. It does not track the second main difference between these stress paths, which is the material's void ratio at the start of devi-

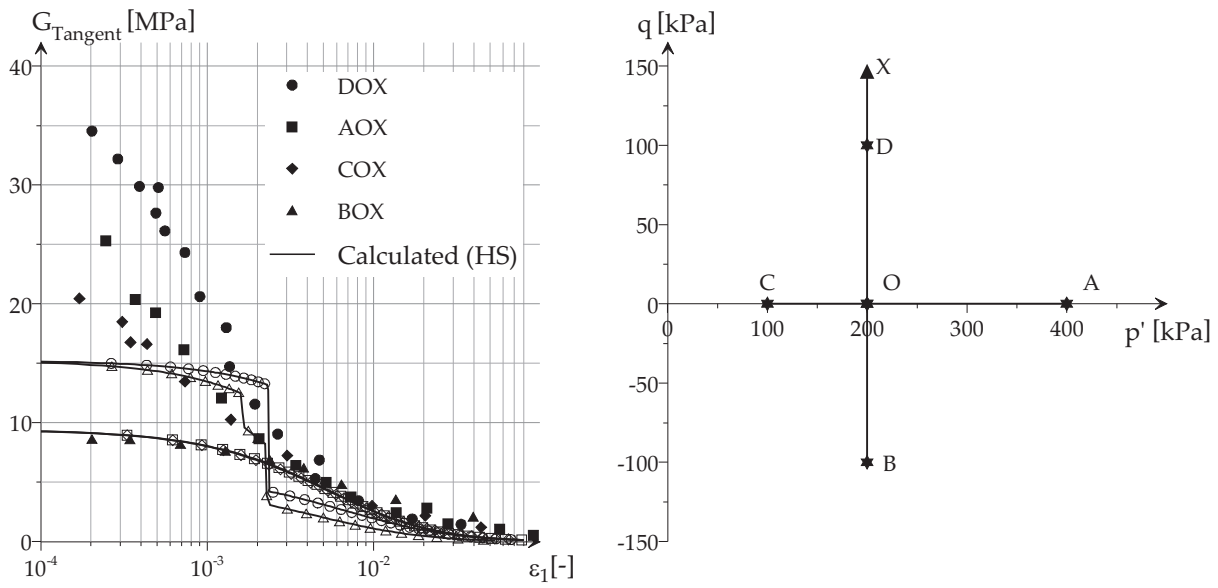


Figure 8.8: HS model predictions for Richardson's [148] tests.

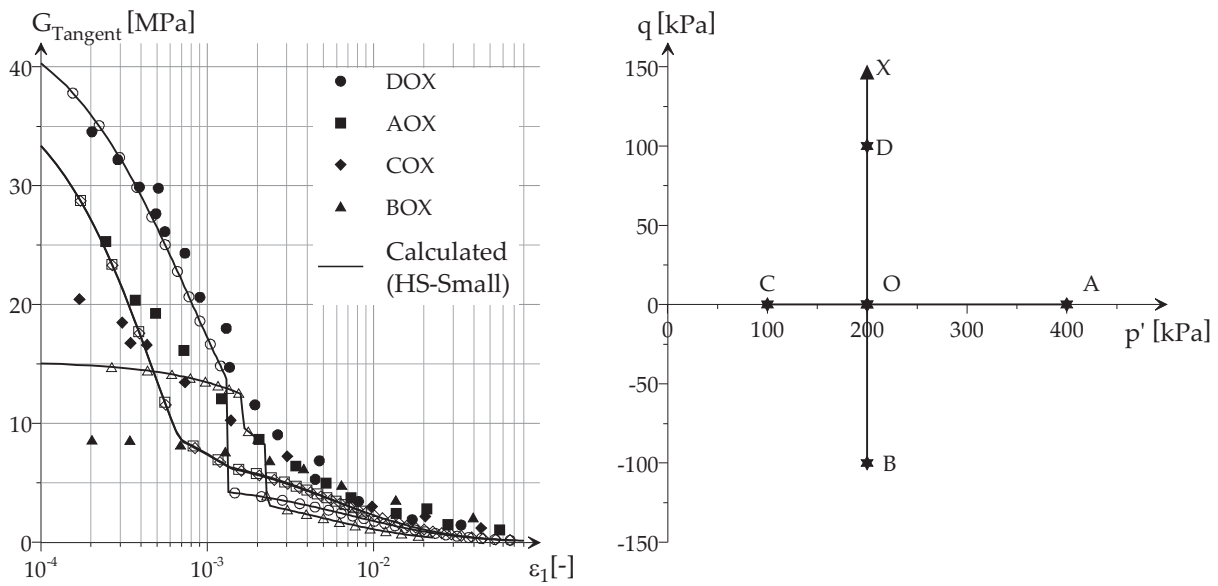


Figure 8.9: HS-Small model predictions for Richardson's [148] tests.

atoric loading. The effect of p_p in $p' = \text{constant}$ loading is negligible.

After having validated the small-strain formulation and the yield criteria of the HS-Small model it remains to evaluate its modified flow rule. As mentioned before, the effects of the modified flow rule in drained conditions are negligible. However, they are not negligible in undrained conditions. Undrained triaxial tests on dense and loose Hostun sand are shown in Figures 8.10, and 8.11 respectively. These Figures include results from all dilatancy modifications discussed in Section 7.3.2.

The undrained test on dense Hostun sand (Figure 8.10) clearly points out the difficulties in using Rowe's formulation for dilatant materials in undrained conditions. Rowe's decoupling of dilatancy and void ratio may lead to notable overestimates in undrained shear strength. Such calculations should thus include a dilatancy cut-off (as optionally available in the HS-Small model), if not a more refined flow rule is available.

Figure 8.11 shows undrained triaxial tests on loose Hostun sand. Here the advantage of the modified flow rule is clearly visible. The overestimated undrained strength from the original HS model is now reduced to the experimentally derived results. The modified flow rule of the HS-Small model does not incorporate additional material parameters. It rather uses a default set of material parameters. Therefore, the results for other materials may not be always in such close agreement to experimentally derived strength values. Finally it should be noted that none of the flow rules considered reproduces the experimentally derived stress path particularly well. Reason for that is again their void ratio independent formulation.

In summary, the validation of the HS-Small model in element tests gave mostly positive results. In comparison to the original HS model, only improvements were found. The lack of void ratio dependency and kinematic hardening have been identified as the main drawbacks of the HS-Small model as well as of the HS model.

8.2 Boundary value problems

In the second part of the model validation process, a set of five boundary value problems is examined. The set of boundary value problems includes two tunnels, two deep excavations and one spread footing foundation. Though model validation, through the comparison of simulated results with experimentally derived results is the main focus of this section, more general issues will also be addressed. These include general finite element issues (i.e. What section of the problem should be meshed?), as well as more specific small-strain stiffness matters (i.e. What impact has small-strain stiffness on different problem classes?).

In the literature, tunnels are probably the most popular examples for validating small-strain stiffness models. In appreciation of that fact, the first problems discussed in this section are tunnelling problems. Secondly, deep excavations will be looked at before the section is closed with a very basic spread footing foundation example.

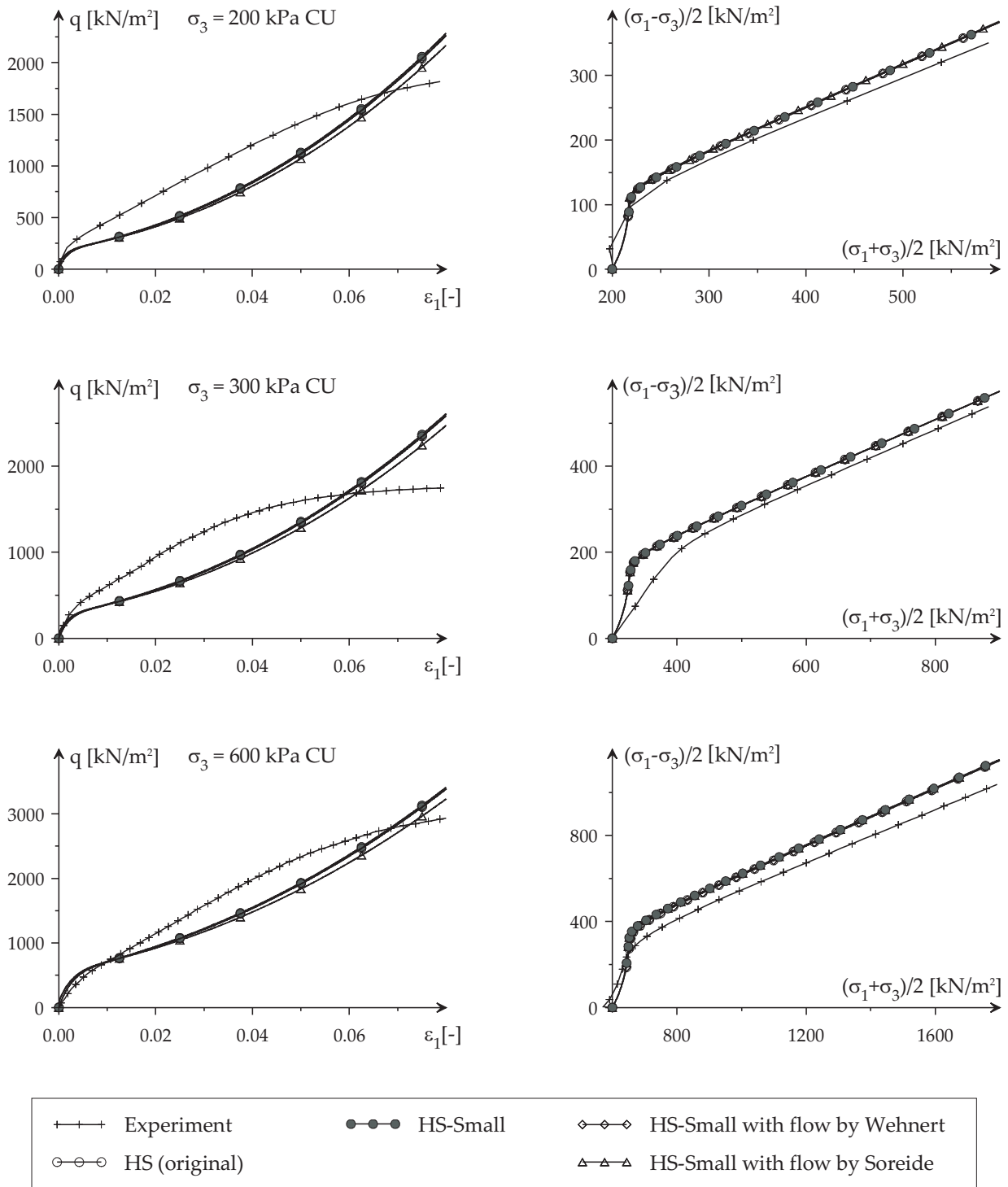


Figure 8.10: Undrained triaxial tests on dense Hostun sand at confining pressures of 200, 300, and 600 kPa. Left: Stress-strain data. Right: s-t diagram.

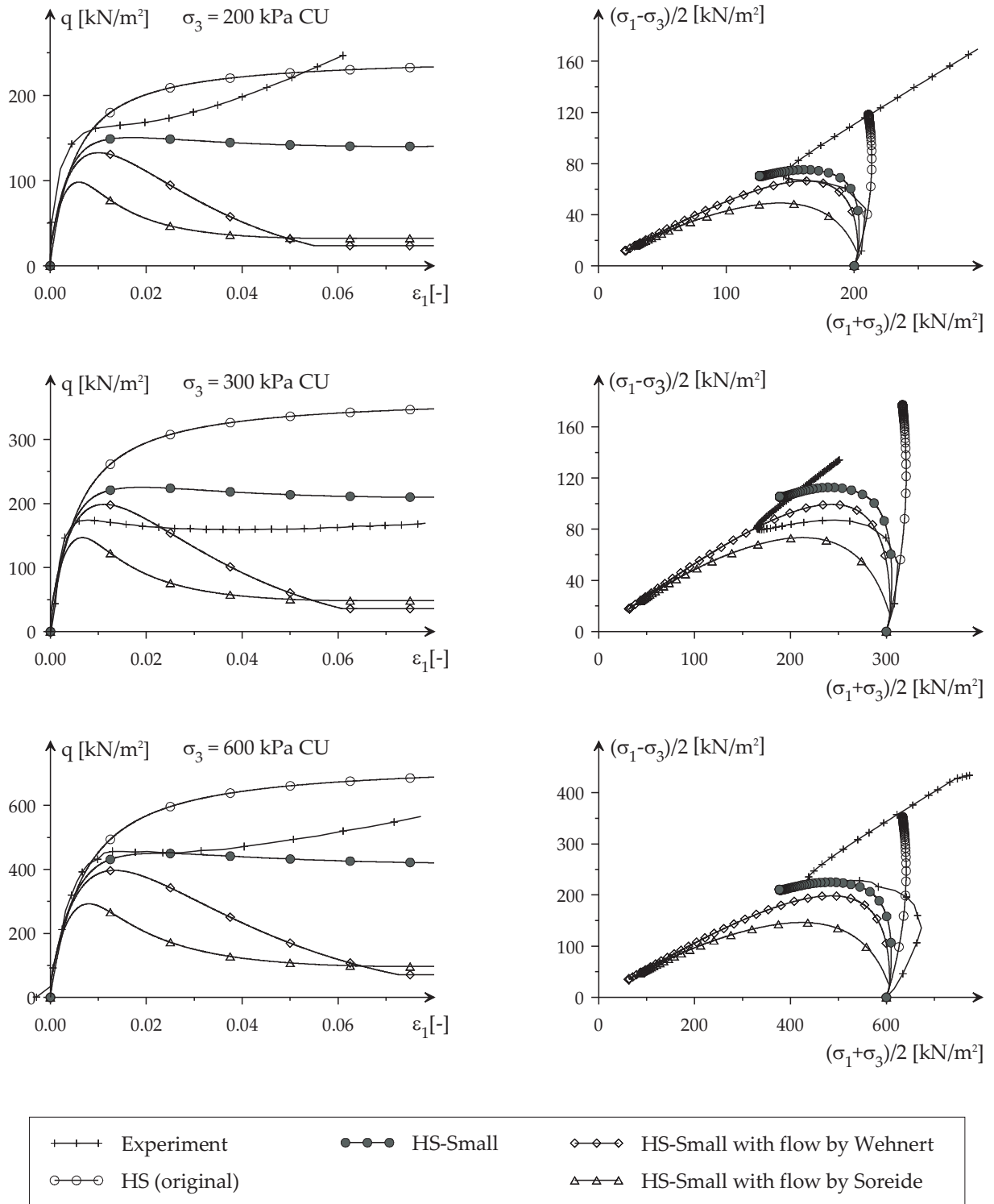


Figure 8.11: Undrained triaxial tests on loose Hostun sand at confining pressures of 200, 300, and 600 kPa. Left: Stress-strain data. Right: s-t diagram.



Figure 8.12: Steinhaldenfeld NATM tunnel before concreting the inner liner.

8.2.1 Tunnels

Schmidt [160] and Peck [135] were the first to propose that green field settlement troughs above tunnels can be approximated by a (Gaussian) distribution function of the form:

$$s(y) = s_{max} \exp\left(-\frac{y^2}{2i^2}\right) \quad (8.1)$$

where s_{max} is the maximum vertical settlement above the tunnel axis, y is the horizontal distance to the tunnel axis, and i is the horizontal distance of the settlement trough's inflection point from the tunnel axis.

The empirical relationship expressed in Equation 8.1 holds very well, independent of the applied tunnelling method. Numerical methods often fail in predicting the correct shape of settlement troughs. Especially, if the applied soil model does not account for small-strain stiffness, numerical methods commonly predict too flat and wide settlement troughs. This can be observed for instance in the following two case studies, where the HS-Small model yields significantly improved results compared to the HS model.

8.2.1.1 Steinhaldenfeld NATM tunnel

Figure 8.12 shows Steinhaldenfeld tunnel, a tunnel near Stuttgart that is constructed using the new Austrian tunnelling method (NATM). The soil layers together with the FE mesh used in the plane strain analysis of Steinhaldenfeld tunnel are shown in Figure 8.13. The lower soil layers (Keuper marl and Limestone) are overconsolidated. The overconsolidation ratio is assumed to be 2.0. The material behavior is drained in all the soil layers. A complete list of the soil layer's material parameters used in the calculation is given in Table D.2.

The weak marl around the tunnel excavation was improved by rock bolts during the NATM construction process. The strength increase due to rock bolting is modeled by

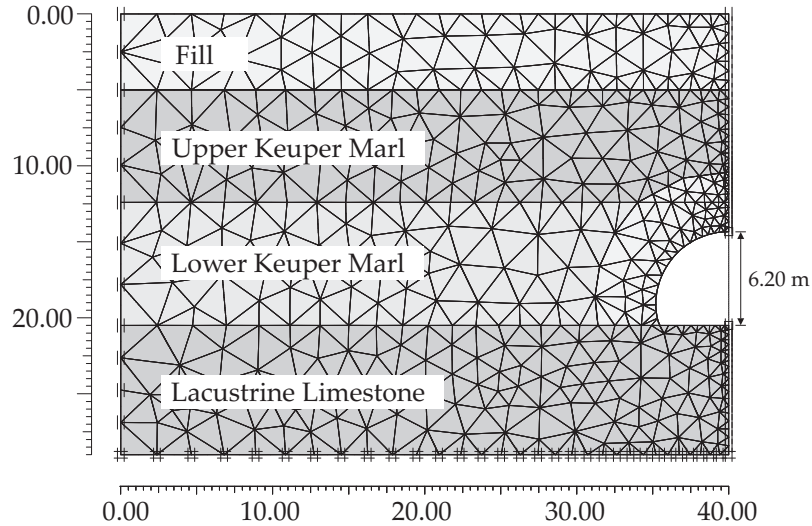


Figure 8.13: Steinholdenfeld NATM tunnel: 2D mesh and soil layers.

introducing additional cohesion of 25 kPa in the bolted area. The tunnel's linear elastic lining plate elements have a stiffness of $EA = 3.75 \cdot 10^6$, a flexural rigidity of $EI = 1.95 \cdot 10^4$, a Poisson's ratio of $\nu = 0.2$, and a unit weight of $\gamma_C = 25 \frac{kN}{m^3}$.

The meshed problem area below the tunnel is relatively small since the Limestone is much stiffer than the overlaying marl. For the mesh boundaries it is generally proposed here to require the stiffness multiplier:

$$G_m \geq 0.8 \frac{G_0}{G_{ur}} \quad (8.2)$$

in the mesh's outermost stress points (at boundaries). For a definition of the stiffness multiplier G_m refer to Section 7.3.1.

For the numerical analysis of Steinholdenfeld tunnel, the stress reduction method is adopted. Using this method, the tunnel excavation remains unsupported by the lining till, an artificial support pressure βp_0 is reached, where p_0 is the initial rock mass pressure before excavation. Then, the tunnel lining is activated and the support pressure is removed completely. The factor $0 < \beta < 1$ is called the load reduction factor.

Figure 8.14 shows results of the numerical analysis. The settlement trough calculated by the HS-Small model is clearly steeper and more accurate compared to that calculated by the original HS model. The remaining discrepancy to the measured settlement trough can possibly be explained by the inadequateness of 2D analysis for 3D problems. Also the small-strain stiffness parameters could be underestimated because they are based solely on literature data and correlations. Set 2 in Figure 8.14 therefore indicates the changes in settlement from a 40 percent increase of the initial stiffness, displayed in Table D.2 (Set 1). The failure criterion (Mohr-Coulomb or Matsuoka-Nakai) has almost no influence on the shape of the settlement trough. However, it has an influence on the load reduction factor. This is chosen so that in all calculations the settlement directly above

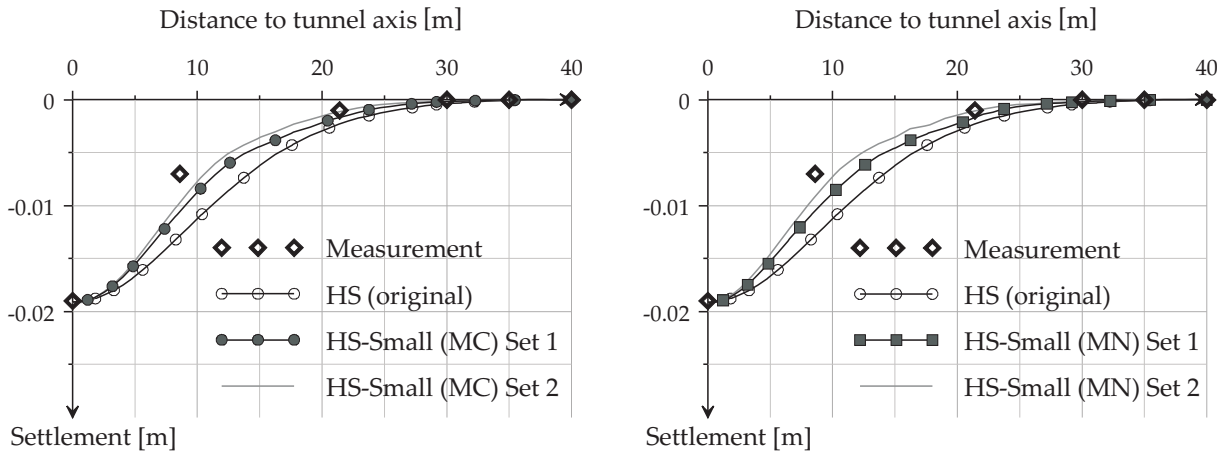


Figure 8.14: Green field settlement trough due to construction of Steinhaldenfeld NATM tunnel. Left: HS-Small(MC) prediction. Right: HS-Small(MN) prediction.

the tunnel axis agrees with the measurement. It is found that the load reduction factor is highest for the HS model $\beta = 0.36$, followed by the HS-Small(MC) model $\beta = 0.32$, and the HS-Small(MN) model $\beta = 0.25$. Unfortunately the load reduction factor cannot be experimentally derived. The difference in the calculated factors is however reasonable: The Matsuoka-Nakai criterion yields the highest strength and stiffness in the given plane strain conditions; its load reduction factor should therefore be least.

8.2.1.2 Heinenoord Tunnel

The second Heinenoord tunnel, south of Rotterdam is a shield tunnel project in largely sandy soils. Figure 8.15 shows the finite element mesh, used in the following plane strain analysis. Figure 8.15 depicts also the different soil layers, for which Table D.3 provides HS material parameters based on the work by Bakker [10]. Drained material behavior is assumed in all soil layers. The lining of the second Heinenoord tunnel is modeled by linear elastic plate elements with $EA = 3.75 \cdot 10^6$, $EI = 1.95 \cdot 10^4$, $\nu = 0.2$, and $\gamma = 25 \frac{kN}{m^3}$.

Several numerical simulation methods for the analysis of shield tunnels can be found in literature. An overview of these methods is given in Möller [121]. Möller concludes that the pressure method is the most suited for shield tunnels. Here, the tunnel excavation is supported by a predefined grout pressure between soil and lining. This pressure is lowest at the top of excavation p_{roof} and increases linearly with depth by the grout's unit weight, which is in the following assumed to $\gamma = 15 \frac{kN}{m^3}$.

Figure 8.17, and 8.16 depict numerical analysis results for the second Heinenoord tunnel employing the pressure method. Again, there is no markable difference in the settlement trough for the two available yield criteria (Mohr-Coulomb, and Matsuoka-Nakai), although there is a difference in material strength. In all analyses, the roof pressure p_{roof} is chosen so that the maximum settlement is in close agreement with the measurement in the tunnel axis. Doing so, the least roof pressure of 125 kPa is obtained from the HS-

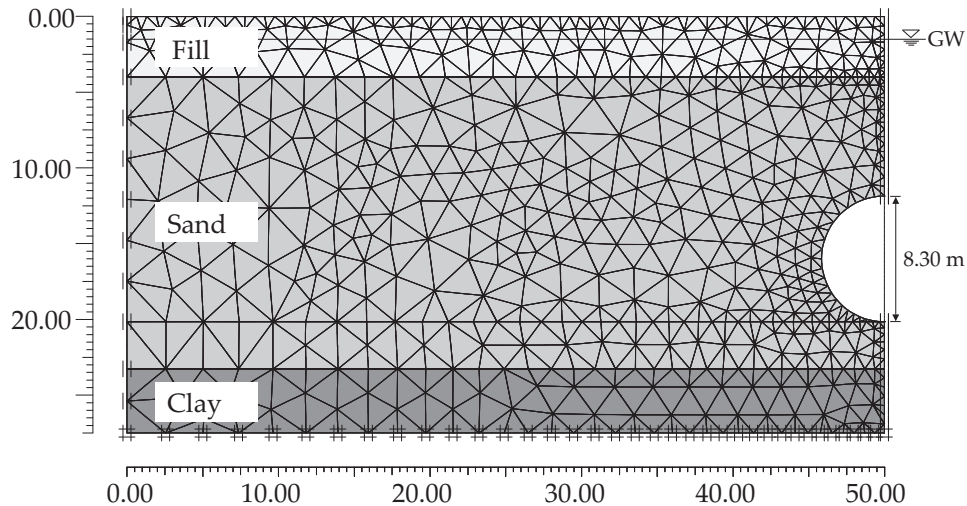


Figure 8.15: Second Heinenoord tunnel: 2D mesh and soil layers.

Small(MN) analysis for its highest strength and stiffness. The highest roof pressure of 130 kPa is obtained in the analysis using the HS model, in between is the HS-Small(MC) analysis with a pressure of 129 kPa. All pressures seem very reasonable as they are of the same size as the overburden pressure.

The Inclinator measurements (Figure 8.16) at a distance of 6, 10, and 16 meters from the tunnel axis, as well as the surface settlement troughs (Figure 8.17) underline again the HS-Small model's improved precision in displacement analysis. The HS-Small model is not perfect though. The Inclinator measurement at a 6 meter distance from the tunnel axis show a somewhat different characteristic to the calculated one. Nevertheless, the decay of displacement with distance from the tunnel axis is modeled nicely. This is entirely due to the new small-strain formulation. The choice of failure criterion, besides its influence on the total material stiffness (see roof pressure), has a negligible effect on the calculated strain distribution.

Due to missing experimental data, the two tunnel examples presented above are not suited to validate the HS-Small model completely. However, it can be concluded that the HS-Small model can improve displacement analysis considerably by causing a diffuse strain localization around the tunnel excavation. Möller [121] comes to a similar conclusion in his work, in which he additionally considers different simulation methods and 3D approaches in the two tunnel examples.

8.2.2 Excavations

Simpson introduced his brick model in a case study of the British Library deep excavation. The House of Parliament underground car park case study is another deep excavation study, that is often cited along with small-strain stiffness. The tilt of Big Ben clock tower right next to this excavation illustrates nicely the effects of advanced (small-strain

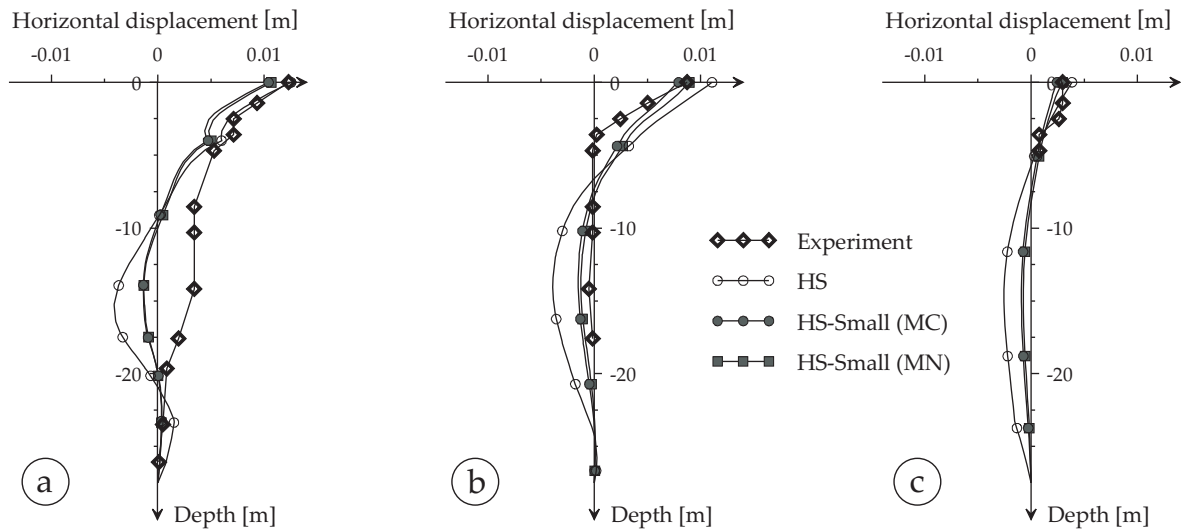


Figure 8.16: Results from Incliner measurements next to the second Heineoord tunnel. Horizontal displacements are displayed at a distance of (a) 6 m, (b) 10 m, and (c) 16 m from the tunnel axis.

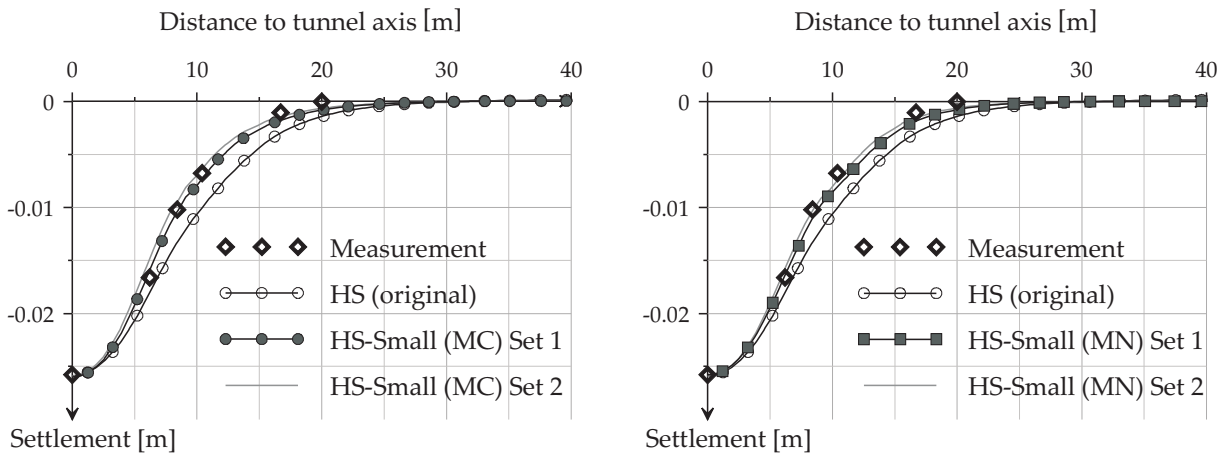


Figure 8.17: Green field settlement trough due to construction of the second Heineoord tunnel. Left: HS-Small(MC) prediction. Right: HS-Small(MN) prediction.

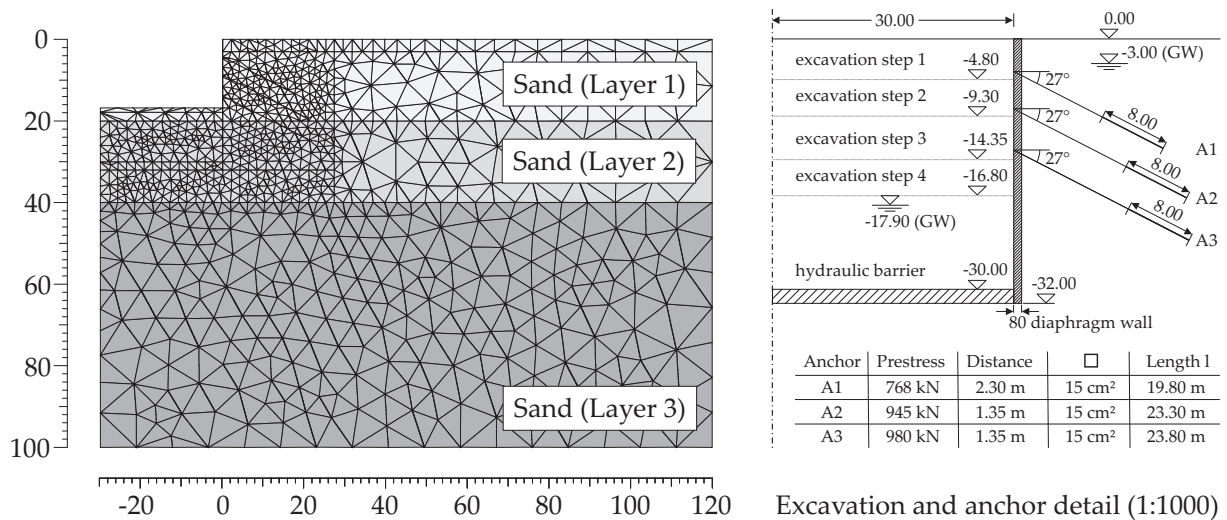


Figure 8.18: Excavation in Berlin sand: 2D mesh and geometry detail (right).

stiffness) models. These can predict the total excavation heave more correctly and thus do not suggest that the clock tower tilts away from the pit, which less refined models may do. Beyond the constitutive model however, there are many more things to consider in the analysis of deep excavations, for example; the interface between soil and retaining structure, initial stress conditions, structural elements, time effects, and pore water pressures. Some of these issues should always be thoroughly considered in excavation analysis (interface, initial stresses, structural elements), others are less critical in less difficult soil conditions. Two examples with less critical soil conditions are chosen for the validation process of the HS-Small model: An excavation in Berlin sand and an excavation in Rupel boom clay.

8.2.2.1 Excavation in Berlin sand

The working group 1.6 Numerical methods in Geotechnics of the German Geotechnical Society (DGGT) has organized several comparative finite element studies (benchmarks). One of these benchmark examples is the installation of a triple anchored deep excavation wall in Berlin sand. The reference solution by Schweiger [161] is used here as the starting point for the next validation example: Both, the mesh shown in Figure 8.18, and the soil parameters given in Table D.3 are taken from this reference solution. However, the bottom soil layer defined by Schweiger could be omitted in the analysis when using the HS-Small model. In the reference solution this layer's only purpose is the simulation of small-strain stiffness due to a lack of small-strain stiffness constitutive models back then.

Figure 8.19, and 8.20 show results from the finite element calculation using the HS-Small(MC), and HS-Small(MN) model respectively. The original reference solution is calculated with the HS model (Figure 8.19, Table D.4). A second 'reference' solution utilizing the HS model with Matsuoka-Nakai failure criterion, but no small-strain stiffness

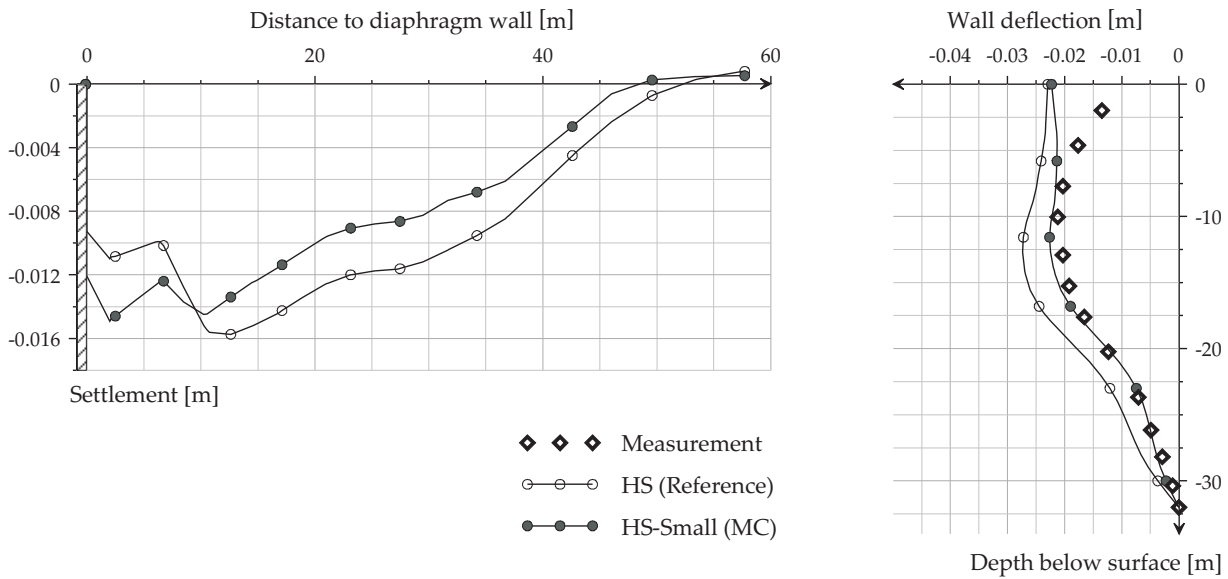


Figure 8.19: Excavation in Berlin sand. HS-Small(MC) model predictions versus measured displacements after the final excavation step. Left: Surface settlement trough. Right: Lateral wall deflection.

formulation (HS(MN)) is shown in Figure 8.20. From the comparison of HS-Small results with the reference solutions, the impact, which a) the small-strain stiffness, and b) the failure criteria have can now be derived.

The small-strain stiffness formulation accumulates more settlements right next to the wall, whereas the settlement trough is smaller. The triple anchored retaining wall is generally deflected less when using the two HS-Small models. The deflection calculated by the HS-Small(MC) almost fits that measured. The Matsuoka-Nakai criterion in the HS-Small(MN) model gives less displacements compared to the Mohr-Coulomb criterion. In comparison to the measured wall deflection, the HS-Small(MN) model even gives lower displacements. However, this might be related to the problem's original reference solution. The chosen parameters are most likely partly back-analyzed from HS model calculations. In this case the Mohr-Coulomb strength parameters already include an increase for plane strain conditions. Additionally increasing the strength by using the HS-Small(MN) model may thus overdo things.

Calculated excavation heaves at the end of excavation are shown in Figure 8.21. The heave, which is due to elastic unloading, is roughly halved when using the HS-Small models, independent of the failure criterion chosen. From Figure 8.21 it can be further concluded that the meshed problem area is not quiet sufficient in the example since the heave is not asymptotically decaying to zero. Figure 8.22 verifies in this respect the criterion proposed in Equation 8.2. The monotonic stiffness multiplier G_m at the end of excavation is well below 3 at the lower mesh boundary.

However, defining the mesh boundary in a depth of 2-3 times the excavation width as

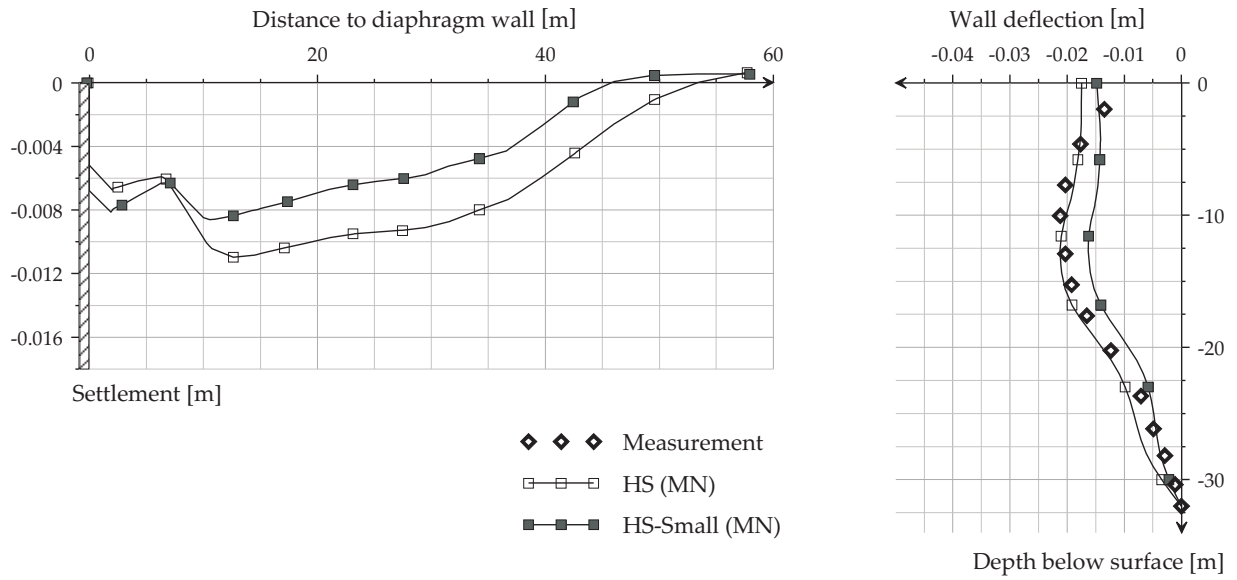


Figure 8.20: Excavation in Berlin sand. HS-Small(MN) model predictions versus measured displacements after the final excavation step. Left: Surface settlement trough. Right: Lateral wall deflection.

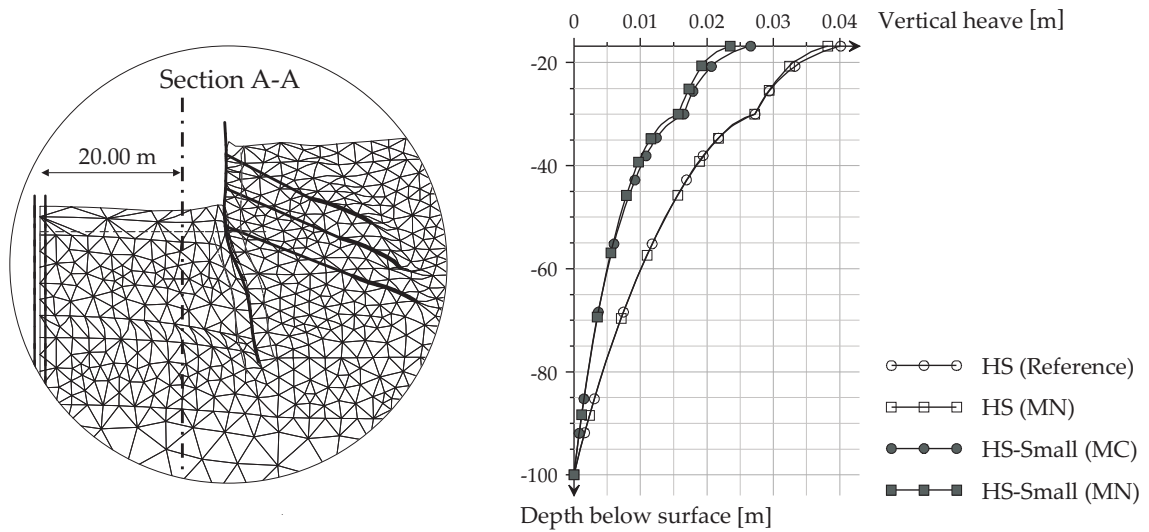


Figure 8.21: Excavation in Berlin sand: Vertical displacements in the excavation pit at a distance of 10 m from the retaining wall.

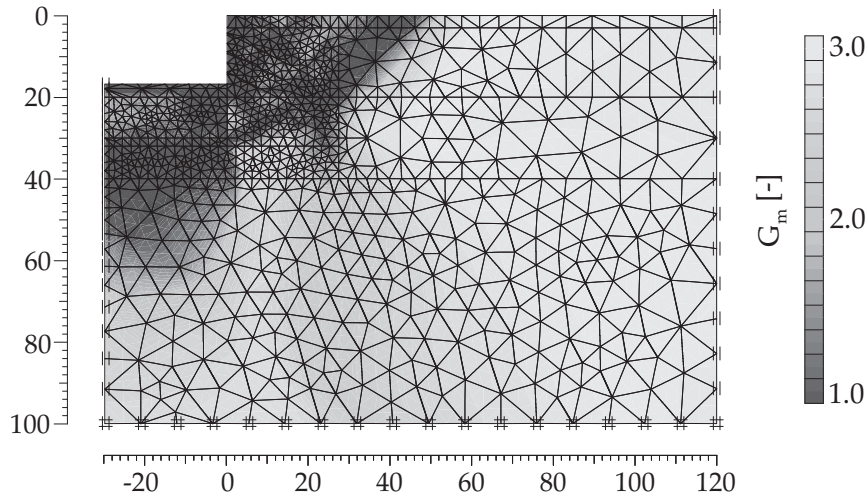


Figure 8.22: Excavation in Berlin sand: Factorized increase of unloading/ reloading stiffness at the end of excavation.

proposed by the AK 1.6, and seen in the reference solution by Schweiger, seems reasonable, too. The error in the excavation heave is relatively small. A mesh according to the requirements of the criterion defined in Equation 8.2 is used in the next example of an excavation in Ruple clay.

8.2.2.2 Excavation in Ruple clay (Offenbach)

Figure 8.23 shows the geometry of an excavation in Offenbach. Similar to the well known subsoil conditions of the neighboring town Frankfurt, the predominant soil here is here a highly overconsolidated clay. Different to Frankfurt clay, the Rupel clay is a oligocene clay, with no solid rock intrusions. Besides the excavation's geometry and measurement data, Krajewski [95] also published a material parameter set for Rupel clay that can be used together with the HS model. The published material parameters have been obtained by back-analysis of lab experiments and a large hopper, built at a neighboring chemical plant. Due to the axisymmetric conditions of all back-analyzed experiments, it can be assumed that the parameter set given is not adjusted for plane strain conditions (as it might have been the case in the Berlin sand excavation). Again, there is no small-strain stiffness testing data available. The parameter set given in Table D.5 is therefore supplemented by correlated small-strain stiffness data. Figure 8.24 shows the 2D plane strain mesh used in the numerical analysis of the excavation.

The retaining wall in the example is a bored pile wall with pile diameter $r = 0.90m$ and axial distance $d = 1.30m$. The struts are IPBs 340 and IBPs 360 with a clearance of 2.45 m, 1.95 m, and 1.80 m in the top, second, and third strut layer respectively.

The Rupel boom clay has an overconsolidation ratio (OCR) well above 2. Using the relationship

$$K_0^{oc} = (1 - \sin \varphi)(OCR)^{\sin \varphi} \quad (8.3)$$

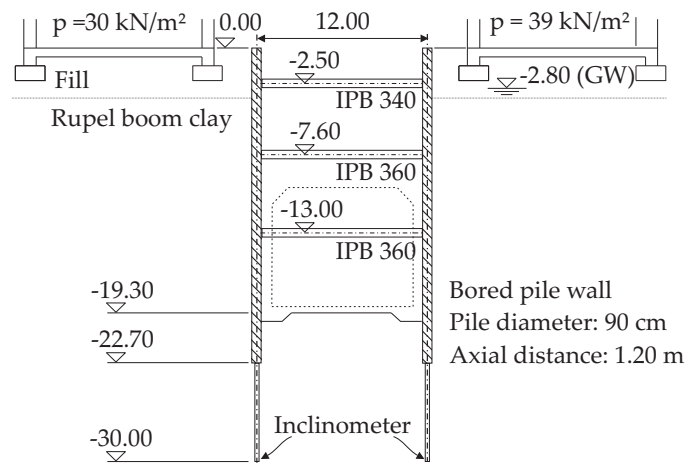


Figure 8.23: Excavation in Rupel clay: Geometry of the Offenbach excavation for a railway tunnel.

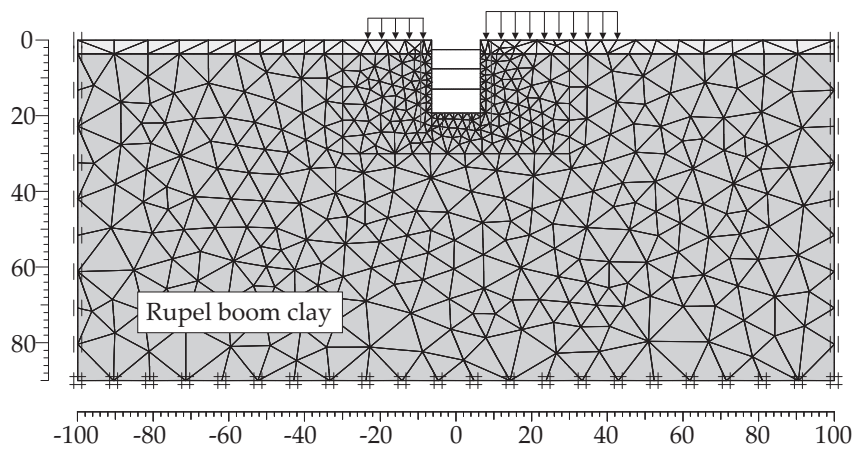


Figure 8.24: Excavation in Rupel clay: 2D mesh used in the plane strain analysis. Neighboring buildings to the excavation are modeled by a line load at the top ground surface.

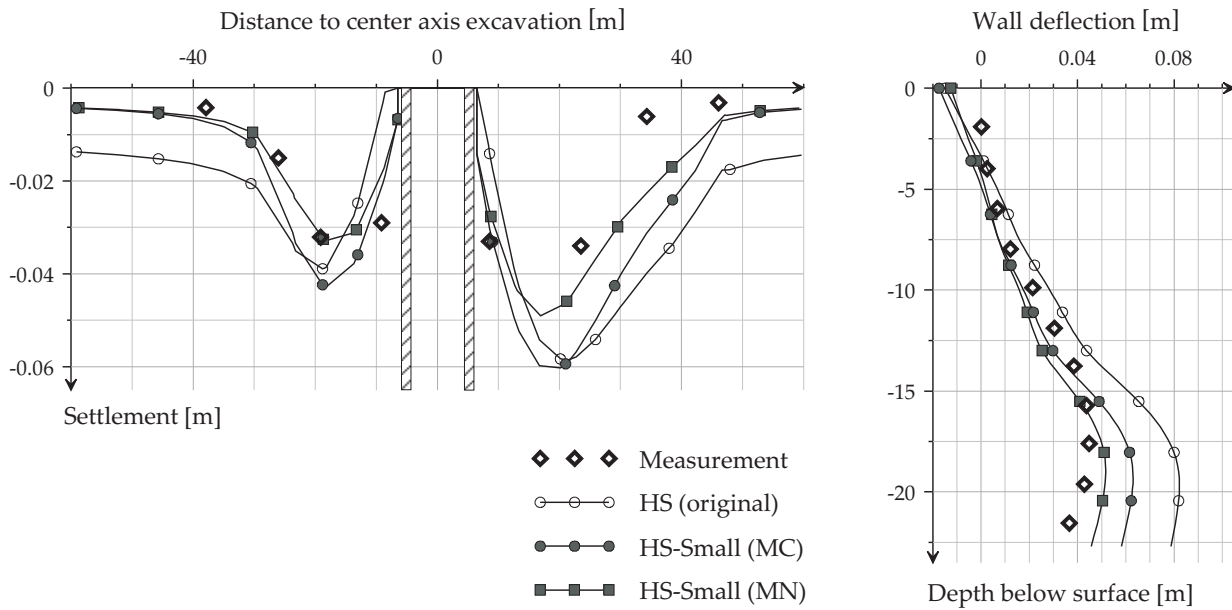


Figure 8.25: Excavation in Rupel clay. HS-Small model predictions versus measured displacements after the final excavation step. Left: Surface settlement trough. Right: Lateral deflection of the left retaining wall.

presented by Mayne & Kulhawy [115], the K_0 value for generating the initial stress field is calculated as ≈ 0.95 , for an assumed OCR of 2.8. Because of stress relaxation, no initial elastic clay behavior is assumed. Consolidation is considered only to the extent that no excess pore pressures built up behind the wall.

Figure 8.25 shows the calculated results in comparison to the available measurements at the end of excavation. The original HS model overall gives too much surface settlements accompanied by too much lateral deformations in the retaining structure. The HS-Small(MC) model improves results significantly, the HS-Small(MN) model gives almost perfect results. The settlements to the right hand side of the excavation are still too big, probably due to a slightly overestimated surcharge at the ground surface. Analogous to the previous example, the settlements right next to the wall increase slightly when using the HS-Small model. This is again related to the reduced excavation heave, which is shown in Figure 8.26. Excavation heave is calculated to be lowest for the HS-Small(MN) model and highest for the HS model.

Figure 8.27 shows the elastic material stiffness at the end of excavation. Here, stiffness is plotted as a factorized increase of the unloading-reloading stiffness (see Equation 6.13). Stiffness increases due to strain reversals are not considered in this representation. In agreement with the criterion defined in Equation 8.2, all calculated displacements (see Figure 8.25, and 8.26) are negligible in areas where $G_m > 0.8 \frac{G_0}{G_{ur}}$.

In conclusion, the HS-Small model(s) performed very well in both excavation examples, although there has been no small-strain stiffness test data available at all. All small-

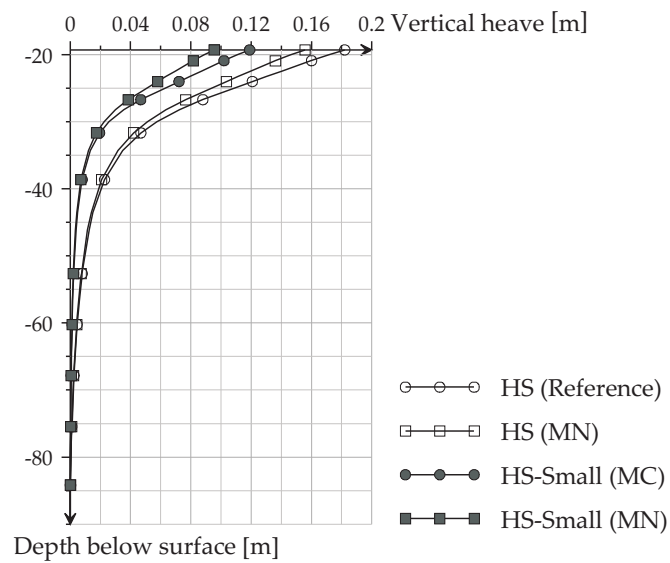


Figure 8.26: Excavation in Rupel clay: Vertical displacements in the excavation pit's symmetry.

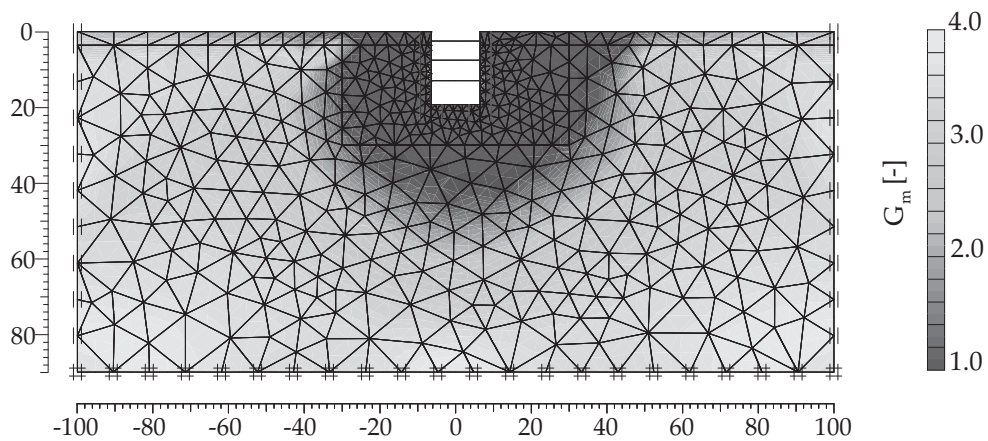


Figure 8.27: Excavation in Rupel clay: Factorized increase of unloading-reloading stiffness at the end of excavation.

strain stiffness parameters have been solely picked on the basis of data and correlations presented in Chapter 3 of this thesis. In order to account for diagenetic effects, small-strain stiffness parameters have been generally chosen in the upper range of possible values. The threshold shear strain $\gamma_{0.7}$ in sand, for example, was generally assumed at 2×10^{-4} .

Two main tendencies could be identified in this section: a) The HS-Small model gives less excavation heave than the HS model and hence, less uplift of the retaining structure and the adjoining soil, and b) the HS-Small model generally yields displacements that are in noticeable better agreement with the experimentally derived results than those of the HS model.

8.2.3 Spread Foundations

Spread foundations seem to be simple problems compared to the analysis conducted before. Most spread footings can be numerically analyzed in a plane strain or axisymmetric approach. Axisymmetric conditions may also be suitable for quadratic footings under service loads. A quadratic footing is also the last verification example presented in this chapter. A small note on the initialization procedure of the HS-Small model is included at the end of this section.

8.2.3.1 Texas A&M University spread footing on sand

Five load tests on spread footings ranging from 1x1 to 3x3 m in size were conducted at Texas A&M University's National Geotechnical Experimental Site [19]. Vertical loads were applied at the center of the footings which rested on flat ground. Load-settlement curves as well as inclinometer and extensometer measurements were recorded for each load test. In particular, the 'North' 3x3 m footing has been chosen for the following HS-Small verification. The footing has a thickness of 1.22 m and an embedded depth of 0.76 m. Figure 8.28 shows the test site as well as the 2D axisymmetric finite element mesh used in the following axisymmetric calculation. In this, the quadratic footing is modeled by a circular one with an equivalent loaded area.

The HS-Small model parameters shown in Table D.6 have been determined from several available triaxial and resonant column tests. Figure 8.29 shows the comparison of experimental data to model simulations using this parameter set. The triaxial tests could be modeled nicely. The resonant column tests scattered too much to allow them to be reasonably well simulated by any model. Nevertheless, the resonant column tests give a first idea of the small-strain stiffness parameters to be used for the sandy site.

Ignoring the available field test data in [19], but strictly applying the parameters determined from laboratory tests, yields the load settlement curves shown in Figure 8.30.a. Note that since the HS-Small(MC) and the HS-Small(MN) models yield almost exactly the same settlement curves in the axisymmetric problem, only one curve is drawn for both models. The well improved load settlement curves shown in Figure 8.30.b are obtained by additionally accounting for the soil's actual initial stress state. From the

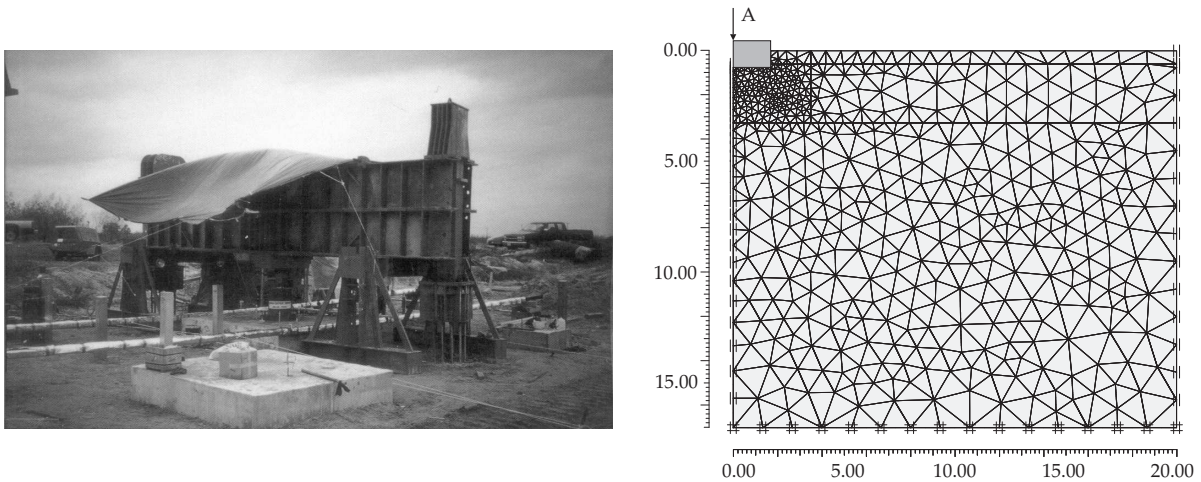


Figure 8.28: Load test on a spread footing on sand. Left: Texas A&M University's National Geotechnical Experimental Site. Right: 2D axisymmetric mesh used in the finite element analysis.

available CPT and Pressuremeter field tests it can be derived that the sandy site is overconsolidated. The amount of overconsolidation is here back-analyzed from the load settlement curves. Yet, the stiffness in initial loading and in unloading-reloading cycles is still underestimated. Increasing the initial stiffness derived from laboratory test data by 40% yields the results presented in Figure 8.30.c. Now, the unloading-reloading stiffness is simulated almost perfectly. However, the overall load settlement curve overestimates soil stiffness slightly, which may be due to the axisymmetric simplification of the given 3D problem.

As shown in Chapter 3, stiffness discrepancies in the magnitude found in the A&M footing example is not very uncommon. Nevertheless, it should be noted that underestimating small-strain stiffness by using laboratory data or correlations is always better than not accounting for small-strain stiffness at all. This, for example, can also be concluded from Figure 8.30: The HS-Small model gives more realistic simulation results than the original HS model regardless of initial stress and stiffness is used.

From a practical point of view, the most important difference in the load settlement curves is probably their initial slope (assuming that ultimate load design can also be handled by other methods). In the given example, service load settlements are overestimated by more than 80% when not using the HS-Small model.

The Texas A&M spread footing example is a nice demonstration of the benefits of small-strain stiffness on the one hand. On the other hand, it demonstrates the sensitivity of numerical calculations to initial stress conditions. As there is also a link between initial stress conditions and a material's strain history, the initialization of strain history is briefly discussed in the next section.

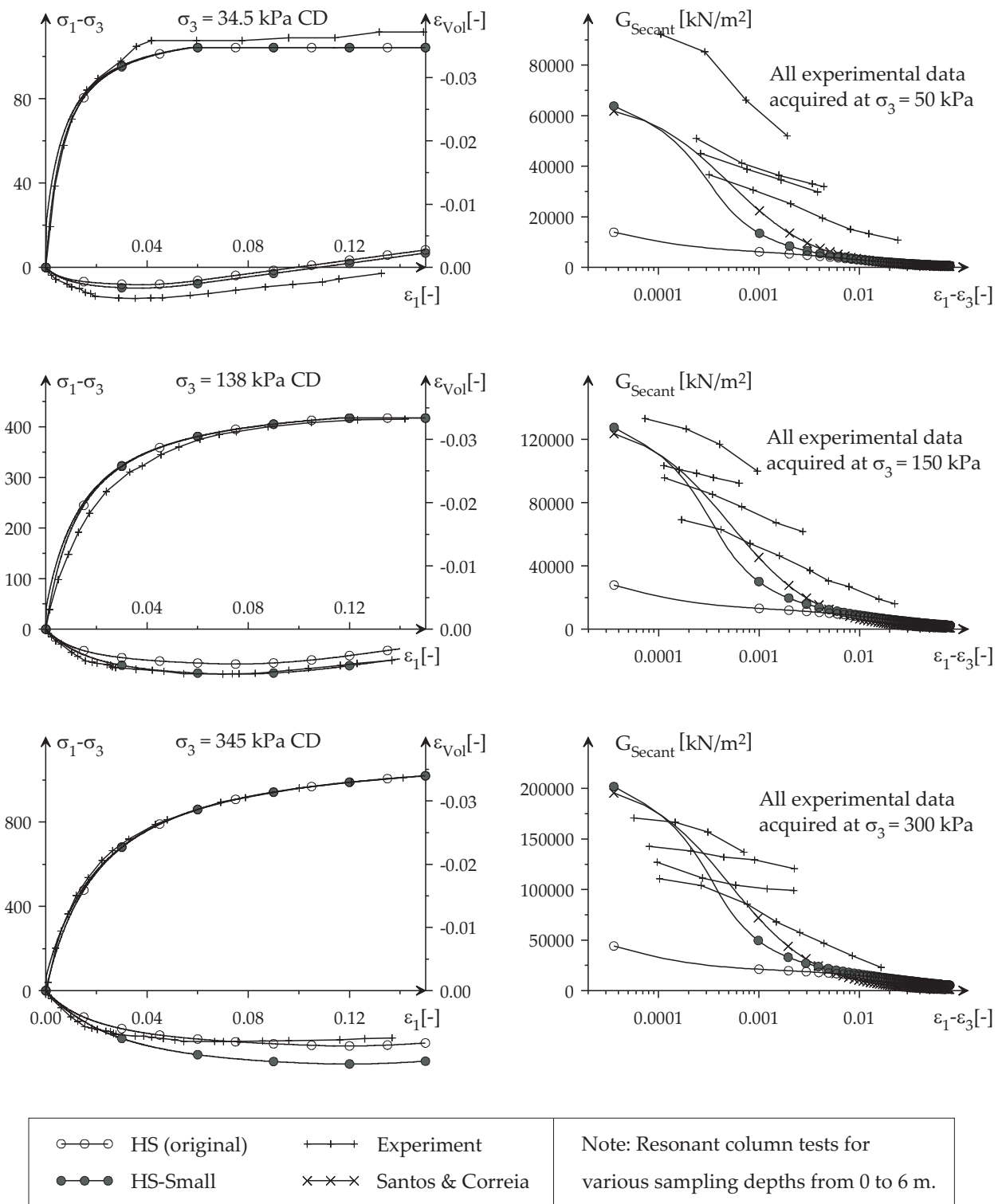


Figure 8.29: Triaxial tests on sand samples from the A&M test site (0.6 m sampling depth). Small-strain stiffness parameters are obtained by averaging the results from several resonant column tests as shown on the right hand side.

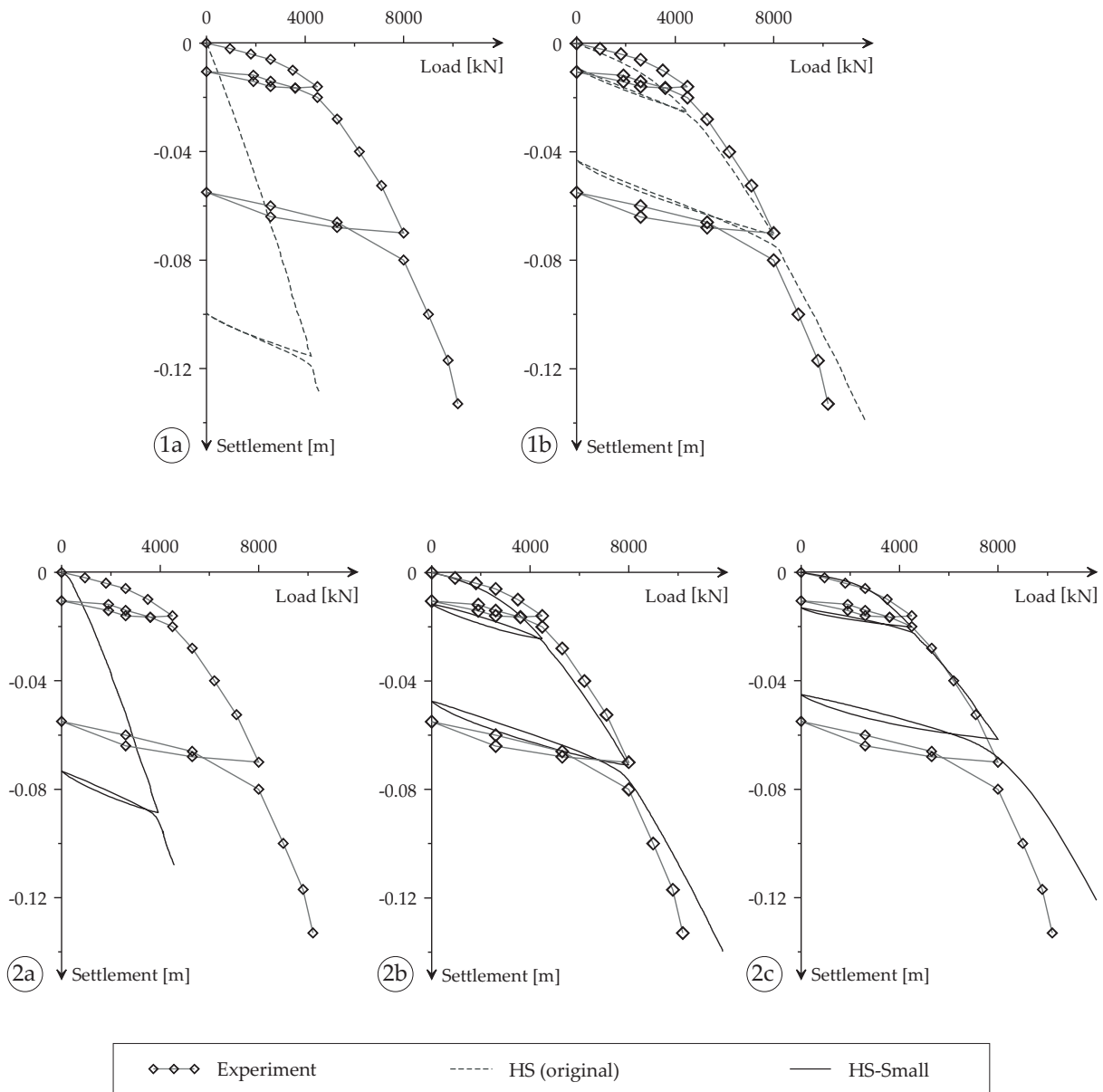


Figure 8.30: Calculated and experimentally derived load-settlement curves for the A&M 3x3 m footing on sand (HS - top row; HS-Small - bottom row): a) NC sand, b) OC sand with laboratory small-strain stiffness, c) OC sand with increased (in-situ) small-strain stiffness.

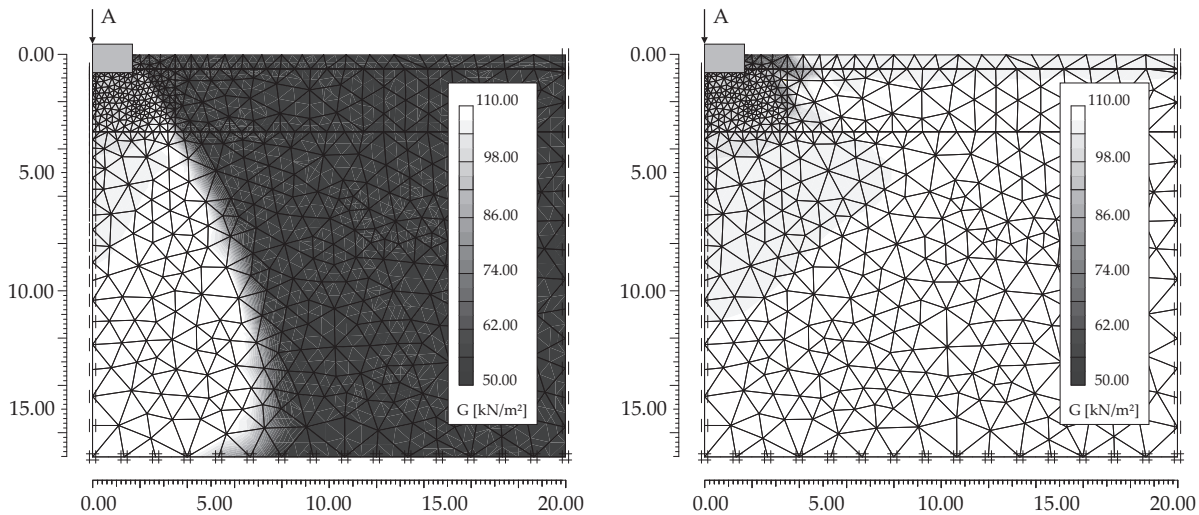


Figure 8.31: Initial elastic stiffness of the HS-Small model obtained by different initialization procedures in the A&M footing example. Left: No strain history reset between removing the surcharge used to model the material's geologic history and construction of the footing. Right: Full strain history reset by applying a small reverse load step before introducing the footing.

8.2.4 Initialization of the HS-Small model

Stress relaxation erases a soil's memory of previous applied stress. Soil ageing in the form of particle (or assembly) reorganization during stress relaxation and formation of bonds between them can erase a soil's strain history. Considering that the second process in a naturally deposited soil develops relatively fast, the strain history should start from zero in most boundary value problems. This is the default setting in the HS-Small model.

However, sometimes an initial strain history may be desired. In this case the strain history can be triggered by applying an extra load step before starting the actual analysis. Such an additional load step might also be used to model overconsolidation. Usually the overconsolidation's cause has vanished long before the start of calculation, so that the strain history should be reset afterwards. However, by adding and removing a surcharge the HS-Small model's strain history is already triggered. In this case the strain history can be reset manually, either by replacing the material or code manipulation. More convenient is sometimes the application of a small reverse load step.

Figure 8.31 shows the A&M footing example after two different initialization runs: On the left hand side the (overconsolidation) surcharge is removed just before the footing is built. By introducing the footing, the previous uplift is reversed below the footing but nowhere else. On the right hand side, a small surcharge is applied after removing the overburden loading and before introducing the footing. This small reverse loading step (in the example 1 kPa is used) resets the entire strain history of the problem. However, the problem is not reset in all of its aspects. The distinction between initial, or virgin loading, and secondary loading is made on the basis of the monotonic strain history.

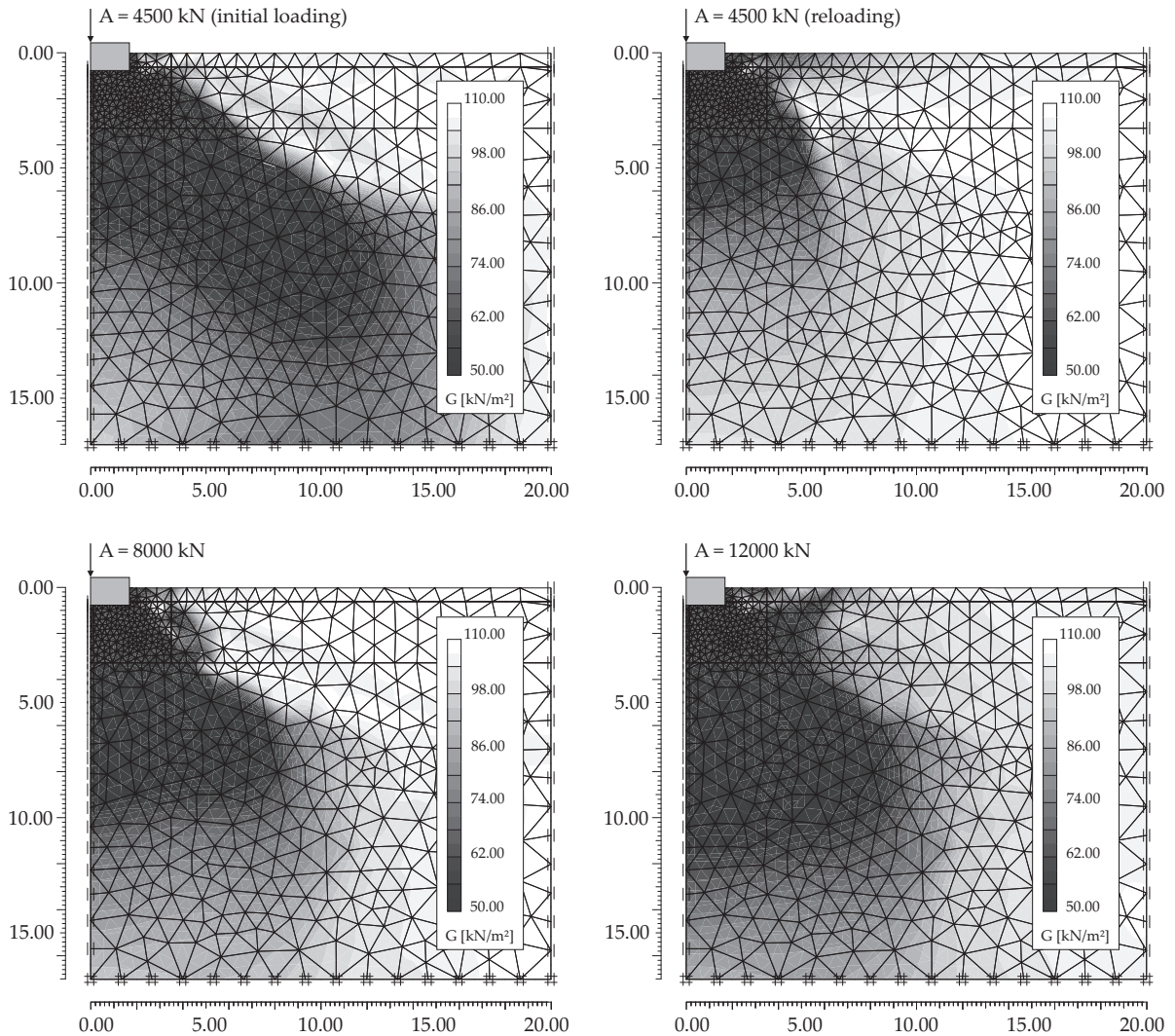


Figure 8.32: Development of elastic stiffness in the A&M footing example.

An overburden surcharge will therefore trigger secondary loading although the strain history is reset. If that is not desired, the monotonic strain history can be manually reset or an initial stress procedure as offered for example in the finite element program PLAXIS, can be used.

In discussing the strain history's reset, loading-unloading-reloading cycles as seen in the A&M footing example, are also worth a closer look. Strain history is fully reset in 180 degree load reversals. Due to isotropic hardening, the accumulated strains are usually less in reloading than in primary loading. Strain history is hence more salient in virgin loading than in reloading. This can be observed for example in the decay of elastic material stiffness shown in Figure 8.32.

8.2.5 Capabilities and limitations of the HS-Small model

The HS-Small model passed all of the above validation tests reasonably well. Its predictions are without exception more reliable than those of the original HS model, even if default small-strain stiffness parameters are used. The HS-Small model with Mohr-Coulomb criterion can therefore be readily recommended for all applications where the HS model could also be used. The HS-Small model with Matsuoka-Nakai failure criterion presumes additional material strength and stiffness. Stiffness is particularly increased in unloading problems due to the extended size of the isotropically hardened yield surface. Therefore, the HS-Small model with Matsuoka-Nakai failure criterion needs to be further validated before it is used in ultimate load design applications.

The main objective of this thesis is to develop a capable small-strain stiffness model for practical applications. This objective has obviously been met by the introduction of the HS-Small model. However, the HS-Small model also has some limitations. As the user of a model should always be aware of its limitations, those of the HS-Small model are summarized here.

Most of the HS-Small model's limitations are purely inherited from the original HS model. As already pointed out in the element test section, these are mainly its void ratio independent formulation and a lack of kinematic hardening. The HS-Small model is therefore not suited for unified modeling (modeling of material at different void ratios with a single set of material parameters) and cyclic modeling. Despite its modified flow rule and as a consequence of the void ratio independent formulation, the HS-Small model should be used with the same care in undrained analysis as the HS model. Undrained calculations with the HS model are explored in more detail in Wehnert [191].

A limitation unique to the HS-Small model is its exaggerated stiffness in isotropic loading conditions (Figure 8.33). The model's assumption that soil grains or assemblies have infinite strength is not validated. This was to be expected. Still, this is not a serious model limitation as pure isotropic loading is unlikely in boundary value problems. In K_0 loading, the model's response correlates very well to experimental data (Figure 8.1).

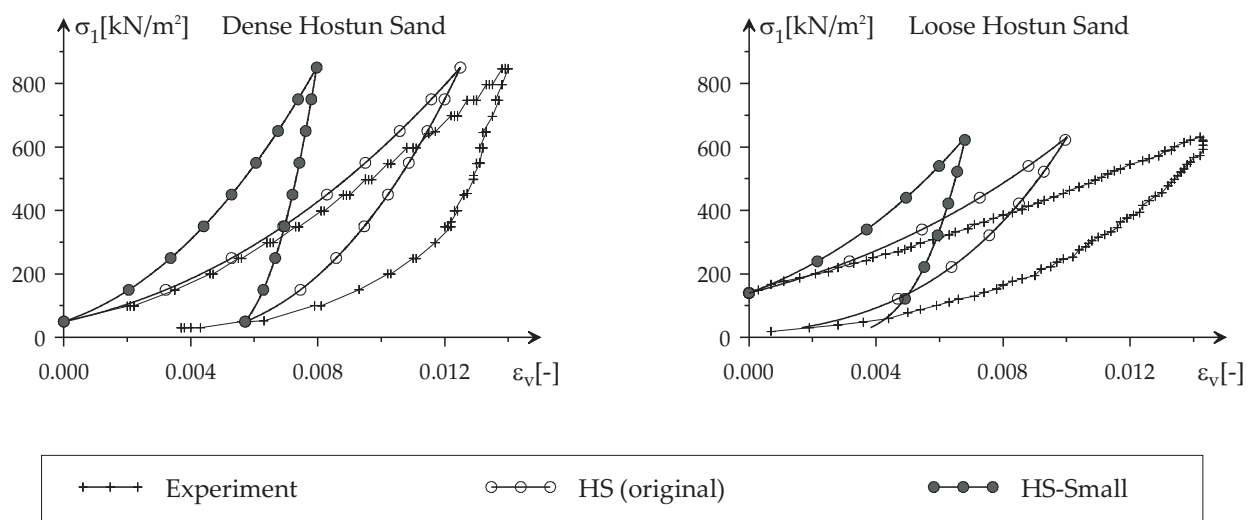


Figure 8.33: Isotropic compression test on dense (left) and loose (right) Hostun sand.

Chapter 9

3D case study Sülfeld Lock

The Mittellandkanal (MLK) links the rivers Rhine, Ems, Weser, and Elbe to Berlin and to eastern Europe's waterways. Eastbound ship traffic is lowered at the Sülfeld Lock from the channel's peak altitude of 65 m to 56 m height above sea level. The existing Sülfeld Lock was constructed between 1934-37 and was opened in 1938. The lock's southern chamber is currently being rebuilt in order to adapt it to raise ship traffic and generations of new ships. The northern lock chamber including its six economizing basins is to be kept fully operational during the 4 year construction period. The high-speed railway link between Hanover and Berlin lies close to the construction site and also needs to be kept operational at all times during construction. Figures 9.1 and 9.2 show the Sülfeld lock and the high-speed railway link passing nearby.

Investigation of the site shows that overconsolidated glacial deposits overlies Lias bedrock. The glacial deposits are composed of clayey silt, sand, and glacial till (Figure 9.3). The cohesive layers (silt and glacial till) were characterized in laboratory tests. A two-

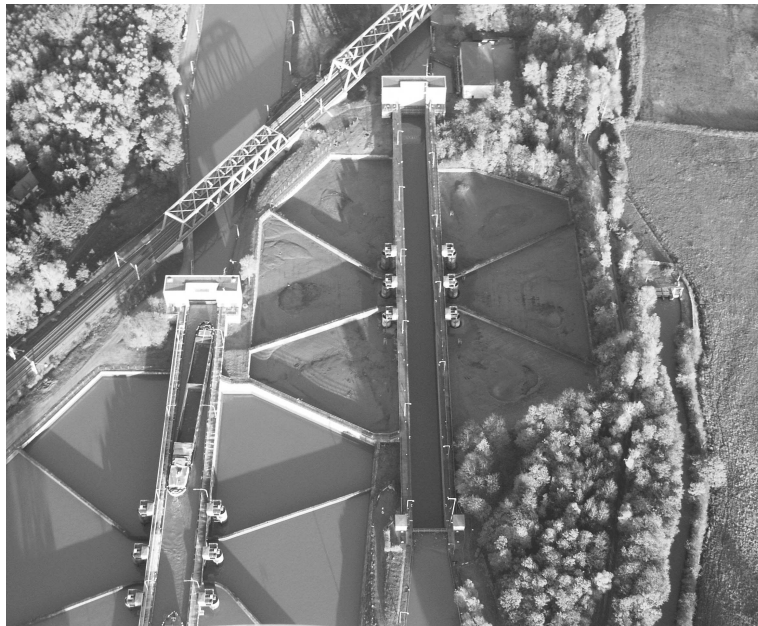


Figure 9.1: Bird's eye view of Sülfeld Lock before excavation. The northern lock chamber (left) is still in operation. The southern lock chamber (right) is currently being rebuilt.



Figure 9.2: Struted and back-anchored Sülfeld excavation near the railway bridge. The section left hand side of the channel's centerline is shown in Figure 9.3.

step model calibration procedure was employed: First, all test results were statistically averaged before secondly, selected tests were back analyzed in numerical element tests. Properties of the sand layer were estimated from in-situ heavy dynamic penetration test results. The obtained material parameters were finally calibrated in a 2D finite element model by comparing calculated displacements of the existing lock during operation to measured ones. In the calibration procedure, the confidence in the correlated small-strain stiffness parameters could be specifically increased. An overview of the final material sets used in the 3D analysis is given in Table D.7.

The excavation for the new lock chamber is fully housed by vertical retaining walls. The selected type of retaining wall is closely related to the type and presence of adjacent structures. A tied back diaphragm wall is built in sections, close to structures that are sensitive to settlements. The most sensitive part of the excavation pit next to the railway link is struted. A cut-off wall is built in all sections where settlements are tolerable. If required by design, the cut-off walls are reinforced by sheet piles.

The HS-Small model is deployed here in a 3D finite element analysis of the interaction between the excavation pit and railway bridge abutments. As solely the Mohr-Coulomb yield criterion is used in the following, the term HS-Small refers to HS-Small(MC) within this chapter. Figure 9.3 shows the geometry, structural features, and excavation stages modeled within the finite element code ABAQUS. The structural features include two abutments on pile foundations, back-anchored and struted retaining walls, sheet pile walls, and a floor slab in the struted section. Embedded elements are used to model the floor slab, sheet pile walls and piles. All other structural features and the subsoil are dis-

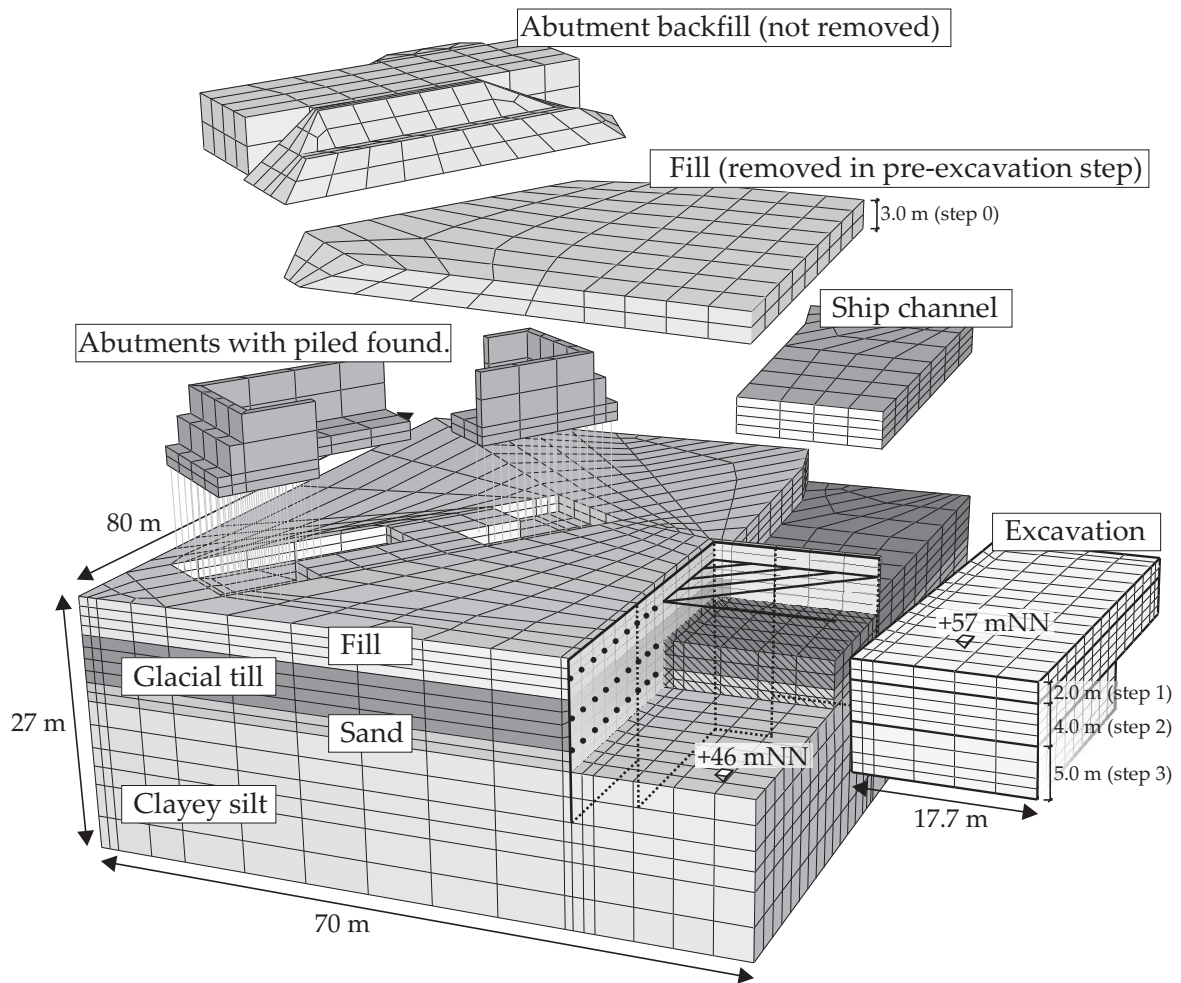


Figure 9.3: Geometry and Geology of the Suelfeld excavation in the 3D FE model. Lias bedrock marks the lower boundary of the model.

cretized by full integrated volume elements. Four excavation stages are introduced: One before wall construction (pre-excavation), and three after wall construction (excavation step 1 to 3). Construction of the retaining walls is not modeled accurately. Instead, they are placed as a whole. The phreatic level is adjusted several times in the calculation due to groundwater discharge in the bedrock or groundwater lowering in the fill. After the final excavation step, the groundwater table is lowered due to works near the pumping station. This change in phreatic level is the final load step considered in the analysis. A list of all calculation stages is given in Table 9.1. As pore water measurements indicate a relatively fast dissipation of excess pore pressures in the vicinity of the excavation pit, drained conditions are assumed.

The Sulfeld analysis' main focus is on displacements of the railway bridge abutments and their backfill. Due the rather unprecise numerical retaining wall placement method, measured and calculated abutment displacements are compared for excavation stages 1

Table 9.1: Stages in the Sülfeld 3D calculation

Stage	Action
1	Initialization
2	Pre-excitation (Excavation to +57 m NN)
3	Installation cut-off wall
4	Phreatic level at +53 m NN (local vacuum)
5	Installation diaphragm wall
6	Phreatic level at +57 m NN
7	Excavation to +55 m NN (excavation step 1)
8	Excavation to +51 m NN (excavation step 2)
9	Excavation to +46 m NN (excavation step 3)
10	Phreatic level at +53 m NN (channel section only)

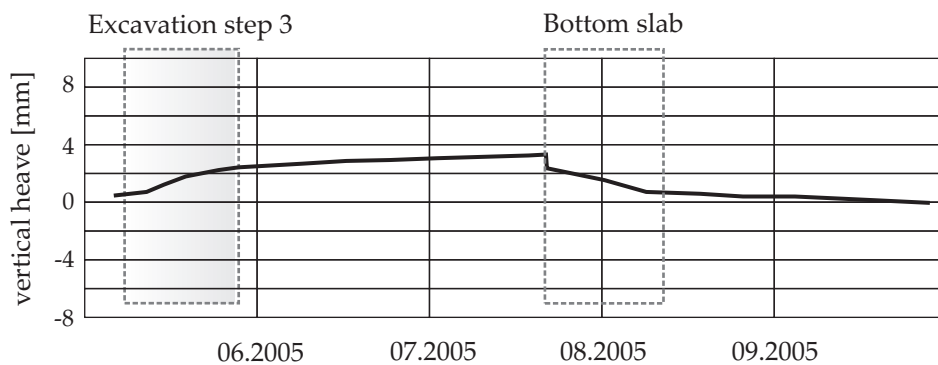
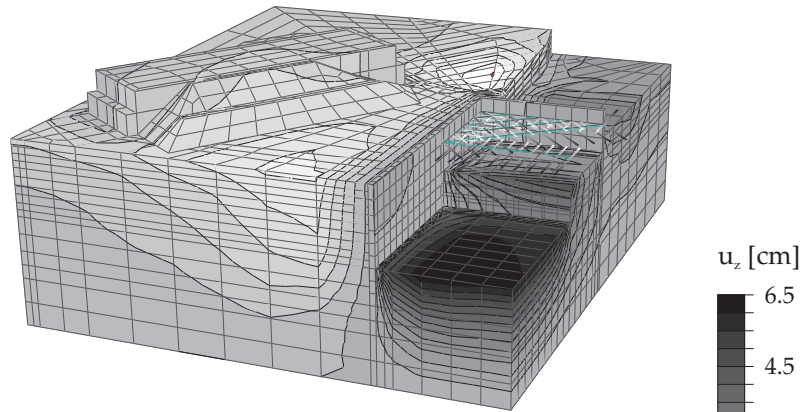


Figure 9.4: Heave measured in the excavation pit during excavation step 3.

to 3 and the final change in phreatic level only. The well equipped site allows for various other comparisons, as well. The excavation heave for example, is presented in Figure 9.4. From extensometer readings in the excavation pit, the final heave during excavation step 3 can be quantified as $\approx 2 - 3$ mm. In the analysis, heave ≤ 4 mm is obtained when using the HS-Small model. The HS analysis over-predicts the excavation heave by more than 8 mm. The overall vertical displacements from the two analysis are compared in Figure 9.5. The measured settlement (extensometer) of the abutment closest to the excavation pit is shown in Figure 9.6. From geodetic measurements it can be additionally derived that the abutments are not tilting. Exactly the same behavior is found in the HS-Small analysis: Almost no tilt of the abutments occurs with a total settlement of ≈ 2 mm. The HS calculation on the other hand, shows settlements of up to 10 mm in combination with tilt.

Figure 9.8 shows a comparison of measured and calculated horizontal displacements of both bridge abutments. Measured displacements were separated in displacements due to pre-excitation and wall construction (not shown) and displacements due to ex-

a.) Vertical displacement u_z - HS



b.) Vertical displacement u_z - HS-Small

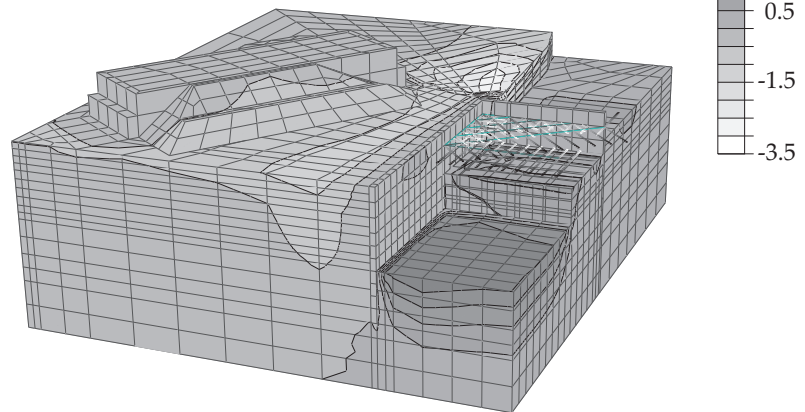


Figure 9.5: Vertical displacements due to excavation (step 1 to 3) and groundwater lowering.

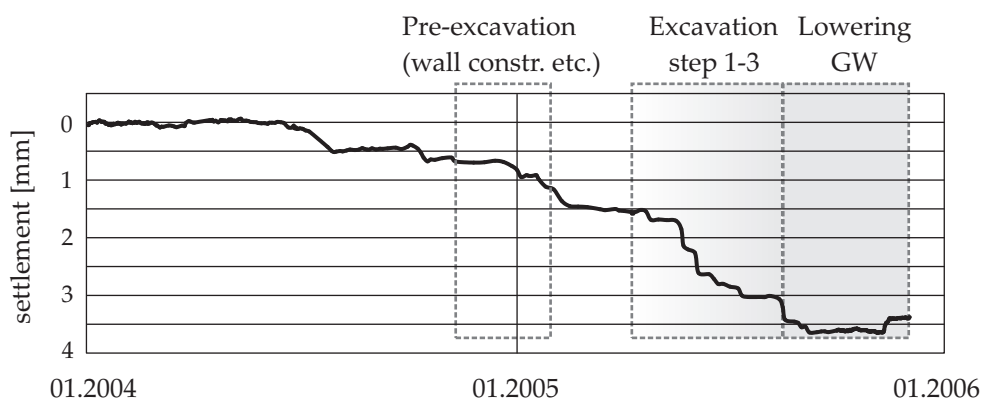


Figure 9.6: Settlement of the abutment closest to the excavation pit.

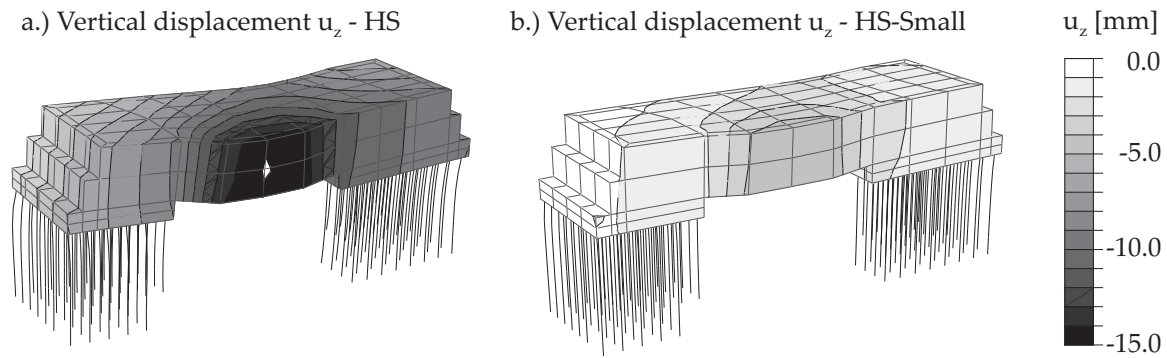


Figure 9.7: Vertical displacements of the abutments due to excavation and groundwater lowering.

cavation step 1 to 3 and final groundwater lowering. The latter can be directly compared to the deformed abutments drawn to scale for both, HS and HS-Small analysis. The overall trend in the HS-Small calculation is in better agreement with the measured displacements compared to those of the HS model. Right next to the abutment front walls, the calculated displacements resemble reasonably well the measured displacements. However, the wing walls do not deform extensively enough, which could be partly due to the linear elastic concrete material model chosen in the calculation.

Figure 9.9 finally depicts the factorized increase of the unloading-reloading stiffness at several calculation stages. For illustration purposes, the factorized stiffness increase is shown in the clayey silt only. It is only towards the end of excavation, that small-strain stiffness disappears with greater distance to the excavation pit. Remarkably is also the effectiveness of the pile foundation. Within the "reinforced" part of the soil, almost no stiffness reduction can be observed.

In summary, the HS-Small model could be successfully deployed in the Sülfeld 3D finite element analysis. It significantly improved all results obtained from the HS model. Same as in the previous calculations, the improvement is achieved with zero strain history at the onset of loading. For complex geometries however, the numerical initialization of the HS-Small model can be challenging. In the ABAQUS code for example, initial stress fields are *not* calculated with reference to surface geometry. Gravity loading on the other hand accumulates much deformation and affects strain history. For users of the ABAQUS code, a remedy to the initialization difficulty is to restart the analysis after initialization.

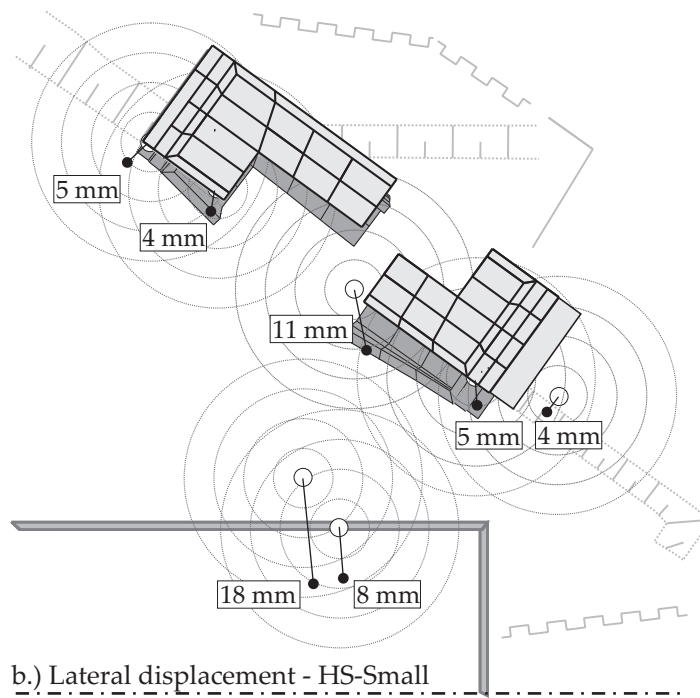
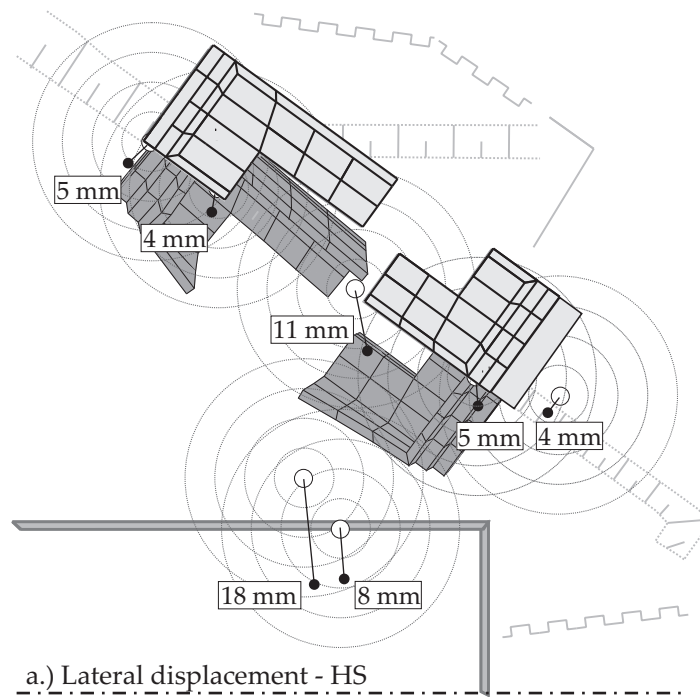


Figure 9.8: Horizontal displacements of the railway bridge abutments.

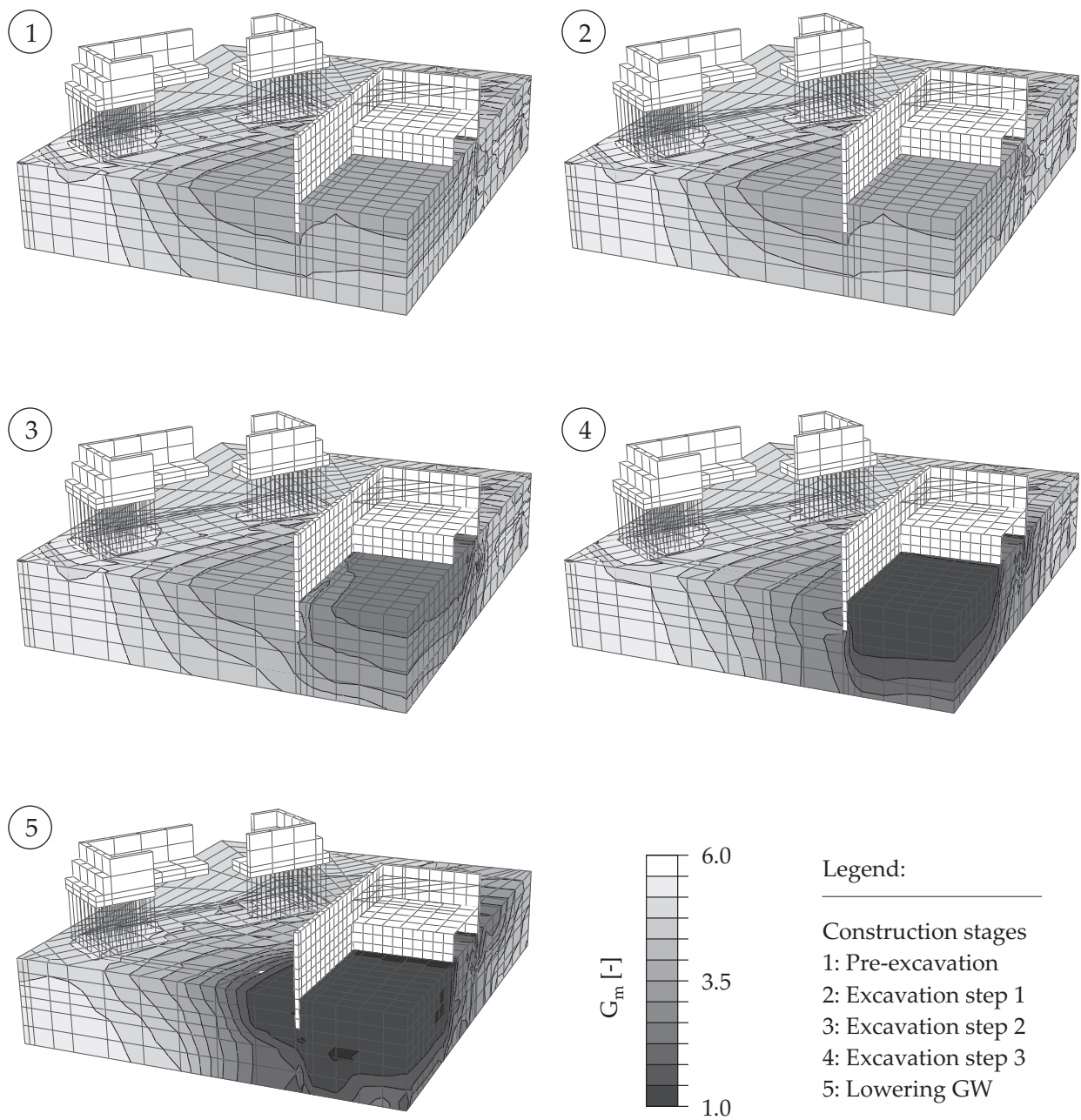


Figure 9.9: Modulus reduction during excavation and GW lowering.

Chapter 10

Conclusions

The strain range in which soils can be considered truly elastic, i.e. where they recover from applied straining almost completely, is very small. With increasing strain amplitude, soil stiffness decays non-linearly: Plotting soil stiffness against $\log(\text{strain})$ yields characteristic S-shaped stiffness reduction curves. Hardin & Drnevich [52] first described these small-strain stiffness reduction curves with a simple hyperbolic formula. Since then, many additional experimental findings have been reported in the literature. These findings concern mainly the qualitative and quantitative influence of various parameters on small-strain stiffness and stiffness reduction curves. Void ratio and mean stress, for example, are two parameters that strongly affect small-strain stiffness. The influence of many other parameters, such as cementation, grain size distribution, plasticity index etc. is likewise appreciated, but is less straightforward to quantify. Recently, inherent and stress induced anisotropic features of small-strain stiffness have become important themes in research. At the same time, engineers working in practice have only very limited possibilities to include small-strain stiffness in design. There is a lack of simple and capable small-strain stiffness models. Those small-strain stiffness models available (Chapter 5) are either research orientated, and/or applicable to specific loading paths only. The objective of this thesis was therefore, to develop a capable small-strain stiffness model suitable for the engineering community.

The Small-Strain Overlay model proposed in this thesis generalizes the hyperbolic Hardin-Drnevich model to multi-axial strain space. Although it takes into account strain induced anisotropy, the overlay model renders small-strain stiffness isotropic. It can therefore be easily combined with many existing elastoplastic constitutive models that are based on isotropic elasticity. In fact, these are the kind of models most commonly used in engineering practice today. One of these is the Hardening Soil (HS) model, as implemented in the finite element code PLAXIS V8 [21]. The combination of the HS model with the small-strain overlay model introduced in this thesis, is named the HS-Small model. The HS-Small model was validated in a single stress point and various boundary value problems. In these, all effects that are commonly attributed to small-strain stiffness in soil-structure interaction could be recognized: The width and shape of settlement troughs, for example, are more precisely modeled and excavation heave is reduced to a realistic value. The overall reliability of numerical displacement analysis is considerably increased. Analysis results are also less sensitive to the choice of proper boundary conditions. Large meshes no longer cause extensive accumulation of displacements, because marginally strained mesh parts are very stiff. Conserved small-strain stiffness at the mesh's boundaries is an indicator for its proper extent.

The HS-Small model with the Mohr-Coulomb failure criterion is recommended for all applications where the HS model could also be used. The HS-Small model with the Matsuoka-Nakai failure criterion seems to perform a little better than its Mohr-Coulomb counterpart. Its increased strength and stiffness should however be further validated before it is applied in design. If, for a certain design situation the original HS model is already at hand, it may be beneficial to also stay with the HS-Small(MC) model: Plane strain calibrated strength and stiffness parameters yield overly high material stiffness and strength using the HS-Small(MN) model.

Application of the HS-Small model is straightforward. Its Small-Strain Overlay extension requires only two additional parameters. These are the very small-strain stiffness G_0 and the threshold shear strain $\gamma_{0.7}$ at which stiffness is reduced to $0.7G_0$. In case no small-strain stiffness in-situ or laboratory test data are available, these two parameters can be correlated with various other soil or test parameters. In the validation process of the HS-Small model, the correlations summarized in Chapter 3 of this thesis could be successfully applied. Although these correlations bear uncertainties, it seems advisable to use them if the only alternative is to neglect small-strain stiffness. Neglecting small-strain stiffness certainly produces higher analysis errors than using correlations with slight uncertainties. Most correlations are at the lower end of in-situ determined small-strain stiffness anyway.

The adaptation of G_0 and $\gamma_{0.7}$ to parameters that affect them within the Small-Strain Overlay model could be improved in future work. In the present implementation, no void ratio dependency is assumed. This is in clear contradiction to the findings presented in Chapter 3. However, as most models that are currently used in engineering practice assume a constant void ratio, this concept is also adopted in the present implementation. The main drawback of void ratio independent constitutive models is that their material parameters have to be adjusted to the actual void ratio via manual user input. Mean stress dependency of small-strain stiffness is taken into account using the same power law as for large strains. In this way, the number of additional material parameters is kept at a minimum. For clays, the large strain power law exponent might be slightly too high, though. The threshold shear strain on the other hand, is not explicitly corrected for mean stress in the present implementation. The latter compensates for overly high power law exponents. Future work on the Small-Strain Overlay model should also include further validation of the strain history mapping presented in Chapter 6. This can presently not be undertaken due to a lack of experimental data.

Future work on the HS-Small model might include the formulation of a cap-type yield loci similar to that of the Cam-Clay model. This would allow for degenerating the HS-Small model to a full Cam-Clay model. Kinematic hardening should be introduced to open up the HS-Small model to cyclic loading applications as well. Within a preliminary implementation, the possibilities of introducing bounding surface plasticity to the HS-Small model are shown in [186]. The resulting model is illustrated in Figure 10.1.

In summary, the HS-Small model is a suitable tool to incorporate small-strain stiffness into routine design. Testing procedures and correlations for determining its small-strain parameters are described in Chapter 3. From experience so far, no situations are known where the HS-Small model gives less reliable results than the often validated HS model.

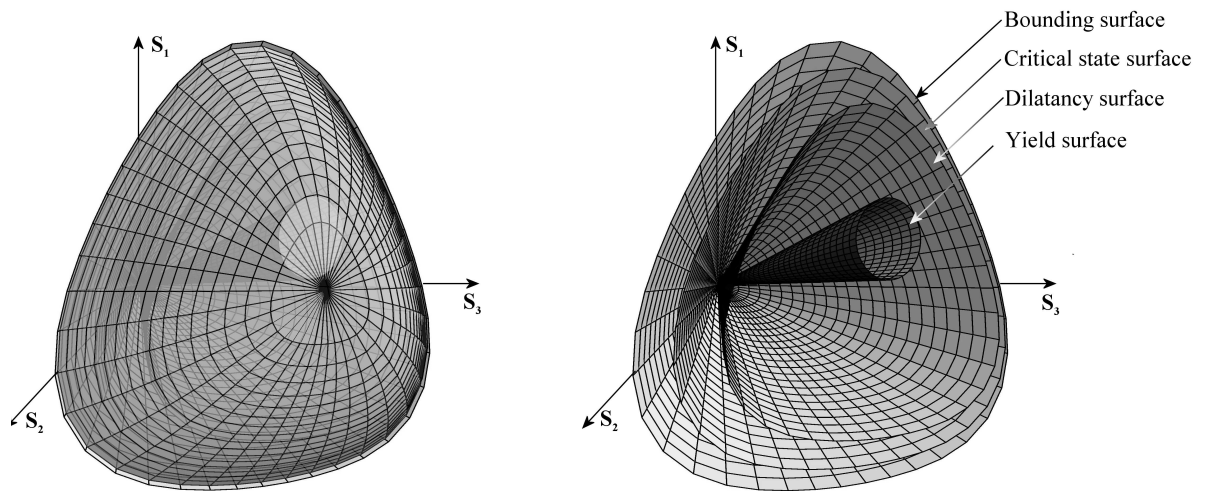


Figure 10.1: Bounding surface model with cap in principal strain space. Only the highlighted cap portion is active. Right: View inside the model onto yield-, dilatancy-, critical-, and bounding surface.

In contrary, analysis results are throughout, in better agreement with experimental findings when the HS-Small model is deployed. Combining the Small-Strain Overlay model with other existing elastoplastic models should turn out to be equally beneficial.

Bibliography

- [1] A. Al-Tabbaa. *Permeability and stress strain response of speswhite kaolin*. PhD thesis, University of Cambridge, 1987.
- [2] A. Al-Tabbaa and D. Muir Wood. An experimentally based 'bubble' model for clay. In S. Pietruszczak and G. N. Pande, editors, *Numerical Models in Geomechanics: NUMOG III*, pages 91–99. London: Elsevier Applied Science, 1989.
- [3] I. Alpan. The geotechnical properties of soils. *Earth-Science Reviews*, 6:5–49, 1970.
- [4] D.G. Anderson and K.H. Stokoe. *Shear modulus: A time-dependent soil property*, chapter Dyn. Geotech. Test., pages 66–89. Number STP 654. ASTM Spec. Tech. Publ., Philadelphia, 1978.
- [5] D.G. Anderson and R.D. Woods. Time-dependent increase in shear modulus of clay. *Proc. ASCE: Journal of the Geotechnical Engineering Division*, 102(GT5):525–537, 1976.
- [6] J.H. Argyris, G Faust, J Szimmat, P Warnke, and K William. Recent developments in finite element analyses of prestressed concrete reactor vessels. *Nuclear Engineering and Design*, 28:42–75, 1974.
- [7] J. H. Atkinson. Non-linear soil stiffness in routine design. *Géotechnique*, 50(5): 487–508, 2000.
- [8] J.H. Atkinson and J.A. Little. Undrained triaxial strength and stress-strain characteristics of a glacial till soil. *Can. Geotech. J.*, 25(3):428–439, 1988.
- [9] J.H. Atkinson and G. Sallfors. Experimental determination of soil properties. In *Proc. 10th ECSMFE*, volume 3, pages 915–956, Florence, 1991. General Report to Session 1.
- [10] J.K. Bakker. *Soil retaining structures - development of models for structural analysis*. PhD thesis, Technical Univesity of Delft, 2000.
- [11] G. Baldi, R. Bellotti, V.N. Ghionna, M. Jamiolkowski, and D.C.F. Lo Presti. Modulus of sands from cpt's and dmt's. In *Proc. 12th Int. Conf. SMFE*, volume 1, pages 165–170, Rio de Janeiro, 1989.
- [12] J.P. Bardet. Lode dependences for isotropic pressure-sensitive elastoplastic materials. *Transactions of the ASME*, 57(9):498–506, 1990.

- [13] K. Been and M.G. Jefferies. A state parameter for sands. *Géotechnique*, 35(2):99–112, 1985.
- [14] R. Bellotti, M. Jamiolkowski, D.C.F. Lo Presti, and D.A. O'Neill. Anisotropy of small strain stiffness in ticino sand. *Géotechnique*, 46(1):115–131, 1996.
- [15] T. Belytschko, W.K. Liu, and B. Moran. *Nonlinear Finite Elements for Continua and Structures*. John Wiley & Sons Ltd., Chichester, 2000.
- [16] J. Biarez and P.-Y. Hicher. *Elementary Mechanics of Soil Behaviour*. Balkema, 1994.
- [17] L. Bjerrum. Problems of soil mechanics and construction on soft clays. In *Proc. 8th Int. Conf. SMFE*, volume 3, pages 111–159, Moscow, 1973.
- [18] P.G. Bonnier. Implementational aspects of constitutive modelling. SCMEP Workshop No 1 at NTNU, August 2000.
- [19] J.-L. Briaud and R. Gibbens. Large scale load tests and data base of spread footings on sand. Final Report FHWA-RD-97-068, U.S. Department of Transportation. Federal Highway Administration, 11 1997.
- [20] E.G.M. Brignoli, M. Gotti, and K.H. Stokoe. Measurement of shear waves in laboratory specimens by means of piezoelectric transducers. *Geotechnical Testing Journal*, 19(4):384–397, 1996.
- [21] R.B.J. Brinkgreve, editor. *PLAXIS, 2D Version 8*. AA. Balkema, 2002.
- [22] B.B. Broms and A.O. Casbarian. Effects of rotation of the principal stress axes and of the intermediate principal stress on the shear strength. In *Proc. 6th Int. Conf. SMFE*, volume 1, pages 179–183, 1965.
- [23] J.B. Burland. Contribution to discussion on session 4. In *Proc. 7th Eur. Conf. Soil Mech.*, volume 4, page 137, Brighton, 1979. SMFE.
- [24] J.B. Burland. Small is beautiful - the stiffness of soils at small strains, Ninth Laurits Bjerrum memorial lecture. *Canadian Geotechnical Journal*, 26:499–516, 1989.
- [25] J.B. Burland, B. Simpson, and H.D. St. John. Movements around excavations in London clay. In *Proc. 7th Eur. Conf. Soil Mech.*, volume 1, pages 13–30, Brighton, 1979. SMFE.
- [26] T.K. Caughey. Sinusoidal excitation of a system with bilinear hysteresis. *Journal of Applied Mechanics, ASME*, 27(4):640–643, 1960.
- [27] C.S. Chang. Micromechanical modelling of constitutive relations for granular material. In M. Satake and J.T. Jenkins, editors, *Micromechanics of Granular Materials*, pages 271–278, Amsterdam, The Netherlands, 1978. Elsevier.

-
- [28] S.K. Chaudhary, J. Kuwano, and Y. Hayano. Measurement of quasi-elastic stiffness parameters of dense Toyoura sand in hollow cylinder apparatus and triaxial apparatus with bender elements. *Geotechnical Testing Journal*, 27(1):1–13, 2004.
- [29] K.W. Cole and J.B. Burland. Observation of retaining wall movements associated with a large excavation. In *Proc. 5th ECSMFE*, volume 1, page 445453, Madrid, 1972.
- [30] M.B. Darendeli and K.H. Stokoe. Development of a new family of normalized modulus reduction and material damping curves. Engrg. Rpt. GD01-1, University of Texas, Austin, Texas, 2001.
- [31] J. Desrues, P.A. Vermeer, and B. Zveschper. Database for tests on Hostun RF sand. Institutsbericht 13, Universität Stuttgart, 2000.
- [32] T. Doanh. *Constitutive Modelling of Granular Materials*, chapter Strain response envelope: a complementary tool for evaluating hypoplastic constitutive equations, pages 375–396. Berlin Heidelberg: Springer, 2000.
- [33] D.C. Drucker. On uniqueness in the theory of plasticity. *Quart. Appl. Math.*, XIV: 35–42, 1956.
- [34] D.C. Drucker. *Introduction to Mechanics of Deformable Solids*. McGraw-Hill, 1967.
- [35] D.C. Drucker and W. Prager. Soil mechanics and plastic analysis or limit design. *Quart. Appl. Math.*, 10(2):157–165, 1952.
- [36] J.M. Duncan and C.-Y. Chang. Nonlinear analysis of stress and strain in soil. *Proc. ASCE: Journal of the Soil Mechanics and Foundation Division*, 96:1629–1653, 1970.
- [37] R. Dyvik and C. Madshus. Lab measurements of G_{max} using bender elements. In *Advances in the Art of Testing Soils Under Cyclic Conditions*, pages 186–196., Detroit, Michigan, 1985. ASCE. ASCE convention.
- [38] W. Ehlers. A single-surface yield function for geomaterials. *Arch. Appl. Mech.*, 65: 246–259, 1995.
- [39] A.L. Fernandez and J.C. Santamarina. Effect of cementation on the small-strain parameters of sands. *Can. Geotech. J.*, 38:191–199, 2001.
- [40] V. Fioravante. Anisotropy of small-strain stiffness of Ticino and Kenya sands from seismic wave propagation measured in triaxial testing. *Soils and Foundations*, 40(4): 129–142, 2000.
- [41] E. Flavigny, J. Desrues, and B. Palayer. Le sable d’Hostun RF. *Rev. Franc. Geotechn.*, 53:67–70, 1990.
-

- [42] D. Forel, T. Benz, and W.D. Pennington. *Seismic Data Processing with Seismic Un*x*. Number 12 in Course Notes. Society of Exploration Geophysicists, Houston, TX, 2005.
- [43] Deutsches Institut für Normung (DIN). DIN EN ISO 14688. Berlin: Beuth Verlag, 11 2004. Geotechnical investigation and testing. Identification and classification of soil.
- [44] V.N. Georgiannou, S. Rampello, and F. Silvestri. Static and dynamic measurements of undrained stiffness on natural over consolidated clays. In *Proc. 10th ECSMFE*, volume 1, pages 91–95, Florence, 1991.
- [45] J.D. Goddard. Nonlinear elasticity and pressure-dependent wave speeds in granular media. *Proceedings of the Royal Society London*, (430):105–131, 1990.
- [46] A. Grammatikopoulou. *Development, implementation and application of kinematic hardening models for overconsolidated clays*. PhD thesis, University of London (Imperial College), 2004.
- [47] G. Gudehus. A comparison of some constitutive laws for soils under radially symmetric loading and unloading. In *Proc. of 3rd Num. Meth. in Geomechanics*, volume 4, pages 1309–1323. A.A. Balkema, 1979.
- [48] M.J. Gunn. The prediction of surface settlement profiles due to tunnelling. In G.T. Houlsby and A.N. Schofield, editors, *Predictive Soil Mechanics*, pages 304–316. Thomas Telford, 1993. Proc. Wroth Memorial Symposium.
- [49] B.O. Hardin. The nature of stress-strain behaviour of soils. In *Proc. Earthquake Engineering and Soil Dynamics*, volume 1, pages 3–90, Pasadena, CA, 1978. ASCE, New York. State-of-the-art report.
- [50] B.O. Hardin and W.L. Black. Vibration modulus of normally consolidated clays. *Proc. ASCE: Journal of the Soil Mechanics and Foundations Division*, 94(SM2):353–369, 1968.
- [51] B.O. Hardin and W.L. Black. Closure to vibration modulus of normally consolidated clays. *Proc. ASCE: Journal of the Soil Mechanics and Foundations Division*, 95(SM6):1531–1537, 1969.
- [52] B.O. Hardin and V.P. Drnevich. Shear modulus and damping in soils: Design equations and curves. *Proc. ASCE: Journal of the Soil Mechanics and Foundations Division*, 98(SM7):667–692, 1972.
- [53] B.O. Hardin and V.P. Drnevich. Shear modulus and damping in soils: Measurement and parameter effects. *Proc. ASCE: Journal of the Soil Mechanics and Foundations Division*, 98(SM6):603–624, 1972.

-
- [54] B.O. Hardin and F.E. Richart Jr. Elastic wave velocities in granular soils. *Proc. ASCE: Journal of the Soil Mechanics and Foundations Division*, 89(SM1):33–65, 1963.
- [55] K. Hashiguchi. Fundamental requirements and formulations of elastoplastic constitutive equations with tangential plasticity. *Int. J. Plasticity*, 9(5):525–549, 1993.
- [56] P. Hepton. Shear wave velocity measurements during penetration testing. In *Penetration Testing in the UK*, pages 275–283, Birmingham, UK, 1989. Thomas Telford, London. Proceedings of the Geotechnology Conference on Penetration Testing in the United Kingdom (PTUK).
- [57] P.-Y. Hicher. Elastic properties of soils. *Journal of Geotechnical Engineering*, 122(8):641–648, 1996.
- [58] R. Hill. *The Mathematical Theory of Plasticity*. Oxford University Press, London, 1950.
- [59] U. Holzlöhner. Dynamische Bodenkennwerte - Meßergebnisse und Zusammenhänge. *Bautechnik*, 65(9):306–312, 1988.
- [60] E. Hoque and F. Tatsuoka. Kinematic elasticity of a granular material. In *Proc. GeoEng2000*, Melbourne, 2000. GEE0085.PDF.
- [61] E. Hoque and F. Tatsuoka. Effects of stress ratio on small-strain stiffness during triaxial shearing. *Géotechnique*, 54(7):429–439, 2004.
- [62] G.T. Houlsby. Critical state models and small-strain stiffness. In *Developments in Theoretical Geomechanics*, pages 295–312. Balkema, 2000. Proc. of the Booker Memorial Symposium (Sydney).
- [63] G.T. Houlsby and C.P. Wroth. The variation of shear modulus of a clay with pressure and overconsolidation ratio. *Soils and Foundations*, 31(3):138–134, 1991.
- [64] C-C. Hsu and M. Vucetic. Dynamic and cyclic behavior of soils over a wide range of shear strains in ngi-type simple shear testing device. UCLA Reserarch Report ENG-02-228, Civil and Environmental Engineering Department, University of California, Los Angeles, 2002.
- [65] T. Hueckel and R. Nova. Some hysteresis effects of the behavior of geological media. *International Journal of Solids and Structures*, 15(8):625–642, 1979.
- [66] T.J.R. Hughes. *The Finite Element Method; Linear Static and Dynamic Finite Element Analysis*. Prentice-Hall, 1987.
- [67] T.J.R. Hughes and R.L. Taylor. Unconditionally stable algorithms for quasi-static elasto/viscoplastic finite element analysis. *Computers and Structures*, 8:169–173, 1978.

- [68] I.M. Idriss and H.B. Seed. Seismic response of horizontal soil layers. *Proc. ASCE: Journal of the Soil Mechanics and Foundation Division*, 94(SM4):1003–1031, 1968.
- [69] T. Imai and K. Tonouchi. Correlation of N-value with S-wave velocity and shear modulus. In *Proc. 2nd European Symposium on Penetration Testing*, pages 66–72, Amsterdam, 1982.
- [70] I. Ishibashi and X. Zhang. Unified dynamic shear moduli and damping ratios of sand and clay. *Soils and Foundations*, 33(1):182–191, 1993.
- [71] K. Ishihara, F. Tatsuoka, and S. Yasuda. Undrained deformation and liquefaction of sand under cyclic stresses. *Soils and Foundations*, 15(1):29–44, 1975.
- [72] J.N. Israelachvili. *Intermolecular and surface forces*. Academic Press, 1992.
- [73] W.D. Iwan. On a class of models for the yielding behaviour of continuous and composite systems. *Journal of Applied Mechanics, ASME*, 34(3):612–617, 1967.
- [74] T. Iwasaki and F. Tatsuoka. Effects of grain size and grading on dynamic shear moduli of sands. *Soils and Foundations*, 17(3):19–35, 1977.
- [75] T. Iwasaki, F. Tatsuoka, and Y. Takagi. Hysteretic damping of sands under cyclic loading and its relation to shear modulus. *Soils and Foundations*, 18(2):25–40, 1978.
- [76] T. Iwasaki, F. Tatsuoka, and Y. Takagi. Shear moduli of sands under cyclic torsional shear loading. *Soils and Foundations*, 18(1):39–56, 1978.
- [77] N. Janbu. Soil compressibility as determined by oedometer and triaxial tests. In *Proc. 3rd ECSMFE*, volume 1, pages 19–25, Wiesbaden, 1963.
- [78] R.J. Jardine, A.B. Fourie, J. Maswoswe, and J.B. Burland. Field and laboratory measurement of soil stiffness. In *Proc. 11th Int. Conf. SMFE*, volume 2, pages 511–514, San Fransisco, 1985.
- [79] R.J. Jardine, D.M. Potts, A.B. Fourie, and J.B. Burland. Studies of the influence of non-linear stress-strain characteristics in soil-structure interaction. *Géotechnique*, 36(3):377–396, 1986.
- [80] R.J. Jardine, M.J. Symes, and J.B. Burland. The measurement of soil stiffness in the triaxial apparatus. *Géotechnique*, 34(3):323–340, 1984.
- [81] P.C. Jennings. Periodic response of a general yielding structure. *Proc. ASCE: Journal of the Engineering Mechanics Division*, 90(EM2):131–166, 1964.
- [82] P.C. Jennings. Earthquake response of a yielding structure. *Proc. ASCE: Journal of the Engineering Mechanics Division*, 91(EM4):41–67, 1965.
- [83] B. Jeremic and S. Sture. Implicit integrations in elastoplastic geotechnics. *Mechanics of Cohesive-Frictional Materials*, 2:165–183, 1997.

-
- [84] H.D. St John. *Field and theoretical studies of behaviour of ground around deep excavations in London Clay*. PhD thesis, University of Cambridge, 1975.
- [85] K.L. Johnson. *Contact Mechanics*. Cambridge University Press, 1985.
- [86] V. Jovicic and M.R. Coop. Stiffness of coarse-grained soils at small strains. *Géotechnique*, 47(3):545–561, 1997.
- [87] F.E. Richart Jr., R.D. Woods, and J.R. Hall Jr. *Vibrations of Soils and Foundations*. Civil Engineering and Engineering Mechanics Series. Prentice-Hall, Inc., Englewood Cliffs, N.J., 1970.
- [88] T.T. Kallioğlu, A. Papadopoulou, and K. Ptilakis. Shear modulus and damping of natural sands. In H. Di Benedetto, T. Doanh, H. Geoffroy, and C. Sauzéat, editors, *Deformation Characteristics of Geomaterials*, pages 401–407. A.A. Balkema, 2003. Proc. IS-Lyon03.
- [89] Stokoe K.H., M.B. Darendeli, R.B. Gilbert¹, F.-Y. Menq, and W.K. Choi. Development of a new family of normalized modulus reduction and material damping curves. In *International Workshop on Uncertainties in Nonlinear Soil Properties and their Impact on Modeling Dynamic Soil Response*, UC Berkeley, CA, 2004.
- [90] T.C. Kim and M. Novak. Dynamic properties of some cohesive soils of ontario. *Canadian Geotech. Journal*, 18(3):371–389, 1981.
- [91] W.T. Koiter. General theorems for elastic-plastic solids. In I.N. Sneddon and R. Hill, editors, *Progress in Solid Mechanics*, volume 1, pages 165–221, North-Holland, Amsterdam, 1960.
- [92] T. Kokusho, Y. Yoshida, and E. Yasuyuki. Dynamic properties of soft clay for wide strain range. *Soils and Foundations*, 22(4):1–18, 1982.
- [93] D. Kolymbas. An outline of hypoplasticity. *Archive of Applied Mechanics*, 61:143–151, 1991.
- [94] R.L. Kondner and J.S. Zelasko. A hyperbolic stress-strain formulation for sands. In *2nd Pan. Am. Conf. Soil Mech. Found. Eng.*, volume 1, pages 289–394, Brazil, 1963.
- [95] W. Krajewski and O. Reul. Erfahrungen zur numerischen Berechnung von Baugruben und Gründungen im Rhein-Main-Gebiet. In T. Schanz, editor, *Workshop AK 1.6 Numerik in der Geotechnik*, number 11 in Schriftenreihe Geotechnik, pages 103–117. Bauhaus-Universität Weimar, 2003.
- [96] R. Kuwano and R.J. Jardine. On the application of cross-anisotropic elasticity to granular materials at very small strains. *Géotechnique*, 52(10):727–749, 2002.
- [97] P.V. Lade. Modelling the strengths of engineering materials in three dimensions. *Mech. Cohes. Frict. Mat.*, 2:339356, 1997.

- [98] P.V. Lade and V. Abelev. Characterization of cross-anisotropic soil deposits from isotropic compression tests. *Soils and Foundations*, 45(5):89–102, 2005.
- [99] P.V. Lade and J.M. Duncan. Elasto-plastic stress-strain theory for cohesionless soil. *Proc. ASCE: Journal of the Geotechnical Engineering Division*, 101(GT10):1037–1053, 1975.
- [100] R. Larsson and M. Mulabdic. Piezocone tests in clay. Technical Report 42, Swedish Geotechnical Institute, Linköping, 1991.
- [101] P.I. Lewin and J.B. Burland. Stress-probe experiments on saturated normally consolidated clay. *Géotechnique*, 20(1):38–56, 1970.
- [102] X.S. Li. A sand model with state-dependent dilatancy. *Géotechnique*, 52(3):173–186, 2002.
- [103] X.S. Li and Y.F. Dafalias. Dilatancy for cohesionless soils. *Géotechnique*, 50(4):449–460, 2000.
- [104] M.L. Lings and P.D. Greening. A novel bender extender element for soil testing. *Géotechnique*, 51(8):713–717, 2001.
- [105] T. Länsivaara and S. Nordal. Loading history model for small strain behavior of soils. In *15th Int. Conf. SMGE, Istanbul*, 2001. Rotterdam: Balkema.
- [106] W. Lode. Versuche über den Einfluß der mittleren Hauptspannung auf das Fließen der Metalle Eisen Kupfer und Nickel. *Physik*, 36:913–939, 1926.
- [107] T.N. Lohani, G. Imai, K. Tani, and S. Shibuya. G_{max} of fine grained soils at wide void ratio range focusing on time-dependent behavior. *Soils and Foundations*, 41(5):87–102, 2001.
- [108] T. Lunne, P.K. Robertson, and J.J.M. Powell. *Cone Penetration Testing in Geotechnical Practice*. E & FN Spon, London, 1997.
- [109] R.J. Mair. Developments in geotechnical engineering research: application to tunnels and deep excavations. *Proceedings of Institution of Civil Engineers, Civil Engineering*, pages 27–41, 1993. Unwin Memorial Lecture 1992.
- [110] W.F. Marcuson and H.E. Wahls. Time effects on dynamic shear modulus of clays. *Proc. ASCE: Journal of the Soil Mechanics and Foundation Division*, 98(SM12):1359–1373, 1972.
- [111] G. Masing. Eigenspannungen und Verfestigung beim Messing. In *Proc. 2nd Int. Congr. Appl. Mech.*, Zurich, 1926.
- [112] L. Matesic and M. Vucetic. Strain-rate effect on soil secant shear modulus at small cyclic strains. *Journal of Geotechnical and Geoenvironmental Engineering*, 129(6):536–549, 2003.

-
- [113] H. Matsuoka. Stress-strain relationships of sands based on the mobilized plane. *Soils and Foundations*, 14(2):47–61, 1974.
- [114] H. Matsuoka and T. Nakai. A new failure criterion for soils in three dimensional stresses. In *IUTAM Conference on Deformation and Failure of Granular Materials*, pages 253–263, Delft, 1982.
- [115] P.W. Mayne and F.H. Kulhawy. K_0 -OCR relationships in soil. *Journal of Geotechnical Engineering*, 108(6):851–872, 1982.
- [116] P.W. Mayne and G.J. Rix. $G_{max} - q_c$ relationships for clays. *Geotechnical Testing Journal*, 16(1):54–60, 1993.
- [117] G. Mesri, T.W. Feng, and J.M. Benak. Postdensification penetration resistance of clean sands. *Journal of Geotechnical Engineering, ASCE*, 116(7):1095–1115, 1990.
- [118] R.D. Mindlin. Compliance of elastic bodies in contact. *Journal of Applied Mechanics, ASME*, 16:259–268, 1949.
- [119] R.D. Mindlin and H. Deresiewicz. Elastic spheres in contact under varying oblique forces. *Journal of Applied Mechanics, ASME*, 20(3):327–344, 1953.
- [120] J.K. Mitchell. *Fundamentals of Soil Behavior*. John Wiley & Sons, 2 edition, 1993.
- [121] S.C. Möller. *Tunnel induced settlements and structural forces in linings*. PhD thesis, Universität Stuttgart, 2006.
- [122] G. Modoni, A. Flora, L.Q. Anh Dan, C. Mancuso, J. Koseki, K. Balakrishnaier, and F. Tatsuoka. A simple experimental procedure for the complete characterization of small strain stiffness of gravels. In M. Jamiolkowski, R. Lancellotta, and D.C.F. Lo Presti, editors, *Pre-Failure Deformation Characteristics of Geomaterials*, pages 123–130. A.A. Balkema, 1999. Proc. IS-Torino99.
- [123] O. Mohr. Welche Umstände bedingen die Elastizitätsgrenze und den Bruch eines Materials? *VDI-Zeitschrift*, 44:1524, 1900.
- [124] J.W. Morse and F.T. Mackenzie. *Geochemistry of sedimentary carbonates*, volume 48 of *Developments in sedimentology*. New York, Elsevier, 1982.
- [125] Z. Mroz. On the description of anisotropic workhardening. *J. Mech. Phys. Solids*, 15:163–175, 1967.
- [126] Z. Mroz, V.A. Norris, and O.C. Zienkiewicz. An anisotropic hardening model for soils and its application to cyclic loading. *Int. J. Numer. Anal. Meth. Geomech.*, 2: 203–221, 1978.
- [127] H. Müllerschön. *Spannungs-Verformungsverhalten granularer Materialien am Beispiel von Berliner Sand*. PhD thesis, Universität Stuttgart, 2000.

- [128] T. Nakai and H. Matsuoka. Deformations of soils in three-dimensional stresses. In *IUTAM Conference on Deformation and Failure of Granular Materials*, pages 275–285, Delft, 1982.
- [129] A. Niemunis and I. Herle. Hypoplastic model for cohesionless soils with elastic strain range. *Mechanics of Cohesive-Frictional Materials*, 2(4):279–299, 1997.
- [130] R.L. Nigbor and T. Imai. The suspension p-s velocity logging method. In *Proc. 13th Int. Conf. SMFE*, volume 1, pages 57–61, New Delhi, India, 1994. TC10.
- [131] J. Ohde. *Grundbaumechanik*, volume 3. Hütte, 1951.
- [132] Y. Ohsaki and R. Iwasaki. On dynamic shear moduli and Poisson's ratio of soil deposits. *Soils and Foundations*, 13(4):61–73, 1973.
- [133] A.G. Papadimitriou and G.D. Bouckovalas. Plasticity model for sand under small and large cyclic strains: a multiaxial formulation. *Soil Dynamics and Earthquake Engineering*, 22:191–204, 2002.
- [134] A.G. Papadimitriou, G.D. Bouckovalas, and Y. F. Dafalias. Plasticity model for sand under small and large cyclic strains. *Journal of Geotechnical and Geoenvironmental Engineering*, 127(11):973–983, 2001.
- [135] R. B. Peck. Deep excavations and tunneling in soft ground. In *7th Int. Conf. SMFE. Sociedad Mexicana de Mecanica de Suelos, A. C.*, 1969.
- [136] D.S. Pennington, D.F.T. Nash, and M.L. Lings. Anisotropy of G_0 shear stiffness in Gault clay. *Géotechnique*, 47(3):391–398, 1997.
- [137] J.M. Pestana and A.J. Whittle. Formulation of a unified constitutive model for clays and sands. *Int. J. Numer. Anal. Meth. Geomech.*, 23:1215–1243, 1999.
- [138] D.M. Potts and L. Zdravkovic. *Finite element analysis in geotechnical engineering: theory*. Thomas Telford, 1999.
- [139] D.C.F. Lo Presti and M. Jamiolkowski. Discussion: Estimate of elastic shear modulus in holocene soil deposits. *Soils and Foundations*, 38(263-265), 1998.
- [140] D.C.F. Lo Presti, M. Jamiolkowski, O. Pallara, and A. Cavallaro. Rate and creep effect on the stiffness of soils. In T.C. Sheahan and V.N. Kaliakin, editors, *Measuring and Modeling Time Dependent Soil Behavior*, number 61 in Geotechnical Special Publication, pages 166–180. ASCE, 1996.
- [141] D.C.F. Lo Presti, O. Pallara, R. Lancellotta, M. Armandi, and R. Maniscalco. Monotonic and cyclic loading behaviour of two sands at small strains. *Geotechnical Testing Journal*, 16(4):409–424, December 1993.
- [142] J.-H. Prevost. Mathematical modelling of monotonic and cyclic undrained clay behavior. *Int. J. Numer. Anal. Meth. Geomech.*, 1(2):195–216, 1977.

-
- [143] R. Pyke. Nonlinear soil models for irregular cyclic loadings. *Proc. ASCE: Journal of the Geotechnical Engineering Division*, 105(GT6):715–726, 1979.
- [144] T. Ramamurthy and P.C. Rawat. Shear strength of sand under general stress system. In *Proc. 8th Int. Conf. SMFE*, volume 1, pages 339–342, Moscow, 1973.
- [145] W. Ramberg and W. R. Osgood. Description of stress-strain curve by three parameters. Technical Note 902, National Advisory Committee for Aeronautics, Washington, DC, 1943.
- [146] K.I. Rammah, D.V. Val, and A.M. Puzrin. Effects of ageing on small-strain stiffness of overconsolidated clays. *Géotechnique*, 54(5):319–322, 2004.
- [147] S. Rampello, G.M.B. Viggiani, and A. Amorosi. Small-strain stiffness of reconstituted clay compressed along constant triaxial effective stress ratio paths. *Géotechnique*, 47(3):475–489, 1997.
- [148] D. Richardson. *Investigations of threshold effects in soil deformation*. PhD thesis, City University, London, 1988.
- [149] F.E. Jr. Richart. Some effects of dynamic soil properties on soil structure interaction. *Proc. ASCE: Journal of the Geotechnical Engineering Division*, 101(GT12):1193–1240, 1975.
- [150] P.K. Robertson, R.G. Campanella, D. Gillespie, and A. Rice. Seismic cpt to measure in-situ shear wave velocity. *Journal of Geotechnical Engineering*, 112(8):791–803, 1986.
- [151] K.H. Roscoe and A.N. Schofield. Mechanical behaviour of an idealised wet clay. In *Proc. 2nd European Conf. SMFE*, volume 1, pages 47–54, Wiesbaden, 1963.
- [152] E. Rosenblueth and I. Herrera. On a kind of hysteretic damping. *Proc. ASCE: Journal of the Engineering Mechanics Division*, 90(EM4):37–47, 1964.
- [153] P.W. Rowe. The stress-dilatancy relation for static equilibrium of an assembly of particles in contact. In *Proc. of the Royal Society of London. Series A, Mathematical and Physical Sciences*, volume 269, pages 500–527, 1962.
- [154] K. Runesson and A. Samuelsson. *Numeta 85 Numerical Methods in Engineering, Theory and Applications*, chapter Aspects on numerical techniques in small deformation plasticity, pages 337–347. A.A. Balkema, 1985.
- [155] J.A. Santos and A.G. Correia. Reference threshold shear strain of soil. Its application to obtain a unique strain-dependent shear modulus curve for soil. In *15th Int. Conf. SMGE*, volume 1, pages 267–270, Istanbul, 2001. A.A. Balkema.
- [156] S.A. Savidis. *Empfehlungen des Arbeitskreises Baugrunderdynamik*. Grundbauinstitut der Technischen Universität Berlin, 2002.

- [157] T. Schanz. Zur Modellierung des mechanischen Verhaltens von Reibungsmaterialien. Mitt. Inst. für Geotechnik 45, Universität Stuttgart, 1998.
- [158] T. Schanz, P.A. Vermeer, and P.G. Bonnier. *Beyond 2000 in Computational Geotechnics*, chapter Formulation and verification of the Hardening-Soil Model, pages 281–290. Balkema, Rotterdam, 1999.
- [159] J.H. Schmertmann. The mechanical aging of soils. *Journal of Geotechnical Engineering*, 117(9):1288–1330, 1991.
- [160] B.F. Schmidt. *Settlements and ground movements associated with tunnelling in soils*. PhD thesis, University of Illinois, Urbana, 1969.
- [161] H.F. Schweiger. Results from numerical benchmark exercises in geotechnics. In P. Mestat, editor, *Numge 2002. 5th European Conference Numerical Methods in Geotechnical Engineering*, volume 1, pages 305–314, Paris, 2002. LCPC.
- [162] H.B. Seed and I.M. Idriss. Soil moduli and damping factors for dynamic response analysis. Report 70-10, EERC, Berkeley, CA, 1970.
- [163] T. Shibata and D. Karube. Influence of the variation of the intermediate principal stress on mechanical properties of normally consolidated clay. In *Proc. 6th Int. Conf. SMFE*, volume 1, pages 359–363, Paris, 1985.
- [164] S. Shibuya, T. Mitachi, S. Yamashita, and H. Tanaka. Effect of sample disturbance on G_{max} of soils - a case study. In S. Shibuya T. Mitachi and S. Miura, editors, *Prefailure Deformations of Geomaterials*, volume 2, pages 77–82. Balkema, Rotterdam, 1995.
- [165] D.J. Shirley and L.D. Hampton. Shear-wave measurements in laboratory sediments. *The Journal of the Acoustical Society of America*, 63(2):607–613, 1978.
- [166] J.C. Simo and T.J.R. Hughes. *Computational Inelasticity*, volume 7 of *Interdisciplinary Applied Mathematics*. Springer, 1998.
- [167] J.C. Simo and R.L. Taylor. Consistent tangent operators for rate-independent elastoplasticity. *Computer Methods in Applied Mechanics and Engineering*, 48:101–118, 1985.
- [168] B. Simpson. Retaining structures: displacement and design, the 32nd Rankine lecture. *Géotechnique*, 42(4):541–576, 1992.
- [169] O.K. Soreide. *Mixed hardening models for frictional soils*. PhD thesis, Norwegian University of Science and Technology (NTNU), Trondheim, 1990.
- [170] S.A. Stallebrass. *Modelling the effect of recent stress history on the deformation of over-consolidated soils*. PhD thesis, City University, London, 1990.

-
- [171] S.E. Stallebrass and R.N. Taylor. The development and evaluation of a constitutive model for the prediction of ground movements in overconsolidated clay. *Géotechnique*, 47(2):235–253, 1997.
- [172] K.H. Stokoe, M.B. Darendeli, R.D. Andrus, and L.T. Brown. Dynamic soil properties: laboratory, field and correlation studies. In *Proc. 2nd Int. Conf. on Earthquake Geotech. Eng.*, volume 3, pages 811–845. A.A. Balkema, 1999.
- [173] K.H. Stokoe and J.C. Santamarina. Seismic-wave-based testing in geotechnical engineering. In *GeoEng 2000: An International Conference on Geotechnical and Geological Engineering*, volume 1, pages 1490–1536, Melbourne, Australia, 2000. Technomic Publishing Company.
- [174] K.H. Stokoe, S.G. Wright, A.B. James, and M.R. Jose. *Geophysical characterization of sites*, chapter Characterization of geotechnical sites by SASW method, pages 15–25. Balkema, A.A., Rotterdam, 1994.
- [175] K.H.I. Stokoe and R.D. Woods. In situ shear wave velocity by cross-hole method. *Proc. ASCE: Journal of the Soil Mechanics and Foundations Division*, 98(SM5):443–460, 1972.
- [176] H.B. Sutherland and M.S. Mesdary. The influence of the intermediate principal stress on the strength of sand. In *Proc. 7th Int. Conf. SMFE*, volume 1, pages 391–399, Mexico City, 1969.
- [177] F. Tatsuoka. Impacts on geotechnical engineering of several recent findings from laboratory stress-strain tests on geomaterials. Department of Civil Engineering Mechanics, Columbia University, 2000. The 2000 Burmister Lecture.
- [178] F. Tatsuoka and K. Ishihara. Yielding of sand in triaxial compression. *Soils and Foundations*, 14(2):63–76, 1974.
- [179] K. Terzaghi, R.B. Peck, and G. Mesri. *Soil Mechanics in Engineering Practice*. Wiley-Interscience; 3 edition (January 1, 1996), 3 edition, 1996.
- [180] S. Toki, S. Shibuya, and S. Yamashita. Standardization of laboratory test methods to determine the cyclic deformation properties of geomaterials in Japan. In S. Shibuya T. Mitachi and S. Miura, editors, *Pre-failure Deformations of Geomaterials*, volume 2, pages 741–784. Balkema, Rotterdam, 1995.
- [181] C. Truesdell and W. Noll. *The Non-Linear Field Theories of Mechanics*, volume III of *Encyclopedia of Physics*. Berlin, Heidelberg: Springer, 1965.
- [182] T.W. and R.V. Whitman. *Soil Mechanics*. John Wiley & Sons, New York, NY, 1969.
- [183] P.A. Vermeer. A double hardening model for sand. *Géotechnique*, 28(4):413–433, 1978.

- [184] P.A. Vermeer. A modified initial strain method for plasticity problems. In *Proc. 3th Int. Conf. Numer. Meth. Geomech.*, pages 377–387. Balkema, Rotterdam, 1979.
- [185] P.A. Vermeer. *Formulation and analysis of sand deformation problems*. PhD thesis, Delft University of Science and Technology, 1980.
- [186] P.A. Vermeer, T. Benz, and R. Schwab. *Modern Trends in Geomechanics*, chapter Two Elastoplastic Models for Small and Large Strains and Their Use in Engineering Practise, pages 175–190. Springer, 2006.
- [187] G. Viggiani and J.H. Atkinson. Stiffness of fine grained soils at very small strains. *Géotechnique*, 45(2):249–265, 1995.
- [188] M. Vucetic and R. Dobry. Effect of soil plasticity on cyclic response. *Journal of Geotechnical Engineering, ASCE*, 117(1):89–107, 1991.
- [189] M. Vucetic and K. Tabata. Influence of soil type on the effect of strain rate on small-strain cyclic shear modulus. *Soils and Foundations*, 43(5):161–173, 2003.
- [190] M. Vucetic, K. Tabata, and L. Matesic. Effect of average straining rate on shear modulus at small cyclic strains. In H. Di Benedetto, T. Doanh, H. Geoffroy, and C. Sauzéat, editors, *Deformation Characteristics of Geomaterials*, pages 321–328. A.A. Balkema, 2003. Proc IS-Lyon03.
- [191] M. Wehnert. *Ein Beitrag zur drainierten und undrainierten Analyse in der Geotechnik*. PhD thesis, Universität Stuttgart, 2006.
- [192] R.V. Whitman. The behaviour of soils under transient loadings. In *Proc. 4th Int. Conf. SMFE*, volume 1, pages 207–210, London, 1957.
- [193] T. Wichtmann and T. Triantafyllidis. Influence of a cyclic and dynamic loading history on dynamic properties of dry sand, Part i: cyclic and dynamic torsional prestraining. *Soil Dynamics and Earthquake Engineering*, 24(2):127–147, 2004.
- [194] R.D. Woods. Measurement of dynamic soil properties. In *Proc. Earthquake Engineering and Soil Dynamics*, volume 1, pages 91–78, Pasadena, CA, 1978. ASCE, New York.
- [195] C.P. Wroth. In-situ measurement of initial stresses and deformation characteristics. In *Proc. Geot. Engng Div. Speciality Conf. on In-situ Measurement of Soil Properties*, pages 181–230, Rayleigh, NC, 1975. ASCE.
- [196] Y. Yamada and K. Ishihara. Anisotropic deformation characteristic of sand under three dimensional stress conditions. *Soils and Foundations*, 19(1):79–94, 1979.
- [197] S. Yimsiri and K. Soga. Effect of surface roughness on small-strain modulus: Micromechanics view. In M. Jamiolkowski, R. Lancellotta, and D. Lo Presti, editors, *Pre-failure Deformation Characteristics of Geomaterials*, volume 1, pages 597–602. A.A. Balkema, Rotterdam, 1999.

- [198] R.N. Yong and R.D. Japp. A flow law for clays in dynamic compression. In *Proc. Int. Symp. Wave Propagation and Dynam. Prop. of Earth Materials*, Albuquerque, N.M., 1967. University of New Mexico Press.
- [199] M.S. Youssef, A.H. El Ramli, and M. El Demery. Relationships between shear strength, consolidation, liquid limit, and plastic limit for remoulded clays. In *Proc. 6th Int. Conf. SMFE*, volume 1, pages 126–129, Montreal, 1965.
- [200] P. Yu and Jr. F.E. Richart. Stress ratio effects on shear modulus of dry sands. *Journal of Geotechnical Engineering*, 110(3):331–345, 1984.
- [201] C. Zambelli. *Modellazione costitutiva del comportamento meccanico in campo dinamico di material granulari*. Tesi di laurea, Politecnico di Milano, 2002.
- [202] L. Zdravkovic and R.J. Jardine. Some anisotropic stiffness characteristics of a silt under general stress conditions. *Géotechnique*, 47(3):407–437, 1997.

Appendix A

Small-Strain Overlay Fortran Code

```
1 | !-----+
2 | !23456789012345678901234567890123456789012345678901234567890123456789|
3 | !-----+
4 | ! Small-Strain Overlay
5 | !-----+
6 | ! Purpose: Add small-strain stiffness to elastoplastic models
7 | !
8 | !           I/O Type
9 | ! Eps0      I  R(6) : total train at start of increment
10 | ! dEps      I  R(6) : strain increment
11 | ! UsrSta0   I  R(*) : state variables at start of inc; uses #2 to #10
12 | ! UsrSta0   O  R(*) : state variables at end of inc; uses #2 to #10
13 | ! Sig0      I  R(6) : stress at start of increment
14 | ! G         I  R      : elastic modulus of background model (larger str.)
15 | ! GFac      I  R      : ratio G0/G where G0 is the small-strain modulus
16 | ! Gam07     I  R      : 70% threshold shear strain
17 | ! GAct      O  R      : Actual elastic modulus to be used for calculation
18 | !
19 | ! The state variables are organized as follows
20 | ! UsrSta( 1) : not used
21 | ! UsrSta( 2) : not used
22 | ! UsrSta( 3) : Strain history component 1
23 | ! UsrSta( 4) : Strain history component 2
24 | ! UsrSta( 5) : Strain history component 3
25 | ! UsrSta( 6) : Strain history component 4
26 | ! UsrSta( 7) : Strain history component 5
27 | ! UsrSta( 8) : Strain history component 6
28 | ! UsrSta( 9) : Actual stiffness GAct for output etc. / redundant
29 | ! UsrSta(10) : Monotonic stiffness; reloading for GAct>G*UsrSt(10)
30 | !
31 | ! Needs: Subroutine PrnSig(dEpsD,xN1e,xN2e,xN3e,dEpsD1,dEpsD2,dEpsD3)
32 | !         that finds the Eigensystem (xN1e,xN2e,xN3e) and Eigenvalues
33 | !         (dEpsD1,dEpsD2,dEpsD3) of the strain increment dEpsD
34 | !-----+
35 | ! Author: Thomas Benz <thomas.benz@wewi-numge.de>
36 | !-----+
37 | !
38 | ! SUBROUTINE Small_Strain ( Eps0,dEps,UsrSta,UsrSta0,Sig0,
39 | ! *                       G,GFac,Gam07,GAct)
40 | !
41 | ! IMPLICIT DOUBLE PRECISION (A-H, O-Z)
42 | !
```

```

43  DIMENSION Eps0(6),dEps(6),UsrSta(*),UsrSta0(*),Sig0(6),
44  2          Trafo(3,3),Hist1(3,3),Hist2(3,3),
45  3          Chi(3,3),GamHis(2),GBct(2),
46  4          xT(3),xN1e(3),xN2e(3),xN3e(3),
47  5          dEpsD(6),Eps(6),DEl(6,6),SigEl(6)
48  ! Initialization
49  Eps = 0.
50  Chi = 0.
51  If (UsrSta0(10).EQ.0.) UsrSta0(10)=10. ! GFactor_max:=10
52  ! Determine new stiffness in the principal system of dEpsD
53  dEpsVol =(dEps(1) + dEps(2) + dEps(3))
54  dEpsD(1) = dEps(1) - dEpsVol/3d0
55  dEpsD(2) = dEps(2) - dEpsVol/3d0
56  dEpsD(3) = dEps(3) - dEpsVol/3d0
57  dEpsD(4) = dEps(4)
58  dEpsD(5) = dEps(5)
59  dEpsD(6) = dEps(6)
60  CALL PrnSig(dEpsD,xN1e,xN2e,xN3e,dEpsD1,dEpsD2,dEpsD3)
61  ! Build fields
62  dEpsD(1) = dEpsD1
63  dEpsD(2) = dEpsD2
64  dEpsD(3) = dEpsD3
65  dEpsD(4) = 0 d0
66  dEpsD(5) = 0 d0
67  dEpsD(6) = 0 d0
68  IF (UsrSta0(3).LE.1) THEN !Init History
69  Hist1(1,1) = 100d0
70  Hist1(2,1) = 0d0
71  Hist1(3,1) = 0d0
72  Hist1(1,2) = 0d0
73  Hist1(2,2) = 100d0
74  Hist1(3,2) = 0d0
75  Hist1(1,3) = 0d0
76  Hist1(2,3) = 0d0
77  Hist1(3,3) = 100d0
78  ELSE
79  Hist1(1,1) = UsrSta0(3)
80  Hist1(2,1) = UsrSta0(6)/2d0
81  Hist1(3,1) = UsrSta0(8)/2d0
82  Hist1(1,2) = UsrSta0(6)/2d0
83  Hist1(2,2) = UsrSta0(4)
84  Hist1(3,2) = UsrSta0(7)/2d0
85  Hist1(1,3) = UsrSta0(8)/2d0
86  Hist1(2,3) = UsrSta0(7)/2d0
87  Hist1(3,3) = UsrSta0(5)
88  END IF
89  Trafo(1,1) = xN1e(1)
90  Trafo(2,1) = xN1e(2)
91  Trafo(3,1) = xN1e(3)
92  Trafo(1,2) = xN2e(1)
93  Trafo(2,2) = xN2e(2)
94  Trafo(3,2) = xN2e(3)

```

```

95     Trafo(1,3) = xN3e(1)
96     Trafo(2,3) = xN3e(2)
97     Trafo(3,3) = xN3e(3)
98     ! Transform starin history in principal system of dEpsD
99     DO i = 1,3
100         DO j = 1,3
101             X1 = 0d0
102             DO k = 1,3
103                 X2 = 0d0
104                 DO l = 1,3
105                     X2 = X2 + Hist1(k,l) * Trafo(l,j)
106                 END DO
107             X1 = X1 + X2 * Trafo(k,i)
108         END DO
109         Hist2(i,j) = X1
110     END DO
111 END DO
112 ! Elongation of uncorrected history
113 DO i = 1,3
114     Chi(1,i) = Hist2(i,i) - 100d0
115 END DO
116 ! Build transformation matrix
117 nCountXT = 0
118 DO i = 1,3
119     xT(i) = 1d0
120     IF (chi(1,i) * dEpsD(i) .LT. 0d0) THEN
121         xT(i) = 10d0/DSQRT(chi(1,i) + 100d0)
122         nCountXT = nCountXT + 1
123     END IF
124 END DO
125 ! Calculate new history
126 DO i = 1,3
127     DO j = 1,3
128         Hist2(i,j) = Hist2(i,j) * xT(i) * xT(j)
129     END DO
130     Chi(2,i) = Hist2(i,i) - 100d0
131     Hist2(i,i) = Hist2(i,i) + dEpsD(i)
132     Chi(3,i) = Hist2(i,i) - 100d0
133 END DO
134 ! Calculate history strain (iso)
135 dEps2 = (dEpsD(1)**2+dEpsD(2)**2+dEpsD(3)**2)
136 DO i = 1,2
137     GamHis(i) = DSQRT(3d0*
138 2         ((dEpsD(1)*Chi(i+1,1))**2 +
139 3         (dEpsD(2)*Chi(i+1,2))**2 +
140 4         (dEpsD(3)*Chi(i+1,3))**2 )/dEps2)
141 END DO
142 ! From strain history to stiffness
143 Fac0 = GamHis(2)-GamHis(1)
144 Fac1 = Gam07/0.385d0 ! use 0.429 for HD
145 DO i = 1,2 ! i=1:=loading; i=2:= reloading
146     IF (i .EQ. 2) Fac1 = 2d0*Fac1

```

```

147     IF ((UsrSta0(10).NE.1) .OR. (i.EQ.2)) THEN
148         GamOff = (DSQRT(GFac)-1d0) * Fac1
149         IF (Fac0 .LE. 0) THEN
150             GBct(i) = G*GFac*(1/(1+GamHis(1)/ Fac1)-
151 2             GamHis(1)/ Fac1/(1+GamHis(1)/ Fac1)**2)
152         ELSE
153             IF (GamHis(1).LT.GamOff .AND. GamHis(2).LT.GamOff) THEN
154                 GBct(i) = G*GFac*(GamHis(2)/(1 d0+GamHis(2)/ Fac1)-
155 2                 GamHis(1)/(1 d0+GamHis(1)/ Fac1))/ Fac0
156             ELSE
157                 IF (GamHis(1).LT.GamOff.AND.GamHis(2).GT.GamOff) THEN
158                     GBct(i) = (G*GFac*(GamOff/(1 d0+GamOff/Fac1)-
159 2                     GamHis(1)/(1 d0+GamHis(1)/ Fac1))+
160 3                     G*(GamHis(2)-GamOff))/ Fac0
161                 ELSE
162                     GBct(i) = G
163                 END IF
164             END IF
165         END IF
166     END IF
167 END DO
168 ! Update StateVar with new history (BackTrafo)
169 DO i = 1,3
170     DO j = 1,3
171         X1 = 0 d0
172         DO k = 1,3
173             X2 = 0 d0
174             DO l = 1,3
175                 X2 = X2 + Hist2(k,l) * Trafo(j,l)
176             END DO
177             X1 = X1 + X2 * Trafo(i,k)
178         END DO
179         Hist1(i,j) = X1
180     END DO
181 END DO
182 UsrSta(3) = Hist1(1,1)
183 UsrSta(4) = Hist1(2,2)
184 UsrSta(5) = Hist1(3,3)
185 UsrSta(6) = Hist1(1,2) + Hist1(2,1)
186 UsrSta(7) = Hist1(2,3) + Hist1(3,2)
187 UsrSta(8) = Hist1(1,3) + Hist1(3,1)
188 ! Loading/ reloading in combination with an elastoplastic model:
189 ! Update of UsrSta(10)
190 IF (UsrSta0(10).NE.1.) UsrSta(10)=MIN(GBct(1)/G,UsrSta0(10))
191 ! Copy stiffness (always reloading in combination with plasticity)
192 GAct = GBct(2)
193 END IF
194 ! Plateau avoids numerical problems in isotropic loading
195 IF (GamHis(2).Lt.1d-6) GAct = G*GFac
196 !
197 !
198 ! Either RETURN here or check stress work...

```

```

199  !
200      Do i=1,6
201          Eps(i) = Eps0(i) + dEps(i)
202      End Do
203      EpsV0=(Eps0(1)+Eps0(2)+Eps0(3))
204      EpsD0=((Eps0(1)-Eps0(2))**2
205      2          +(Eps0(2)-Eps0(3))**2
206      3          +(Eps0(3)-Eps0(1))**2)/6 d0
207      4          +(Eps0(4)/2 d0)**2+(Eps0(5)/2 d0)**2+(Eps0(6)/2 d0)**2
208      IF ( DABS(EpsV0) .Lt. 1 d-12 .OR.
209      2          DABS(EpsD0) .Lt. 1 d-12          ) THEN
210          ! No Check - or alternative code
211      ELSE
212          SigV0=(Sig0(1)+Sig0(2)+Sig0(3))/3 d0
213          SigD0=((Sig0(1)-Sig0(2))**2
214      2          +(Sig0(2)-Sig0(3))**2
215      3          +(Sig0(3)-Sig0(1))**2)/6 d0
216      4          +(Sig0(4))**2+(Sig0(5))**2+(Sig0(6))**2
217          xxK=SigV0/EpsV0
218          xxG=DSQRT(SigD0/EpsD0)/2 d0
219          xxF1=xxK+4.d0*xxG/3.d0
220          xxF2=xxK-2.d0*xxG/3.d0
221          DEL=0
222          DO i=1,3
223              DO j=1,3
224                  DEL(i,j) = xxF2
225              END DO
226              DEL(i,i) = xxF1
227              DEL(i+3,i+3) = xxG
228          END DO
229          xWElasticD2 = DOT.PRODUCT(MATMUL(DEL,Eps ),Eps )-
230      2          DOT.PRODUCT(MATMUL(DEL,Eps0),Eps0)
231      END IF
232      IF (xWElasticD2 .LT. 0 d0) THEN ! Unloading
233          GAct=MAX(GAct,xxG)          ! Correction
234      END IF
235      ! For output etc.
236      UsrSta(9) = GAct
237      RETURN
238      END SUBROUTINE Small.Strain

```


Appendix B

Return mapping in Fortran code

```
1 | !-----+
2 | !23456789012345678901234567890123456789012345678901234567890123456789|
3 | !-----+
4 | ! A cutting plane algorithm after Boris Jeremic
5 | !-----+
6 | ! Purpose: Implicit return mapping
7 | !
8 | !      I/O Type
9 | ! D      I  R(6,6) : elastic stiffness matrix
10 | ! Sig0   I  R(6)   : stress at start of increment
11 | ! SigE   I  R(6)   : elastic trial stress
12 | ! dEps   I  R(6)   : strain increment
13 | ! UstrSta0 I R(*)   : state variables at start of increment
14 | ! UstrSta O R(*)   : state variables at end of increment
15 | ! Sig     O R(6)   : stress at end of increment
16 | ! R0,Q0  I  R      : internal variables at start of increment
17 | ! R ,Q   O  R      : internal variables at end of increment
18 | ! ...    I  R or I : model specific parameters
19 | !
20 | ! Needs: Derivatives of the yield function(s) and plastic potential(s)
21 | ! * Surface1 (yield surface):   dfdSig:=n
22 | ! * Surface1 (plastic potential): dgdSig:=m, d2gdSig2:=m2
23 | ! * Surface1 (int. variables):   R
24 | ! * Surface2 (yield surface):   dfdSig:=u
25 | ! * Surface2 (plastic potential): dgdSig:=w, d2gdSig2:=w2
26 | ! * Surface2 (int. variables):   Q
27 | ! Assumes: dmdR=0 and dwdQ=0
28 | !-----+
29 | ! Thomas Benz <thomas.benz@wewi-numge.de>
30 | !-----+
31 |
32 | !-----+
33 | ! Case 1: Single surface return
34 | !-----+
35 |
36 | ! 1. Initialize
37 |
38 |     it=0
39 |     itmax=20
40 |     xTol =1d-9
41 |     Unity=0.0d0
42 |     Unity(1,1)=1.0d0
```

```

43      Unity(2,2)=1.0d0
44      Unity(3,3)=1.0d
45      R = R0
46
47      ! 2. Starting Point
48
49      Sig = SigE
50      xF1 = f1(Sig,R...)
51      xF1Tol = xTol*DAbs(xF1)
52      CALL Calc_Derivatives1(Sig,R,n,n2,m,...)
53      xLI1 = xF/(DOT_PRODUCT(n,MAIMUL(D,m))-(dF1dR*dR))
54      Sig = SigE-xLI1*MAIMUL(D,m)
55      R = R0 + dR*xLI1
56      xF1 = f1(Sig,R...)
57
58      ! 3. Euler Backward ... (Iteration)
59
60      DO WHILE (ABS(xF1).GT.xF1Tol .AND. it.LE.itmax)
61          CALL Calc_Derivatives1(Sig,R,n,n2,m,...)
62          Res = Sig-(SigE-xLI1*MAIMUL(D,m))
63          T=Unity+xLI1*MAIMUL(D,m2)
64          CALL MatInv33(T,Ti)
65          dLI1 = (xF1-DOT_PRODUCT(n,MAIMUL(Res,Ti)))
66          dLI1 = dLI1/(DOT_PRODUCT(n,MAIMUL(MAIMUL(D,m),Ti))-(dF1dR*dR))
67          xLI1 = xLI1 + dxLI1
68          Sig = Sig-MAIMUL(Res+dxLI1*MAIMUL(D,m),Ti)
69          R = R0 + dR*xLI1
70          xF1 = f1(Sig,R...)
71          it=it+1
72      END DO
73
74      IF (xLI1.Gt.0 .AND. it.LE.itmax) THEN
75          ! Return mapping OK
76      ELSE
77          ! Numerical problem (starting point)?
78      END IF
79
80      RETURN
81      END
82
83      !-----+
84      ! Case 2: Two surface return |
85      !-----+
86
87      ! 1. Initialize
88
89      it=0
90      itmax=20
91      xTol =1.0d-9
92      Unity=0.0d0
93      Unity(1,1)=1.0d0
94      Unity(2,2)=1.0d0

```

```

95     Unity(3,3)=1.0 d0
96     R = R0
97     Q = Q0
98
99     ! 2. Starting Point
100
101     Sig = SigE
102     xF1 = f1(Sig,R...)
103     xF2 = f2(Sig,Q...)
104     xF1Tol = xTol*DAbs(xF1)
105     xF2Tol = xTol*DAbs(xF2)
106     CALL Calc_Derivatives1(Sig,R,n,n2,m,...)
107     CALL Calc_Derivatives2(Sig,Q,u,u2,w,...)
108     xOmega11 = - dF1dR*dR + DOT_PRODUCT(n,MATMUL(D,m))
109     xOmega12 = DOT_PRODUCT(n,MATMUL(D,w))
110     xOmega21 = DOT_PRODUCT(u,MATMUL(D,m))
111     xOmega22 = - dF2dQ*dQ + DOT_PRODUCT(u,MATMUL(D,w))
112     xLI1      = (xF1      * xOmega22 - xF2      * xOmega12)/
113     2          (xOmega11 * xOmega22 - xOmega12 * xOmega21)
114     xLI2      = (xF2      * xOmega11 - xF1      * xOmega21)/
115     2          (xOmega11 * xOmega22 - xOmega12 * xOmega21)
116     Sig = SigE-(xLI1*MATMUL(D,m) + xLI2*MATMUL(D,w))
117     R = R0 + dR*xLI1
118     Q = Q0 + dQ*xLI2
119     xF1 = f1(Sig,R...)
120     xF2 = f2(Sig,Q...)
121
122     ! 3. Euler Backward ... (Iteration)
123
124     DO WHILE ((ABS(xF1).GT.xF1Tol .OR.
125     2          ABS(xF2).GT.xF2Tol .OR.)
126     3          .AND. it.LE.itmax)
127         CALL Calc_Derivatives1(Sig,R,n,n2,m,...)
128         CALL Calc_Derivatives2(Sig,Q,u,u2,w,...)
129         Res = Sig-(SigE-xLI1*MATMUL(D,m)-xLI2*MATMUL(D,w))
130         T=Unity+xLI1*MATMUL(D,m2)+xLI2*MATMUL(D,w2)
131         CALL MatInv33(T,Ti)
132         xOmega11 = DOT_PRODUCT(n,MATMUL(MATMUL(D,m),Ti))
133     2          -dF1dR*dR
134         xOmega12 = DOT_PRODUCT(n,MATMUL(MATMUL(D,w),Ti))
135         xOmega21 = DOT_PRODUCT(u,MATMUL(MATMUL(D,m),Ti))
136         xOmega22 = DOT_PRODUCT(u,MATMUL(MATMUL(D,w),Ti))
137     2          -dF2dQ*dQ
138         xOmegaF1 = F1 - DOT_PRODUCT(Res,MATMUL(Ti,n))
139         xOmegaF2 = F2 - DOT_PRODUCT(Res,MATMUL(Ti,u))
140         dxLI1 = (xOmegaCo * xOmega22 - xOmegaCa * xOmega12)/
141     2          (xOmega11 * xOmega22 - xOmega12 * xOmega21)
142         dxLI2 = (xOmegaCa * xOmega11 - xOmegaCo * xOmega21)/
143     2          (xOmega11 * xOmega22 - xOmega12 * xOmega21)
144         xLI1 = xLI1 + dxLI1
145         xLI2 = xLI2 + dxLI2
146         Sig = Sig-MATMUL(Res+dxLI1*MATMUL(D,m)

```

```
147      2                                +dxLI2*MATMUL(D,w) , Ti)
148      R = R0 + dR*xLI1
149      Q = Q0 + dQ*xLI2
150      xF1 = f1(Sig,R...)
151      xF2 = f2(Sig,Q...)
152      it=it+1
153      END DO
154
155      IF (xLICone.Gt.0 .AND. xLICap.GT.0 .AND. it.LE.itmax) THEN
156        ! Return mapping OK
157      ELSE
158        ! Numerical problem (starting point)?
159      END IF
160
161      RETURN
162      END
```

Appendix C

Two surface return strategy

```
1 | !-----+
2 | !2345678901234567890123456789012345678901234567890123456789|
3 | !-----+
4 | ! HS gray corner strategy or when to activate cone , cap , or both |
5 | !-----+
6 | ! After P.G. Bonnier (2000) |
7 | !-----+
8 | !     1. Init(Small-strain stiffness , Dilatancy , etc.)
9 | !     2. Trial stress
10 | !     3. Check yield surfaces and return stress
11 | !       IF (Cone yield surface is violated) THEN
12 | !         CALL Cone_Return ! Return and harden cone
13 | !         IF (Failure criteria is violated) THEN
14 | !           CALL Cone_Failure ! Return to ultimate cone
15 | !           IF (Tension criteria is exceeded) THEN
16 | !             CALL Tension_CutOff ! Do a 3-surface tension return
17 | !           END IF
18 | !         END IF
19 | !       IF (Cap yield surface is violated) THEN
20 | !         CALL Cap_Return ! Return and harden cap
21 | !         IF (Cone yield surface is violated) THEN
22 | !           CALL Mixed_Return ! Return and harden cone and cap
23 | !           IF (Failure criteria is violated) THEN
24 | !             CALL Cap_Failure ! Return to cap and ultimate cone
25 | !           END IF
26 | !         END IF
27 | !       END IF
28 | !     ELSE ! No friction hardening (yet): check Cap only
29 | !       IF (Cap yield surface is violated) THEN
30 | !         CALL Cap_Return ! Return and harden cap
31 | !         IF (Cone yield surface is violated) THEN
32 | !           CALL Mixed_Return ! Return and harden cone and cap
33 | !           IF (Failure criteria is violated) THEN
34 | !             CALL Cap_Failure ! Return to cap and ultimate cone
35 | !           END IF
36 | !         END IF
37 | !       END IF
38 | !     END IF
39 | !     END IF
40 | !     4. Check Apex; Update stress and state variables; Exit
```


Appendix D

Material data

Table D.1: Element tests - HS-Small parameters

Parameter (Symbol)	Unit	Sand(D)	Sand(L)	Clay
<i>I. User defined parameters</i>				
E_{50}^{ref}	$\left[\frac{kN}{m^2} \right]$	30000	12000	2150
$E_{\text{oed}}^{\text{ref}}$	$\left[\frac{kN}{m^2} \right]$	30000	16000	1050
$E_{\text{ur}}^{\text{ref}}$	$\left[\frac{kN}{m^2} \right]$	90000	60000	11500
m	$[-]$	0.55	0.75	0.80
c	$\left[\frac{kN}{m^2} \right]$	0.00	0.00	0.00
φ	$[\circ]$	42.0	34.0	20.0
ψ	$[\circ]$	16.0	0.0	0.0
ν_{ur}	$[-]$	0.25	0.25	0.20
p^{ref}	$\left[\frac{kN}{m^2} \right]$	100	100	100
K_0^{nc}	$[-]$	0.40	0.44	0.66
R_f	$[-]$	0.90	0.90	0.90
σ_{Tension}	$\left[\frac{kN}{m^2} \right]$	0.00	0.00	0.00
E_0^{ref}	$\left[\frac{kN}{m^2} \right]$	270000	168000	80000
$\gamma_{0.7}$	$[-]$	0.0002	0.0001	0.0002
<i>II. Internal parameters</i>				
E_i^{ref}	$\left[\frac{kN}{m^2} \right]$	65488	23800	14050
α	$[-]$	1.47	1.56	0.78
K_S/K_C	$[-]$	1.84	2.01	4.76

Table D.2: Steinhaldenfeld NATM tunnel - HS-Small parameters

Parameter (Symbol)	Unit	Fill	Keuper (up)	Keuper (lo)	Limestone
<i>I. User defined parameters</i>					
γ_{unsat}	$\left[\frac{kN}{m^3}\right]$	20.0	24.0	23.0	23.0
γ_{sat}	$\left[\frac{kN}{m^3}\right]$	-	-	-	-
E_{50}^{ref}	$\left[\frac{kN}{m^2}\right]$	10000	33000	16000	190000
$E_{\text{oad}}^{\text{ref}}$	$\left[\frac{kN}{m^2}\right]$	10000	33000	16000	190000
$E_{\text{ur}}^{\text{ref}}$	$\left[\frac{kN}{m^2}\right]$	30000	100000	48000	575000
m	$[-]$	0.50	0.40	0.40	0.30
c	$\left[\frac{kN}{m^2}\right]$	10.00	25.00	25.00	200.00
φ	$[\circ]$	25.0	25.0	25.0	35.00
ψ	$[\circ]$	0.0	0.0	0.0	0.0
ν_{ur}	$[-]$	0.20	0.20	0.20	0.20
p^{ref}	$\left[\frac{kN}{m^2}\right]$	100	100	100	100
K_0^{nc}	$[-]$	0.58	0.58	0.58	0.43
R_f	$[-]$	0.90	0.90	0.90	0.90
σ_{Tension}	$\left[\frac{kN}{m^2}\right]$	0.00	0.00	0.00	0.00
E_0^{ref}	$\left[\frac{kN}{m^2}\right]$	120000	400000	192000	2400000
$\gamma_{0.7}$	$[-]$	0.0002	0.0002	0.0002	0.00005
<i>II. Internal parameters</i>					
E_i^{ref}	$\left[\frac{kN}{m^2}\right]$	24206	81216	39353	415649
α	$[-]$	0.80	0.83	0.83	1.52
K_S/K_C	$[-]$	1.62	1.72	1.71	1.95

Table D.3: Heinenoord tunnel - HS-Small parameters

Parameter (Symbol)	Unit	Fill	Sand	Clay
<i>I. User defined parameters</i>				
γ_{unsat}	$\left[\frac{kN}{m^3} \right]$	17.5	-	-
γ_{sat}	$\left[\frac{kN}{m^3} \right]$	17.5	20.0	20.0
E_{50}^{ref}	$\left[\frac{kN}{m^2} \right]$	14000	35000	12000
$E_{\text{oed}}^{\text{ref}}$	$\left[\frac{kN}{m^2} \right]$	14000	35000	7000
$E_{\text{ur}}^{\text{ref}}$	$\left[\frac{kN}{m^2} \right]$	42000	105000	35000
m	$[-]$	0.50	0.50	0.90
c	$\left[\frac{kN}{m^2} \right]$	3.00	0.00	7.00
φ	$[^\circ]$	27.0	35.0	31.0
ψ	$[^\circ]$	0.0	0.0	0.0
ν_{ur}	$[-]$	0.20	0.20	0.20
p^{ref}	$\left[\frac{kN}{m^2} \right]$	100	100	100
K_0^{nc}	$[-]$	0.55	0.43	0.48
R_f	$[-]$	0.90	0.90	0.90
σ_{Tension}	$\left[\frac{kN}{m^2} \right]$	0.00	0.00	0.00
E_0^{ref}	$\left[\frac{kN}{m^2} \right]$	126000	240000	210000
$\gamma_{0.7}$	$[-]$	0.0002	0.0002	0.0002
<i>II. Internal parameters</i>				
E_i^{ref}	$\left[\frac{kN}{m^2} \right]$	32786	72888	34582
α	$[-]$	0.88	1.43	0.93
K_S/K_C	$[-]$	1.62	1.64	1.93

Table D.4: Deep excavation in sand (Berlin) - HS-Small parameters

Parameter (Symbol)	Unit	Sand (L1)	Sand (L2)	Sand (L3)
<i>I. User defined parameters</i>				
γ_{unsat}	$\left[\frac{kN}{m^3} \right]$	19.0	19.0	19.0
γ_{sat}	$\left[\frac{kN}{m^3} \right]$	20.0	20.0	20.0
E_{50}^{ref}	$\left[\frac{kN}{m^2} \right]$	45000	75000	105000
$E_{\text{oed}}^{\text{ref}}$	$\left[\frac{kN}{m^2} \right]$	45000	75000	105000
$E_{\text{ur}}^{\text{ref}}$	$\left[\frac{kN}{m^2} \right]$	180000	300000	315000
m	$[-]$	0.55	0.55	0.55
c	$\left[\frac{kN}{m^2} \right]$	1.00	1.00	1.00
φ	$[^\circ]$	35.0	38.0	38.0
ψ	$[^\circ]$	5.0	6.0	6.0
ν_{ur}	$[-]$	0.20	0.20	0.20
p^{ref}	$\left[\frac{kN}{m^2} \right]$	100	100	100
K_0^{nc}	$[-]$	0.43	0.38	0.38
R_f	$[-]$	0.90	0.90	0.90
σ_{Tension}	$\left[\frac{kN}{m^2} \right]$	0.00	0.00	0.00
E_0^{ref}	$\left[\frac{kN}{m^2} \right]$	405000	675000	na
$\gamma_{0.7}$	$[-]$	0.0002	0.0002	na
<i>II. Internal parameters</i>				
E_i^{ref}	$\left[\frac{kN}{m^2} \right]$	96662	154447	208642
α	$[-]$	1.48	1.87	1.88
K_S/K_C	$[-]$	2.15	2.07	1.59

Table D.5: Excavation in Rupel clay - HS-Small parameters

Parameter (Symbol)	Unit	Fill	Rupel Clay
<i>I. User defined parameters</i>			
γ_{unsat}	$\left[\frac{kN}{m^3}\right]$	18.0	19.0
γ_{sat}	$\left[\frac{kN}{m^3}\right]$	20.0	20.0
E_{50}^{ref}	$\left[\frac{kN}{m^2}\right]$	20000	15000
$E_{\text{oed}}^{\text{ref}}$	$\left[\frac{kN}{m^2}\right]$	20000	15000
$E_{\text{ur}}^{\text{ref}}$	$\left[\frac{kN}{m^2}\right]$	60000	50000
m	$[-]$	0.50	0.70
c	$\left[\frac{kN}{m^2}\right]$	1.00	25.00
φ	$[^\circ]$	32.0	20.0
ψ	$[^\circ]$	2.0	0.0
ν_{ur}	$[-]$	0.20	0.15
p^{ref}	$\left[\frac{kN}{m^2}\right]$	100	100
K_0^{nc}	$[-]$	0.43	0.66
R_f	$[-]$	0.90	0.90
σ_{Tension}	$\left[\frac{kN}{m^2}\right]$	0.00	0.00
E_0^{ref}	$\left[\frac{kN}{m^2}\right]$	180000	207000
$\gamma_{0.7}$	$[-]$	0.00015	0.00025
<i>II. Internal parameters</i>			
E_i^{ref}	$\left[\frac{kN}{m^2}\right]$	43421	39992
α	$[-]$	1.16	5.31
K_S/K_C	$[-]$	1.63	1.36

Table D.6: Load test on a spread footing on sand - HS-Small parameters

Parameter (Symbol)	Unit	Sand (Triaxial)	Sand (Site)
<i>I. User defined parameters</i>			
γ_{unsat}	$\left[\frac{kN}{m^3} \right]$	18.0	18.0
γ_{sat}	$\left[\frac{kN}{m^3} \right]$	20.0	20.0
E_{50}^{ref}	$\left[\frac{kN}{m^2} \right]$	16000	16000
$E_{\text{oed}}^{\text{ref}}$	$\left[\frac{kN}{m^2} \right]$	22000	22000
$E_{\text{ur}}^{\text{ref}}$	$\left[\frac{kN}{m^2} \right]$	90000	90000
m	$[-]$	0.50	0.50
c	$\left[\frac{kN}{m^2} \right]$	0.00	0.00
φ	$[\circ]$	37.0	37.0
ψ	$[\circ]$	1.5	1.5
ν_{ur}	$[-]$	0.20	0.20
p^{ref}	$\left[\frac{kN}{m^2} \right]$	100	100
K_0^{nc}	$[-]$	0.41	0.41
R_f	$[-]$	0.90	0.90
σ_{Tension}	$\left[\frac{kN}{m^2} \right]$	0.00	0.00
E_0^{ref}	$\left[\frac{kN}{m^2} \right]$	260000	390000
$\gamma_{0.7}$	$[-]$	0.0002	0.0004
<i>II. Internal parameters</i>			
E_i^{ref}	$\left[\frac{kN}{m^2} \right]$	30785	30785
α	$[-]$	5.08	5.08
K_S/K_C	$[-]$	2.38	2.38

Table D.7: Sülfeld excavation - HS-Small parameters

Parameter (Symbol)	Unit	Sand(D)	Glacial Till	Clayey silt
<i>I. User defined parameters</i>				
γ_{unsat}	$\left[\frac{kN}{m^2} \right]$	18.5	18.5	18.5
γ_{sat}	$\left[\frac{kN}{m^2} \right]$	20.5	21.5	21.5
E_{50}^{ref}	$\left[\frac{kN}{m^2} \right]$	40000	8500	8500
$E_{\text{oed}}^{\text{ref}}$	$\left[\frac{kN}{m^2} \right]$	38000	6150	6000
$E_{\text{ur}}^{\text{ref}}$	$\left[\frac{kN}{m^2} \right]$	120000	25750	23000
m	$[-]$	0.50	0.70	0.90
c	$\left[\frac{kN}{m^2} \right]$	0.10	6.00	30.00
φ	$[\circ]$	37.5	28.0	32.0
ψ	$[\circ]$	5.0	6.0	10.0
ν_{ur}	$[-]$	0.20	0.29	0.30
p^{ref}	$\left[\frac{kN}{m^2} \right]$	100	100	100
K_0^{nc}	$[-]$	0.80	0.80	0.80
R_f	$[-]$	0.90	0.90	0.90
σ_{Tension}	$\left[\frac{kN}{m^2} \right]$	0.00	0.00	0.00
E_0^{ref}	$\left[\frac{kN}{m^2} \right]$	480000	154500	138000
$\gamma_{0.7}$	$[-]$	0.0002	0.0003	0.0003
<i>II. Internal parameters</i>				
E_i^{ref}	$\left[\frac{kN}{m^2} \right]$	82037	27783	20715
α	$[-]$	1.62	0.90	1.10
K_S/K_C	$[-]$	1.65	2.78	2.22

Curriculum Vitæ

14.05.1971 Geboren in Tübingen

1991-1993 Universität Tübingen
Studium der Physik (Vordiplom)

1993-1997 Universität Stuttgart
Studium des Bauingenieurwesens (Dipl.-Ing.)

1997-1999 Michigan Technological University
Studium der Geophysik (M.Sc.)

1998-2000 Schlumberger Geco-Prakla, Nord- und Südamerika
Field Geophysicist

2000-2002 Leonhardt, Andrä und Partner, Stuttgart
Projektingenieur Brückenbau

2002-2006 Bundesanstalt für Wasserbau, Karlsruhe, Referat Grundbau
Wissenschaftlicher Angestellter

2002-2006 Universität Stuttgart, Institut für Geotechnik
Wissenschaftlicher Mitarbeiter

20.09.2006 Promotion

Mitteilungen des Instituts für Geotechnik

- Nr. 01 Thamm, B. R. (1974) Anfangssetzungen und Anfangsporenwasserüberdrücke eines normalverdichteten wassergesättigten Tones.
€ 5,11
- Nr. 02 Gußmann, P. (1975) Einheitliche Berechnung von Grundbruch und Böschungsbruch.
€ 2,56
- Nr. 03 Feeser, V. (1975) Die Bedeutung des Kalziumkarbonats für die bodenphysikalischen Eigenschaften vom Löß.
Vergriffen
- Nr. 04 Du Thin, K. (1976) Standsicherheit von Böschungen: Programm-Dokumentation.
Vergriffen
- Nr. 05 Smoltczyk, U. / Pertschi, O. / Hilmer, K. (1976) Messungen an Schleusen in der UDSSR. Schleusennorm der UDSSR (SN 30365).
Vergriffen
- Nr. 06 Hilmer, K. (1976) Erddruck auf Schleusenkamerwände.
€ 9,20
- Nr. 07 Laumans, Q. (1977) Verhalten einer ebenen, in Sand eingespannten Wand bei nichtlinearen Stoffeigenschaften des Bodens.
€ 9,20
- Nr. 08 Lächler, W. (1977) Beitrag zum Problem der Teilflächenpressung bei Beton am Beispiel der Pfahlkopfanschlüsse.
Vergriffen
- Nr. 09 Spotka, H. (1977) Einfluß der Bodenverdichtung mittels Oberflächenrüttelgeräten auf den Erddruck einer Stützwand bei Sand.
Vergriffen

- Nr. 10 Schad, H. (1979) Nichtlineare Stoffgleichungen für Böden und ihre Verwendung bei der numerischen Analyse von Grundbauaufgaben.
Vergriffen
- Nr. 11 Ulrich, G. (1980) Verschiebungs- und kraftgesteuerte Plattendruckversuche auf konsolidierenden Böden. Zum Modellgesetz der Konsolidation.
Gußmann, P.
€ 10,23
- Nr. 12 Salden, D. (1980) Der Einfluß der Sohlenform auf die Traglast von Fundamenten.
€ 12,78
- Nr. 13 Seeger, H. (1980) Beitrag zur Ermittlung des horizontalen Bettungsmoduls von Böden durch Seitendruckversuche im Bohrloch.
€ 12,78
- Nr. 14 Schmidt, H.H. (1981) Beitrag zur Ermittlung des Erddrucks auf Stützwände bei nachgiebigem Baugrund.
€ 12,78
- Nr. 15 Smolczyk, U. / Schweikert, O. (1981) Vorstudie über bauliche Alternativen für Durchgangsstraßen in Siedlungen.
€ 6,14
- Nr. 16 Malcharek, K. / Smolczyk, U. (1981) Vergleich nationaler Richtlinien für die Berechnung von Fundamenten.
€ 7,67
- Nr. 17 Gruhle, H.D. (1981) Das Verhalten des Baugrundes unter Einwirkung vertikal gezogener Ankerplatten als räumliches Problem des Erdwiderstandes.
Vergriffen
- Nr. 18 Kobler, W. (1982) Untersuchungen über Böschungs- und Grundbruch bei begrenzten Lastflächen.
€ 12,78
- Nr. 19 Lutz, W. (1983) Tragfähigkeit des geschlitzten Baugrunds neben Linienlasten.
€ 12,78
- Nr. 20 Smolczyk, U. (1983) Studienunterlagen Bodenmechanik und Grundbau; überarbeitete Ausgabe 1983.
€ 20,45

- | | | | | |
|--------|--|--------|---|------------|
| Nr. 21 | Schweikert, O. | (1984) | Der Einfluß des Böschungswinkels auf die Berechnung des aktiven Erddrucks. | € 10,23 |
| Nr. 22 | Vogt, N. | (1984) | Erdwiderstandsermittlung bei monotonen und wiederholten Wandbewegungen in Sand. | Vergriffen |
| Nr. 23 | Buchmaier, R. | (1985) | Zur Berechnung von Konsolidationsproblemen bei nichtlinearem Stoffverhalten. | € 12,78 |
| Nr. 24 | Schad, H.
Smolczyk, U. /
Schad, H. /
Zoller, P. | (1985) | Möglichkeiten der Böschungssicherung bei kleinen Baugruben.
Sonderkonstruktionen der Böschungssicherung. | € 17,90 |
| Nr. 25 | Gußmann, P. | (1986) | Die Methode der Kinematischen Elemente. | € 10,23 |
| Nr. 26 | Steinmann, B. | (1985) | Zum Verhalten bindiger Böden bei monotoner einaxialer Beanspruchung. | Vergriffen |
| Nr. 27 | Lee, S.D. | (1987) | Untersuchungen zur Standsicherheit von Schlitzten im Sand neben Einzelfundamenten. | Vergriffen |
| Nr. 28 | Kolb, H. | (1988) | Ermittlung der Sohlreibung von Gründungskörpern unter horizontalem kinematischen Zwang. | € 12,78 |
| Nr. 29 | Ochmann, H. | (1988) | Ebene Grenzzustände von Erdböschungen im stochastischen Sicherheitskonzept. | € 12,78 |
| Nr. 30 | Breinlinger, F. | (1989) | Bodenmechanische Stoffgleichungen bei großen Deformationen sowie Be- und Entlastungsvorgängen. | € 15,34 |
| Nr. 31 | Smolczyk, U. /
Breinlinger, F. /
Schad, H. /
Wittlinger, M. | (1989) | Beitrag zur Bemessung von Tunneln in offener Bauweise. | € 12,78 |

- | | | | | |
|--------|---|--------|---|------------|
| Nr. 32 | Gußmann, P. /
Schanz, T. /
Smoltczyk, U. /
Willand, E. | (1990) | Beiträge zur Anwendung der KEM (Erddruck,
Grundbuch, Standsicherheit von Böschungen) | |
| | | | | Vergriffen |
| Nr. 33 | Gruhle, H.D. | (1990) | Der räumliche Erdwiderstand vor über-
wiegend horizontal belasteten Ankerplatten. | |
| | | | | Vergriffen |
| Nr. 34 | Henne, J. | (1995) | Zur Bewehrung von verformten Boden-
schichten durch Einsatz zugfester Geokunst-
stoffe. | |
| | | | | € 15,34 |
| Nr. 35 | Wittlinger, M. | (1994) | Ebene Verformungsuntersuchungen zur Weck-
ung des Erdwiderstandes bindiger Böden. | |
| | | | | € 15,34 |
| Nr. 36 | Schad, H. | (1992) | Zeit- und geschwindigkeitsabhängiges Materi-
alverhalten in der Geotechnik – Experimentelle
Erfassung und numerische Analyse. | |
| | | | | € 15,34 |
| Nr. 37 | Belz, I. | (1992) | Zur Ermittlung dynamischer Bodenkennwerte
in situ aus der Systemantwort des Erregers. | |
| | | | | € 15,34 |
| Nr. 38 | Ma, J. | (1994) | Untersuchungen zur Standsicherheit der durch
Stützscheiben stabilisierten Böschungen. | |
| | | | | € 15,34 |
| Nr. 39 | Smoltczyk, U. | (1994) | Sonderheft: 25 Jahre Lehre und Forschung in
der Geotechnik. | |
| | | | | € 15,34 |
| Nr. 40 | Rilling, B. | (1994) | Untersuchungen zur Grenztragfähigkeit bindi-
ger Schüttstoffe am Beispiel von Lößlehm. | |
| | | | | € 17,90 |
| Nr. 41 | Vermeer, P.A. | (1996) | Deponiebau und Geotechnik. | |
| | | | | € 17,90 |
| Nr. 42 | Vermeer, P.A. | (1997) | Baugruben in Locker- und Festgestein. | |
| | | | | € 17,90 |
| Nr. 43 | Brinkmann, C. | (1998) | Untersuchungen zum Verhalten von Dich-
tungsübergängen im Staudammbau. | |
| | | | | € 17,90 |

- | | | | | |
|--------|------------------------|--------|---|---------|
| Nr. 44 | Fiechter-Scharr,
I. | (1998) | Beeinflussung von Erdbaustoffen durch Beimischen eines organophilen Bentonits. | € 17,90 |
| Nr. 45 | Schanz, T. | (1998) | Zur Modellierung des mechanischen Verhaltens von Reibungsmaterialien. | € 17,90 |
| Nr. 46 | Akinrogunde,
A.E. | (1999) | Propagation of Cement Grout in Rock Discontinuities Under Injection Conditions. | € 17,90 |
| Nr. 47 | Vogt-Breyer, C. | (1999) | Experimentelle und numerische Untersuchungen zum Tragverhalten und zur Bemessung horizontaler Schraubanker. | € 17,90 |
| Nr. 48 | Vermeer, P.A. | (1999) | Neue Entwicklungen in der Geotechnik. | € 17,90 |
| Nr. 49 | Marcher, T. | (2002) | Resultate eines Versuchsprogramms an Beaucaire-Mergel. | € 17,90 |
| Nr. 50 | Marcher, T. | (2003) | Nichtlokale Modellierung der Entfestigung dichter Sande und steifer Tone. | € 17,90 |
| Nr. 51 | Ruse, N.M. | (2004) | Räumliche Betrachtung der Standsicherheit der Ortsbrust beim Tunnelvortrieb. | € 17,90 |
| Nr. 52 | Beutinger, P.H. | (2005) | Ein geotechnischer Beitrag zur Standsicherheit mobiler Baumaschinen. | € 17,90 |
| Nr. 53 | Wehnert, M. | (2006) | Ein Beitrag zur drainierten und undrainierten Analyse in der Geotechnik. | € 17,90 |
| Nr. 54 | Möller, S.C. | (2006) | Tunnel induced settlements and forces in linings | € 17,90 |
| Nr. 55 | Benz, T. | (2007) | Small-Strain Stiffness of Soils and its Numerical Consequences. | € 17,90 |

